Inaugural Dissertation in partial fulfilment of the requirement for the degree of Doctor of the Natural Science

Dielectronic Recombination Experiments with Tungsten Ions at the Test Storage Ring and Development of a Single-Particle Detector at the Cryogenic Storage Ring

Kaija Spruck

May 2015

Institut für Atom- und Molekülphysik,
Justus-Liebig-Universität Gießen

Zusammenfassung

Experimente zur dielektronischen Rekombination von Wolfram-Ionen am Schwerionen-Speicherring TSR und Entwicklung eines Einzelteilchendetektors für den kryogenen Speicherring CSR — Diese Arbeit befasst sich mit Elektron-Ion Stoßexperimenten an den Ionenspeicherringen des Max-Planck-Instituts für Kernphysik in Heidelberg. Am Schwerionen-Speicherring TSR wurden absolute Rekombinationsratenkoeffizienten von hochgeladenen Wolfram-Ionen mit offener 4-f Schalenstruktur gemessen. Die daraus abgeleiteten Plasmaratenkoeffizienten wurden benutzt, um die Aussagekraft von neu entwickelten, theoretischen Berechnungen zu testen. Plasmaratenkoeffizienten von hochgeladenen Wolfram-Ionen sind insbesondere für die Entwicklung von Plasmamodellen an Fusionsreaktoren interessant, da Wolfram als unvermeidbare Verunreinigung in Fusionsplasmen vorliegt. Die experimentellen Ergebnisse liegen im relevanten Temperaturbereich um bis zu einem Faktor 10 höher als die bisher verwendeten, theoretischen Daten, was die Notwendigkeit von verlässlicheren theoretischen Rechnungen unterstreicht. Im Zuge dieser Arbeit wurde des Weiteren, in Anlehnung an die Detektoren, die bei den Experimenten am TSR zum Einsatz kamen, ein beweglicher Einzelteichendetektor für Elektron-Ion Rekombinationsmessungen am kryogenen Speicherring CSR entwickelt. Das Gerät wurde speziell im Hinblick auf die niedrigen Ionenenergien und die kryogene Umgebungstemperatur des CSR entwickelt. In einer Serie von Tests wurde der Detektor sorgfältig charakterisiert und erfolgreich auf seine Kompatibilität mit diesen Anforderungen getestet. Der Detektor war Teil der Infrastruktur bei der Inbetriebnahme des CSR bei Raumtemperatur (2014) und wird aktuell im ersten kryogenen Betrieb des CSR (2015) als Teilchendetektor eingesetzt.

Abstract

Dielectronic Recombination Experiments with Tungsten Ions at the Test Storage Ring and Development of a Single-Particle Detector at the Cryogenic Storage Ring — This work is about electron-ion collision experiments at the ion storage rings of the Max Planck Institute for Nuclear Physics in Heidelberg. Absolute recombination rate coefficients of highly-charged tungsten ions featuring an open 4-f-shell structure have been measured at the heavy-ion storage ring TSR. The resulting plasma rate coefficients have been used to probe the significance of newly developed theoretical approaches. Plasma rate coefficients of highly-charged tungsten ions are in particular interesting for the development of plasma models for nuclear fusion reactors, since tungsten is a foreseeable impurity in the fusion plasma. In the relevant temperature range, the experimental results exceed the theoretical data used so far by up to a factor of 10, showing the need for more reliable theoretical calculations. Furthermore, based on the design of the detectors which have been used in the experiments at TSR, a movable single-particle detector for electron-ion recombination studies at the cryogenic storage ring CSR has been developed and installed within the scope of this work. The device has been designed specifically to meet the requirements of the CSR regarding low ion energies and cryogenic ambient temperature conditions. In a series of experiments, the detector was carefully characterised and successfully tested for its compatibility with these requirements. The detector was part of the infrastructure used for the room-temperature commissioning of CSR (2014) and is currently operated as a single-particle counter during the first cryogenic operation of CSR in 2015.

Contents

List of Figures

List of Tables

1. Introduction

Interaction of ions with other particles–neutral atoms or molecules, free electrons, or photons–are important processes in a wide range of natural or man-made plasma environments. Understanding of these processes allows to link the microscopic, quantum state of the single particle to macroscopic, classical-statistical properties of the plasma, like pressure and temperature.

Storage rings are powerful devices for reaction studies on heavy ions since they provide efficient ways of beam manipulation and diagnostics, as well as of detection of product particles. In combination with electron coolers, they not only deliver initial-state prepared parent beams, but also means for precise electron-ion collision studies. Storage ring experiments on electron recombination and collisional ionisation processes provide insight into fundamental atomic structure and dynamics. In plasmas, the charge-state balances of atoms are dependent on the cross sections of the involved processes, which renders the data valuable for technical plasma applications. As the amount of data needed exceeds what experiments can deliver in foreseeable time, theory needs to be developed to the point where it can predict the data with acceptable accuracy. Still, high-quality, reliable, experimental data on at least a few selected processes is needed as benchmarks.

As one example, nuclear fusion reactors are a much anticipated possibility of ecologically 'clean' and virtually unlimited energy production. In order to develop concepts for the fusion power demonstration plant DEMO, last experiments will be conducted at the international tokamak ITER. One of the technical challenges is the preservation of the fusion condition in spite of the presence of plasma impurities which are created by sputtering from the tokamak walls. Since tungsten is foreseen as a coating material, reliable data on ionisation and recombination cross sections of highly-charged tungsten ions are needed as input parameters for the relevant plasma models.

Within the scope of this work, merged-beams electron-ion recombination experiments on three species of open 4-f-shell highly-charged tungsten ions were conducted at the heavy-ion storage ring TSR. With recombination rate coefficients among the highest ever measured, these experiments drove the apparatus to its technical limits. Nevertheless, a collection of reliable energy-resolved recombination rate coefficients for W^{18+}, W^{19+} and W^{21+} could be obtained. The data has already served as a

test bench for a promising new class of theoretical models for recombination of open f-shell ions.

The second half of this work is part of an effort to reimplement the successful electron-ion merged-beams technique at the new heavy-ion storage ring CSR in Heidelberg. CSR is a next-generation all-cryogenic and electrostatic storage ring with emphasis on studies of heavy molecular ions. The cryogenic storage volume, which mimics the conditions found in cold interstellar plasmas, allows to prepare these ions in their rovibrational ground states. Cold interstellar media, like e.g. the cores of dark molecular clouds, have been the topic of scientific research for decades. Plasma models have been developed to give insight into their chemical evolution under the typical conditions of very low temperature and particle density. In the last few years, new findings concerning the role of singly-charged atomic cations in these reaction chains have drawn some attention towards a lack of accurate recombination data for the corresponding atomic species.

The future electron-ion merged-beams set-up at CSR will be an ideal platform to establish trustworthy empirical datasets of these recombination rates. As part of the full apparatus, a highly efficient, movable single-product-particle detector for recombination or ionisation experiments at CSR was designed, tested and installed at the storage ring. While much general experimental expertise could be gained from the experiments at TSR, the new storage ring imposed many technical challenges on the way to a successfully operating detector set-up, mainly related to the cryogenic vacuum environment.

The general structure of this work is the following: A brief introduction to resonant and non-resonant recombination processes is given in Chapter 2. The impact of recombination processes on equilibrium conditions in plasmas is discussed in detail, and general theoretical approaches to dielectronic recombination rate coefficients are presented. As examples which are directly related to this work, the role of recombination processes of tungsten ions in hot fusion plasmas and of recombination processes of singly-charged ions in cold, interstellar plasmas are discussed.

The basics of storage rings are presented in Chapter 3. The main focus is on electron-cooler storage rings and their application in merged-beams experiments. The two electron-cooler storage rings, TSR and CSR, of the Max Planck Institute for Nuclear Physics in Heidelberg, Germany, are described in detail.

Chapter 4 reports on experiments and results of the electron-ion recombination measurements of said three open 4-f-shell charge states of tungsten ions at the heavy-ion storage ring TSR. The results were used to generate experimental plasma recombination rate coefficients, which are compared with the heuristic model data used to-date by the fusion community. Two new, more elaborate theoretical approaches for ions with open f-shell structures are described and their predictions are compared

to the experimental results. At last, the experimental results and their relevance to the field of fusion physics are summarised.

A detailed description of the development and testing of a single-particle detector for the merged-beams set-up at CSR is given in Chapter 5. The design of the detector is presented in detail. Extensive offline tests of the detector prior to integration into CSR were performed, demonstrating, among others, the reliable cryogenic operation of the device. For the characterisation of the particle sensor, a theoretical description of the detection efficiency was developed and probed against experiment. The first operation of the particle detector in CSR is briefly reported. The chapter closes with a summary and a brief outlook to future applications of the detector.

Chapter 6 summarises the two experimental chapters and presents further possibilities enabled by the results of this work.

2. Electron-Ion-Recombination in Plasmas

A plasma is a mixture of free particles of which at least some carry electric charge. This so-called 'fourth state of matter' is generated by adding energy (in the form of pressure, temperature or radiation) such that electrons can escape from the binding potential of atoms or molecules. While the biosphere, our direct natural environment, consists primarily of neutral atoms and molecules, this state of matter is somewhat exceptional on the universal scale: From the hot bodies of stars to the cold interstellar medium, most of the known matter of our galaxy exists in the form of plasma.

Depending on physical properties like temperature and particle density, or on external fields, i.e., electric, magnetic, and gravitational fields, plasma can appear in various types. Figure 2.1 sketches boundary conditions for different classes of so-called 'weakly coupled' plasmas, where the thermal energy of the plasma particles is significantly higher than their binding energy. This is the relevant regime for natural or technical fusion plasmas and the molecular plasmas of the cold interstellar space which are the main topics of this work. More examples are provided within the figure.

Relativistic plasmas, as found near astrophysical high-energy sources appear at high temperatures only, but can cover a wide range of particle densities. Their differentiation from non-relativistic plasmas is defined, more or less arbitrarily, at a thermal velocity of 33% of the speed of light c. Besides temperature, the particle density is an important quantity for the characterisation of plasmas. A classical plasma is defined by a de Broglie wavelength [2] that is significantly smaller than the mean next-neighbour particle distance in the electron gas, i.e. by

$$\lambda_{dB} = \frac{h}{p} \ll \lambda_n = n_e^{-1/3} \tag{2.1}$$

where p is the particle momentum, h Planck's constant, and n_e the electron density. If λ_{dB} is similar or even larger than the interparticle distance, quantum effects become important and the plasma is degenerate. A well-known example for plasmas of this type are quantum electron gases in metals. In spite of their high temperature, also electrons in white dwarfs exist as degenerate plasmas, in contrast to the electrons of main-sequence stars, which—at much lower density—form a classical plasma.

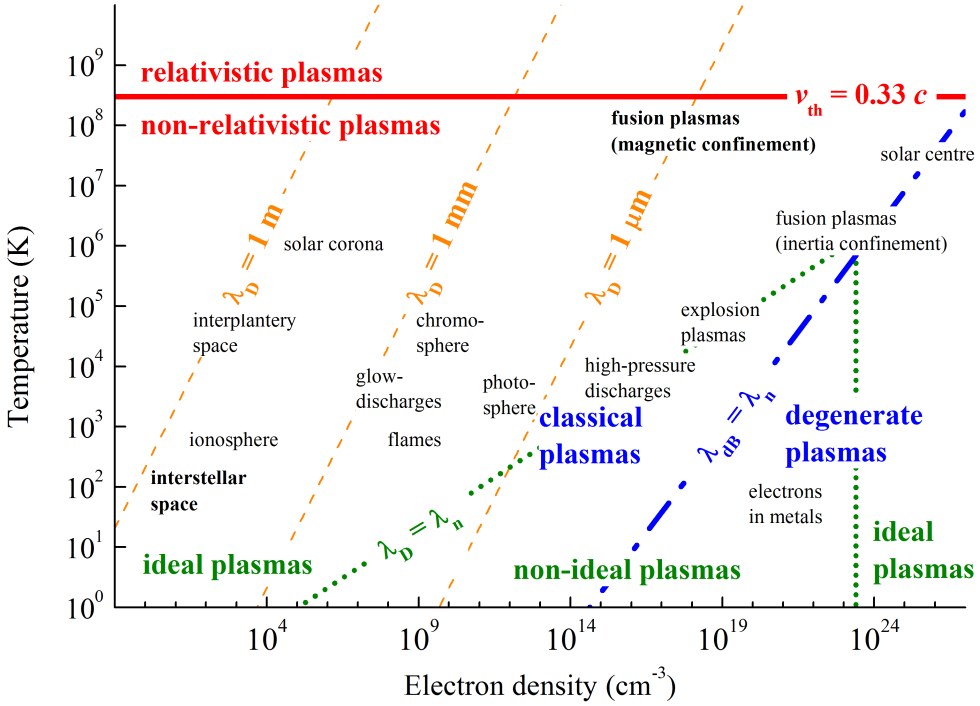

Figure 2.1.: Different plasma types characterised by their temperature and electron density [1]. A few examples of man-made and natural plasmas are given. This work deals with fusion plasmas and plasmas in the cold interstellar space.

Usually, both classical and degenerate plasmas are macroscopically quasi-neutral since the ratio between negative and positive charges is approximately 1. Due to the Coulomb attraction, electrons form clouds of negative charge around the positively charged ions A^{q+}, neutralising part or all of its actual charge qe for a distant observer. This phenomenon is known as shielding or screening. The Debye length [3] is the characteristic shielding distance, given by

$$\lambda_D = \sqrt{\frac{\epsilon_0 k_B T}{n_e e^2}} \tag{2.2}$$

where ϵ_0 is the dielectric constant, k_B the Boltzmann constant, T the temperature, and e the elementary charge. In an ideal plasma, the potential Coulomb energy is smaller than the thermal energy of the particles, hence

$$\lambda_D < \lambda_n \quad . \tag{2.3}$$

For a classical plasma, the Debye length provides the effective range of the Coulomb interaction.

2.1. Charge Balance in Plasmas

Dynamic ionisation balances for man-made and natural plasmas in non-thermal equilibrium are generally calculated in a temporal and spatial 'transport model'. Therein processes increasing ('sources') or decreasing ('sinks') the density n_q of particles A^{q+} are considered. Assuming a cylindrical geometry, this creates a set of equations of the form [4]

$$\frac{\partial n_q}{\partial t} = -\frac{1}{r}\frac{\partial}{\partial r}\left(r J_q\right) \; + \; \text{sources} \; - \; \text{sinks} \tag{2.4}$$

where J_q is the flux of particles of charge state q which has to be derived analytically. In steady-state equilibrium at a plasma temperature T, the balance is described by the simpler equation

$$\text{sources} = \text{sinks} \quad . \tag{2.5}$$

The equilibrium of collisionally ionised plasmas is determined by the balance of electron-collisional ionisation and high-temperature recombination [5]. Equation 2.5 transforms to the explicit form of

$$\dot{N}_{q+1,q} + \dot{N}_{q-1,q} = \dot{N}_{q,q-1} + \dot{N}_{q,q+1} \quad . \tag{2.6}$$

The sources of the charge state q are the recombination rate from the higher charge state $q+1$, $\dot{N}_{q+1,q}$, and the ionisation rate from the lower charge state $q-1$, $\dot{N}_{q-1,q}$. Correspondingly, the sinks are the recombination ($\dot{N}_{q,q-1}$) and ionisation rates ($\dot{N}_{q,q+1}$) of the charge state q.

Since in a steady-state equilibrium Eq. 2.6 is true for all charge states q, it simplifies further to

$$\dot{N}_{q-1,q} = \dot{N}_{q,q-1} \quad . \tag{2.7}$$

When denoting by $\widetilde{\alpha}_q$ the ionisation rate coefficient of A^{q+}, the ionisation rate for ions with charge state $q-1$ is given by

$$\frac{dN_{q-1,q}}{dt} = n_e N_{q-1} \widetilde{\alpha}_{q-1} \tag{2.8}$$

where n_e is the electron density and N_{q-1} gives the number of ions with charge state $q-1$. Correspondingly, the recombination rate for ions with charge state q can be written as

$$\frac{dN_{q,q-1}}{dt} = n_e N_q \alpha_q \tag{2.9}$$

where α_q is the recombination rate coefficient of A^{q+}. The equilibrium condition is

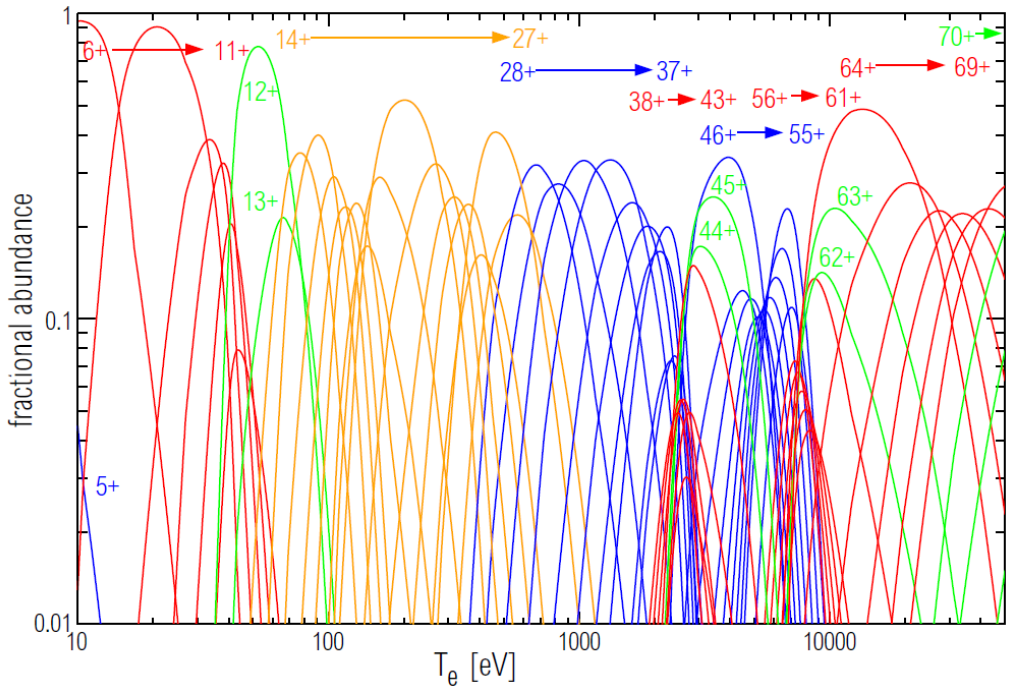

Figure 2.2.: Charge-state balance of tungsten ions in a fusion plasma of an electron density $n_e = 10^{14}$ cm^{-3} [6]. The different colours indicate the angular momentum quantum numbers of the outermost electron(s) of the ground configuration: f electrons have orange lines, d shells are blue, red stands for p shell electrons and green for s shell electrons. The employed ionisation cross sections were calculated using a distorted wave method [7], while the recombination cross sections were derived by the ADAS code '408 ' [8].

described by

$$\frac{N_q}{N_{q-1}} = \frac{\widetilde{\alpha}_{q-1}}{\alpha_q} \quad . \tag{2.10}$$

Accurate modelling of the equilibrium state requires thus knowledge of the recombination and ionisation rate coefficients of the involved charged states. As an example, the modelled charge state balance of highly charged tungsten ions in a fusion plasma as a function of plasma temperature is given in Fig. 2.2.

2.2. Applications of Plasmas

The knowledge of recombination and ionisation processes along with the corresponding rate coefficients is mandatory for accurate modelling of charge balances (cf. Eq. 2.10) in most types of astrophysical and laboratory plasmas. This work is con-

centrating on two fields, specifically high temperature fusion plasmas in tokamak devices and cold astrophysical plasmas, as they can be found in dense molecular clouds of the interstellar medium (ISM). In the following, the relevance of data on dielectronic recombination processes for both research fields is discussed in detail.

2.2.1. Fusion Plasmas

In tokamak fusion plasmas, radiative power-loss is an important issue since this determines the device's capability of maintaining ignition conditions. This power-loss originates to a large extent from impurity ions which are collisionally excited within the fusion plasma and decay via emission of photons. Since the ionisation equilibrium is established within 0.1% to 10% of the plasma confinement time [9], recombination and ionisation rate coefficients for the relevant charge states of the impurity species are needed for reliably modelling the ionisation balance.

Tungsten is foreseen as a coating material for plasma facing components in future fusion tokamaks due to its thermo-mechanical properties. Tungsten coatings have already been used successfully at ASDEX Upgrade [10] and are part of ongoing studies at JET [11]. Tungsten is the material of choice for the divertor sections [12] of ITER [13,14] (see Fig. 2.3), currently under construction in the CEA Cadarache Research Center in France [13–18]. ITER will investigate the scientific and technological feasibility of fusion energy in order to pave the way towards future fusion power plants.

The use of tungsten as a coating material in the heavily-exposed divertor sections inevitably means that tungsten will be sputtered off the walls and contaminate the fusion plasma. The initially neutral tungsten atoms are subsequently ionised via collision processes, producing tungsten of many different ionisation stages. Above a certain level of tungsten concentration in the core plasma, the tokamak operation is limited by radiative losses from these ions. Plasma model calculations suggest that the fraction of tungsten ions in the core plasma must not exceed a few 10^{-5} to be able to maintain fusion conditions [21]. Ionisation and recombination processes involving tungsten ions are therefore of major interest for the fusion plasma community.

Studies on radiative cooling processes in high and low temperature plasmas, specifically caused by impurities of tungsten ions, have been published in recent years [22–24]. Therein, the plasma modelling [15, 21] uses theoretical recombination rate coefficients from the ADAS (Atomic Data and Analysis Structure) data base [25]. The so-calculated charge-state balance for tungsten ions in a fusion plasma of $n_e = 1{\times}10^{14}$ cm^{-3} is shown in Fig. 2.2 as a function of plasma temperature. As discussed by Badnell et al. [26], the ADAS database contains calculations which are based on

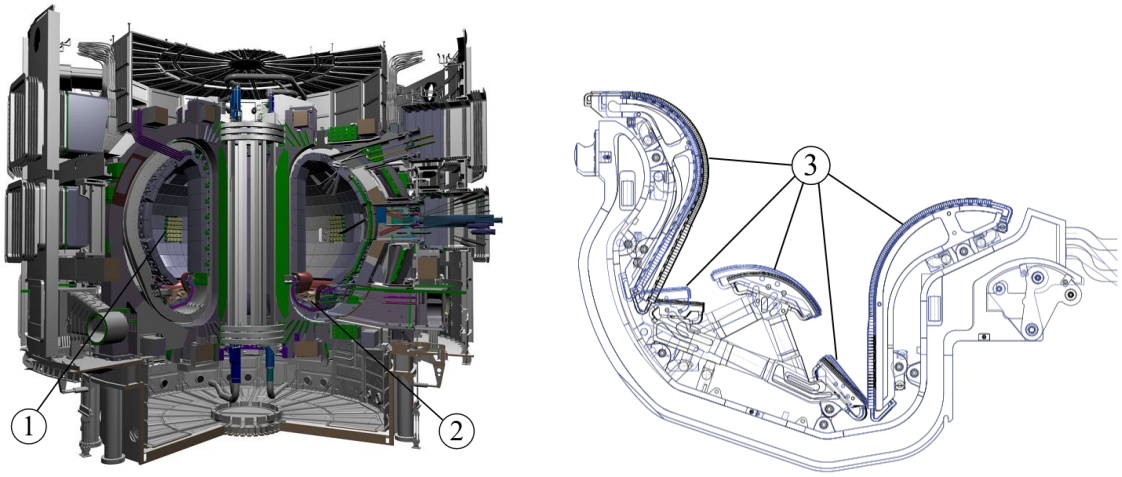

Figure 2.3.: Cut-open illustration of the ITER vacuum vessel (1) adapted from [19]. The divertor (2) is situated at the bottom of the vessel. Right panel: Lateral cut of an ITER divertor model [20]. All plasma-facing components (3) of the device are foreseen to have full tungsten platings. Parts of the divertor can be aligned (indicated by the blue and black surfaces) to the expected particle flux.

the semi-empirical Burgess General Formula [27] (see Sect. 2.3.1). This is a high-temperature (and low-density) approximation which does not include low-energy dielectronic recombination (DR, see Sect. 2.3) resonances. However, recent studies on highly charged tungsten have revealed that DR of low-collision energies can have impact on the plasma rate coefficient at higher collision energies.

In their spectroscopic investigation of tungsten line emission at ASDEX Upgrade, Pütterich et al. [6] had to introduce scaling factors for the ADAS recombination rates in order to match models of population densities to the observed line intensities. Even by doing so, a good semi-empirical model could only be constructed for charge states above W^{26+}. Modelling became increasingly difficult towards lower ionisation states as the emission lines originating from their high number of energy levels could not be disentangled easily. The resulting quasi-continuum in the spectrum prevented identification of individual charge states. In order to reproduce the observed line intensities by models, accurate rate coefficients for the dominating ionisation and recombination processes are needed. Theoretical predictions, especially of open 4-f-shell tungsten, are challenging because of the complex electronic structure involved (cf. Sect. 2.3.1) and experimental data are required to benchmark theory.

2.2.2. The Interstellar Medium

In comparison to fusion plasmas, temperatures and particle densities in the interstellar medium are many orders of magnitudes lower (see Fig. 2.1). In cold interstellar gases, as found in dark molecular clouds [28], typical temperatures are below 100 K [28, 29] and gas densities in the range of $n_0 = 100$ to 1000000 cm^{-3} [30, 31]. The chemical evolution [32, 33] of these cold media heavily depends on barrierless reactions involving charged particles, i.e., ion-neutral and electron-ion collisions, which act as driving mechanisms in the formation of larger molecules [32]. Hence, the study of the ion chemistry in the ISM requires among others knowledge about cross sections for the recombination of molecular ions with low-energy electrons.

In addition, singly-charged atomic ions, like C^+, N^+ and O^+, are present in molecular clouds and have a significant impact on their chemical evolution. Until recently the only recombination process accounted for in the models was radiative recombination [34]. By inclusion of theoretical DR rate coefficients by Badnell et al. [35] into gas-grain models of dense, cold interstellar clouds, Bryans et al. found that DR of these singly-charged species could potentially change their abundances by more than a factor of 10 [34]. As shown below, energy conservation causes DR resonances associated with an ionic-core excitation of energy E_{ex} to occur at collision energies

$$E_\mathrm{r} = E_\mathrm{ex} - E_b \tag{2.11}$$

where E_b is the binding energy of the initially free electron. Important DR channels in molecular clouds of temperatures $T \lesssim 100$ K are associated with core excitations $E_\mathrm{ex} \sim k_B T \lesssim 0.01$ eV.

For the singly-charged atoms of astrophysical interest, H^+, He^+, C^+, N^+, O^+, F^+, Na^+, Mg^+, Si^+, P^+, S^+, Cl^+, theoretical calculations of DR processes have so far been carried out only for He^+, C^+, N^+, O^+, F^+, Na^+, and Mg^+. At magnetic storage rings like TSR (Sect. 3.4.1), recombination of light systems, e.g. D^+, He^+, Li^+ and Be^+ [36–38], has been studied experimentally. Measurements on the heavier systems were restrained by the background from electron capture by the stored ions from the residual gas as well as by field ionisation of high Rydberg states by the strong deflecting fields of the storage rings. In CSR, however, collision studies with slow, heavy ions will be possible (cf. Sect. 3.4.2). Given the number of levels in the ground term caused by fine structure splitting, significant DR contribution can be expected also for Fe^+, Si^+, P^+ and Cl^+ [34]. These elements have a first ionisation potential below that of H (13.6 eV), hence they may be ionised in the molecular clouds by UV radiation, particle collisions and cosmic rays [39]. However, the database on reliable recombination rate coefficients of the relevant species is only incomplete and most of the available data come from theory. Laboratory collision-studies of electron-ion

recombination processes are required to complete the database and to guide the development of accurate theoretical approaches.

2.3. Atomic Processes in Plasmas

Of the two fundamental processes governing the charge balance of plasmas as laid out above, collisional ionisation and electron recombination, the latter is the main focus of this work. A broader overview over all collisional atomic processes in plasma can be found, e.g., in Müller et al. [40].

Recombination in a plasma may generally proceed in two fundamentally different ways: Via non-resonant or via resonant processes.

Radiative recombination (RR) is a non-resonant, two body-process. A free electron e is captured by a cation A^{q+} of charge state q. The energy surplus is translated into a photon which is emitted, leaving the ion with a charge state of $q-1$. RR is the time-reversed photo-ionisation process and can be described by the equation

$$e^- + \mathrm{A}^{q+} \rightarrow \mathrm{A}^{(q-1)+} + h\nu \qquad . \tag{2.12}$$

The simplest of the resonant processes is dielectronic recombination (DR) [41] which involves (at least) three collision partners in the sense that the initial ion A^{q+} holds at least one bound electron. After an electron capture from a continuum state, the ion remains in an intermediate, excited state. The potential energy of the captured electron is transferred into excitation of one (or several) bound electrons by electromagnetic interaction. This first step is called dielectronic capture or inverse Auger process. In a second step the daughter ion stabilises by emission of $\widetilde{n}$ photons to a final state which lies energetically below the first ionisation threshold. The equation

$$e^- + \mathrm{A}^{q+} \rightarrow \left[\mathrm{A}^{(q-1)+}\right]^* \rightarrow \mathrm{A}^{(q-1)+} + \widetilde{n} \cdot h\nu \quad \widetilde{n} \geq 1 \tag{2.13}$$

describes these two steps of DR. In competition to that, the ion may autoionise from the excited intermediate state and thereby restore the original ionisation stage. The net process is resonant electron scattering.

The two recombination reactions paths RR and DR, can be identified by the characteristic resonant fingerprint of DR in the recombination signal or by the spectrum of the emitted photons [42]. While the RR process may proceed at any collision energy, the resonant process of DR occurs only at specific collision energies between the free electron and the ion. The sum of the kinetic energy of the initially free electron and its binding potential after the capture process has to match the excitation energy of one shell electron (see Eq. 2.11). For each given ionic core excitation, there is a

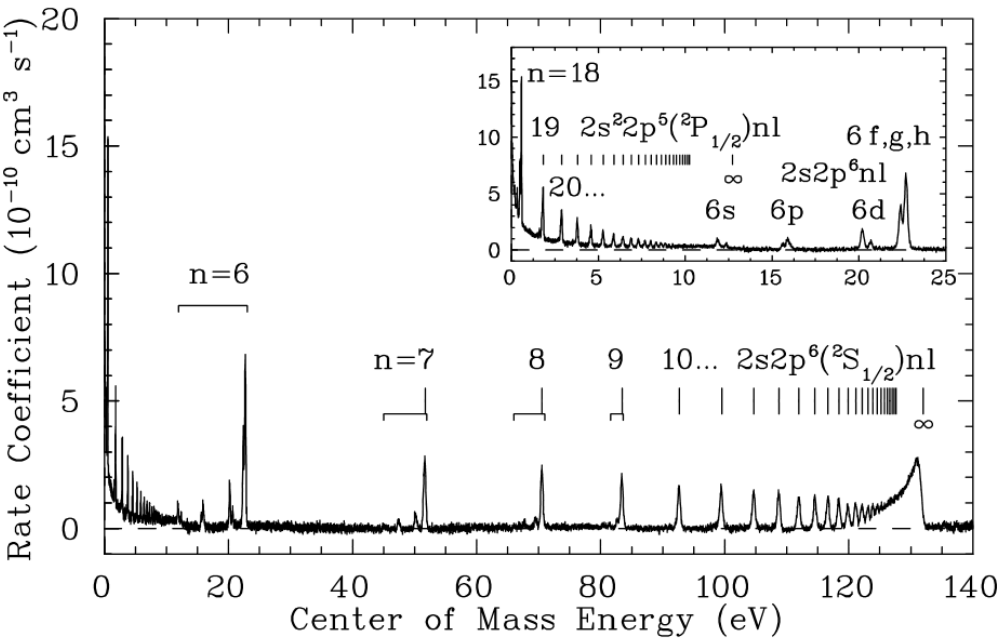

Figure 2.4.: Recombination rate coefficient of Fe^{17+} featuring Rydberg series of DR resonances associated with $2s^22p^5\ ^2P_{3/2} \rightarrow 2s2p^6\ ^2S_{1/2}$ and $2s^22p^5\ ^2P_{3/2} \rightarrow 2s^22p^5\ ^2P_{1/2}$ core excitations [43].

number of highly-excited Rydberg states nl where the free electron can be captured into. These energy levels $E_{b'}$, which appear as characteristic resonance structures at collision energies $E_{r'}$ in the recombination rate coefficient, are called Rydberg series. The series limit, where $E_{b'} \rightarrow 0$, corresponds to the excitation energy E_{ex} of the core electron. In case of many-electron systems, dense DR resonance series may also appear for collision energies close to zero, as many, nearly degenerate fine structure core excitations of the ion are then possible, each marking the high-energy limit of an infinite Rydberg series of recombination resonances. An example for a recombination rate coefficient featuring distinct non-resonant and resonant contributions is given in Fig. 2.4.

In general, multi-electron recombination processes with three or more electrons involved are conceivable, and have been observed in experiments [44,45]. Trielectronic recombination proceeds, in contrast to the above described basic DR process, via excitation of two initially bound electrons. Each excited core-electron configuration again features its own Rydberg series. Hence, by expanding these considerations to multi-electron excitations, the number of resonant levels increases strongly. Theoretical modelling of these extreme cases can become challenging due to the number of involved autoionising levels and the thus required computing power. Experimental studies of multi-electron recombination processes revealed that the numerous,

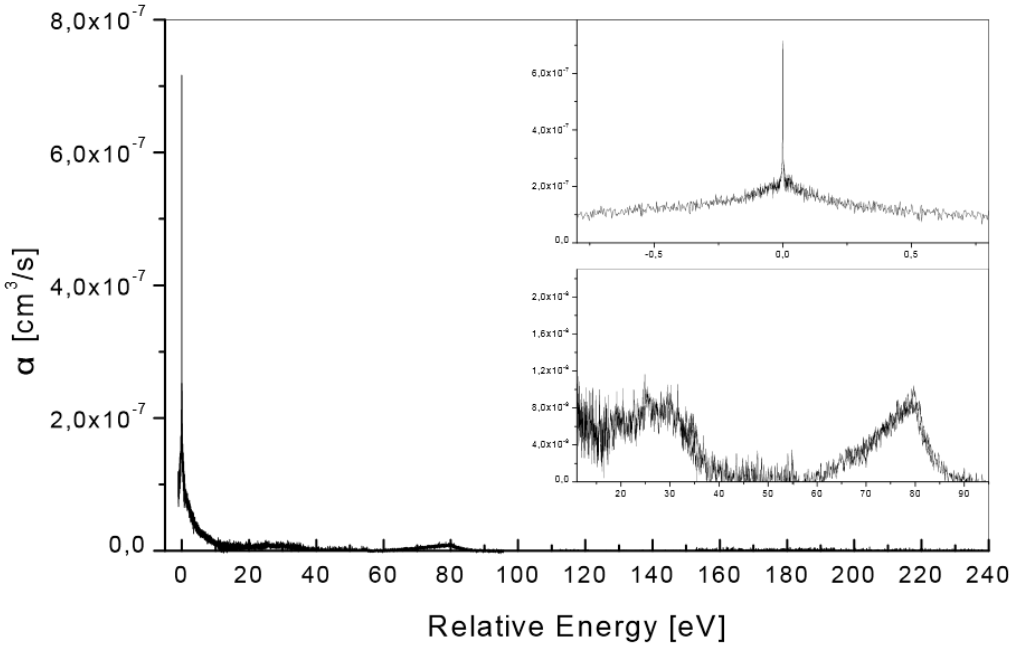

Figure 2.5.: Recombination rate coefficient of Au^{25+}, an open 4-f-shell ion. The data and figure are reproduced from [46]. The rate coefficient of forming Au^{24+} shows no apparent DR resonances but a strong enhancement of the rate coefficient near 0 eV collision energy.

overlapping Rydberg series result in broad, resonance structures, preventing an unambiguous assignment of the corresponding energy levels. This behaviour has been observed for ions with complicated shell structures, e.g. near half-open 4-f-shell structure, as featured by Au^{25+} (Fig. 2.5) and the tungsten charge states that are reported on in this work (Sect. 4.2).

2.3.1. Theoretical Description of Electron-Ion Recombination

Even though, quantum mechanically, dielectronic and radiative recombination are indistinguishable processes which interfere with each other, Pindzola et al. [47] found this effect to be very small. Hence, in the independent processes approximation (IPA), dielectronic and radiative recombination are normally considered separately.

Radiative Recombination was first described theoretically by Kramers [48] for the simple case of hydrogenic ions. The cross section $\sigma_{\mathrm{sc}}^{(\mathrm{RR})}(E', n)$ for RR of a bare ion A^{q+} with the charge state q, forming an ion $A^{(q-1)+}(n)$ which is characterised

by the main quantum number n of the captured electron, is in a semi-classical approximation given by

$$\sigma_{\mathrm{sc}}^{(\mathrm{RR})}(E', n) = \frac{2.105 \times 10^{-22}\mathrm{cm}^2}{nE'\,(1 + n^2 E')} \tag{2.14}$$

where

$$E' = \frac{E}{q^2 R} \qquad . \tag{2.15}$$

E is the centre-of-mass energy, and R is the Rydberg constant. However, this approach is not sufficient to describe systems with higher collision energies. Stobbe [49] provided the first quantum mechanically correct description of radiative recombination into arbitrary nl states assuming that RR originates from free-bound dipole transition. This non-relativistic approach is appropriate for light ions only. Several studies on theoretical radiative recombination cross section have been published (e.g. [50–53]), where the latest relativistic approaches also consider multipole-transitions [52] and QED effects [53].

Dielectronic Recombination can be described by using an isolated resonance approach (IRA). There, resonances are assumed to be narrow and to not overlap with neighbouring resonances of the same symmetry. Within the IRA the DR resonance strength for an ion A^{q+} of an initial state i can be calculated as [54]

$$\widetilde{\sigma}_{f,i}^{u}(E_{\mathrm{r}}) = \frac{(2\pi a_0 I_{\mathrm{H}})^2 \tau_0}{E_{\mathrm{r}}} \frac{\omega_u}{2\omega_i} \frac{A_{\mathrm{a}}(u \to i) \sum_f A_{\mathrm{r}}(u \to f)}{\sum_{i'} A_{\mathrm{a}}(u \to i') + \sum_{f'} A_{\mathrm{r}}(u \to f')} \tag{2.16}$$

where u denotes the unstable, intermediate state, and A_{a} and A_{r} are the rates of autoionisation and radiative relaxation processes to the possible final states i, i', f, and f'. The statistical weights of the initial level i and the intermediate level u are given by ω_i and ω_u. E_{r} is the resonance collision energy, matching the excitation energy of the intermediate level u. The remaining parameters are the ionisation energy of the hydrogen atom I_{H}, the atomic time unit τ_0, and the Bohr radius a_0. The summation over f accounts for all radiative transitions into states which lie energetically below the ionisation threshold, while the summation over f' accounts for all states which are accessible via radiative decay of the intermediated level u.

For application in plasma physics, the DR cross section, which is composed of the sharp resonances described by Eq. 2.16, is convoluted with the Maxwellian collision energy distribution of a plasma temperature $k_B T$:

$$\alpha_{\mathrm{plasma}}(k_B T) = (k_B T)^{-3/2} \frac{4}{\sqrt{2 m_e \pi}} \int_0^\infty dE \sigma_{f,i}^{u}(E)\, E\, e^{-E/k_B T} \tag{2.17}$$

where m_e is the electron mass. When the DR resonances are approximated by delta-functions, i.e. for $\sigma^u_{f,i}(E) = \widetilde{\sigma}^u_{f,i}(E_\mathrm{r})\delta(E - E_\mathrm{r})$, the plasma rate coefficient is given by [41]

$$\alpha_\mathrm{plasma}(k_BT) = \left(\frac{4\pi a_0^2 I_\mathrm{H}}{k_BT}\right)^{3/2} \frac{\omega_u}{2\omega_i} \frac{A_\mathrm{a}(u \to i) \sum_f A_\mathrm{r}(u \to f)}{\sum_{i'} A_\mathrm{a}(u \to i') + \sum_{f'} A_\mathrm{r}(u \to f')} e^{-E_\mathrm{r}/k_BT} \tag{2.18}$$

wherein the relations $a_0 I_\mathrm{H} = e^2(8\pi\epsilon_0)^{-1}$ and $\tau_0 = 2\epsilon_0^2 h^3(\pi m_e e^4)^{-1}$ were used. This expression can be simplified by assuming that, on the one hand, the radiative de-excitation rate is small in comparison to the autoionisation rate, $A_\mathrm{r} \ll A_\mathrm{a}$, and, on the other hand, that the contribution of autoionisation processes into excited states is negligible, thus $A_\mathrm{a}(u \to i') = 0 \; \forall \; i' \neq i$. By further replacement of $2I_\mathrm{H} = \alpha^2 m_e c^2$, with α being the fine-structure constant, the plasma rate coefficient transforms into the simpler form of

$$\alpha_\mathrm{plasma}(k_BT) = \sqrt{2\pi}\alpha^2 a_0 h c^2 \frac{E_\mathrm{r}^2}{(m_e c^2 k_B T)^{3/2}} \frac{1}{\omega_i} \sum_f \omega_f \widetilde{f}(f \to u)\, e^{-E_\mathrm{r}/k_BT} \tag{2.19}$$

where the radiative de-excitation rate $A_\mathrm{r}(u \to f)$ is expressed by the dimensionless absorption oscillator strength $\widetilde{f}(f \to u)$ of the recombining ion as

$$A_\mathrm{r}(u \to f) = \left(\frac{E_\mathrm{r}}{hc}\right)^2 \frac{\pi e^2}{\epsilon_0 m_e c} \frac{\omega_f}{\omega_u} \widetilde{f}(f \to u) \quad . \tag{2.20}$$

The widely used Burgess General Formula (GF) [27] is a numerical fit to Eq. 2.20 which is applicable to ions with different charge states q. By summation over all intermediate states u which are accessible from the initial state i, the plasma rate coefficient can be calculated using

$$\alpha_\mathrm{GF} = \frac{3.0 \times 10^{-21}}{T_e^{3/2}} B(q) \sum_u \widetilde{f}(i \to u)\, A(x)\, e^{-E/k_BT}\ \mathrm{cm}^3\ \mathrm{s}^{-1} \tag{2.21}$$

where

$$\begin{aligned} x &= (1+q) \cdot \left(n_u^{-2} - n_i^{-2}\right) \\ A(x) &= x^{1/2} / \left(1 + 0.105x + 0.015x^2\right) && x > 0.05 \\ B(q) &= \left[q(1+q)^5/(q^2+13.4)\right]^{1/2} && q \leq 20 \\ E/k_BT &= 1.58 \times 10^{-7}(1+q)^2 / \left[T_e \cdot \left\{1 + 0.015q^3/(1+q)^2\right\}\right] && E/kT \leq 5.0 \end{aligned}$$

T_e is the electron temperature, $\widetilde{f}(i \to u)$ is the weighted absorption oscillator strength of the recombining ion, and n_u and n_i are the effective principal quan-

tum numbers of the initial states i and the intermediate state u, respectively.

This approximation is popular, since it does not require the computation of autoionisation rates. However, it is strictly applicable to high-temperature [55] and low particle-density ($n_0 \lesssim 10^8$ cm^{-3}) [56] plasmas only. In plasmas of higher densities, collisions can interrupt radiative de-excitations cascades and cause the state population to redistribute. This is the typical case for many applications of plasma physics [57–59].

Different approaches, described, e.g., by Badnell et al. [26, 60], are based on LS-coupling or intermediated-coupling (IC) schemes. The LS-coupling scheme is a frequently used approach for light elements only. Fine-structure transitions are neglected by the term-based LS-coupling scheme which could result in an underestimation of the low-temperature rate coefficient [61] due to LS-forbidden autoionisation processes which are enabled by nuclear-spin orbit mixing. For medium and heavy ions, calculations which are based on the fine-structure resolving IC schemes are more accurate.

While the level-resolved, IC approach was found to be in agreement even with the experimental data of complex system like Au^{20+} [62, 63], these theories reach their numerical limit when the number of involved fine-structure levels become excessively high, resulting in a quasi-chaotic structure of the system which gives rise to multi-electron recombination processes. This behaviour was first observed for open 4-f-shell Au^{25+} ions [46]. Figure 2.5 shows the measured recombination rate coefficient, which apparently lacks any clearly distinguishable resonant structures, as the density of resonances is far beyond the experimental energy resolution. There, a new theoretical approach had to be developed since level-to-level calculations of these numerous states would also largely exceed the available computational power. State-of-the art theories describing these chaotic systems are presented in Sect. 4.3.

2.4. Summary

Plasma modelling of fusion or astrophysical plasmas, requires knowledge of the cross sections of all relevant processes. However, experimental data are only available for a limited amount of systems and, hence, theoretical cross sections are needed to complete the database.

Theoretical calculations can in particular be challenging for complex systems like highly charged tungsten, which is known to be present in hot fusion plasmas. These data are of importance for the fusion community since the concentration of tungsten in the fusion plasma can constrain an efficient operation of the device. Many-body recombination processes which are enabled by the complex shell structure of highly

charged tungsten ions cannot be described by standard approximations. Hence, experimental studies of chosen systems are needed to enable the development of new theoretical approaches.

The formation of molecules in space are in the focus of ongoing theoretical and experimental studies. There, the role of dielectronic recombination processes of singly-charged ions has been neglected for a long time. Recently, theoretical studies revealed that by inclusion of theoretical DR cross section of singly-charged ions, the results of the chemical network models can change significantly. Since theoretical studies are presently not available for all relevant systems, experimental data is needed to complete the database.

3. Storage-Ring Experiments on Electron-Ion Collisions

Experimental studies of ionisation and recombination processes provide insight into fundamental atomic structure and dynamics. As has been shown in the previous section, this information is valuable in various applications of plasma science since the charge-state balances in ionised gases depend on the cross sections of the involved processes. Due to the multitude of possible charge states, the amount of cross section data exceeds by far what has been measured or what experiments can realistically be expected to deliver in the future. Hence theoretical models of the cross sections are developed. In order to assure the accuracy of these theories, experimental data of selected processes are still needed as benchmarks. Due to their systematic relevance, these benchmark data sets have to be measured under experimental conditions that are particularly well understood.

Since charged particles are sensitive to magnetic as well as to electric fields, various types of devices for the storage and the manipulation of ions, both at low and high energy, have been developed. One possibility is to form ions in a plasma and study them in-situ. Electron Beam Ion Traps (EBITs) [64] are an example of a very successful realisation of this idea. Here, atomic ions are created within an intense electron beam. The ions are trapped practically at rest in the negative space charge potential of the latter, and their interactions can be studied in the very same source plasma that produced them. However, controlled production of specific charge or excitation states is practically impossible in this way.

One of these limitations can be overcome by extracting the ions from their source, forming a fast charged particle beam. This beam can be charge-to-mass selected by magnetic fields. Subsequently, a specific charge state can be guided onto an experimental target with which to react. However, due to the short time-of-flight between the ion source and the experiment, such a 'singe-pass' set-up (e.g. [65]) still does not allow excited ion states, that typically form in the source or acceleration stages, to decay to the ground level.

Heavy ion storage rings certainly offer the most advanced possibilities of charge-to-mass selection and initial-state control, at the expense of being rather large devices featuring external ion sources and accelerators. Technically, they were derived from the proton synchrotrons [66, 67] developed in the 1950s to fulfil the needs

of nuclear and high-energy physics research, but have since established themselves as workhorses also in the fields of atomic and molecular physics. Ionic atoms or molecules are created and accelerated prior to injecting them into the ring. In the storage ring, particles are confined and accumulated on a closed orbit in a vacuum system by magnetic or electric deflector and focussing elements. Generally, these 'rings' are in fact closed polygons with straight sections between the deflectors which can be used for beam manipulation or experimental equipment. Since these straight sections may be kept field-free, the stored ions perform a well-predictable drift motion there, allowing for experiments under controlled conditions. The storage of highly-energetic ion beams features several advantages, e.g., easy detection schemes, high energy resolution, and low perturbation due to interaction with residual-gas molecules. Especially experiments with low cross sections benefit from the fact that high beam intensities can be reached by beam stacking [68] and that the parent beam is 'recycled', i.e., passes by the experiment multiple times, limited only by the storage lifetime in the ring. In addition, during storage of atomic and molecular ion species their excited states have time to decay to the ground level and beam manipulations such as electron cooling (Sect. 3.3.1) can take place.

Storage rings hence provide ample opportunities for atomic, molecular and cluster physics. Magnetic storage rings represent the 'first generation' of heavy-ion storage rings. Various devices, e.g. TSR (Sect. 3.4.1), CRYRING [69] or ESR [70], have been built and operated in the last decades. They enabled measurements on electron-ion recombination and ionisation of highly-charged ions [71–73], molecular dissociation [74], QED effects [75], DR of cluster ions [76], lifetimes of metastable states [77], and studies on biomolecules [78, 79]. Their experimental potential has not yet been exhausted and new experimental set-ups are still being built, e.g. the FAIR facility [80] at GSI, or the set-up of TSR at the HIE-ISOLDE facility [81] at CERN.

With ELISA [82], the first fully electrostatic storage ring was conceived and today, several off-springs of this facility are in operation or in construction [83–87]. CSR, as further described in Sect. 3.4.2, features not only an all-electrostatic design, but also a fully cryogenic ($\sim$10 K) beam line and hence provides perfect conditions for experiments on low-energetic particle beams. In comparison to similar, electrostatic and cryogenic storage rings in operation [83] and in construction [87], CSR is the only one that will feature an electron cooler and, hence, allow studies of ion-neutral, ion-photon, and ion-electron collisions with cooled, low-emittance stored beams. DESIREE [83] is a storage device in operation at Stockholm University, Sweden, which consists of a double ring structure allowing to store ion beams of opposite charge and to merge them under cryogenic operating temperatures. The electrostatic and cryogenic storage ring under construction at RIKEN [87], Japan, is dedicated to experiments on atomic and molecular ions employing tunable laser and merged neutral beams. Another facility of the same type is the TMU electrostatic ion storage ring [84], Japan. In contrast to CSR, DESIREE and RIKEN, this ring is

operated at a more elevated temperature of 77 K.

CSR, as shown in Fig. 3.5, will enable experiments at an ambient temperature of ∼10 K at extremely high vacuum (XHV) conditions of 1×10^{-13} mbar room temperature equivalent (RTE) pressure. CSR will allow to re-enact processes which were restricted to the ISM before, since they would not take place under standard laboratory conditions. As a proof of concept for the cryogenic design of CSR, a cryogenic electrostatic trap for fast ion beams (CTF) [88] has been built and operated successfully during the last years.

3.1. Characteristics of Storage Rings

Storage rings are characterised by an acceptance which limits the phase-space volume within which particles can be stored on a closed orbit. Collisions with residual-gas molecules lead to beam losses, hence the rings are evacuated to a vacuum pressure of typically about 10^{-10} to 10^{-11} mbar in order to minimise them. Moreover, stable orbits are only possible for particles of a certain charge-to-mass ratio. Experiments exploit that fact, since charge-changed products and fragments generally leave the closed orbit in the bending elements following the experimental sections. These daughter particles can be studied with detectors placed near the closed orbit without affecting the stored beam. In case of neutral products, stationary particle detectors can be used, while for charged products moveable detectors are necessary to account for the different trajectories of the daughter products due to their specific charge-to-mass ratios.

The equation of motion for charged particles in a static electro-magnetic field takes into account the sum of the electric and Lorentz forces

$$\mathbf{F} = qe \cdot (\mathbf{E}_{\mathrm{el}} + \mathbf{v} \times \mathbf{B}) = m\ddot{\mathbf{r}} \tag{3.1}$$

with m, q and v being the ions mass, charge state, and velocity, respectively, e denoting the elementary charge, and $\mathbf{E}_{\mathrm{el}}$ and $\mathbf{B}$ the electric field strength and magnetic induction. For a circular trajectory this is equal to the centripetal force at a radius r

$$|\mathbf{F}| = F = \frac{mv^2}{r} \quad . \tag{3.2}$$

In case of a purely magnetic storage ring, like TSR which is described in Sect. 3.4.1, the bending radius r_m in the deflecting dipoles depends on the absolute value B of the magnetic induction $\mathbf{B}$, as well as on the charge-to-mass ratio q/m of the stored particles:

$$r_m = \frac{mv}{qe \cdot B} \quad . \tag{3.3}$$

The magnetic rigidity

$$r_m B = \frac{p}{qe} \tag{3.4}$$

characterises the ability of the specific ring to store particle of momentum p and charge qe.

While magnetic storage rings are valuable devices for experiments on highly-charged ions, that are characterised by a relatively low charge-to-mass ratio, the power consumption of the magnets causes high operating costs of these devices.

In order to provide new experimental possibilities, especially for massive molecular ions, several electrostatic storage rings have been constructed during the last years. As first demonstrated by the ground-breaking ELISA storage ring [82], they have proven to work as reliably as magnetic ones. The bending radius in the electric deflectors r_e is dependent on the charge-to-mass ratio according to

$$r_e = \frac{mv^2}{qeE_{\mathrm{el}}} \tag{3.5}$$

where E_{el} is the electric field strength. As easily seen from Eq. 3.5, and in contrast to Eq. 3.4, the bending radius now depends on the kinetic energy rather than the momentum of the particle. At given energy and charge state, there is no explicit dependence on the particle mass. This is a great practical advantage, as in a fully electrostatic facility it is possible to change the mass of the stored ion without modifying the deflecting or focussing fields. In analogy to Eq. 3.4, the rigidity of an electrostatic storage ring can be defined as

$$r_e E_{\mathrm{el}} = \frac{mv^2}{qe} = \frac{2E_{\mathrm{kin}}}{qe} \quad . \tag{3.6}$$

Even though ordinary storage rings, magnetic as well as electric, can cover a wide range of experiments, in the study of processes relevant to the cold ISM they meet their limitations in respect to ambient temperature and vacuum quality (cf. Sect. 2.2.2). Hence, new, cryogenic storage devices have been designed specifically for reaction studies of ion species which are known to be abundant in the ISM. The cryogenic environment improves the vacuum pressure due to cryo-adsorption and simultaneously limits the thermal black-body radiation which is particular important in the studies of molecular ions.

Excitation energies for rotational levels of molecular ions can be as low as a few meV and thus these levels are easily excited by thermal radiation from the surroundings. Wien's displacement law approximates the photon wavelength $\lambda_m(T)$ where the energy density of the black-body radiation of the vacuum chamber has its maximum

at a given temperature T:

$$\lambda_m(T) = \frac{2897.8\ \mu\mathrm{m} \cdot \mathrm{K}}{T} \quad . \tag{3.7}$$

For an ambient temperature of 300 K this wavelength is in the infra-red region and thermal radiation of this energy is able to excite rotational states in most molecules [89]. Unless for the rare case of molecular ions of zero electric dipole moment, this makes studies on ground-state molecular ions impossible in room-temperature storage devices. Hence, in order to enable ground-state studies on various molecular species, the ambient temperature of the beam-guiding vacuum chamber should not exceed ∼10 K.

The residual-gas pressure in a storage device is limited by gas desorption from the surfaces of the walls of the vacuum vessel. Since this value is temperature dependent, the vacuum pressure can be greatly improved by cooling of the whole vacuum system. Thus, a cryogenic storage ring features long storage times, enabling experiments also on very heavy, singly-charged ions of very low velocities.

The lifetime τ of a stored ion beam is limited by the residual-gas particle density n_0, since it is connected to the mean free path length l, the cross section σ, and the ion velocity v by

$$\tau = \frac{l}{v} = \frac{1}{v\, n_0 \sigma} \quad . \tag{3.8}$$

The particle density n_0 is itself given by

$$n_0 = \frac{P}{k_B T} \tag{3.9}$$

with the residual-gas pressure P, the temperature T, and the Boltzmann constant k_B. At a given particle density, which represents the quality of the vacuum, the pressure is temperature dependent and it is therefore convenient to specify the pressure in room temperature equivalent (RTE) units.

3.2. Merged-Beams Experiments

Today, the merged-beams technique is a well-established method for interaction studies with high energy resolution on atomic and molecular species [90, 91]. The essence of this technique is that two fast particle beams (atoms, ions, electrons or photons) are forced onto a common (collinear) trajectory for a finite distance of typically several tens of centimetres. For massive particles, this configuration allows for experiments at very low collision energies given that the two beams can have similar velocities.

Following the interaction region, the massive collision products can in many cases be easily collected by particle detectors arranged in the forward direction of the experimental section. This is also true for daughter particles which have large scattering angles in the centre-of-mass (CMS) frame of the collision process, given that the energy released in the reaction is normally small in comparison to the kinetic energy in the laboratory frame. If the geometrical overlap and density distributions of the two merged beams are known, absolute measurements of the reaction cross sections are possible.

Storage rings provide excellent conditions for merged-beams experiments as, due to the principle of 'recycling' the stored particles, repeated interactions with targets are possible. In addition, long storage times may allow for accumulation of high beam currents and state-selective preparation of molecular and atomic ion species. Electron coolers, as described in Sect. 3.3.1, can be used for phase-space cooling of the stored ions and, since they feature long electron-ion interaction regions, as merged-beams targets for electron collision experiments.

The deflectors following a merged-beams interaction region separate the product particles according to their different charge-to-mass ratios compared to the parent beam, allowing for the collection of the daughter products without interacting with the stored beam.

The reaction cross section of a certain product forming at a rate R in an interaction volume V is given by [91]

$$\sigma = \frac{R}{\Omega} \frac{v_e v_i}{|v_e - v_i|} \tag{3.10}$$

where v_e and v_i are the target and ion beam velocities, respectively, and the beam overlap integral Ω over the reactant particle fluxes J_e and J_i (of dimension $\mathrm{cm}^{-2}\mathrm{s}^{-1}$) is defined by

$$\Omega = \iiint_V J_e J_i dV \qquad . \tag{3.11}$$

In case of extended beam envelopes, determination of this beam overlap integral can be challenging.

3.3. Electron-Cooler Storage Rings

In order to be able to control the fundamental parameters of electron-ion collision experiments, ion beams of low divergence, small diameter, and small longitudinal momentum spread are desired. In the accompanying CMS system this means to lower the effective temperature and therefore 'cool' the ion beam. Static external, electromagnetic fields can only change the shape of the phase space of the beam

particles, but not change its volume or increase the particle density therein. Besides several other methods, e.g., radiative damping or stochastic cooling, electron cooling [92] is a simple and efficient method of phase-space cooling which has been developed in the early 1960s. While electron cooling is also feasible in ion traps [93], its genuine realm of application is the storage ring.

3.3.1. Electron Cooling

In an electron cooler a cold, single-pass electron beam is merged with the stored, hot ion beam at an average relative velocity of practically zero. The intense electron beam is normally guided by a weak (few tens of mT) magnetic solenoid field. Collisions between electrons and ion transfer (thermal) kinetic energy to the cold electrons. By passing the hot particle beam repeatedly through the cold electron bath, the stored, hot particle beam is cooled down towards the temperature T_e of the electrons resulting in a decreasing phase space volume, i.e., the stored beam is spatially compressed and its internal velocity spread is reduced. As the single-pass electron beam is continuously renewed, no heating of the electron beam occurs. Still, the equilibrium temperature is somewhat larger than T_e, as heating by intra-beam scattering (IBS) in the ion beam competes with the electron cooling. The time needed for the cooling of a 'hot' ion beam of mass m_i and charge state q to the equilibrium temperature is [94]

$$\tau \sim \frac{m_i}{q^2} \cdot \frac{T_e^{3/2}}{n_e} \tag{3.12}$$

where n_e is the electron beam density.

The requirement of equal average velocities of electron and ion beam ($\overline{v_e} = \overline{v_i}$) leads to the following dependence between the electron kinetic energy E_e and the ion energy E_{ion} [94]

$$E_{e,\text{cool}} = \frac{m_e}{m_i} \cdot E_{\text{ion}} \tag{3.13}$$

where m_e is the electron mass. In the following, $E_{e,\text{cool}}$ is referred to as the 'cooling energy' of the electron for a given stored ion beam.

3.3.2. Electron Target

As mentioned above, by detuning of the electron energy E_e, the electron cooler can also serve as an electron target for collision experiments at non-zero collision velocities. In a relativistic calculation, the collision (or 'detuning') energy E_d can

be derived from the (laboratory) kinetic energies of the electrons and ions, E_e and E_{ion}, by [95]

$$E_d = m_i c^2 \left(1 + \frac{m_e}{m_i}\right) \cdot \left(\sqrt{1 + 2\frac{m_e}{m_i}\left(1 + \frac{m_e}{m_i}\right)^{-2}(G-1)} - 1\right) \tag{3.14}$$

where

$$G = \gamma_i \gamma_e - \cos\Theta \sqrt{(\gamma_i^2 - 1)\,(\gamma_e^2 - 1)} \tag{3.15}$$

depends on the angle Θ between the two beams and on the relativistic factors $\gamma_i = 1 + E_{\text{ion}}/m_i c^2$ and $\gamma_e = 1 + E_e/m_e c^2$. In the classical limit and $\Theta = 0°$ a much simpler result is obtained: [96]

$$E_d = \frac{1}{2} m_e v_d^2 = \left(\sqrt{E_e} - \sqrt{E_{e,\text{cool}}}\right)^2 \tag{3.16}$$

with $E_{e,\text{cool}}$ from Eq. 3.13. In the merging and de-merging sections of an electron cooler an angle appears between the trajectories of the electron and ions leading to an increase of the average detuning energy E_d. In order to account for this effect, a deconvolution procedure has been developed [97].

In an electron-cooler used as merged-beams target, Eq. 3.10 and Eq. 3.11 simplify significantly, as the cooled ion beam is fully contained within the electron beam of homogeneous density n_e. The rate of reaction products is then:

$$R = n_e \langle \sigma v_d \rangle \frac{L_{\text{eff}}}{C} N_i \tag{3.17}$$

with the detuning velocity $v_d = |\overline{v_e} - \overline{v_i}|$ (derived from the mean velocities of electrons $\overline{v_e}$ and ions $\overline{v_i}$) and the number of stored ions N_i. In order to receive the effective number of ions interacting with the electron beam, N_i has to be scaled with the ratio between the electron-ion overlap length L_{eff} and the full storage ring circumference C. Since L_{eff} and C are known parameters and the reaction rate R, ion number N_i, and density n_e can be measured, $\langle \sigma v_d \rangle$ can be derived experimentally. The latter is called the merged-beams reaction rate coefficient and in a relativistically correct calculation given by [98]

$$\alpha(E_d) = \langle \sigma v_d \rangle = \frac{R}{(1 - \beta_i \beta_e) n_e N_i L_{\text{eff}}/C} \tag{3.18}$$

where $(1 - \beta_i \beta_e)$ is a relativistic correction factor with $\beta = v/c$.

3.3.3. Energy Resolution

Both particle beams, ions and electrons, are characterised by certain velocity spreads which determine the energy resolution of the merged-beams experiment. Under cooling condition, the average velocity of electrons $\overline{v_e}$ and ions $\overline{v_i}$ are equal and the beam temperatures in the co-moving frame are given by

$$T_e = \frac{(\delta v_e)^2 m_e}{f_e k_B} \tag{3.19}$$

$$T_i = \frac{(\delta v_i)^2 m_i}{f_i k_B} \tag{3.20}$$

where f_e and f_i are the numbers of degrees of freedom of electrons and ions, and δv_e and δv_i their respective velocity spreads along a certain direction in space. In principle, the ions could transfer energy to the electrons until a thermal equilibrium ($T_i = T_e$) of

$$\delta v_i = \left(\frac{f_e m_e}{f_i m_i}\right)^{1/2} \delta v_e \tag{3.21}$$

is reached so that δv_i is much smaller than δv_e. In reality, as noted above, IBS competes with the electron cooling. The finally achieved ion temperature is hence limited by the balance between electron cooling and IBS induced heating. However in most experiments T_i stabilises close enough to T_e, so that the overall collision velocity spread is still dominated by the electron temperature.

In the co-moving frame of the beam, the electron temperature T_e is characterised by a transverse and a longitudinal component, $T_{e\perp}$ and $T_{e\parallel}$. Since the guiding magnetic field suppresses thermalisation among the transverse and longitudinal degrees of freedom of the electrons, the two temperatures may be different. As long as the (average) detuning energy E_d is much larger than the transverse thermal energy of the electrons $k_B T_{e\perp}$, the collision energy spread δE_d and, hence, the experimental energy resolution, is limited by $k_B T_{e\parallel}$, while at very low average collision energies, it converges to $k_B T_{e\perp}$. The overall energy resolution at a collision energy E_d is given by [99]

$$\delta E_d = \sqrt{\left(k_B T_{e\perp} \ln(2)\right)^2 + 16 E_d k_B T_{e\parallel} \ln(2)} \quad . \tag{3.22}$$

Figure 3.1.: Photography of the Heidelberg TSR, in operation until end of 2012. In the front section, the injection (1) and extraction (2) beam lines are shown.

3.4. Storage Rings of the Max Planck Institute for Nuclear Physics

Within this work, measurements at two different storage rings were performed. Both storage rings are located at the Max Planck Institute for Nuclear Physics (Max-Planck-Institut für Kernphysik, MPIK) in Heidelberg, Germany.

3.4.1. Test Storage Ring (TSR)

The Test Storage Ring (TSR) [81, 100–103] (Fig. 3.1), is a heavy-ion storage ring that was operated at MPIK until the end of 2012. It features a maximum rigidity (Eq. 3.4) of 1.5 Tm [104]. At TSR, the beam intensities of stored ions can be increased by a combination of multiturn injection and electron cooling-stacking [68], which can enhance the stored ion current by a factor of several thousands compared to that of the injection accelerator. The TSR's vacuum conditions in the range of 10^{-11} mbar are achieved mainly by Ti sublimation and ion getter pumps [101]. In addition, the storage ring is designed for a bake-out temperature of 300°C.

During its operation time of 24 years, a multitude of experiments (e.g. [105–110]) employing different ion sources, accelerators and detectors have been conducted. In the following, only the parts of the set-up relevant for the here described experiments are presented.

3.4.1.1. General Design

In TSR, ions are confined on a closed orbit of 55.4 m circumference by four sets of pairs of 45°dipole magnets, five quadrupole magnets and three sextupole magnets arranged in the corner sections of the ring (see Fig. 3.2). In addition, TSR features four 5.2 m long straight sections used for injection and extraction of the beam, beam diagnosis, and experiments. As a unique characteristic, TSR is equipped with two electron beam devices dubbed 'Cooler' [111] and 'Target' [112]. In spite of those names, both can be used for electron cooling and collision experiments. In order to collect the products created in electron-ion reactions, the corner sections behind these devices are equipped with several kinds of particle detectors.

3.4.1.2. TSR Electron Coolers

The original TSR electron cooling device, Cooler for short, creates an electron beam from a thermionic emitter cathode heated to ∼1100°C [111]. As schematically depicted in Fig. 3.3, the electron beam is guided by solenoids into a toroid magnet, where the electrons are bent by an angle of 45° and are merged with the stored ion beam. The subsequent interaction section is embedded into a solenoid surrounding both particle beams. The ion and electron beams can be steered such that the ion beam is fully contained within the electron beam. Effectively, of the 5.2 m long straight section only 1.5 m are actually used for electron cooling in order to avoid conflicts with the dipole magnetic fields [113]. Since, in the toroids, the velocity vectors of the electrons are not yet perfectly aligned to the ion beam axis, the effective interaction length L_{eff} where ions and electrons have the specified collision energy is even shorter than those 1.5 m, as will be discussed in Chapter 4.

The transversal temperature $k_B T_{e\perp,\text{cath}}$ of electrons emitted by the cathode is about 0.1 eV. However, implementation of an adiabatic expansion system [114,115] allows for further reduction of this temperature. The expansion factor ξ of the Cooler can be varied between 1 and 30 [81,116]. The transversal electron temperature is hence given by

$$k_B T_{e\perp} = \frac{k_B T_{e\perp,\text{cath}}}{\xi} \quad . \tag{3.23}$$

In the standard operating mode $\xi = 9.6$, the transversal electron temperature is about 10 meV.

The second electron cooler 'Target' [112,118,119] for high-resolution collision experiments was installed at TSR in 2003. From 2007, a LN_2-cooled photocathode was employed as an electron source. As compared with a hot thermionic cathode, this leads to a much decreased electron temperature and improved energy resolution. With the Target in place, the Cooler was mostly used for phase-space cooling of the

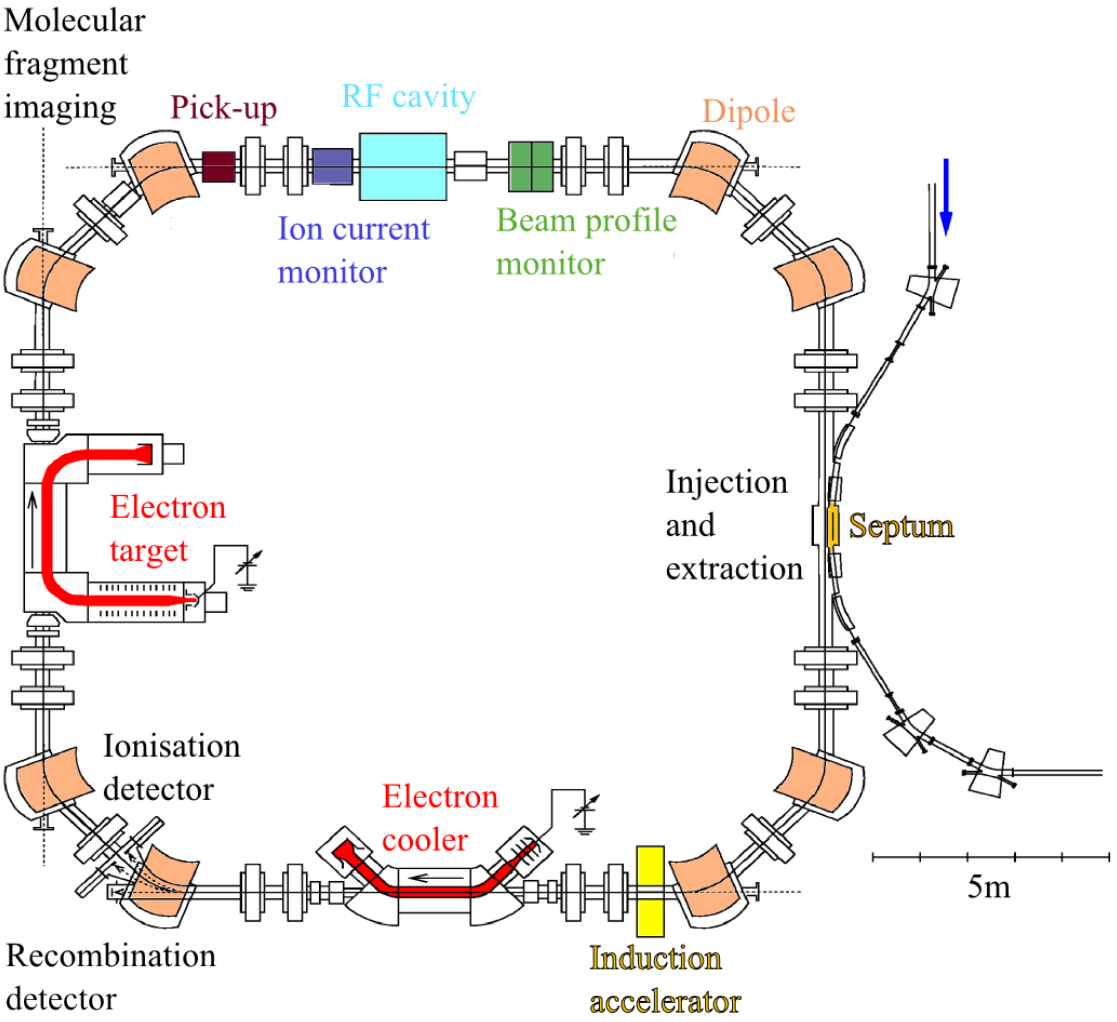

Figure 3.2.: Schematic layout of TSR including the electron beam devices 'Cooler' and 'Target', the injection and the extraction beam lines. Each corner section of the storage ring following the experimental sections of the two electron coolers house a number of various particle detectors.

ion beam while the Target served as target for collision studies. However, due to the limited quantum efficiency of the photocathode, the Target can only provide a maximum emission current of few mA [119] while the Cooler can provide currents up to 1 A and is therefore still used as target for collision experiments where the expected reaction rate is only small due to a low cross section or a small number of stored ions.

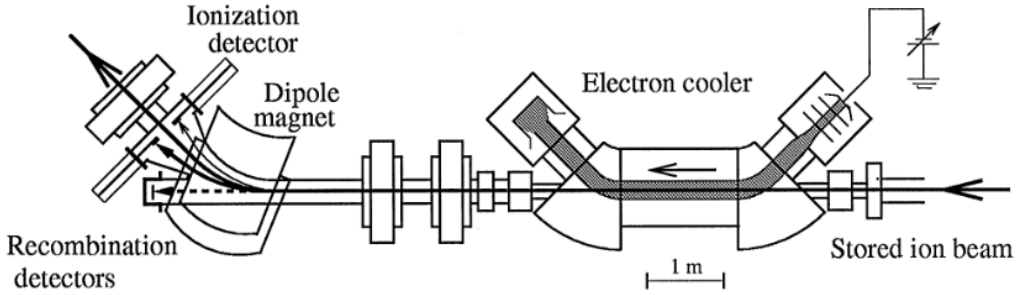

Figure 3.3.: Schematic layout of the TSR electron 'Cooler' section including the detector array which is situated behind the subsequent dipole magnet of TSR [117]. The ionisation products are collected with the inner single-particle detector, while the charged and neutral recombination products are detected on devices located outside the closed orbit.

3.4.1.3. TSR Ion-Sources and Accelerators

At the TSR facility, several ion sources and accelerators were available. A high current injector (HSI) consisting of radio-frequency quadrupoles (RFQ) and an associated drift-tube linear accelerator (LINAC) could provide high intensities of ion beams produced, e.g., in a CHORDIS ion source (low-charged ions) or an electron cyclotron resonance (ECR) source (highly-charged ions) [120].

For most measurements on highly-charged ions, a 12-MV Tandem Van-de-Graaff accelerator [120] was employed. It was fed by a high voltage platform which could be equipped with several kinds of negative ion sources (e.g., a charge exchange duoplasmatron for light ions and a high intensity sputter source for heavier ions). Electron stripping of the ions was done by gas or foil strippers at various energy stages within and after the Tandem beam line.

A second Van-de-Graaff accelerator with a maximum acceleration voltage of 2.7 MV could be used either as a negative ion injector for the 12-MV Tandem accelerator or directly as a source for positively charged molecular ions.

All accelerators were backed by a drift-tube postaccelerator [120] section for further increase in ion energy, which also provided additional strippers and charge-state selecting magnets.

3.4.1.4. TSR Detectors

At TSR, among others, experiments on ionisation and recombination rate coefficients of highly-charged atomic ions have been conducted [71,72,98,121,122]. In the corner sections following the TSR electron coolers, the charge-changed reaction products

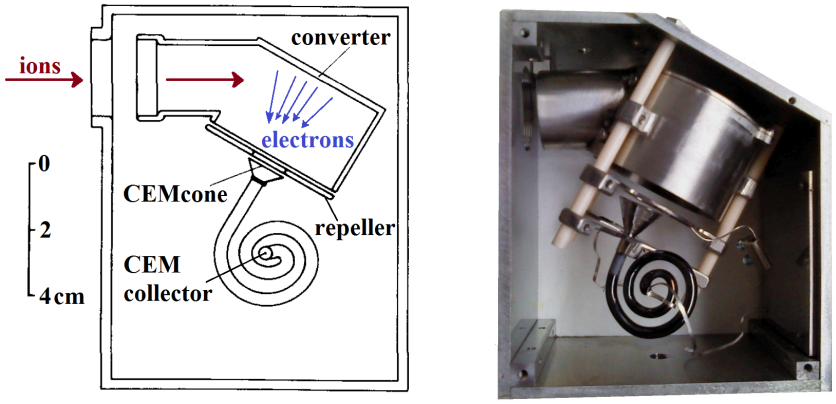

Figure 3.4.: Schematic drawing and open view of a CEM single-particle detector [123] as it is used at TSR. The CEM is situated in the focal point of the converter cathode. The left figure has been adapted from Rinn el al. [123].

Table 3.1.: The standard operating potentials of the TSR CEM-detectors (Fig. 3.4). Even though a potential difference of $\Delta U_{\mathrm{CEM}} \approx 3$ kV between CEM cone and collector is feasible, it is normally operated with the given lower gain voltage.

$U_{\mathrm{converter}}$	-1.1 kV
U_{repeller}	-800 V
U_{CEMcone}	-700 V
ΔU_{CEM}	1.8 kV

are separated from their parent beam by dipole magnets according to their charge-to-mass ratio. In order to collect daughter particles produced in collision experiments with the TSR Cooler, moveable single-particle counting detectors as developed by Rinn et al. [123] are situated in the following corner section (cf. Fig. 3.3). They are driven from outside the experimental vacuum chamber by linear actuators which are sealed by long edge-welded bellows. One detector is situated on the inner side of the closed orbit for detection of ionisation products, while its counterparts for collecting recombination products is mounted at an opposite flange at the outside of the storage ring. The actual particle sensor is a secondary-electron converter cathode backed by a channel electron multiplier (CEM) detector with a repelling electrode in a grounded housing (Fig. 3.4). Secondary electrons, generated by ions impinging onto the converter, are accelerated towards the CEM funnel creating an electron avalanche which can be measured as a current pulse at the end of the CEM channel. The standard operating potentials are given in Tab. 3.1.

The geometry of the converter, repeller and CEM is such that the detector has got an effective counting efficiency of practically 100% [123] for energetic ions. The

Figure 3.5.: Photography of CSR during preparation of the room-temperature commissioning phase in spring 2014. At this point, the isolation vacuum chamber was still open, showing the copper-wrapped beam-guiding vacuum chamber. During commissioning, the outer chamber was closed in order to provide safe high-voltage operation. Since the thermal shields were not yet completely installed at this time, the storage ring could not yet operate in cryogenic mode.

detector features a circular opening of 20 mm diameter, which is sufficiently large to collect the entire daughter beam. Since the vertical acceptance window of TSR for stored parent beams is larger than this aperture, the detectors are not only moveable horizontally, but also vertically.

3.4.2. Cryogenic Storage Ring (CSR)

CSR, as shown in Fig. 3.5, is an electrostatic, cryogenic storage ring with a maximum design energy of 300 keV per unit charge for the stored particles, equivalent to an electric rigidity of ∼600 kV according to Eq. 3.6.

3.4.2.1. General Design

The storage ring, as schematically depicted in Fig. 3.6, has got a circumference of about 35 m and a fourfold symmetry. Each lattice section consists of two sets of quadrupole doublets, two 39° dipole and two 6° dipole deflectors. Each corner sector starts with a focussing quadrupole, followed first by a 6° deflector and second, behind a drift region, by the first 39° deflector. A second, shorter drift region is followed by the same elements but in reverse order, forming an effective deflecting angle of 90°.

In between these corners there are four 2.4 m long, straight drift sections. Three of these sections are reserved for experiments, the fourth straight section is used for beam diagnostics. Except for the experimental section reserved for the future electron cooler ((J) in Fig. 3.6, described in Sect. 3.4.2.2), all straight sections feature two pairs of capacitive beam position pick-up electrodes ((E) in Fig. 3.6) following and preceding the quadrupole doublets. In addition to that, the diagnostic section is equipped with an ion current pick-up electrode and a Schottky-noise pick-up electrode. The single turn, destructive beam-imaging system consists of three beam viewers equipped with off-the-shelf MCP-phosphor-screen stacks (BOS-40 by *Beam Imaging Solutions*). A radio-frequency system for beam bunching and synchrotron acceleration is integrated into the first straight section following the injection corner, from which ion beams are fed into CSR in single-turn mode, by fast switching of one of the 6° deflectors [86].

The corners following the experimental sections of the CSR will be equipped with various kinds of detectors. The initial defecting angle of 6° is small enough to allow for separation and detection of a variety of charge-changed reaction products, but still large enough to allow neutral particles to pass the following 39° deflector in order to be collected on dedicated detectors next to the latter. By integrating two 39° deflectors instead of one 78° deflector, an additional drift section between the 39° dipoles provides an opportunity for fine-grained separation of product particles of charge-to-mass ratios close to that of the stored parent beam. For the first CSR experiments two detectors ((K) in Fig. 3.6) have been installed in the corner following the electron cooler section, one of which was developed as part of the here reported work (Sect. 3.4.2.3).

3.4.2.2. Low-Energy Electron Cooler

An electron cooler with an interaction section of 1 m will be included in CSR in 2015 (c.f. Fig. 3.6). It will be used for electron cooling and in addition serve as target for electron collision experiments. The electron cooler will re-use the TSR photocathode system [119] for generating low energy, cold electron beams of kinetic energies down to 1 eV [124] allowing for phase-space cooling of singly-charged 300-keV ions with masses of up to 160 u [125].

The electron source will be installed in the room-temperature part of the new electron cooler system. The merging and de-merging sections connecting the room-temperature parts to the cryogenic parts of the new cooler, had to be redesigned completely. Particle energies at CSR are significantly lower than at TSR. In order to avoid irreversible disturbance of the ions by the toroidal magnetic field, a combination of superconducting toroidal deflectors and dipole magnets, shown in Fig. 3.7, is used for merging of the beams. In the new design, the toroidal deflectors do not

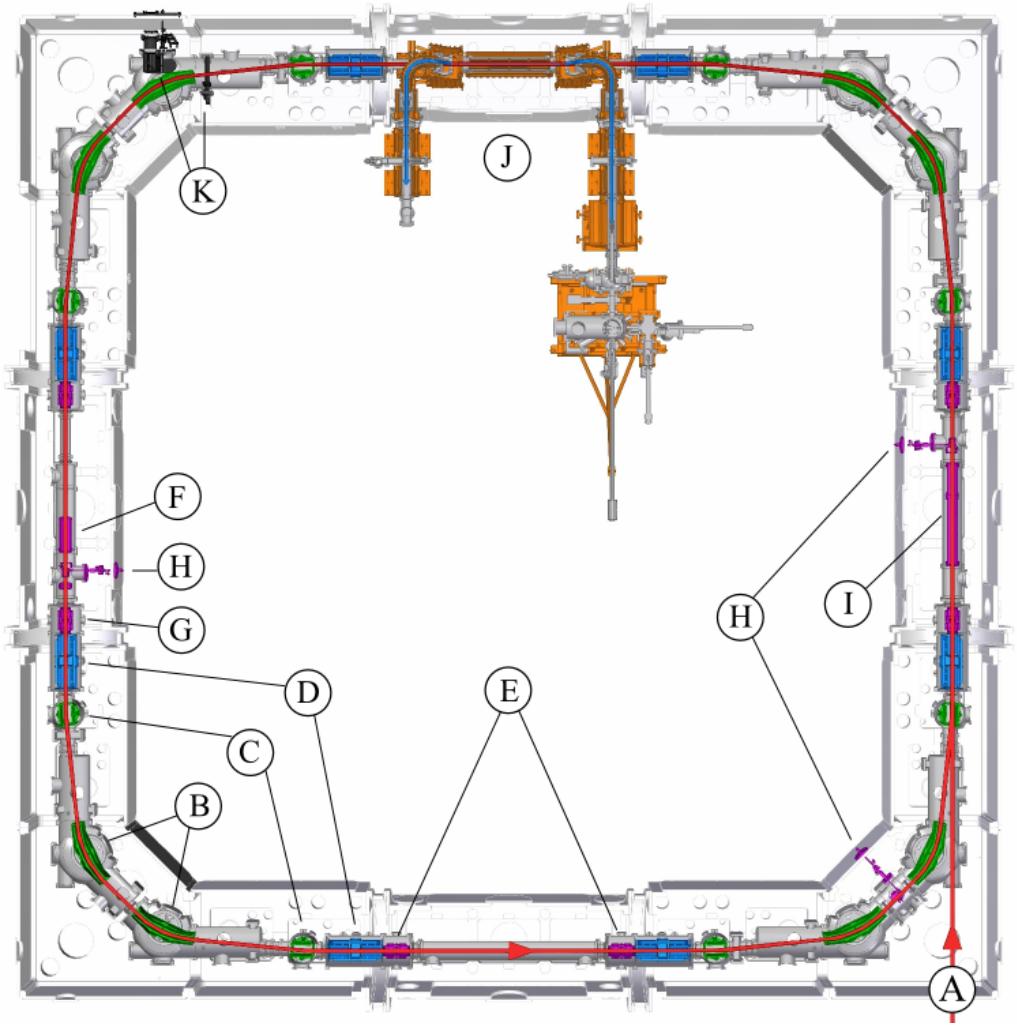

Figure 3.6.: Schematic top-view illustration of CSR including injection (A), beam bending and focussing optics (39° deflectors (B), 6° deflectors (C) and quadrupoles (D)), beam diagnostics (position pick-ups (E), Schottky pick-up (F), current pick-up (G), RF (I) and beam viewers (H)), the future electron cooler (J) and product detectors (K).

influence the stored beam and the remaining disturbance of the ions by the dipole merging field can be corrected for by compensation elements preceding and following the electron cooler section. The newly designed, cryogenic merging and interaction section of the electron cooler will replace the temporary laser interaction section which is used as experimental section in the first cryogenic beamtime at CSR.

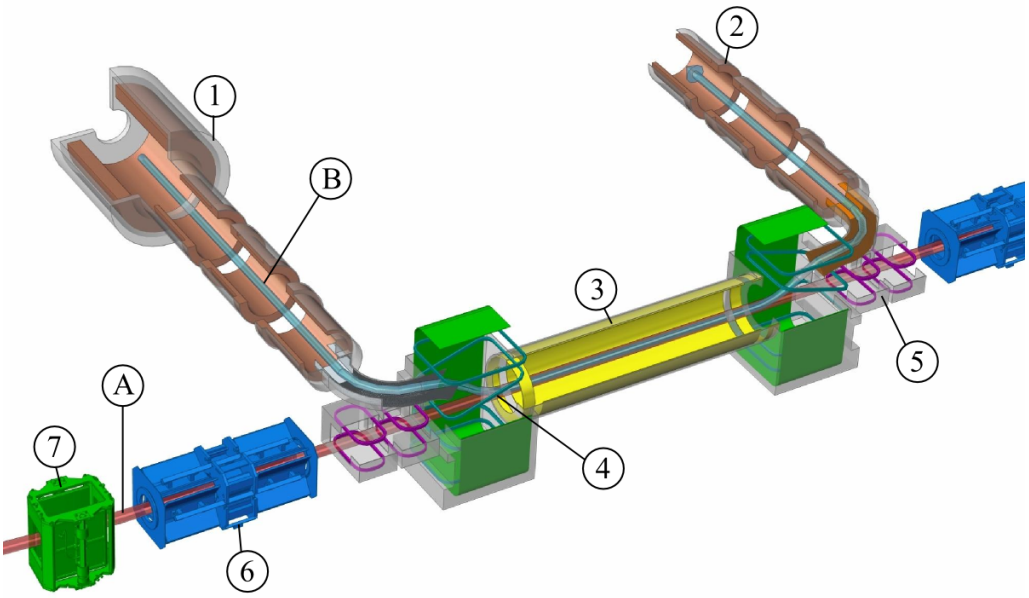

Figure 3.7.: Sketch of the CSR electron cooler. The cooler consists of three parts: two room-temperature sections ((1) and (2)) and the cryogenic merging and interaction beam line is incorporated in the isolation vacuum vessel of CSR. The TSR photocathode system will be mounted to the injection side (1), while the opposite side (2) will house the electron collector. The electrons (B) are merged with the ion beam (A) in the interaction section (3). The disturbances of the ion trajectories by the magnetic fields of the toroids (4) can be corrected for with additional dipole magnets (5) situated in front of and after the interaction section. (6) and (7) are the quadrupole dublett and the 6° deflector of the neighbouring CSR corner sectors.

3.4.2.3. CSR Detectors

In 2014, two particle detectors have been installed at CSR in the corner section following the future electron cooler section. A neutral imaging detector [126] with a large sensitive area of 120 mm diameter is installed ahead of the electron cooler section. It consists of a chevron MCP stack backed by a phosphor screen which will be monitored from the room-temperature side of the set-up by a fast camera system. This detector, called NICE (Neutral Imaging in Cryogenic Environment), will allow for analysis of fragmentation processes by imaging and timing of near-coincident neutral product particles. In addition, a movable particle counter [127], in detail described in Chapter 5, for detection of charge or mass-changed daughter products, is situated after the first 6° deflector of the corner following the future

electron cooling section.

3.4.2.4. Structure of CSR Vacuum System and Thermal Shields

In order to reach an ambient temperature below 10 K, CSR consists of two vacuum systems [128]. The beam-guiding vacuum system is made of stainless steel vacuum chambers which are cooled by liquid helium down to a temperature below 10 K in the cryogenic operating mode of CSR. The helium pipes are connected via thick copper meshwork to the chamber walls, which, in order to provide an overall good thermal conductance, are themselves completely wrapped in thin copper sheets.

The envisaged vacuum pressure of the beam-guiding chamber is 10^{-13} mbar RTE in cryogenic operation mode. In order to reach UHV (10^{-11} mbar) condition also in room-temperature operation, the beam-guiding vacuum chamber can be baked to up to 250°C. At room temperature, the experimental vacuum is mainly pumped by non-evaporative getter pumps (NEGs), ion-getter and charcoal cryo pumps. In the cryogenic operating mode, these pumps are supplemented by cryo-condensation of hydrogen at 2 K cold surfaces which are thermally coupled to the superfluid liquid helium circuit.

The beam-guiding vacuum chamber is completely enclosed by the isolation vacuum system. Its purpose is mainly to protect the cryogenic vacuum chambers from thermal heat load through convection from the room-temperature surfaces. In addition, as it is shown in Fig. 3.8, there are two thermal radiation shields inside the isolation vacuum chamber. The inner shield directly surrounding the beam-guiding vacuum chamber is kept below 40 K during cryogenic operation. The shield rests on titanium supports on the bottom of the isolation vacuum chamber. Identical titanium posts hold the beam-guiding vacuum chamber on top of the 40-K stage.

The second thermal shield, surrounding the 40 K shield, is held at a temperature of below 80 K during cryogenic operation. It is wrapped with several layers of thermal multi-layer insulation (MLI) [129, 130]. As this material cannot withstand the high bake-out temperature of 250°C, the 80 K shield is equipped with water cooling pipes to keep the temperature below 100°C during bake-out.

CSR is designed to allow also experiments on ions of very low rigidity. This is the main reason for the all non-magnetic design of CSR. Particles of small velocities and high charge-to-mass ratio are easily distracted by magnetic fields. In order to avoid any disturbances of the ion trajectories by remanent fields in the ring itself and in order to allow for the future possibility to compensate the Earth's magnetic field by external coils, all materials installed in vicinity of the stored beam orbit are required to be of very low relative magnetic permeability ($\mu_r \leq 1.01$).

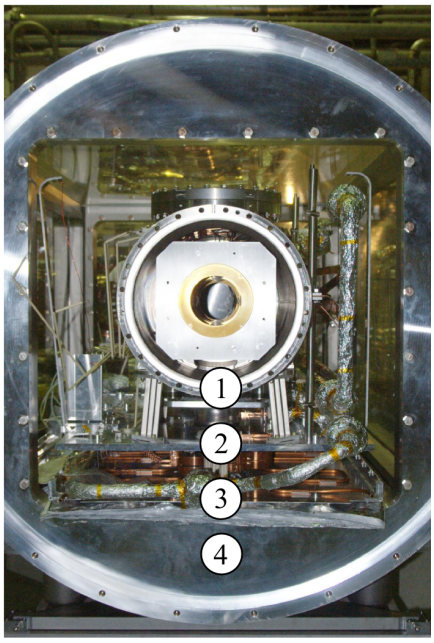

Figure 3.8.: The two vacuum chambers and the thermal shield structure of CSR. The 40 K and 80 K shields surrounding the beam-guiding vacuum chamber (1) are fully contained within the isolation vacuum vessel (4). Since the side and top plates of the shields are not yet installed here, (2) and (3) mark only the base plates of the 40 K shield and the 80 K shield including the surrounding multi-layer insulation. The 40 K base plate is used for mounting of the beam-guiding vacuum chamber, which is resting on titanium posts, and of the 80 K shield, which is hanging on thin Inconel wires.

3.4.2.5. Ion Sources

The storage ring is fed by an ion injector platform, which can be biased at positive or negative potentials of up to 300 kV and equipped with different kinds of ion sources, e.g., sputter ion sources for negative ions, Penning sources, ECR ion sources for positive ions, a buffer-gas 22-pole-trap for creating precooled ions [131], or an electrospray source for large biomolecular ions. A second, smaller source for production of anions with a kinetic energy of up to 60 keV will be attached to the ring in 2015. Using the same injection beam line as the standard CSR ion source platform, these negatively-charged ions are neutralised via laser interaction prior to injection into CSR [132]. This set-up will then enable collision studies between neutral atoms and ions stored in CSR.

3.4.2.6. Present Status and Future Experiments

CSR has been commissioned at room-temperature operation in spring 2014. Although the beam-guiding vacuum chamber had been baked out at 120°C, due to limited pumping facilities then installed the pressure in the beam-guiding vacuum chamber was not better than 1×10^{-7} mbar causing the lifetimes of the stored particles to be as short as 1 ms [86]. Still, 50-keV Ar^+ and N_2^+ were successfully stored and first performance tests with the beam diagnostics and the detector array [127], as reported in Sect. 5.3.1, took place.

In the present status of CSR, the ring is equipped with a laser interaction section at the position where the CSR electron cooler will be installed later. The set-up allows for experiments with crossed ($\theta_L = 90°$) or grazing angle ($\theta_L = 2.7\ °$) beams, the latter results in an interaction length which is ∼20 times larger. In March 2015, the CSR has been cooled down to cryogenic temperatures and the first experiments on photodetachment and dissociation of molecular ions at a temperature of less than 10 K are presently being prepared. An Optical Parametric Oscillator (OPO) laser (EKSPLA NT 342B with a SH/SF generator) will be used for first studies on rotationally cold molecular ions. The first candidate molecular ion is OH^-. Photodetachment studies on molecular OH^- of a rotational temperature of 57±6 K have been preformed previously [133] showing a change of cross sections at given photon energy due to the closing of detachment channels with ongoing rotational de-excitation of the anion. Therefore OH^- can act as a molecular 'thermometer' and demonstrate the CSR's capability of storing internally cold ions.

Later in 2015 the laser interaction section will be replaced by the new CSR electron cooler. In addition, the above mentioned neutral interaction section will be installed in the first straight section following the injection. With the electron cooler available the subsequent cryogenic beamtime can be used for experiments on recombination of cooled atomic ions and molecular fragmentation via electron capture.

4. Experimental Recombination Rate Coefficients of Tungsten Ions

As discussed in Chapter 2, the understanding of the temperature-dependent concentration of tungsten ions in man-made fusion plasmas is critical as it limits the parameter space for plasma ignition and can hence hamper efficient operation of fusion reactors. Since highly-charged tungsten is known to be abundant in the fusion plasma, accurate data on their electron-ion recombination cross sections is valuable knowledge for the fusion community. The only data available for intermediate charge states of tungsten with open 4-f-shells, were, until recently, the theoretical recombination rate coefficients of the ADAS database. However, experimental studies on half open 4-f-shell gold ions [46] revealed that the recombination rate coefficient is enhanced towards lower collision energies due to multi-electron excitations [134] which were enabled by the chaotic nature of the system. Hence, the ADAS data for tungsten ions with similar electron-configuration were expected to be inaccurate since these processes were neglected in the calculations. Laboratory studies on electron-ion recombination of highly-charged tungsten serve as test-benches that are needed to rebut, support and eventually improve new theoretical approaches.

Before the here reported work, only few direct measurements of recombination rate coefficients of highly-charged tungsten ions had been published [72,135]. By investigating recombination of W^{20+} forming W^{19+}, Schippers et al. [72] found that the rate coefficient in the energy region below 50 eV is dominated by resonant processes like DR while the contribution from RR is negligible. These strong, mutually overlapping low-energy recombination resonances have a significant impact on the overall thermal plasma recombination rate coefficient even at the rather high temperatures of interest for fusion devices. A discrepancy of a factor of four was found between the experimental results and the ADAS rate coefficient, showing the need for more sophisticated, theoretical calculations.

In an effort to understand these experimental findings, and similar effects in other open f-shell ions [46], new theoretical approaches for calculating recombination rate coefficients of highly-charged tungsten ions with an open 4-f-shell have been developed [60, 136, 137]. The calculations are technically challenging since the large number of energy levels that these configurations support yield numerous, multi-electron excitation channels. However, two approximation approaches, a statistical theory by Dzuba et al. [137] and the partitioned-damped level-resolved calculations

by Badnell et al. [60, 135], have proven their ability to reproduce the experimental data better than any other theoretical approach that is presently available.

Based on the experimental expertise gathered in the measurements on W^{20+}, and in order to provide a series of experimental recombination rate coefficients of four neighbouring f-shell highly-charged tungsten ions, storage-ring measurements on W^{18+} forming W^{17+}, W^{19+} forming W^{18+}, and W^{21+} forming W^{20+} have been performed. Parts of this work have previously been published by Spruck et al. [135]. The experimental procedure including measurement schemes and a discussion of systematic uncertainties are given in Sect. 4.1. The experimental results are presented in Sect. 4.2. The latest theoretical models, developed by Dzuba et al. [136] and Badnell et al. [135], for reproducing these findings are briefly discussed in Sect. 4.3. The comparison between experiment and theoretical results is given in Sect. 4.3.3. The findings are summarised in Sect. 4.4.

4.1. Experiment

In a series of measurements, absolute rate coefficients of W^{18+} [135], W^{19+} [138], and W^{21+} were studied at the TSR heavy-ion storage ring, already depicted in Sect. 3.4.1. The employed experimental procedure and data analysis have also been described for the previously published measurement of W^{20+} [72] and many other experiments on DR performed at the TSR storage ring. After creating a parent beam of $\sim$10 μA of negatively-charged tungsten carbide in a sputter ion source, the WC^- ions were injected into the 12-MV Tandem Van-De-Graaff accelerator (see Sect. 3.4.1.3). They passed a thin carbon stripping foil at the high voltage terminal of the accelerator (at 10 to 11 MV). Therein, the molecular bond was broken and several electrons were stripped off. After passing a second carbon stripping foil at higher particle energies, isotopically pure tungsten of the desired charge state was momentum-selected with a dipole magnet behind the accelerator. The time-averaged, electrical ion-beam current at this point was typically a few 100 pA. 169-MeV $^{182}W^{18+}$, 186-MeV $^{186}W^{19+}$ or 208-MeV $^{184}W^{21+}$, respectively, were selected and then multiturn-injected [81] into the storage ring, accumulating to ion currents of several 10 nA. In all tungsten measurements presented here, the TSR Cooler (Sect 3.4.1.2) was both used for electron cooling of the ion beam and as an electron target for recombination measurements.

The here presented experiments on tungsten ions were rather challenging. First, the ion currents after the stripping process were only weak. Therefore, even after multiturn-injection into TSR, a direct measurement of the ion current was not possible. Hence, alternative methods of determining the absolute rate coefficient (cf.

Eq. 3.17) were required. In addition, the very high recombination rate at zero collision energy (Sect. 4.2) resulted in very short beam lifetimes of a few seconds only as soon as electron cooling was switched on. The transverse cooling time (Eq. 3.12) of the TSR Cooler can be approximated as [139]

$$\tau_c \approx \frac{m_i}{q^2} \times 3 \text{ s} \tag{4.1}$$

where q and m_i are charge state and mass (in atomic mass units) of the stored ions, resulting in expected cooling times of 1.7 s for $^{182}W^{18+}$, 1.5 s for $^{186}W^{19+}$ and 1.3 s for $^{184}W^{21+}$. Since these cooling times are of the order of the beam lifetimes, the ion currents after cooling were an order of magnitude smaller than immediately after injection. Data taking took, thus, place with a very small number of stored ions in the ring, such that comparatively long measurement times were required for reaching an acceptable level of statistical uncertainty.

In the corner section of the storage ring following the electron cooler (Fig. 3.3), the recombination and single-ionisation products of electron collisions were separated from the stored beam and counted simultaneously by two moveable single-particle detectors (see Sect. 3.4.1.4) installed behind the next dipole magnet of the TSR. Both detectors were adjusted horizontally and vertically such that recombined and ionised product ions were fully collected within the circular detector openings of 20 mm diameter. These are significantly larger than the size of a cooled beam. Count rates of up to a few 10^4 s^{-1} were recorded. Hence, dead time effects were negligible as the data acquisition system is able to process count rates of up to several 10^5 s^{-1} [140]. Since the absolute scaling of the measured recombination rate coefficients was determined by separate lifetime measurements (cf. Sect. 4.1.3), the effective counting efficiency of the detectors does not contribute to the measured recombination rate coefficient. Nevertheless, the effective counting efficiency for energetic ions is expected to be practically 100% [123].

At the beginning of each measurement cycle, tungsten ions of the desired charge state were injected into the storage ring and first cooled for 1.5 s, with the Cooler electron-beam energy adjusted for matching electron and ion velocities. Due to the low beam intensities and the short beam lifetimes, this initial cooling time was kept as short as possible. The 1.5 s correspond to the above estimated transverse cooling times for a stored beam of W^{18+} and W^{19+} ions. However, for a stored beam of W^{21+} ions, Eq. 4.1 yields a value of 1.7 s. Nevertheless, while cooling, the beam profile of the stored W^{21+} ions as a function of time was continuously monitored. If was found that, after 1.5 s, this profile was not changing anymore. Hence, it could be assumed that the stored W^{21+}-ion beam was cooled already by then and an initial cooling time of 1.5 s is sufficient also for this charge state.

Following this initial cooling time, two kinds of measurements were conducted. Rel-

ative recombination rate coefficients (cf. Sect. 4.1.2) were obtained by varying the cathode voltage of the electron cooler, and hence the electron energy, in order to perform a scan over a predefined collision energy range. As mentioned above, the low ion currents stored in TSR prevented a direct measurement of the absolute recombination rate coefficient. The measured relative recombination rate coefficients were put on an absolute scale by normalising to the absolute recombination rate coefficients at zero collision energy obtained by a separate measurement as described in Sect. 4.1.3.

4.1.1. Level Populations

A consequence of the ion production scheme described above is that various excited level can be populated during the foil stripping process. While levels with short lifetimes decay during the initial cooling time, long-lived metastable levels can survive and, hence, also contribute to the measured electron-ion recombination signal. The measured recombination rate coefficient σ is, in general, a mixture of the recombination rate coefficients σ_i which originate from these different energy levels i:

$$\sigma = \sum_i p_i \sigma_i \tag{4.2}$$

where p_i denotes the corresponding level population. Electron-ion recombination from excited levels of the parent ion is normally strongly suppressed due to the additional amount of energy available, opening autoionisation channels which compete with the actual recombination. Hence any residual presence of excited levels in the ion population during the measurements might lead to an underestimation of the rate coefficient which has to be accounted for (cf. Eq. 4.4).

Lifetimes of metastable levels of the here investigated tungsten charge states were calculated employing the *AUTOSTRUCTURE* [141] atomic structure code to estimate the remaining metastable fraction in the cooled-ion beam. The code delivered E1, E2, and M1 radiative rates from excited levels of the given configurations into all lower levels accessible by the corresponding dipole or quadrupole transition [142]. These transition rates were used to simulate the time-dependent level populations by numerical solution of the corresponding coupled rate equation [143]. Although the physical level population produced in the fast foil-stripping process is unlikely to be thermal [143], a Boltzmann distribution of levels with an electron temperature of $k_B T$ = 510 eV (W^{18+}), 560 eV (W^{19+}), and 620 eV (W^{21+}), respectively, corresponding to the particular ion beam energy, was assumed as initial condition. However, the resulting distributions are largely independent of the assumed initial distribution and hence they are believed to reflect the actual beam compositions of the experiments. Results for each charge state are given in the following. The code of

Table 4.1.: Lifetimes of W^{18+} levels of the [Kr] $4d^{10}$ $4f^{10}$ configuration. Listed are only levels with lifetimes longer than 10 ms. E_{ex} denotes the excitation energy from the $^5I_8$ ground level.

E_{ex} (eV)	level	lifetime (s)
0	$4f^{10}\ ^5I_8$	∞
2.977	$4f^{10}\ ^5I_6$	2.13×10^{-2}
3.543	$4f^{10}\ ^5I_5$	2.22×10^{-1}
4.273	$4f^{10}\ ^5F_5$	2.55×10^{-2}
4.390	$4f^{10}\ ^5I_4$	7.19×10^{-2}
4.650	$4f^{10}\ ^3F_2$	$3.79\times10^{+8}$
5.271	$4f^{10}\ ^5F_4$	3.80×10^{-2}
5.862	$4f^{10}\ ^5S_2$	4.13×10^{-2}
5.982	$4f^{10}\ ^5F_3$	4.28×10^{-2}
6.331	$4f^{10}\ ^5F_1$	1.72×10^{-2}
7.090	$4f^{10}\ ^3L_9$	3.41×10^{-2}
8.032	$4f^{10}\ ^5G_3$	1.29×10^{-2}
8.049	$4f^{10}\ ^3K_6$	1.16×10^{-2}
8.498	$4f^{10}\ ^3M_{10}$	0.23×10^{-1}
9.542	$4f^{10}\ ^3P_0$	1.97×10^{-2}
12.050	$4f^{10}\ ^5D_2$	1.21×10^{-2}
19.775	$4f^9\ 5s\ ^5M_{11}$	6.29×10^{-1}
19.988	$4f^9\ 5s\ ^5M_{10}$	1.74×10^{-2}
26.484	$4f^9\ 5s\ ^3O_{12}$	3.71×10^{-2}

the *WOLFRAM MATHEMATICA* [144] program used for the solution of the above mentioned coupled rate equation and for the calculation of the level distribution, is provided in Appendix A.

4.1.1.1. Level Populations for W^{18+} ions

The ground level for W^{18+} is found to be [Kr] $4d^{10}$ $4f^{10}$ $^5I_8$ as predicted earlier [145]. Lifetimes of 1 970 excited levels from the [Kr] $4d^{10}$ $4f^{10}$, [Kr] $4d^{10}$ $4f^9$ 5s, and [Kr] $4d^{10}$ $4f^9$ 5p electron configurations with energies of up to 114 eV above the ground level were calculated using the *AUTOSTRUCTURE* atomic code [142]. However, only one ($^3F_2$) of these levels was found to have a lifetime above 1.5 s. Since the ion beam was initially cooled for 1.5 s, this was expected to be the only metastable level to be present in the parent ion beam during the measurement. In Tab. 4.1 lifetimes of the long-lived 19 levels with lifetimes of more than 10 ms are given.

Figure 4.1 shows the time dependent fractional abundance of the same 19 levels of W^{18+} modelled as described above. After the initial cooling time of 1.5 s, a fraction of 10% of the ions remains in the metastable $^3F_2$ level, which has a lifetime in the order of 10^8 s. Since all other excited levels have by then decayed, the remaining 90% are in the ground level. Due to the long lifetime of the $^3F_2$ level, this fraction is not changing during the recombination measurement time of 2 s for W^{18+}.

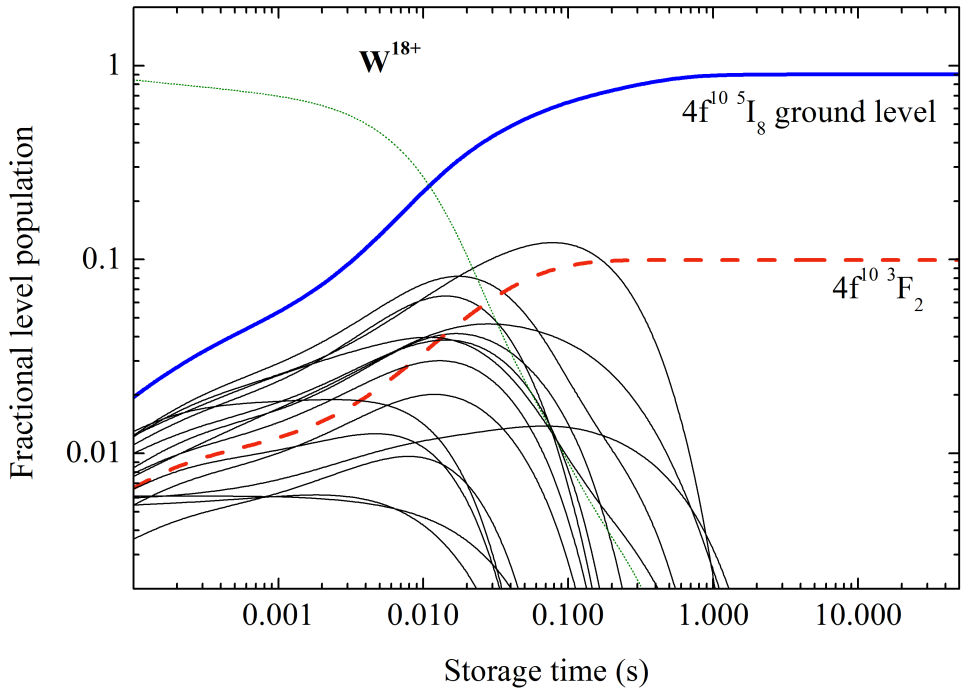

Figure 4.1.: Level populations of W^{18+}. The blue, thick solid line represents the ground level ($^5I_8$), the red, dashed line the metastable level ($^3F_2$) and the black, thin solid lines the remaining 17 levels from Tab. 4.1. The green, dotted line represents the sum over the remaining 1 670 excited levels with lifetimes below 10 ms.

4.1.1.2. Level Populations for W^{19+} ions

In the same way as for W^{18+}, the level population for W^{19+} was derived. Lifetimes of 2 468 excited levels from the [Kr] $4d^{10}$ $4f^8$, [Kr] $4d^{10}$ $4f^8$ 5s, and [Kr] $4d^{10}$ $4f^8$ 5p electron configurations with excitation energies of up to 129 eV above the ground level were calculated. The latter is found to be [Kr] $4d^{10}$ $4f^9$ $^6H_{15/2}$ as predicted earlier [145]. The 15 levels with lifetimes of more than 20 ms are listed in Tab. 4.2.

Figure 4.2 shows the level populations of W^{19+} derived from the tabulated lifetimes. It was found, that after 1.5 s of initial cooling time, only 65% of the ions have

Table 4.2.: Lifetimes of W^{19+} levels of the [Kr] $4d^{10}$ $4f^8$ and [Kr] $4d^{10}$ $4f^8$ 5s configurations. Listed are the 15 levels with lifetimes longer than 20 ms. E_{ex} denotes the excitation energy from the $^6H_{15/2}$ ground level.

E_{ex} (eV)	level	lifetime (s)
0	$4f^9\ ^6H_{15/2}$	∞
2.114	$4f^9\ ^5H_{11/2}$	1.54×10^{-1}
2.523	$4f^9\ ^5F_{9/2}$	$8.88\times10^{+1}$
2.588	$4f^9\ ^5F_{11/2}$	4.17×10^{-2}
2.979	$4f^9\ ^5H_{9/2}$	3.53×10^{-2}
3.422	$4f^9\ ^3H_{7/2}$	4.90×10^{-2}
3.602	$4f^9\ ^5F_{7/2}$	4.57×10^{-2}
3.839	$4f^9\ ^5H_{5/2}$	2.83×10^{-1}
4.178	$4f^9\ ^5F_{3/2}$	$3.48\times10^{+1}$
4.524	$4f^9\ ^5F_{1/2}$	3.41×10^{-1}
6.025	$4f^9\ ^3M_{21/2}$	∞
6.065	$4f^9\ ^5K_{17/2}$	4.23×10^{-2}
6.343	$4f^9\ ^3L_{19/2}$	$2.31\times10^{+0}$
12.117	$4f^9\ ^3O_{23/2}$	4.78×10^{-2}
28.278	$4f^8\ 5s\ ^3H_{25/2}$	6.39×10^{-2}

accumulated in the ground level $^6H_{15/2}$. The remaining 35% are distributed among the four most long-lived metastable levels $4f^9\ ^4L_{19/2}$, $^5F_{3/2}$, $^5F_{9/2}$, $^4M_{21/2}$, which are listed in Tab. 4.2. During the experimental measurement time of 2 s, the beam composition slightly changes due to the lifetime of only 2.31 s of the $^3L_{19/2}$ level. Its level population decreases from 4% to 2% during the measurement time between 1.5 s and 3.5 s in Fig 4.2. As other systematic uncertainties are much larger, this effect on the 10^{-2} scale is neglected in the following. However, the presence of metastable levels during the measurement cannot be neglected and has to be considered in the analysis and interpretation of the measured recombination data below.

4.1.1.3. Level Populations for W^{21+} ions

For W^{21+}, lifetimes of 2 597 excited levels of the [Kr] $4d^{10}$ $4f^7$ electron configuration with excitation energies of up to 169 eV above the ground level have been calculated. The latter is found to be [Kr] $4d^{10}$ $4f^7$ $^8H_{7/2}$ in accordance with previous findings [145]. Table 4.3 lists the 15 states with lifetimes of more than 10 ms.

Figure 4.3 shows the derived level populations of W^{21+}. After 1.5 s of cooling time, about 48% are in the ground level $^8S_{7/2}$. A large fraction of 33% has accumulated in the $^6I_{17/2}$ level and 10% can be found in the $^6I_{13/2}$ level. Less than 5% are in the

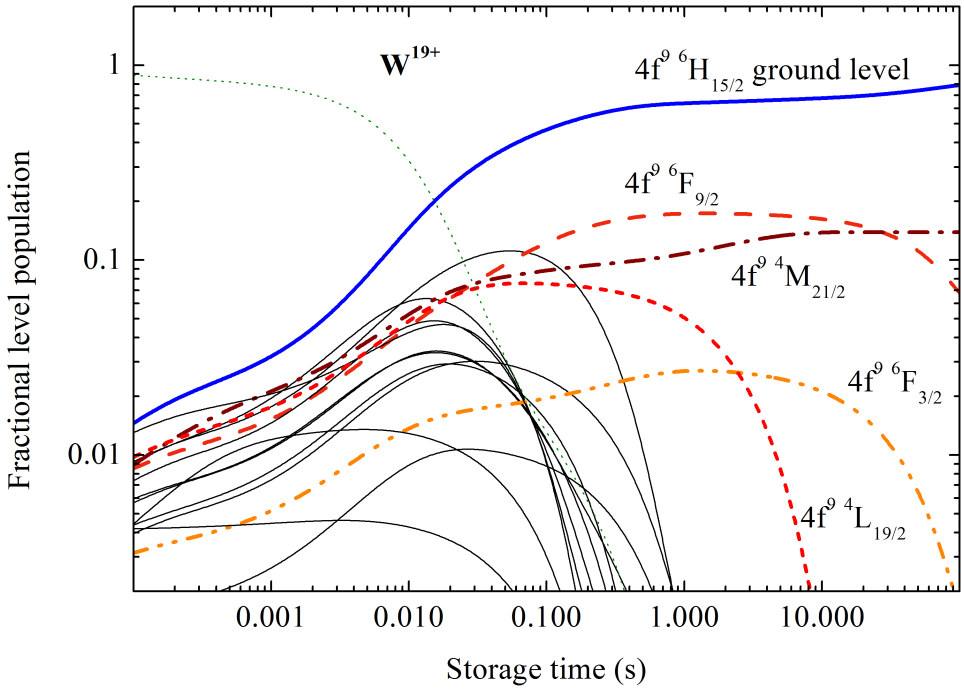

Figure 4.2.: Level populations of W^{19+}. The blue, thick solid line represents the ground level ($^6H_{15/2}$). The four metastable levels with lifetimes of more than 1 s are $^6F_{9/2}$ (red, long-dashed), $^4M_{21/2}$ (dark red, dot-dashed), $^4L_{19/2}$ (red, short-dashed) and $^6F_{3/2}$ (orange, dot-dot-dashed). The black, thin solid lines represent the sum of the ten remaining levels from Tab. 4.2. The green, dotted line represents the sum over the remaining 2 468 excited levels with lifetimes below 10 ms.

$^4N_{23/2}$ level, while both, the $^6I_{15/2}$ and the $^6I_{11/2}$ level, have level populations below 2%. The contribution of the $^6I_{9/2}$ level can be neglected since the level population is less than 0.3%.

The measurement times of the recombination measurements of W^{21+} ranged up to 13 s. During this time span, starting after 1.5 s of cooling time, the level populations are changing on the 10% level. The fraction of ions in the ground level rises from 48% to 58%, while in the same time the population of the $^6I_{13/2}$ level decreases from initially 10% to 1%. The population of the $^6I_{17/2}$ level rises only slightly from 33% to 36%. The level population of the $^4N_{23/2}$ level stays at 5%, whereas the population of the $^6I_{15/2}$ and $^6I_{11/2}$ levels drops to below 0.2%. This change of level population during the experiment is not negligible and has to be considered in the analysis as well as in the theoretical modelling and interpretation of the experimental data below.

Table 4.3.: Lifetimes of W^{21+} levels of the [Kr] $4d^{10}$ $4f^7$ configuration. Listed are the 14 levels with lifetimes longer than 10 ms. E_{ex} denotes the excitation energy from the $^8S_{7/2}$ ground level.

E_{ex} (eV)	level	lifetime (s)
0	$4f^7\ ^8S_{7/2}$	∞
8.906	$4f^7\ ^6P_{3/2}$	3.64×10^{-1}
9.007	$4f^7\ ^6I_{7/2}$	1.57×10^{-2}
9.397	$4f^7\ ^6I_{9/2}$	8.19×10^{-2}
9.474	$4f^7\ ^6I_{17/2}$	∞
9.722	$4f^7\ ^6I_{11/2}$	6.12×10^{-1}
9.852	$4f^7\ ^6I_{15/2}$	7.23×10^{-1}
9.869	$4f^7\ ^6I_{13/2}$	$6.37\times10^{+0}$
14.792	$4f^7\ ^4N_{19/2}$	3.52×10^{-2}
14.876	$4f^7\ ^4N_{23/2}$	$1.51\times10^{+12}$
15.278	$4f^7\ ^4N_{21/2}$	3.50×10^{-1}
16.268	$4f^7\ ^4L_{19/2}$	1.91×10^{-2}
18.312	$4f^7\ ^2Q_{25/2}$	6.35×10^{-2}
18.719	$4f^7\ ^4M_{19/2}$	1.64×10^{-2}

4.1.2. Relative Merged-Beams Recombination Rate Coefficient

4.1.2.1. Measurement Scheme

Relative rate coefficients of collision energies between few 100 μeV and 300 eV (W^{18+} and W^{19+}), and between few 10 μeV and 590 eV (W^{21+}), respectively, were measured by scanning the electron cooler cathode voltage through a preselected range of values, corresponding to the desired range of collision energies E_d. In each measurement step, the electron energy E_e is derived from the measured cathode voltage U_{cath} and the electron current I_e by [146]

$$E_e = eU_{cath} - eU_{sp} = eU_{cath} - \frac{I_e r_e m_e c^2}{e v_e}\left[1 + \ln\left(\frac{b}{a}\right)\right] \tag{4.3}$$

where r_e is the classical electron radius, m_e and v_e are the electron mass and velocity, respectively, and b and a are the known diameters of the beam tube and of the electron beam, respectively. Since v_e depends on the space charge potential U_{sp} via E_e, U_{sp} is calculated recursively. The effective collision energy E_d is then derived from Eq. 3.14.

DR measurements on ions with simpler shell structures, e.g. Fe^{14+} [103] or Fe^{17+} [43]

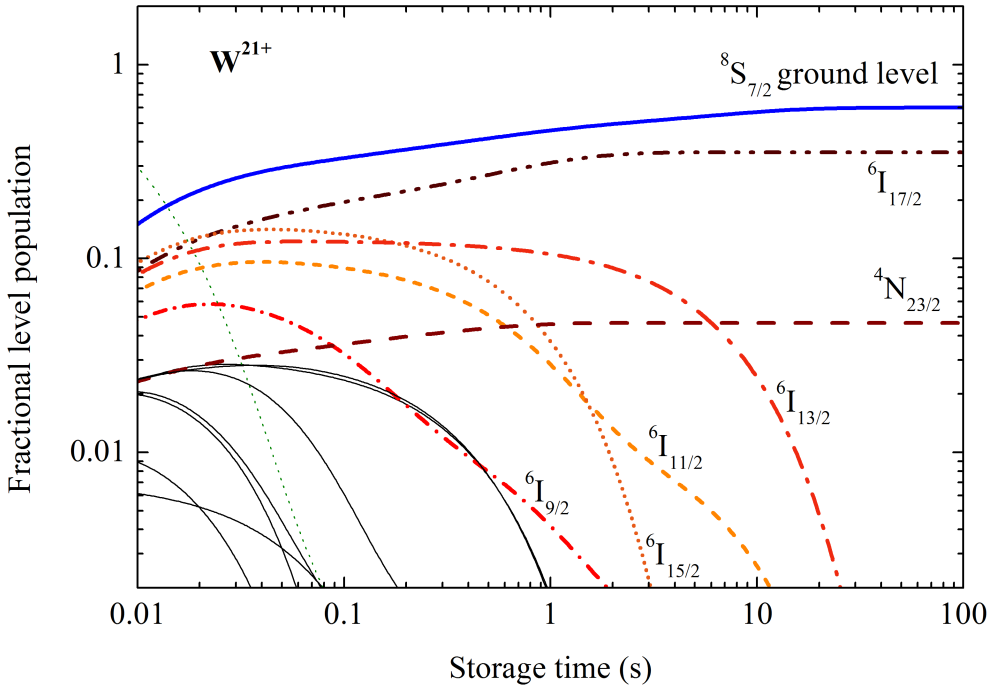

Figure 4.3.: Level populations of W^{21+}. The ground state $^8S_{7/2}$ is represented by the blue, thick solid line. Six metastable levels were found to have a share of more than 0.002 fractional level population present in the parent ions beam after the initial cooling time of 1.5 s: $^6I_{17/2}$ (dark-red, dot-dot-dashed), $^4N_{23/2}$ (dark-red, long-dashed), $^6I_{13/2}$ (red, dot-dashed), $^6I_{11/2}$ (orange, short-dashed), $^6I_{15/2}$ (dark-orange, dotted) and $^6I_{9/2}$ (red, dot-short-dashed). The black, thin solid lines represent the seven remaining levels with lifetimes above 10 ms from Tab. 4.3. The green, dotted line is the sum over the remaining 2 597 excited levels with lifetimes below 10 ms.

(Fig. 2.4), are characterised by clear resonance series which can be used for an accurate calibration of the energy axis by fitting of the data to the well-understood Rydberg levels given by the hydrogenic Dirac formula. However, within the measured recombination rate coefficient of highly-charged tungsten presented in the course of this work, no sharp resonances were observed and it was hence not possible to clearly assign the measured structures to Rydberg series and thereby improve the accuracy of the energy calibration. The uncertainty of the collision energy in the here presented measurements is thus given by the uncertainty of the above described procedure (see Sect. 4.1.5).

The measurement scheme used for the recombination measurements on W^{18+} and W^{19+} featured a dwell time for each collision energy of 1 ms, with each scan containing 2 000 distinct energy steps, resulting in a measurement time of 2 s. For the

recombination measurements on W^{21+}, various measurement schemes with dwell times ranging from 1 ms to 10 ms for each measurements step and different numbers of steps were employed. In addition, few measurements included three steps per individual measurement point: Each measurement step was accompanied by a cooling step, where the cathode potential was adjusted for matching velocities, and a reference step at a predefined collision energy common to all measurements in the scan. This special mode of operation resulted in overall measurement times of up to 13 s.

On the basis of Eq. 3.18, the merged-beams recombination rate coefficients α of a collision energy E_d is in each measurement step derived by [98]

$$\alpha(E_d) = \frac{R(E_d) f_c}{(1 - \beta_i \beta_e) \epsilon N_i n_e L_{\text{eff}} / C} - \alpha_{\text{BG}}(E_d) \tag{4.4}$$

where R is the measured product ion rate at the recombination detector, n_e the electron density and N_i the number of stored ions in the ring. As described already in Sect. 3.2, N_i is scaled with the ratio between the effective interaction length $L_{\text{eff}} = 1.4$ m and the storage ring circumference $C = 55.4$ m. For each collision energy, the corresponding background $\alpha_{\text{BG}}(E_d)$ has to be subtracted. The relativistic correction $(1 - \beta_i \beta_e)$ is small in these measurements since for all charge states the velocities are below 5% of the speed of light c. The remaining correction factors, ϵ and f_c account, respectively, for the detection efficiency of the recombination detector ($\epsilon = 0.97$) and for the fraction of ground-state ions in the stored beam (Sect. 4.1.1).

As noted above, a challenge of the here presented measurements on highly-charged tungsten was the low ion current. The TSR beam diagnostic is not capable to reliably measure ion currents on the nA scale. However, as long as the maximum electron-ion collision energy is below the ionisation threshold for the individual charge state, ionisation of parent tungsten ions could occur only in collision between ions and residual-gas molecules and the ionisation rate, thus, only depends on the stored parent ion current and the density of the residual gas. The maximum collision energy for all charge states is below the ground-level ionisation threshold E_I (462 eV for W^{18+}, 503 eV for W^{19+} and 595 eV for W^{21+} [145]). Nevertheless, since metastable levels are known to be present in all measurements (Sect. 4.1.1), the ionisation thresholds of these levels have also to be take into account. The long-lived metastable levels found for W^{18+} and W^{19+} (Tab. 4.1 and Tab. 4.2) have ionisation thresholds (E_I -ΔE) which are more than 100 eV above the maximum collision energy and hence do not interfere with the measurements. The metastable levels of W^{21+} which are populated during the measurements have excitation energies ΔE ranging roughly from 9 to 15 eV. Hence, their ionisation thresholds lie within the experimental energy range which end only few eV below the ionisation threshold of the ground level. However, towards the end of the experimental energy range, the signal of the ioni-

sation detector was examined carefully during the measurements and no additional decrease of the rate due to the opening of ionisation channels could be observed. Thus, in all measurements, the signal of the ionisation detector could be used as a proxy for the ion current. As a result, all recombination rate coefficients obtained by this method are only relative.

4.1.2.2. Data Acquisition and Analysis

The mileDAQ software [140] was used for data acquisition and experiment control. At each collision energy, the count rates of both detectors, the dwell time, the cathode voltage, and the electron current were recorded in a (VME) multichannel scaler. The thus recorded signal rates were written into a 'raw-file' and were the basis for all further analysis.

For a given collision energy range, the measurement scheme described above was repeated for usually about 1 h to accumulate data. Hence, each measurement contains fully time resolved rate signals of several (1 000s) identical injection cycles. During the offline analysis, these data were integrated into a single histogram of counts versus cathode voltage, which was then converted to a recombination rate coefficient versus collision energy.

The full experimental energy range was obtained by joining several of the above described scan measurements, each covering a different collision energy range. Each energy scan was prepared such that it had an effective overlap of 50% with its predecessor. This characteristic was used in the offline data analysis to eliminate systematic effects between the single scans, e.g., changes in the residual gas pressure or the discriminator threshold of the detectors, which had to be increased during the experiment in order to suppress electrical noise on the signal line. The latter operation reduced the measured count rate such, that, even though the detectors themselves feature a detection efficiency of practically 100% [123], their effective counting efficiency in the experiment was less. Knowing that the recombination rate coefficient has to have the same value for a given collision energy, the relative rate coefficients of scans with deviating results were scaled to match them to the remaining measurements. However, this was only necessary for measurements with changed discriminator settings of the detectors. Most of the measurements could be joined without further scaling.

Traditionally, in TSR measurements, each measurement step of a scan is accompanied by a cooling step and a reference step for the determination of the background signal due to electron capture from the residual gas (see e.g. [74, 147, 148]). However, as already mentioned above, most of the here described measurements included only a measurement step, since the low ion currents in combination with the high recombination rate coefficients limited the available measurement time after injection.

Hence, the level of the background signal had to be derived by choosing a flat region of the recombination spectrum, and subtracting a background count rate in such a way that the residual count rate at this chosen energy matched the theoretically calculated pure RR recombination rate coefficients.

An absolute scaling of the measured relative recombination rate coefficient was done only in the last step of data reduction, by pinning the rate coefficient value at zero collision energy to the absolute measurements described in Sect. 4.1.3.

4.1.3. Absolute Recombination Rate Coefficient

The absolute recombination rate coefficient α at 0 eV collision energy was determined by analysing the lifetime of the stored ions beam with the electron cooler switched on and off, respectively. The rate of recombination products on the associated detector is monitored as a function of storage time. While the lifetime of the parent ion beam without electron cooling (Cooler off) is only limited by collisions with residual-gas particles, it is reduced significantly by electron recombination as soon as the intense electron beam is overlapped with the ion beam (Cooler on). The $1/e$-lifetimes of the stored ion beam in both cases can be measured by fitting of exponential decay functions of the type $f(x) = A \cdot e^{-x/\tau}$ to the measured count rate as a function of time (Fig. 4.4).

Assuming that the electron and the residual gas densities, as well as the level populations of the tungsten ions are constant during the time of the measurement, the absolute value of α is derived from the decay constants via [149, 150]

$$\alpha(0\ \mathrm{eV}) = \frac{\tau_{\mathrm{on}}^{-1} - \tau_{\mathrm{off}}^{-1}}{n_e L_{\mathrm{eff}}/C} \quad . \tag{4.5}$$

This determination of $\alpha(0\ \mathrm{eV})$ is independent of an absolute knowledge of the stored ion current or the detector efficiency. As already mentioned in Sect. 4.1.2, the absolute value should be corrected for the fraction of metastable ions contained in the parent ion beam as it is done in Eq. 4.4, in order to yield the true recombination rate from the ground-level only.

As already discussed in Sect. 4.1.1, the population of metastable levels can reduce the measured recombination rate coefficient. These metastable levels would induce a double (or multiple) exponential decay in the measured rate over the time of the lifetime measurement (a few seconds after production). Even though it was found (Sect. 4.1.1) that metastable levels were populated during the time of the measurement, no additional exponential decay could be observed for any of the measured charge states. It should be noted that, due to the short measurement

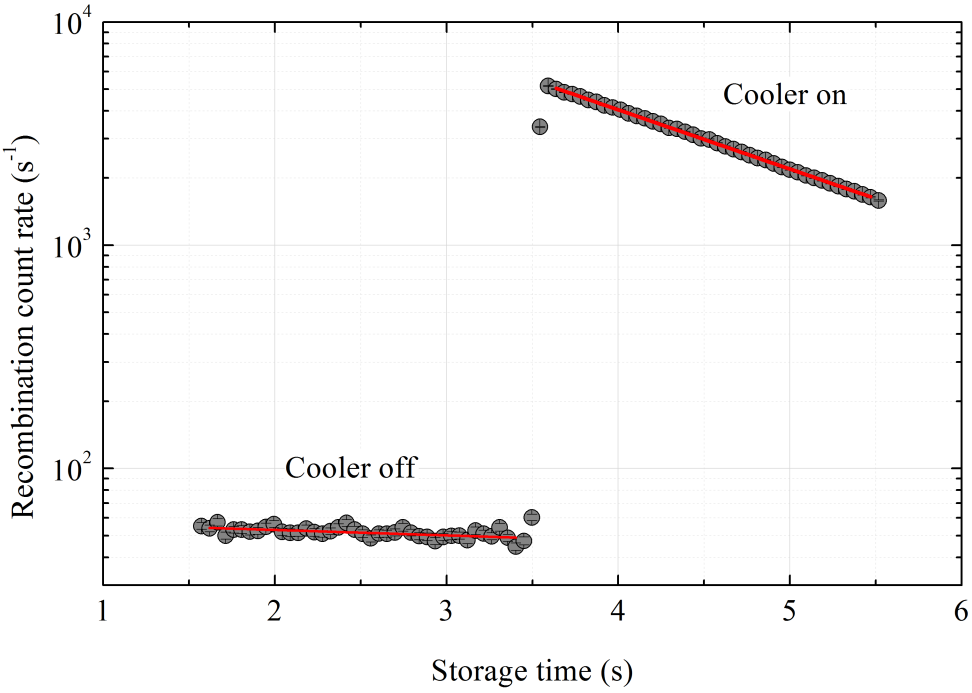

Figure 4.4.: The absolute recombination rate coefficients at 0 eV collision energy is obtained by analysing the lifetimes of the stored ion beam with the electron cooler switched on and off, respectively. The absolute electron-induced recombination rate α can be derived from only the decay constants in both cases, as well as from the electron density and geometry of the Cooler (Eq. 4.5). As an example, the lifetime measurements of W^{18+} forming W^{17+} is given here. The obtained decay constants were $\tau_{\mathrm{off}} = 14\,(4)$ s with Cooler off and $\tau_{\mathrm{on}} = 1.62\,(2)$ s for Cooler on, resulting in an absolute recombination rate coefficient at 0 eV collision energy of $2.16\,(9) \times 10^{-6}$ cm^3 s^{-1}.

time, only levels featuring lifetimes which are at maximum of the same dimension as the lifetimes of the ground level could have been observed.

The metastable level population for W^{18+} (Fig. 4.1) was found to be on a constant level of 10% during the time of the measurement. This could mean that either the long lived levels presented in Sect. 4.1.1 are not significantly populated or the recombination cross sections for metastable and ground-level ions are too close to distinguish them by their recombination-induced lifetimes. It was concluded that the absolute value of $\alpha(0\ \mathrm{eV})$ is not sensitive to the population of the metastable levels and taken to correspond to the value for a pure ground-level population.

In contrast to that, the level populations of W^{19+} (Fig. 4.2) and especially of W^{21+} (Fig. 4.3) showed not only a high (more than 35%) population of several metastable

levels, but also a development in time of this fraction. It has to be assumed that the observed recombination signal contains contributions of not only the ground-level ions but also of a mixture of ions in metastable levels. Still, in all lifetime measurements of both charge states, only one decay constant could be identified. In absence of further possibilities to analyse, the absolute recombination rate coefficient at zero collision energy was derived after Eq. 4.5 without any further corrections. The parameter f_c of Eq. 4.4, which accounts for the fraction of metastable levels in the stored beam, was thus set to 1 for all measurements.

It should be noted, that this method of obtaining an absolute value for the recombination rate coefficient at zero collision energy is also applicable when monitoring the ionisation rate over time while switching the Cooler on and off. However, in most of the measurements the ionisation signal was only weak and the absolute recombination rate coefficient was deduced from the recombination signal.

4.1.4. Energy Resolution

The experimental findings are compared with the theoretical calculations [60, 136] described in Sect. 4.3.1 for the various charge states. To this end, the theoretical recombination cross section has been convoluted with the flattened Gaussian collision velocity distribution of the merged-beams experiment [146]. This distribution is, for a cooled ion beam, represented by the parallel and perpendicular electron beam temperatures, which, based on previous measurements, were assumed to be $k_B T_{e\parallel} = 0.1$ meV and $k_B T_{e\perp} = 10$ meV, respectively, in our experiment. Given the results from Eq. 4.1, all tungsten beams can be expected to be cold enough at the beginning of the recombination measurements, so that the velocity spread of the ions is negligible compared to the electron temperature. However, since, as described in Sect. 4.1.2, the majority of the measurement scans did not include a cooling step in between the measurement steps, the ion-beam temperature increased during the measurement due to intra beam scattering (IBS). Moreover, due to the low ion current of some 10 nA, the adjustment of the electron cooler was difficult and imperfect alignment is likely to have introduced an additional deterioration of the experimental energy resolution. The magnitude of these effects could only be estimated, in absence of sensitive beam diagnostics. By comparison of the experimental and the theoretical merged-beams recombination rate coefficients, values of $k_B T_{\parallel} \approx 0.2$ meV and $k_B T_{\perp} \approx 20$ meV were derived for W^{18+} [135]. Since measurement schemes and currents were similar, these values have been adapted also for the measurements on W^{19+} and W^{21+}, resulting in an experimental energy resolution (Eq. 3.22) of 0.05 eV at collision energies of 1 eV, 0.80 eV at 290 eV, and 1.14 eV at 590 eV.

4.1.5. Uncertainties

The electron acceleration voltage which corresponds to 0 eV collision energy (matching electron and ion velocities) was first calculated from the ion energy. Since the latter is known only to a limited accuracy, a more precise calibration of the energy axis had to be performed. Therefore, a high-resolution energy scan around the expected electron energy for 0 eV collision energy was conducted. The recombination rate coefficient is known to reach its maximum for matching velocities and hence the corresponding electron energy could be derived from the position of this peak. The voltage difference to this point, together with the energy dependent space-charge potential of the electron beam (see Eq. 4.3), defines the experimental electron-ion collision energy. The systematic error lies in the sub-meV scale at 0 eV collision energy and increases towards higher collision energies. It is conservatively estimated [146] to be 0.3 eV at 10 eV, 1.2 eV at 290 eV and 1.5 eV at 590 eV collision energy.

Apart from the counting statistical error on each data point, there are several sources for systematic errors arising from the measurement procedure. Since these uncertainties are independent of each other, they have to be summed up in quadrature in order to obtain an absolute uncertainty. All uncertainties are given at a 90% confidence level.

An energy independent uncertainty arises from the absolute rate coefficient at 0 eV collision energy. Here, the total uncertainty is derived from the uncertainties of the electron density and of the beam lifetimes τ_{on} and τ_{off} (see Sect. 4.1.3). An additional contribution is introduced by the length of the interaction section. The effective interaction length L_{eff} of Eq. 4.5 is shorter than the geometrical length L of the electron cooler (1.5 m) since the velocity vectors of electrons and ions have different directions in the merging and de-merging sections at the beginning and at the end of the overlap region. These differences cause ions and electrons to have collision energies higher than the selected relative velocity at the edges of the cooler. This broadens the measured rate coefficient which is in particular visible in energy ranges with steep gradients of $\alpha(E_d)$. By using the known geometry of the guiding field of the electron cooler to calculate the effective collision energy along the beam axis, a deconvolution procedure which corrects for these effects was developed by Lampert et al. [97]. However, this procedure requires knowledge of the recombination rate coefficient at higher energies beyond the experimental energy range. This is presently not available and therefore the deconvolution method has not been applied to the here presented results. Hence, in order to provide a correct normalisation value for the recombination rate coefficient at zero collision energy, the effective interaction length L_{eff} has to be determined. Even though the geometry of the guiding magnetic field of the Cooler is known, this value is not easy to access. Finally, a value of $L_{\mathrm{eff}} = 1.4\,(1)$ m was chosen for all measurements since this is the mean value of the

geometrically shortest (1.3 m, excluding the toroidal sections) and longest (1.5 m, cooler length) overlap lengths, with the uncertainty being half the difference between these two values. Nevertheless, assuming that the recombination rate coefficient at higher energies is zero, the effect of the deconvolution procedure on the experimental plasma rate coefficient (see Sect. 4.1.6) was briefly investigated. The difference between the deconvolved and the non-deconvolved plasma rate coefficient was within the given uncertainties and thus the error introduced by the broadening of the measured rate coefficient is believed to be negligible. The combined uncertainties on the absolute recombination rate coefficients at zero collision energy are given for each charge state separately (see Sect. 4.2).

As described in Sect. 4.1.2, the background signal was obtained from the lowest measured recombination rate coefficient. The low counting statistics in the corresponding energy region introduced an uncertainty to the size of the background signal. By performing the background subtraction, this systematic uncertainty was propagated to the rate coefficient at lower collision energies and also to the correspondent plasma rate coefficient (see Sect. 4.1.6).

A further source of systematic uncertainty arising from the background subtraction should be mentioned. In principle the assumption that the part of the spectrum chosen for background subtraction consisted of a pure RR signal might be erroneous. As no individual DR resonances are observed in these measurements, it is in principle possible, that the seemingly flat parts of the data consist of unresolved arrays of resonances. Hence, in this case, too much 'background' have been subtracted. Therefore, purely empirically, our results may be regarded as a lower limit for the actual recombination rate coefficient. However the theoretical results which are presented in Sect. 4.3.3 indicate that for the highest measured energies no resonances should expected.

In storage rings, while travelling towards the detectors through the magnetic or electric fields of the deflectors, recombined particles experience a motional electric field F. This results in field ionisation of high Rydberg states above a certain quantum number n_{cut}. Consequently the measured recombination rate is smaller than the total recombination rate. The limiting quantum number of the weakly bound Rydberg electron can be estimated to be [151]

$$n_{\mathrm{cut}} = \left(\frac{q^3}{9F}\right)^{1/4} \tag{4.6}$$

where q is the charge of the stored particle and F is the electric field in atomic units. For the TSR dipole magnet, n_{cut} is calculated for each tungsten charge state. The critical principal quantum numbers for field ionisation of Rydberg states in the magnetic fields of the dipole magnets are $n_{\mathrm{cut}} = 67$ for W^{18+}, $n_{\mathrm{cut}} = 69$ for W^{19+}

and $n_{\mathrm{cut}} = 74$ for W^{21+}. The corresponding systematic error in the plasma rate coefficient is estimated by theoretical calculations to be less than 5%.

4.1.6. Plasma Rate Coefficient

The experimental merged-beams recombination rate coefficient was measured for distinct collision energies, limited only by the experimental resolution of the electron-target set-up (see Sect. 3.3.3). In order to reproduce the distribution of tungsten ions and electrons in plasmas, the measured merged-beams recombination rate coefficient had to be convolved with a thermal collision velocity distribution. As the merged-beams rate coefficient α is the convolution of the recombination cross section σ with the collision energy distribution, $\alpha = \langle \sigma v \rangle$, this in principle requires first a deconvolution from the distribution of electron velocities v, and then a renewed folding of the resulting experimental cross section with the isotropic Maxwellian collision energy distribution characteristic of each given plasma electron temperature $k_B T$. In practice, this procedure is only necessary for plasma temperatures where the relative collision energy E_d is smaller than the experimental energy spread (Sect. 4.1.4). Since these small collision energies are not relevant for the recombination of tungsten ions in fusion plasmas, the plasma rate coefficient could be derived by using a simplified procedure [121]. There, the reaction cross section is calculated by

$$\sigma(E) = \frac{\alpha(E)}{\sqrt{2E/m_e}} \tag{4.7}$$

where E is the relative collision energy given by Eq. 3.14. The plasma rate coefficient can then be derived by Eq. 2.17.

4.2. Experimental Results

Results on recombination rate coefficients for the three tungsten charge states that have been measured within this work are given in the following sections. Since the previously published W^{20+} [72] also belongs to that series, it is discussed as well to some extent. An overview of the recombination rate coefficients for W^{18+} to W^{21+} including the state-of-the-art theory described in Sect. 4.3.1 is given in Sect. 4.3.4.

4.2.1. Electron-Ion Recombination of W^{18+}

The recombination rate coefficient of W^{18+} [135] was measured employing the schemes described above. $^{182}W^{18+}$ was selected and injected into TSR at an energy of 169-

MeV.

The TSR lifetime of the stored beam was $\tau_{\text{off}} = 14\,(4)$ s with electron cooler off and $\tau_{\text{on}} = 1.62\,(2)$ s when electron cooling was applied (see Sect. 3.3.1). With these values an absolute recombination rate coefficient at 0 eV collision energy of $2.16\,(9) \times 10^{-6}$ cm^3 s^{-1} was obtained by using Eq. 4.5. This value could be reproduced in repeated measurements within the given uncertainty at a confidence level of 90%. As already discussed in Sect. 4.1.1, after the initial cooling time of 1.5 s, 10% of the stored ions were believed to have accumulated in a metastable level (Fig. 4.1). However, since no double exponential decay was observed (cf. Sect. 4.1.3), it is concluded that the measured value can be taken to represent a pure ground-level population of ions.

The relative recombination rate coefficient between 0.2 meV and 290 eV collision energy was measured employing the schemes described above, background subtracted, and normalised to the independently found value at 0 eV. Since no reference steps were included in the measurements, the lowest measured recombination rate coefficient (at 260 eV) was used for background subtraction. The resulting recombination rate coefficient is shown in Fig. 4.5, together with the calculated RR rate coefficient (Eq. 2.14). Between 0 eV and 5 eV the experimental rate coefficient decreases by approximately two orders of magnitude. Between 5 eV and 230 eV, broad resonance features are visible. Their widths are much larger than the experimental energy spread given in Sect. 4.2, hence they are not due to few individual autoionising levels, but likely originate from dense arrays of unresolved resonances. Above 230 eV and up to the end of the experimental energy range, the measured rate coefficient approaches zero. Up to collision energies of at least 100 eV, the measured recombination rate coefficient exceeds the RR rate coefficient by two orders of magnitude.

The uncertainties of the recombination rate coefficient, as described in Sect. 4.1.5, result in an energy dependent combined experimental error bar. The value of the independently measured rate coefficient at 0 eV is not affected by the uncertainty of the background subtraction procedure. The statistical error at 0 eV collision energy is 4.7% and the total uncertainty together with the systematic error amounts to 8%. Towards higher collision energies, the background subtraction causes an additional systematic error which is 2% at 1 eV, 25% at 30 eV and 80% at 220 eV collision energy. In combination with the counting statistical error, the total uncertainties at a confidence level of 90% amount to 8% at 0 eV, 9% at 1 eV, 38% at 30 eV and 120% at 220 eV collision energy.

At energies below 10 meV, an enhancement in the recombination rate coefficient is observed. The solid yellow line in Fig. 4.5 is an extrapolation of the measured rate coefficient starting from a few meV towards lower collision energies. The lowest energy ‘peak’ above that extrapolated line is a known artifact of the merged-beams

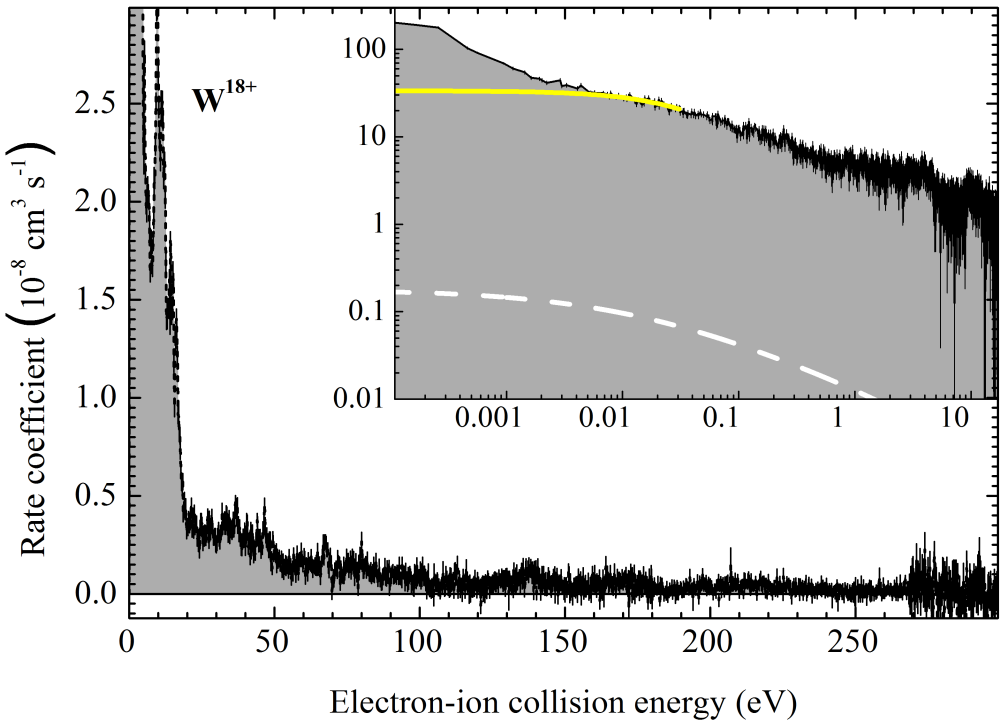

Figure 4.5.: The experimental recombination rate coefficient for W^{18+} is shown together with theoretical calculations. The inset shows a magnification of the lower energies range of the same datasets. The black, filled circles is the experimental rate coefficient obtained within this work, while the white, dashed line represents the calculated, theoretical RR rate coefficient (Eq. 2.14). The rate coefficient above the solid, yellow line is an experimental artifact due to time-dependent electric and magnetic field (see text). The error bars given for the experimental results are the statistical uncertainties in each measuring point.

method and most likely caused by additional electron capture and radiative stabilisation in the time-dependent electric and magnetic fields seen by the stored tungsten ions when travelling through the electron cooler [152, 153]. However, these effects are of importance only at very low collision energies and are not relevant for the plasma rate coefficient in the temperature range of interest.

The merged-beams recombination rate coefficient and the calculated RR rate coefficient (Eq. 2.14) were converted into plasma recombination rate coefficients as described in Sect. 4.1.6. The results for a plasma temperature range of k_BT = 1 to 1000 eV are shown in Fig. 4.6. The uncertainties of the recombination rate coefficient, as discussed above, were propagated to the plasma rate coefficient and are exemplarily given as 10% at 10 eV and 36% at 150 eV plasma temperature.

Table 4.4.: The fit parameters for the parametrisation of the experimentally derived plasma recombination rate coefficient of W^{18+} using Eq. 4.8. In the plasma temperature range from 1 to 1000 eV, the fit deviates by less than 0.5% from the experimental findings.

i	c_i (cm^3 $s^{-1}K^{3/2}$)	E_i (eV)
1	0.1652	1.05797
2	0.5085	4.96985
3	0.8513	13.7193
4	0.8128	40.6401
5	0.8851	102.876
6	0.6247	232.047

The experimental plasma rate coefficient is $5{\times}10^{-8}$ cm^3 s^{-1} at 1 eV and decreases monotonously down to 10^{-10} cm^3 s^{-1} at 1000 eV. The relative difference to the much smaller RR plasma rate coefficient is more than two orders of magnitude at low temperatures, and still a factor of 80 at 1000 eV. The plasma rate coefficient from the ADAS [25] database roughly coincides with the here derived RR plasma rate coefficient in the range below 17 eV. This indicates that the resonant processes, which cause the enhancement of the experimental merged-beams recombination rate coefficient at low collision energies, are not included therein. The ADAS plasma rate coefficient exceeds the RR plasma rate coefficient towards higher plasma temperatures, with a maximum at 130 eV, slowly approaching the newly derived experimental plasma rate coefficient up to a minimum relative difference of less than an order of magnitude at the end of the shown energy scale of 1000 eV. The energy range where W^{18+} is expected to be most abundant in collisionally ionised plasmas can be taken from Fig. 2.2 to lie roughly between 90 and 190 eV. In this energy range (shaded area in Fig. 4.6), the relative difference varies between a factor of 5 to 10. This situation roughly corresponds to what has been previously discovered for W^{20+} [72].

In order to easily incorporate the here reported experimentally derived plasma rate coefficient into numerical models, the latter was fitted in the range $k_BT = 1$ to 1000 eV by the following 12-parameter empirical formula:

$$\alpha_{fit}(T) = T^{-3/2} \sum_{i=1}^{6} c_i e^{-E_i/(k_BT)} \tag{4.8}$$

The fit parameters are given in Tab. 4.4. The fit deviates by less than 0.5% from the experimentally derived plasma rate coefficient in the temperature range from 1 to 1000 eV.

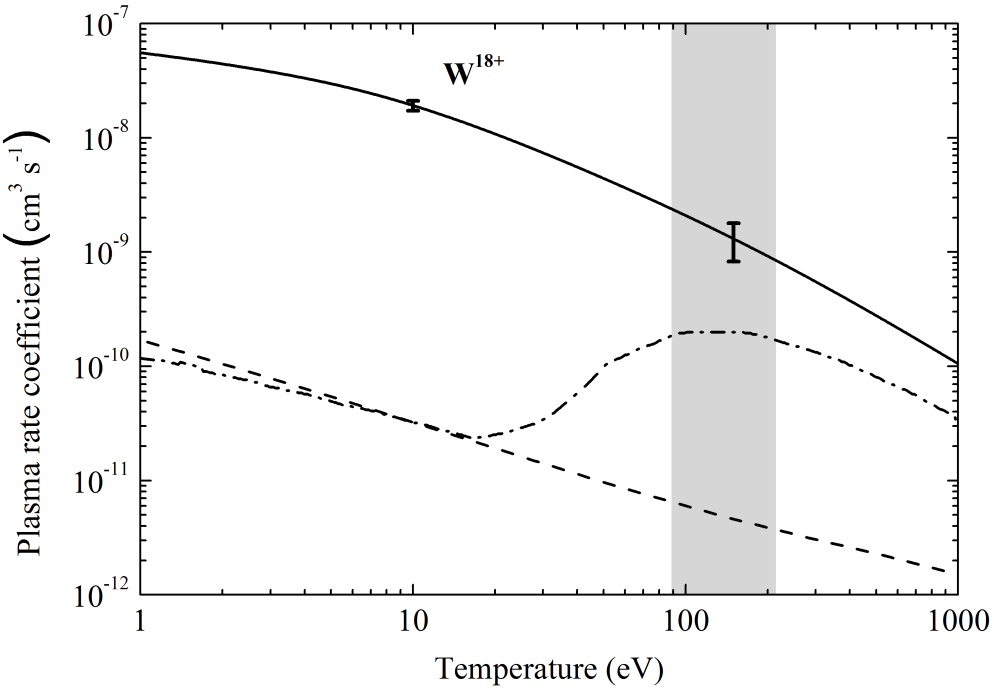

Figure 4.6.: The experimentally derived plasma rate coefficient for W^{18+} (solid line) obtained from the measured recombination rate coefficient by convolving with a Maxwellian energy distribution. The error bars represent the experimental uncertainty at a 90% confidence limit given for 10 eV and 150 eV plasma temperature. The dashed line is the theoretical plasma rate coefficient for RR and the dashed-dotted line is the plasma rate coefficient from the ADAS database [25]. The grey-shaded area highlights the plasma temperature, where W^{18+} is expected to have an abundance of more than 0.01 in a collisionally ionised plasma (cf. Fig. 2.2 in Sect. 2.2.1).

4.2.2. Electron-Ion Recombination of W^{19+}

The recombination rate coefficient of W^{19+} was experimentally investigated [138] employing the same measurement scheme as for W^{18+}. The lifetimes of the stored $^{186}W^{19+}$ beam with an energy of 186 MeV were $\tau_{\text{off}} = 12\,(5)$ s with electron cooler off and $\tau_{\text{on}} = 1.51\,(3)$ s when electron cooling was applied. The absolute rate coefficient at 0 eV collision energy (Eq.4.5) is $2.08\,(14) \times 10^{-6}$ cm^3 s^{-1} at a confidence level of 90%. This value could be reproduced by repeated measurements within the given uncertainty. Even though metastable levels (cf. Fig. 4.2) are know to be present in the parent W^{19+} ion beam, a significant contribution to the measured absolute rate coefficient was not observed, a conclusion that was drawn based on similar grounds than for W^{18+}. Hence, the rate coefficient is directly derived from Eq. 4.5 without

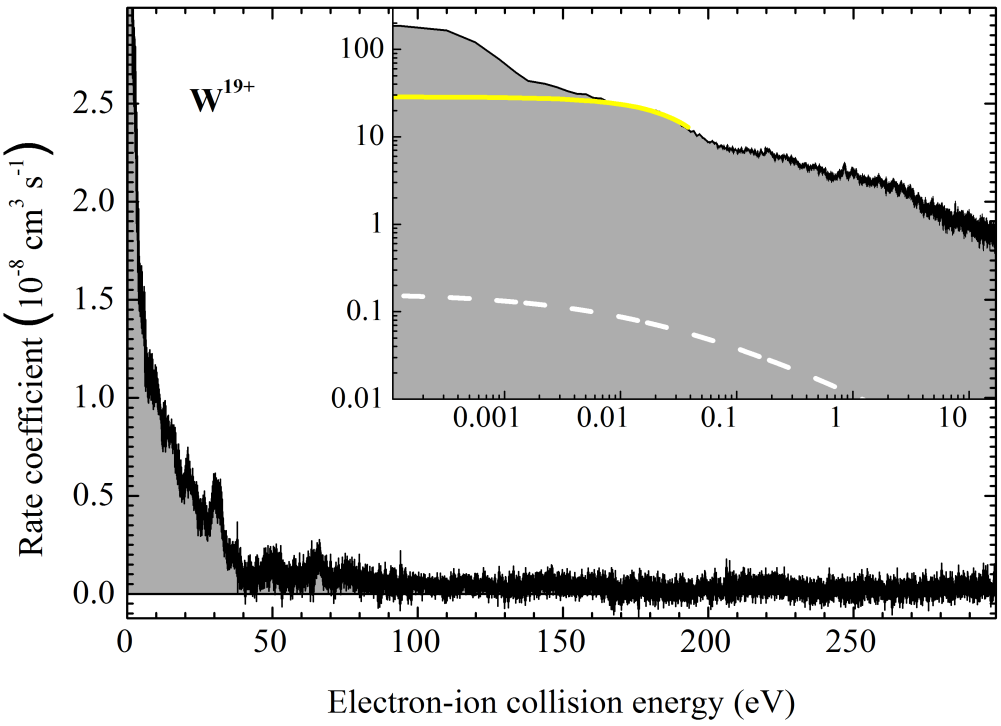

Figure 4.7.: The experimental recombination rate coefficient for W^{19+} in the experimental energy range from 0 eV up to 300 eV. The inset depicts a magnification of the lower energies range of the same datasets. The black, filled circles is the experimental rate coefficient obtained within the scope of this work while the white, dashed line represents the calculated, theoretical RR rate coefficient for W^{19+} (Eq. 2.14). The rate coefficient above the solid, yellow line is an experimental artifact due to time-dependent electric and magnetic field. The error bars given for the experimental results are the statistical uncertainties in each measuring point.

further corrections ($f_c = 1.0$).

The results of the merged-beams recombination rate coefficient measurements between 0.1 meV and 300 eV collision energy are presented in Fig. 4.7. The lowest measured recombination rate coefficient (at a collision energy of 170 eV) was used for background subtraction. Using the same procedure as described above, the rate coefficient was first normalised to the ionisation signal and, in a second step, scaled to the absolute value at 0 eV collision energy obtained by the lifetime measurements. As already observed for W^{18+}, the rate coefficient is enhanced artificially at collision energies below a few meV by the influence of the magnetic field of the electron cooler. In the energy range between 0 eV to 5 eV the experimental rate coefficient decreases by approximately two orders of magnitude. Between 5 eV and 40 eV broad, non-

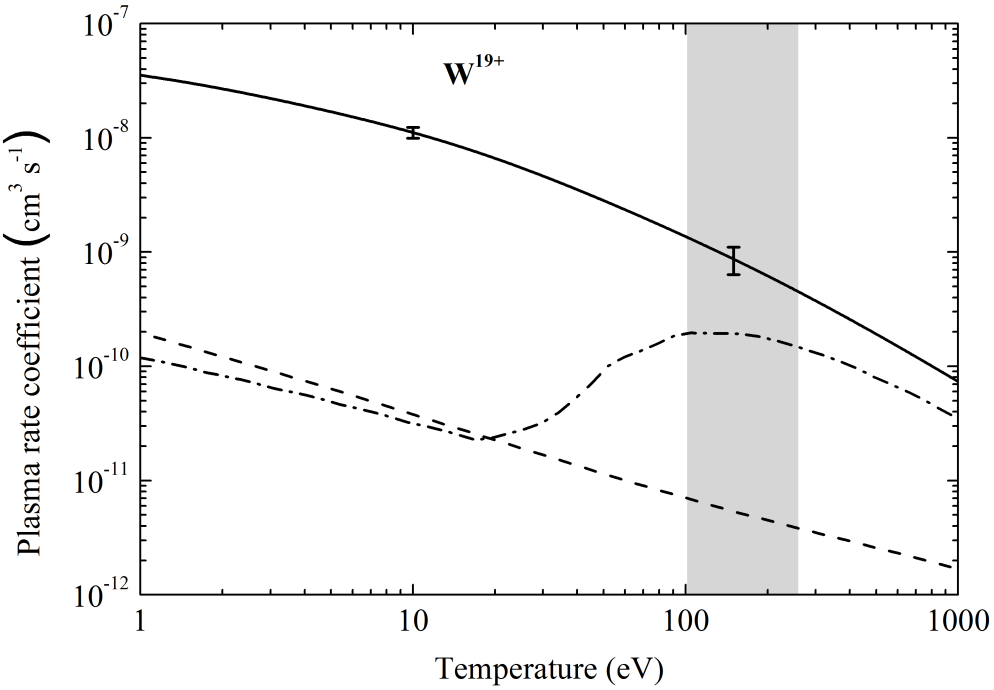

Figure 4.8.: Experimentally derived plasma rate coefficient for W^{19+}. The solid line gives the experimental results with the error bars representing the total uncertainty at a 90% confidence limit given for plasma temperatures of 10 eV and 150 eV. The dashed line is the theoretical plasma rate coefficient for RR and the dashed-dotted line is the plasma rate coefficient from the ADAS database [25]. The grey-shaded area indicates the plasma temperature, where W^{19+} is expected to have an abundance of more than 0.01 in a collisionally ionised plasma [6].

resolved resonance structures cause strong but slow variations of the rate coefficient with energy, while on the average it decreases by one more magnitude. Up to a collision energy of 170 eV, further unresolved resonance arrays are visible, even though they are weaker than those at lower collision energies. Starting from 170 eV to the end of the experimental energy range, the recombination rate coefficient approaches zero within the accuracy and the precision of the measurement. As shown in the inset of Fig. 4.7 for the low collision energy range, the theoretically calculated RR rate coefficient (Eq. 2.14) is, up to energies of about 100 eV, again two orders of magnitude smaller than the experimental rate coefficient.

At 0 eV collision energy, the statistical error is 6.8% and sums up with the systematic error to a total uncertainty of 9.9%. At higher collision energies, the background subtraction causes an additional uncertainty, which is of 2% at 1 eV, 9% at 30 eV and 55% at 150 eV collision energy. In combination with the counting statistical error, the total uncertainties at a confidence level of 90% amount to 10% at 0 eV,

Table 4.5.: The fit parameters for the parametrisation of the experimentally derived plasma rate coefficient of W^{19+} using Eq. 4.8. In the plasma temperature range from 1 to 1000 eV, the fit deviates by less than 1% from the experimental findings.

i	c_i ($cm^3\ s^{-1}K^{3/2}$)	E_i (eV)
1	0.05484	0.55425
2	0.16475	2.58134
3	0.2892	7.18355
4	0.51843	16.28191
5	0.56981	34.37625
6	0.64806	85.96273
7	0.90815	212.12071

11% at 1 eV, 16% at 30 eV and 155% at 150 eV collision energy.

The experimentally derived plasma rate coefficient in the temperature range of 1 to 1000 eV is shown in Fig. 4.8. The given error bars stem from the uncertainties on the recombination rate coefficient mentioned above. The absolute, relative uncertainty is 12% at 10 eV and 27% at a plasma temperature of 150 eV. The experimental plasma rate coefficient is 3.5×10^{-8} $cm^3\ s^{-1}$ at 1 eV and decreases monotonously down to 10^{-9} $cm^3\ s^{-1}$ at 1000 eV. In comparison to the above described W^{18+} this is a factor of 2 less. The difference to the much smaller RR plasma rate coefficient is more than two orders of magnitude at low temperatures, reducing to only a factor of 50 at 1000 eV. The plasma rate coefficient which can be found in the ADAS [25] database is in the temperature region of up to 17 eV similar to the RR plasma rate coefficient and exceeds it significantly only towards higher plasma temperatures. It has got its maximum at 105 eV and approaches the experimentally derived plasma rate coefficient, until, at a temperature of 1000 eV, the deviation is less than a factor of 3. In the energy range where W^{19+} is expected to be most abundant in collisionally ionised plasmas (see Fig. 2.2), roughly from 100 to 260 eV, the relative difference varies between a factor 3 to 8.

The experimentally derived plasma rate coefficient was fitted using Eq. 4.8 for easy approximate numerical reproduction of the result. The fit parameters are given in Tab. 4.5. The fit deviates by less than 1% from the experimentally derived plasma rate coefficient in the temperature range of 1 to 300 eV.

4.2.3. Electron-Ion Recombination of W^{21+}

W^{21+} was the last tungsten charge state stored in the TSR at the MPIK facility. In contrast to the measurements on W^{18+} and W^{19+}, W^{21+} was measured over a broader collision energy range of 0.04 meV to 590 eV.

208-MeV $^{184}W^{21+}$ was injected into TSR. After an initial cooling of 1.5 s duration, scan measurements employing different measurement schemes were conducted. The predefined cathode voltage was ramped in 100 to 6500 steps, while the measurements time for each collision energy varied between 1 and 10 ms, resulting in overall measurement times of up to 15 s. In order to provide a sufficiently strong parent beam for such long measurements, W^{21+} was accumulated in TSR by up to 3 multi-turn injections before starting the measurement with the help of cooler assisted ion stacking [68]. Some measurements included, in addition to the measurement step, a reference and a cooling step for each collision energy. While rough scans over the entire experimental energy range were used for to gain overview rate coefficient spectra, fine scans of smaller step widths were added in energetic regions exhibiting resonances in the measured recombination rate coefficient.

The absolute value for $\alpha(E = 0\ \text{eV})$ of W^{21+} was derived from four lifetime mea-

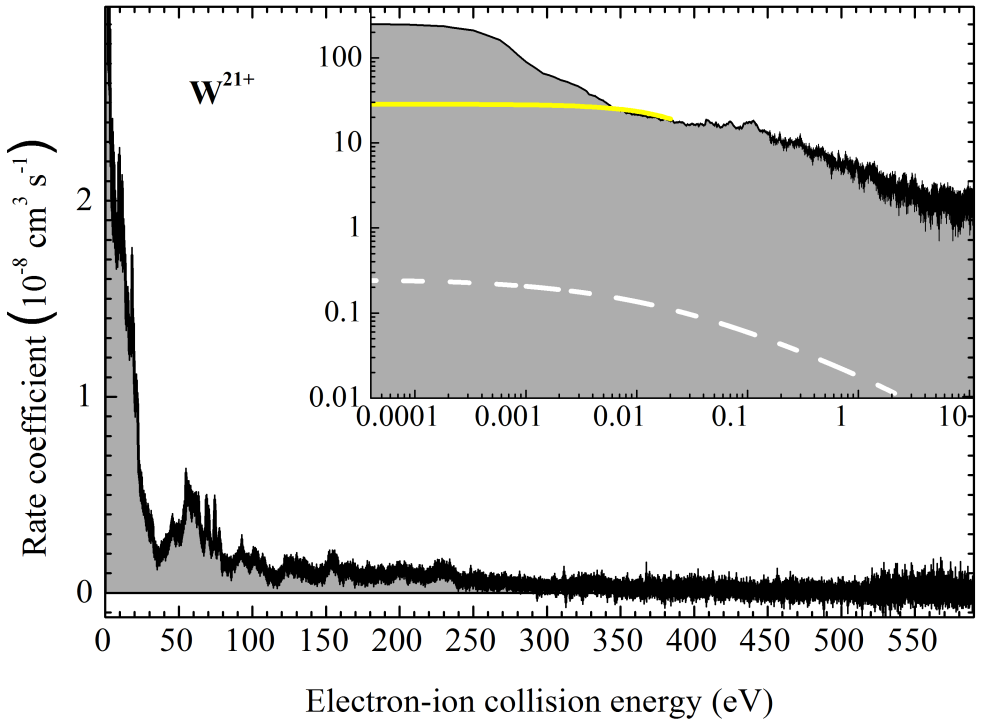

Figure 4.9.: The experimental recombination rate coefficient for W^{21+} in the energy range from 0 to 590 eV (filled black circles). The inset is a magnification of the low energy range of the same datasets. The error bars represent the statistical uncertainties. The white, dashed line represents the calculated, theoretical RR rate coefficient for W^{21+} (Eq. 2.14). The rate coefficient above the solid, yellow line is an experimental artifact due to time-dependent electric and magnetic field.

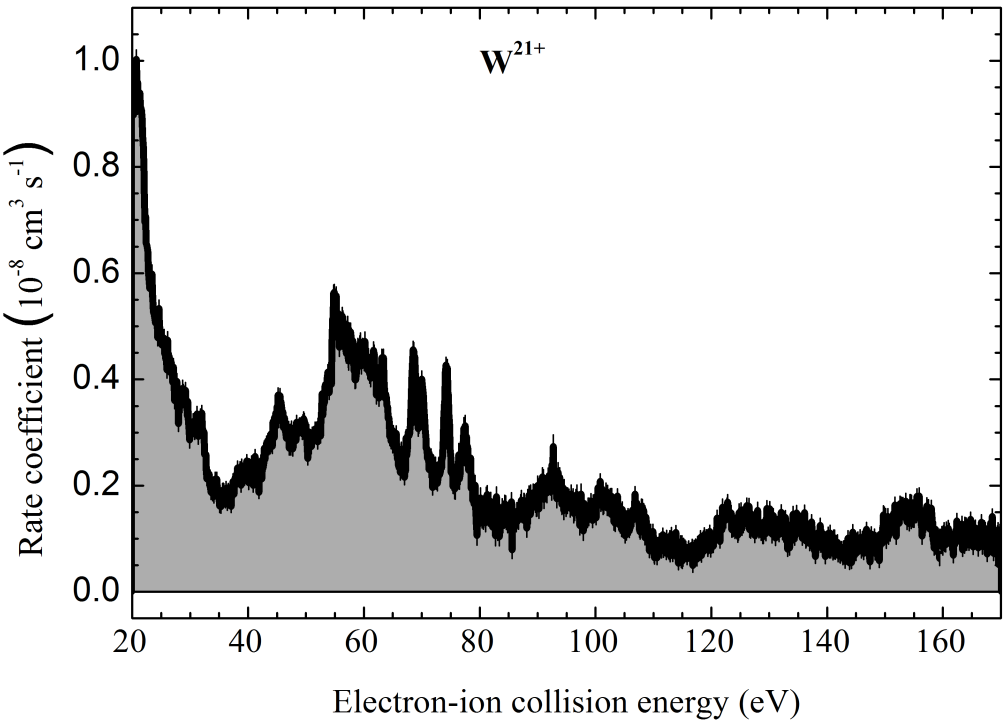

Figure 4.10.: Experimental recombination rate coefficient of W^{21+} in the energy range which exhibits strong resonance features.

surements employing the method described in Sect. 4.1.3. The count rates of both detectors, the ionisation and the recombination detector, were sufficiently high to delivere an analysable signal proportional to the stored ion number. Thus one measurement provided at least two possibilities for the determination of α. In addition, during three out of the four measurements the electron cooler was switched twice (on-off-on) and therefore two exponential decays could be fitted. Other than the two previously measured tungsten charge states, for W^{21+} no decay of the stored ions due to collisions with the residual-gas paticles (electron cooler off) could be observed. The value for α was thus only determined by an exponential fit to the decay rates for 'Cooler on'. Altogether, 12 fits could be performed and an average value of $\tau_{\mathrm{on}} = 1.34\,(15)$ was found. This led to an absolute value for the rate coefficient at 0 eV collision energy of $\alpha(E = 0\ \mathrm{eV}) = 2.47\,(27) \times 10^{-6}\ \mathrm{cm}^3\ \mathrm{s}^{-1}$ at a confidence level of 90%.

It has to be noted, that, as already shown in Fig. 4.3, several metastable states are predicted to be present in the parent W^{21+} ion beam also after cooling in the storage ring. During the lifetime measurement time of up to 14 s, the state population changes significantly. However, since a contribution of metastable level could neither

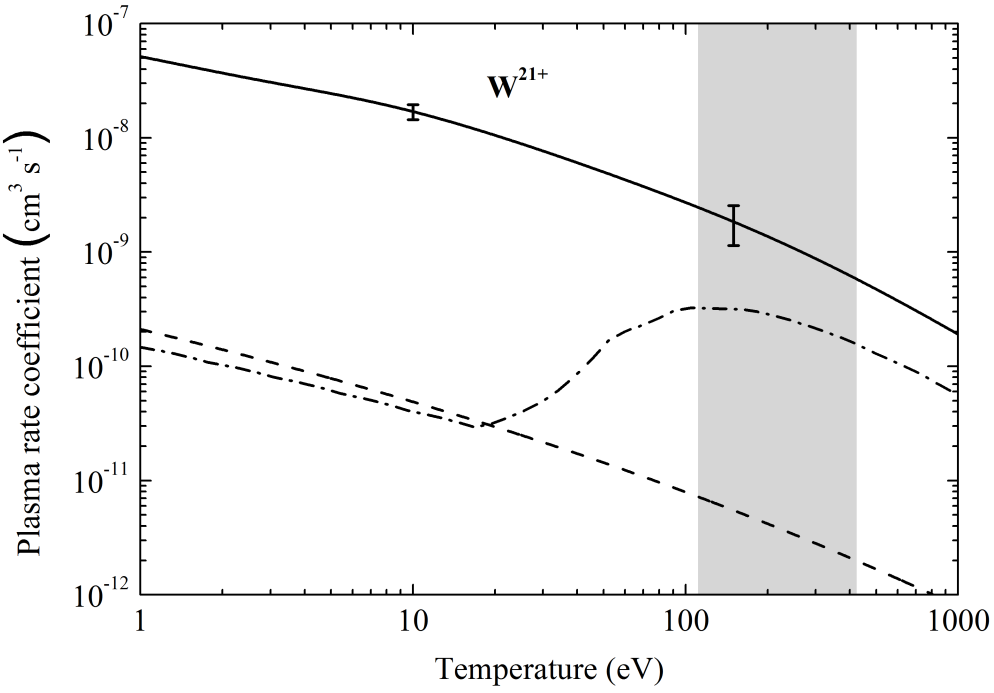

Figure 4.11.: Experimentally derived plasma rate coefficient for W^{21+} in the plasma temperature range from 0 to 1000 eV. The solid line represents the experimental results with the error bars representing the total uncertainties at a 90% confidence level, exemplarily given for 10 eV and 150 eV plasma temperatures. The dashed line is the theoretical RR plasma rate coefficient and the dashed-dotted line is the plasma rate coefficient from the ADAS database [25]. The grey-shaded area indicates the plasma temperature, where W^{21+} is most abundant in a collisionally ionised plasma [6].

be excluded nor isolated, the given value for $\alpha(E = 0\,\text{eV})$ was used for normalisation of the relative rate coefficients without further correction.

The resulting experimental recombination rate coefficient is shown in Fig. 4.9. Below collision energies of a few meV, the rate coefficient is enhanced due to the time-dependent electric and magnetic fields seen by the ions by transmitting the electron cooler. As also observed for the other charged states, from $2.47\,(27) \times 10^{-6}$ cm^3 s^{-1} at 0 eV collision energy the rate coefficient decreases by about two orders of magnitude up to collision energies of 3 eV. Starting from collision energies of 3 eV broad resonances can be observed. Since this region was measured with low statistical uncertainty, a detailed plot of these resonances can be shown in Fig. 4.10. Weaker resonance structures are still visible up to 300 eV and the experimental recombination rate coefficient is about two orders of magnitude higher than the calculated RR rate coefficient. At collision energies higher than 300 eV, no resonances are

Table 4.6.: The fit parameters for the parametrisation of the experimentally derived plasma recombination rate coefficient of W^{21+} using Eq. 4.8. In the temperature range from 1 to 1000 eV, the fit deviates by less than 1% from the experimental findings.

i	c_i ($cm^3\ s^{-1}K^{3/2}$)	E_i (eV)
1	0.12161	0.73046
2	0.32102	4.01224
3	0.77705	11.06334
4	0.880	23.58157
5	1.70193	61.15095
6	2.46946	147.0257
7	2.38031	326.72464

observed anymore and the background corrected, measured rate recombination rate coefficient approaches zero.

As already mentioned, the absolute recombination rate coefficient at 0 eV collision energy has a statistical error of 11.0%. By including the systematic error, a combined uncertainty of 13% is obtained. The error caused by the background subtraction is 3% at 1 eV, 35% at 30 eV and 58% at 150 eV collision energy. Together with the counting statistical error, which is lower for this charge state in comparison to W^{18+} and W^{19+}, the total uncertainties at a 90% confidence level amount to 14% at 0 eV, 14% at 1 eV, 39% at 30 eV and 65% at 150 eV collision energy.

The experimentally derived plasma rate coefficient for W^{21+} in the temperature range from 1 to 1000 eV is shown in Fig. 4.11. The error bars of 15% at 10 eV and 38% at a plasma temperature of 150 eV result from the absolute uncertainties of the merged-beams recombination rate coefficient. The experimental plasma rate coefficient is 5×10^{-8} $cm^3\ s^{-1}$ at a plasma temperature of 1 eV and decreases monotonously to 2×10^{-10} $cm^3\ s^{-1}$ at 1000 eV. The difference to the much smaller RR plasma rate coefficients is more than two orders of magnitude for the entire plasma temperature range considered. The plasma rate coefficient from the ADAS [25] database roughly corresponds to the RR plasma rate coefficient in the temperature region of up to 17 eV and exceeds it towards higher plasma temperatures. The relative difference between ADAS and the experimental plasma rate coefficient is still about a factor of 3 at a plasma temperature of 1000 eV. The ADAS recombination rate coefficient reaches its maximum at a temperature of 105 eV. In the energy range where W^{21+} is expected to be most abundant in collisionally ionised plasmas (see Fig. 2.2), roughly between 110 and 420 eV, the relative difference varies between factors of 4 to 8.

Similar to the previously mentioned charge states, the handling of the experimental plasma rate coefficient was simplified by fitting with seven exponential functions

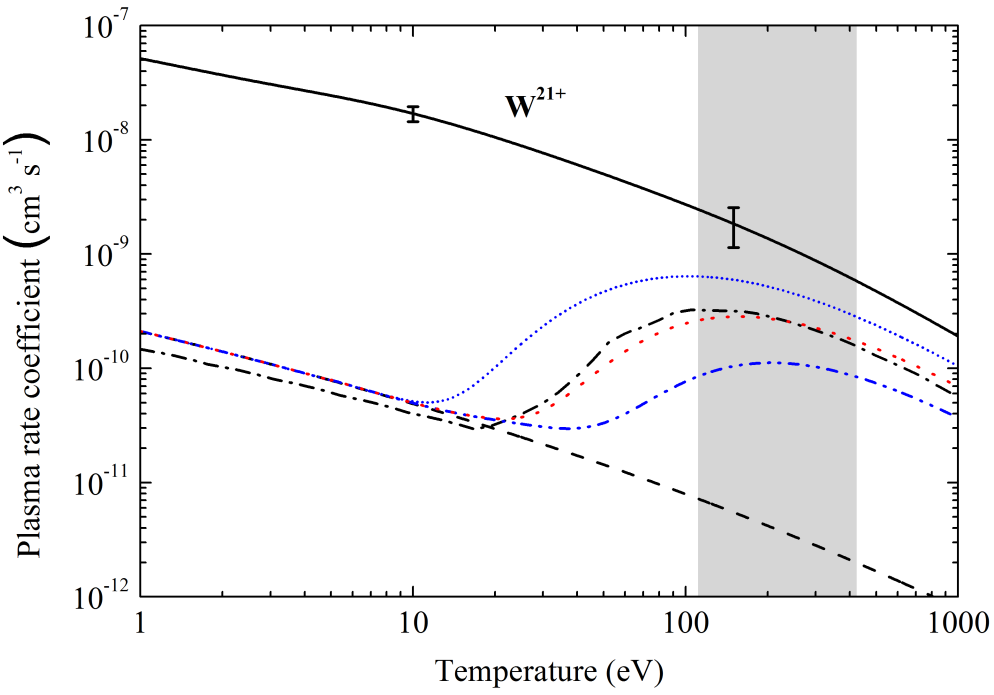

Figure 4.12.: Experimentally derived plasma rate coefficient for W^{21+} in comparison with theoretical and artificial plasma rate coefficients. The dashed line is the RR plasma rate coefficient, the dashed-dotted line is the ADAS plasma rate coefficient [25], the red-dotted line is the artificial plasma rate coefficient neglecting all DR contributions below an electron-ion collision energy of $E_{\mathrm{neg}} = 160$ eV, and the two blue, short-dotted and dotted-dotted-dashed lines are the artificial plasma rate coefficient for $E_{\mathrm{neg}} = 80$ eV and 240 eV, respectively. The grey-shaded area indicates the plasma temperature range, where W^{21+} is most abundant in a collisionally ionised plasma [6].

using Eq. 4.8. The parameters for which the function reproduces the experimentally derived plasma rate coefficient on a plasma temperatures scale of 1 to 1000 eV with less than 1% deviation are listed in Tab. 4.6.

Using the example of W^{21+}, the relation of the measured data to the published ADAS plasma rate coefficient is examined further. Therefore a synthetic plasma rate coefficient was generated by neglecting all resonances of the experimental merged-beams recombination rate coefficient at low collision energies. In a first attempt, only the strong resonances below $E_{\mathrm{neg}} = 80$ eV were omitted by replacing the experimental recombination rate coefficient at low collision energies by the RR rate coefficient. In a second attempt, this was repeated for all resonances below 240 eV. As shown in Fig. 4.12, both plasma rate coefficients could not reproduce the ADAS results. Last, a mean energy of $E_{\mathrm{neg}} = 160$ eV was chosen. The result is in good agreement with the

ADAS plasma rate coefficient when using the theoretical RR rate coefficient instead of the experimental recombination rate coefficient at collision energies below 160 eV. For W^{18+} and W^{19+}, this energy is about $E_{neg} = 100$ eV. Schippers et al. found a similar connection between the ADAS data and their experimental results on W^{20+} ($E_{neg} = 47$ eV). These finding may suggest that autoionising resonant contributions to the recombination at smaller energies are neglected in the calculations used by ADAS.

4.3. Theoretical Interpretation of the Results

Theoretical physics has put forward various approaches for calculation of electron-ion recombination cross sections of tungsten cations. Simpler systems of highly-charged tungsten ions have been theoretically treated, e.g., by employing the Flexible Atomic Code FAC [154] which is based on relativistic, level resolved configuration interaction [155, 156]. However, these methods meet their limitation for more complex systems due to the large number of involved electrons and energy levels. In extreme cases, such as provided by half open 4-f-shell W^{18+}, the density of levels exceeds 10^7 eV^{-1} [157]. The resulting chaotic nature of such half open 4-f-shell systems has already been pointed out for Au^{25+} by Gribakin and Sahoo [134].

The striking disagreement between the experimental findings and the rate coefficients from the ADAS data base has spawned two similar, more elaborate theoretical calculations for the recombination of open 4-f-shell tungsten ions. Section 4.3.1 discusses the new theory by Badnell et al. [60, 135], while Sect. 4.3.2 provides a brief introduction to the purely statistical approach of Dzuba et al. [136]. Both theories are tested against the measured experimental recombination rate coefficients. The results are presented within Sect. 4.3.3.

4.3.1. Level-Resolved DR Calculations

The approach followed by Badnell et al. [60, 135] is based on level-resolved, intermediate coupling (IC) calculations of one electron promotions plus dielectronic capture. However, as discussed before, the complex level structure of open-f-shell tungsten also allows for multi-electron promotion processes and, hence, a single-promotion calculation cannot be expected to reproduce the full natural recombination rate. While, for the here presented theoretical calculations, only one-electron promotions of 4d or 4f electrons into $n'l'$ levels with $n' = 4{,}5$ are included in the capture step of the recombination process, the contribution of multi-excited autoionising levels is accounted for by allowing mixing between these DR levels.

The *AUTOSTRUCTURE* atomic code [141] was employed to calculate all significant energy levels, radiative rates, and autoionisation rates. Using an independent process, isolated resonance plus distorted wave approximation, the resonance strength for a transition between an initial state i, via an intermediate state u of a resonance energy E_r, and to a final state f, can be calculated using Eq. 2.16. It is convenient to 'bin' the rate coefficient into energy intervals of a binwidth ΔE [158, 159]. The energy-averaged, recombination rate coefficient $\overline{\sigma}_i$ is composed by summation over all accessible, intermediate states u whose excitation energies E_r correspond to the given energy interval, and over all associated final states f of the recombined ion:

$$\overline{\sigma}_i(E_n) = \sum_u \overline{\sigma}_i^u(E_\mathrm{r}) = \sum_{u,f} \overline{\sigma}_{f,i}^u(E_\mathrm{r}) \;\forall E_\mathrm{r} \in [E_n, E_{n+1}) \tag{4.9}$$

The width ΔE can be chosen arbitrarily, e.g. linear or logarithmic. For linear spaced energy widths, E_n is defined by $E_n = E_{n-1} + \Delta E$. The energy averaged, recombination rate coefficient $\overline{\sigma}_{f,i}^u(E_\mathrm{r})$ is given by

$$\overline{\sigma}_{f,i}^u(E_\mathrm{r}) = \frac{(2\pi a_0 I_\mathrm{H})^2 \tau_0}{\Delta E\, E_\mathrm{r}} \frac{\omega_u}{2\omega_i} \times \frac{A_\mathrm{a}(u \to i)\, A_\mathrm{r}(u \to f)}{\sum_{i'} A_\mathrm{a}(u \to i') + \sum_{f'} A_\mathrm{r}(u \to f')} \quad . \tag{4.10}$$

The presence of multi-excited electron configuration results in an enhancement of the effective cross section. These levels are not directly populated from the initial level i, but via so-called 'doorway states', which are directly coupled to the ground level. Hence, for these multi-excited levels, there are more radiative de-excitation than autoionising channels available, $\sum_i A_\mathrm{a}(u \to i) \ll \sum_f A_\mathrm{r}(u \to f)$, while for the doorway states the autoionising channel is still dominant, $\sum_i A_\mathrm{a}(u \to i) \gg \sum_f A_\mathrm{r}(u \to f)$. Considering these extreme cases in Eq. 4.10, the total recombination cross section in the presence of many multi-excited electron configurations is enhanced by a factor of $\sum_i A_\mathrm{a}(u \to i) / \sum_f A_\mathrm{r}(u \to f)$.

In order to account for the contributions of these multiple excitation of bound electrons, Badnell et al. allows for mixing of DR levels within an energy interval $\Gamma = 10$ eV [160]. Thus, instead of taking into account only intermediate states u with $E_u = E_\mathrm{r} - E_i$, also transitions to neighbouring states $\overline{u}$ are allowed. By this, the rate coefficient is enhanced due to the number of 'forbidden' transitions which are included. A new set of autoionising levels $\overline{u}$ for the use in Eq. 4.9 and Eq. 4.10 is introduced. The dielectronic capture/autoionisation rates $A_\mathrm{a}(\overline{u} \to i)$ are weighted by a Breit-Wigner distribution:

$$L_{\overline{u}}(E_\mathrm{r}) = \frac{1}{2\pi} \frac{\Gamma}{(E_{\overline{u}} + E_u)^2 + \Gamma^2/4} \tag{4.11}$$

where $E_{\overline{u}}$ is the energy of the forbidden level $\overline{u}$ and the energy of the autoionising doorway state u is given by the energy difference between the initial level and the

resonance energy. The outcome of the calculation is not sensitive to the precise value of Γ. The autoionisation rate $A_a(\overline{u} \rightarrow i)$ in Eq. 4.10 can then be replaced by $L_{\overline{u}}(E_r)A_a(u \rightarrow i)$. Using this approach, a sufficient agreement between theory and experiment for low energies, up to 1 eV for W^{20+}, could be achieved [60].

However, this approach exceeds the experimental rate coefficient at higher collision energies. This is due to alternative, autoionising channels via higher-energetic, excited fine-structure states which then become energetically accessible for the forbidden levels. Hence, in a next step of the calculation, the partitioned theory is damped by a non-unity fluorescence yield

$$\omega_f = \frac{A_r(u \rightarrow f)}{\sum_{i'} A_a(u \rightarrow i') + \sum_{f'} A_r(u \rightarrow f')} \quad . \tag{4.12}$$

Autoionisation widths are therefore recomputed at each partitioned energy to account for the closing-off/opening-up of channels at lower/higher re-distributed bin energies.

4.3.2. Statistical Theory

The statistical theory by Dzuba et al. [136] takes advantage of the chaotic characteristics of the open 4-f-shell system. Theoretical rate coefficients are obtained by employing artificial compound eigenstates, each originating from a dielectronic doorway state which is directly coupled to the initial state. Multi-electron processes are introduced by mixing of these doorway states with a large number of adjacent energy levels which are weighted by a Breit-Wigner distribution [160]. This method is based on the idea, that one captured electron can distribute it's energy via collisions with other bound electrons to many internal, multiply excited eigenstates of the same symmetry. Electron capture as well as autoionisation is only possible for the dielectronic entrance (doorway) state. By averaging over all accessible eigenstates $|\phi_j\rangle$, a compound state $|\Psi_\nu\rangle$ is formed as a linear superposition

$$|\Psi_\nu\rangle = \sum_k C_j^\nu \, |\phi_j\rangle \tag{4.13}$$

with the eigenvalues

$$E_j = \langle \phi_j | H | \phi_j \rangle \tag{4.14}$$

where C_j^ν correspond to nearly random mixing coefficients for the states j of the energies E_j and H is the Hamiltonian operator. The distribution of eigenstates for

one respective doorway states has a spreading width of

$$\Gamma_{\text{spread}} = 2\pi \frac{\langle \phi_k | H | \phi_j \rangle^2}{D} \tag{4.15}$$

where D is the mean level spacing between the eigenstates of a given total angular momentum and parity J^π. The C_j^ν are the diagonal matrix elements for $k = j$:

$$C_j^{\nu\,2} = \frac{D}{2\pi} \frac{\Gamma_{\text{spread}}}{(E_j - E)^2 + \Gamma_{\text{spread}}^2/4} \tag{4.16}$$

The energy-averaged total cross section $\overline{\sigma}$ for recombination through the compound resonance is approximately given by [137]

$$\overline{\sigma} = \frac{\pi}{2E} \frac{\rho}{\omega_i} \frac{A_\text{r} A_\text{a}}{(A_\text{r} + A_\text{a})} \quad . \tag{4.17}$$

where $\rho = \sum_{J^\pi} \omega_J \rho_{J^\pi}$ is the total level density of the compound state with ω_J being the corresponding statistical weights, E is the energy of the incident electron, and i denotes the initial (ground) state with the statistical weight ω_i. The parameters A_r and A_a represent, respectively, the average radiative and autoionisation rate of the compound state. By assuming a fluorescence shield of $\omega_f \approx 1$ (Eq. 4.12), Dzuba et al. derived the recombination cross section from the energy-averaged cross section for electron capture into the compound state,

$$\overline{\sigma}_\text{c} = \frac{\pi^2}{2E} \frac{\rho}{\omega_i} A_\text{a}(m \to i, E) \tag{4.18}$$

by summation over the dielectronic doorway states. An explicit expression for this formula is given in [136, 137]. For low collision energies, they restrict their calculations to the energy interval

$$E = I \pm \widetilde{\Delta E} \tag{4.19}$$

where I is the ionisation energy of the ground state. $\widetilde{\Delta E}$ is derived iteratively with the initial assumption that $\widetilde{\Delta E} \approx \Gamma_{\text{spread}}$. The latter is derived by Eq. 4.15. There, $\langle \phi_k | H | \phi_j \rangle$ is found by averaging over N_{spread} eigenstates whose corresponding energies E_j lie within the energy interval, and the mean level spacing is D is derived by $\widetilde{\Delta E}/N_{\text{spread}}$. With this approximation, a good agreement to the experimentally derived recombination rate coefficient of Au^{25+} [46] could be achieved in the collision energy range below 1 eV [161].

At energies above few eV alternative de-excitation channels open up as the captured electron has more energy than needed for the autoionisation process [137]. Since this path is neglected in the assumption of $\omega_f \approx 1$, theory using this approximation will overestimate the DR rate coefficient towards higher collision energies. A better

agreement with the experimental results can be achieved by deriving the fluorescence shield by calculating A_r and A_a [137]. However, Dzuba et al. did, up to now, not provide any updated results on the theoretical calculations of W^{18+}, W^{19+}, and W^{21+}. Hence, the single data points [136] presented in Sect. 4.3.3 were derived from Eq. 4.18 as described before.

4.3.3. Theoretical Results for Tungsten Ions

Both theoretical approaches presented above predicted recombination rate coefficients for W^{20+} that could be tested against the measured data for that charge state which has been published prior to this work [72]. The partitioned results from the level-resolved calculations of Badnell et al. [60] achieve a sufficiently good agreement with the experimental results in the low collision energy region up to 1 eV. However, their theory overestimates the recombination rate coefficient largely for higher collision energies. The statistical approach of Dzuba et al. [136] was initially in similarly good agreement with the experimental finding in the collisions energy region of up to 1 eV. Later, they refined their calculations and could achieve good agreement with the experimental recombination rate coefficient up to collision energies of 120 eV [137].

To date, however, Dzuba et al. [136] provide only single data points for the recombination rate coefficients of the other tungsten charge states between W^{18+} and W^{25+} at 1 eV collision energy. Meanwhile, Badnell et al. have improved their model by inclusion of damping into their partitioned results as described in Sect. 4.3.1, now achieving much better agreement with the experimental results at higher collision energies. They provide theoretical merged-beams and plasma recombination rate coefficients for W^{18+} [135] and W^{19+} [138] covering the entire experimental energy range. The results are discussed in the following section.

4.3.3.1. Theoretical Recombination Rate Coefficients

Figure 4.13 shows the experimental merged-beams recombination rate coefficient of W^{18+} together with the state-of-the-art theory of Badnell et al. and the single data point at 1 eV collision energy by Dzuba et al. [136]. As shown in the inset, the intermediate coupling result is greatly underestimating the recombination rate coefficient at lower energies, while it is capable of delivering a reasonable agreement to experiment for collision energies of 70 to 170 eV. The partitioned-damped result is in agreement with the experiment at collisions energies of up to 10 eV (inset Fig. 4.13) and, even though it does not reproduce the resonances between 10 and 20 eV collision energy, it is in reasonable agreement with experiment for collision energies starting from 20 eV. The enhancement at collision energies below few meV, which

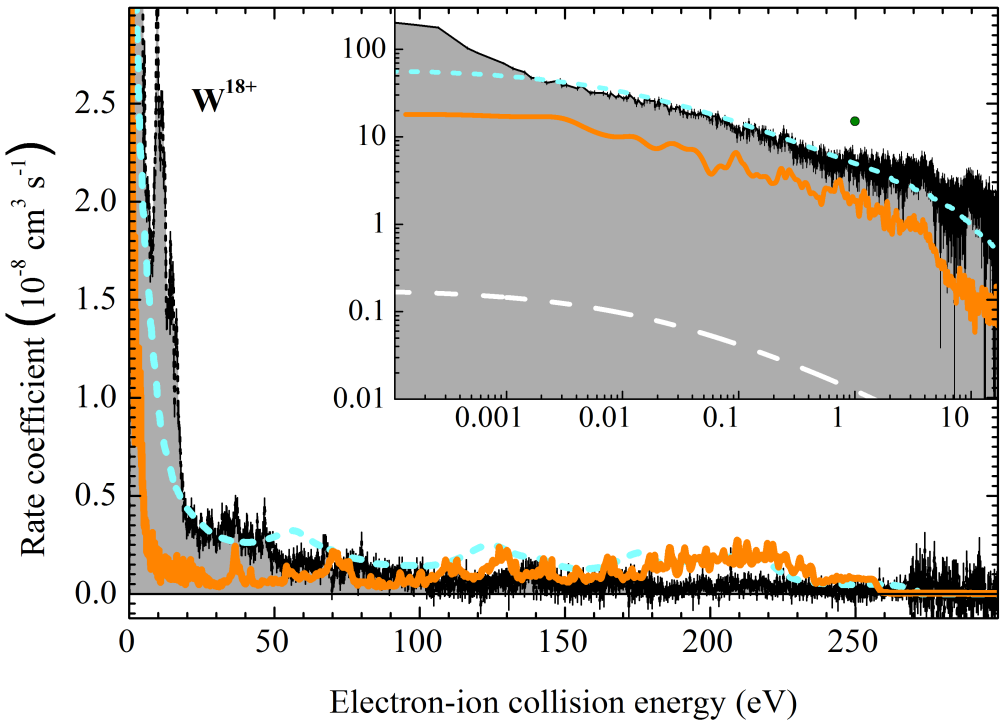

Figure 4.13.: Experimental and theoretical merged-beams recombination rate coefficients for W^{18+}. The inset shows a magnification of the low-energy range of the same datasets. The black, green-filled circle is the theoretical recombination rate coefficient at 1 eV collision energy provided by Dzuba et al. [136]. The orange, solid line is the IC result, while the light-blue, short-dashed line is the corresponding PD result by Badnell et al. [135]. The black, filled circles are the experimental rate coefficient, while the white, dashed line represents the calculated, theoretical RR rate coefficient for W^{18+}. The error bars given for the experimental results are the statistical uncertainties only.

has already been discussed in Sect. 4.2, is naturally not reproduced by theory. Both theories, IC and PD, exceed the experimental results in the collision energy range between 170 and 230 eV. The data point provided by Dzuba et al. overestimates the recombination rate coefficient at 1 eV by a factor of about 3.

The partitioned-damped result for the recombination rate coefficient of W^{19+} is shown together with the experimental findings in Fig. 4.14. Even though up to a collision energy of 1 eV the theoretical approach is slightly overestimating the rate coefficient, it is in nearly perfect agreement with experiment between 1 and 35 eV. For higher collision energies, similar to the results for W^{18+}, theory is overestimating the experimental results. The data point provided by Dzuba et al. overestimates

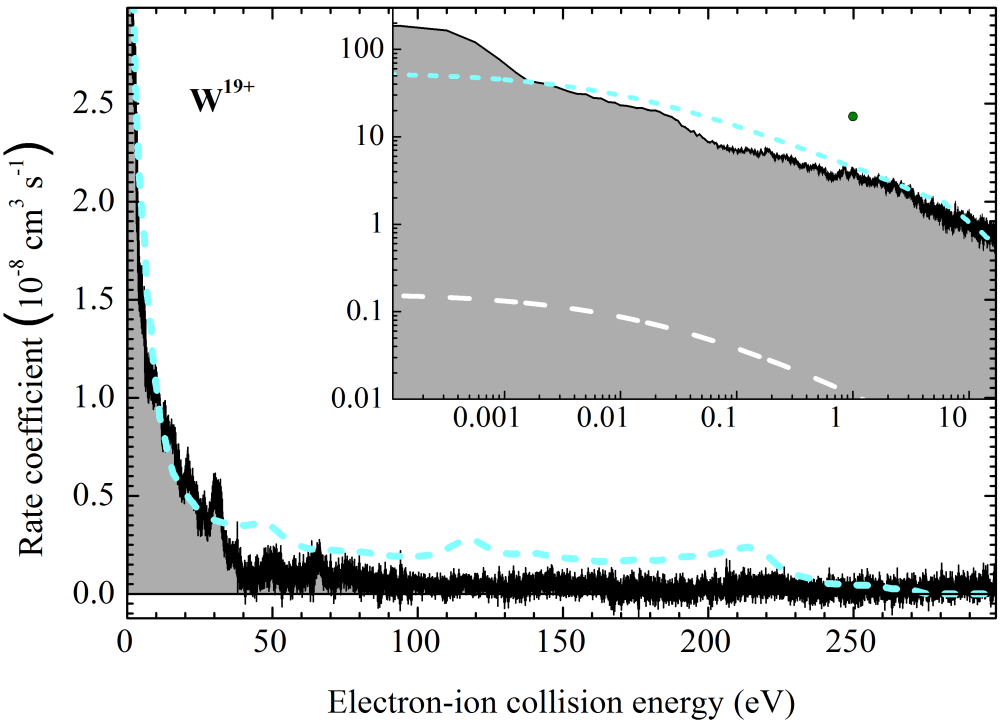

Figure 4.14.: Experimental and theoretical merged-beams recombination rate coefficients for W^{19+}. The inset shows a magnification of the low-energy range of the same datasets. The light-blue, short-dashed line is the PD result of the level-resolved calculations of Badnell. The black, green-filled circle is the theoretical recombination rate coefficient at 1 eV collision energy provided by Dzuba et al. [136]. The black, filled circles represents the experimental rate coefficient while the white, dashed line is the calculated, theoretical RR rate coefficient for W^{19+}. The error bars given for the experimental results are the statistical uncertainties only.

the recombination rate coefficient at 1 eV by a factor of about 4.5 .

Up to now, there are no state-of-the-art theoretical results available for W^{21+}, apart from the single data point at 1 eV collision energy provided by Dzuba et al.. As shown in Fig. 4.15, it overestimates the rate coefficient by a factor of about 4, similar to the other two charge states already discussed.

As already mentioned, this systematic overestimation of the recombination rate coefficient at 1 eV collision energy of statistical theory is most likely due to neglecting alternative autoionisation channels opening up at higher collision energies. This is a deficit of the initial statistical theory of Dzuba et al. that has recently been addressed successfully in the case of W^{20+} [137]. However, for the remaining charge

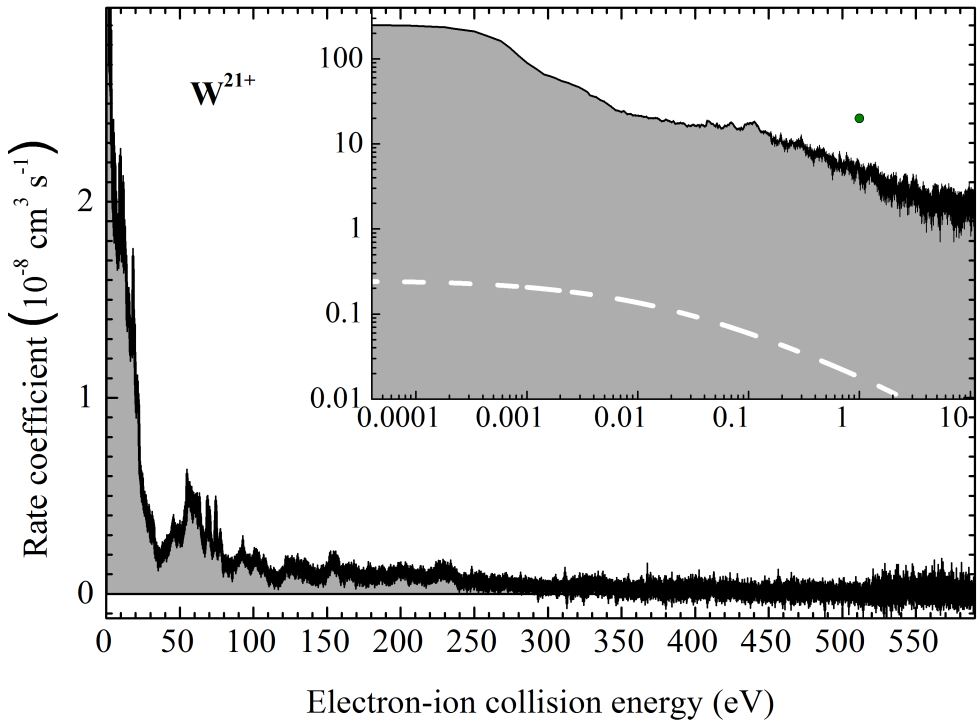

Figure 4.15.: Experimental and theoretical merged-beams recombination rate coefficients for W^{21+}. The inset shows a magnification of the low-energy range of the same datasets. The black, green-filled circle is the theoretical recombination rate coefficient at 1 eV collision energy provided by Dzuba et al. [136]. The black, filled circles are the experimental rate coefficient, while the white, dashed line represents the calculated, theoretical RR rate coefficient for W^{21+}. The error bars given for the experimental results are the statistical uncertainties only.

states, updated theoretical calculations have not been published yet. Badnell et al. have successfully addressed the same issue by damping of their partitioned result, as they first demonstrated on the example of W^{18+} [135]. Even though this new theory cannot yet predict every feature of the measured rate coefficient, it is in overall good agreement with the experimental finding for W^{18+} and W^{19+}. For comparison, all experimental and theoretical recombination rate coefficients presented within the scope of this work are shown together with the results for W^{20+} of Schippers et al. in Sect. 4.3.4, Fig. 4.18.

In an effort to assign the observed structures in the rate coefficient of W^{21+} at least roughly to atomic levels, the Los Alamos National Laboratory (LANL) Atomic Physics Codes [162] have been used to calculate excitation energy for W^{21+} ions of the [Kr] $4d^{10}$ $4f^{7}$ ground-level configuration. However, for the transitions from

ground level to the [Kr] $4d^{10}$ $4f^6$ $5s^1$ and [Kr] $4d^{10}$ $4f^6$ $5p^1$ configurations, more than 2 500 transition energies have been found and it was hence not possible to assign the observed resonance structures to single autoionising DR levels on the basis of these calculations.

4.3.3.2. Theoretical Plasma Rate Coefficients

The theoretical merged-beams recombination rate coefficients of Badnell et al. for W^{18+} and W^{19+} were used to generate theoretical plasma rate coefficients for use in plasma modelling codes.

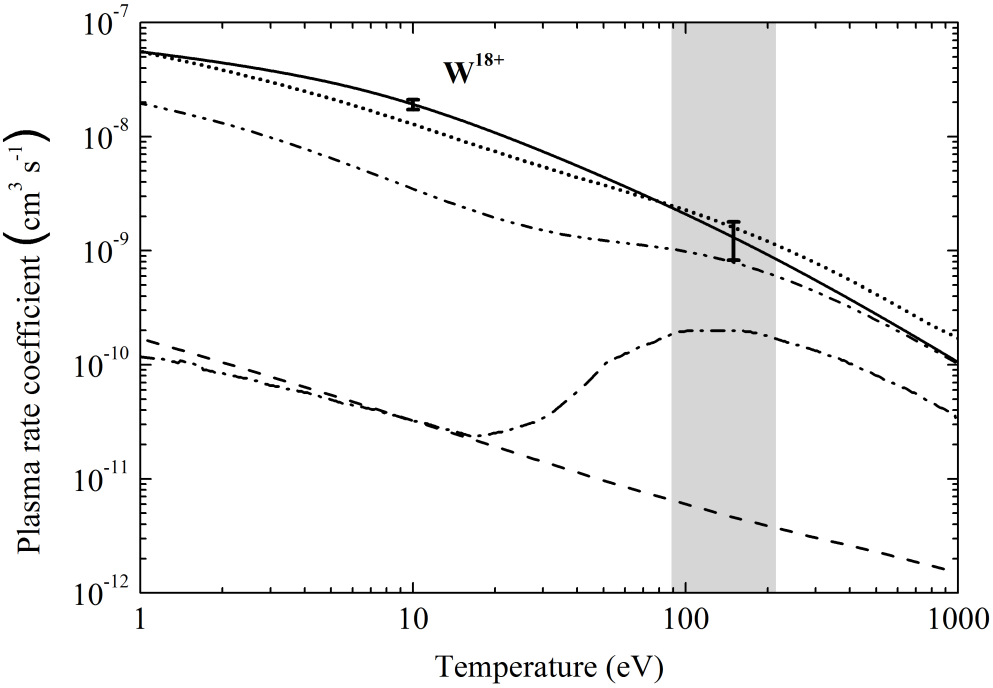

Figure 4.16.: Experimentally derived plasma recombination rate coefficient for W^{18+} in comparison with theoretical results. The solid line with the error bars represents the experimental results, the dashed line is the RR plasma rate coefficient and the dot-dashed line is the ADAS plasma rate coefficient [25]. The dot-dot-dashed line is the plasma rate coefficient derived from the IC result and the dotted line is the final PD result [135]. The grey-shaded area indicates the plasma temperature where W^{18+} is most abundant in a collisionally ionised plasma [6].

Figure 4.16 shows the experimentally derived plasma rate coefficient and the theoretical IC and PD results for W^{18+}. At a temperature of 1 eV the IC results is about a factor of 3 lower than experiment, a relative difference which is even increasing

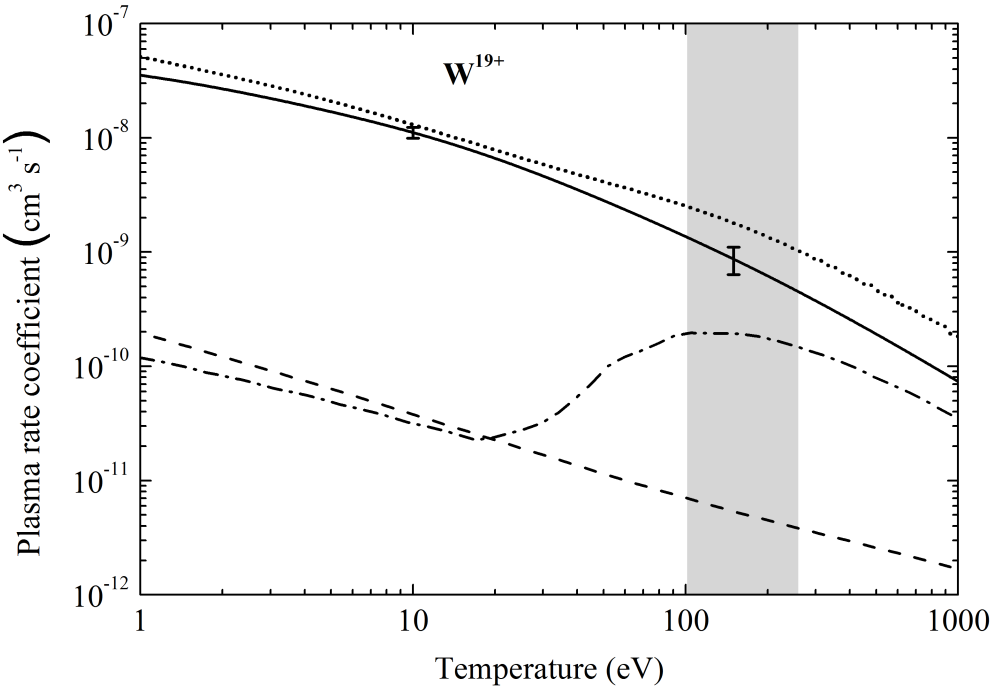

Figure 4.17.: Experimental and theoretical plasma recombination rate coefficients for W^{19+}. The solid line with the error bars represents the experimental results, the dashed line is the RR plasma rate coefficient and the dot-dashed line is the ADAS plasma rate coefficient [25]. The dotted line is the PD plasma rate coefficient by Badnell at al. [138]. The grey-shaded area indicates the plasma temperature where W^{19+} is most abundant in a collisionally ionised plasma [6].

for plasma temperatures of few 10 eV. On the other hand, in the temperature range where W^{18+} is estimated to be most abundant (shaded area in Fig. 4.16) the IC result is again 100% to 25% lower than the experimental result, while it is in nearly perfect agreement at temperatures above 300 eV. The PD result on the other hand, is in agreement with the experimentally derived rate coefficient at plasma temperatures below 100 eV, but is exceeding the experimental findings toward higher plasma temperatures. At 200 eV this deviation is about 43%. However, the PD results do provide a much better overall agreement with the experimentally derived plasma rate coefficient than the IC result or the ADAS dataset.

The theoretical results for the plasma recombination rate coefficient of W^{19+} are shown in Fig. 4.17 together with the experimentally derived plasma rate coefficient. Up to a plasma temperature of 30 eV, theory exceeds the experimental results by about 25%. This discrepancy rises towards higher temperatures. In the energy range of interest (shaded aera in Fig. 4.17) it reaches 50% at 100 eV and 230% at 260 eV. In comparison, theory is in better agreement with experiment for W^{18+}. Most-likely,

this reflects the overestimation of the experimental merged-beams recombination rate coefficient of W^{19+} towards higher collision energies starting at 30 eV.

Up to date, except for the already discussed ADAS data, no theoretical plasma rate coefficient for W^{21+} is available. In order to provide an overview over all experimental and theoretical plasma recombination rate coefficients for the tungsten charge states investigated in the campaign at TSR, Fig. 4.19 shows results for W^{18+} to W^{21+}.

4.3.4. Comparison of Results on Open 4-f-Shell Tungsten Ions

Considering also the previously published results on W^{20+} forming W^{19+}, merged-beams recombination rate coefficients for four highly-charged tungsten ions featuring an open 4-f-shell configuration have been measured. Figure 4.18 shows the absolute, experimental merged-beams recombination rate coefficients of W^{18+} forming W^{17+}, W^{19+} forming W^{18+}, W^{20+} forming W^{19+}, and W^{21+} forming W^{20+}. The results share two main characteristics: The recombination rate coefficients at zero collision energy are among the highest atomic recombination rate coefficients which have been measured, about 2×10^{-6} cm^3 s^{-1}, decreasing rapidly towards higher collision energies. Such high rate coefficients are normally observed only in recombination of molecular cations. Above a collision energy of 30 eV all rate coefficients are in the 10^{-9} cm^3 s^{-1} range and below. A second characteristic are the broad structures which originate from mutually overlapping resonances. The fast recombination at 0 eV collision energy as well as the lack of isolated DR resonances had also been observed for the recombination rate coefficient of Au^{25+} (see Fig 2.5). Both phenomena originate from numerous overlapping autoionisation resonances. The results of the partitioned-damped level-resolved calculations, also shown in Fig. 4.18, are only available for two of the depicted charged states. However, this approach can reproduce the experimental findings to a high degree.

The experimentally derived, plasma recombination rate coefficients of W^{q+} (q = 18, 19, 20, 21) are shown in Fig. 4.19. The plasma rate coefficients start at a value of about 3×10^{-8} cm^3 s^{-1} at 1 eV and then decrease towards higher plasma temperatures, reaching 10^{-10} cm^3 s^{-1} range for the plasma temperatures of interest (shaded areas of Fig. 4.19). There, for all four charge states, discrepancies of up to a factor of 10 between the experimental result and the ADAS theory were found. The results of the new partitioned-damped theoretical model of Badnell et al., to date only available for two of the shown charge states, is in much better agreement with experiment.

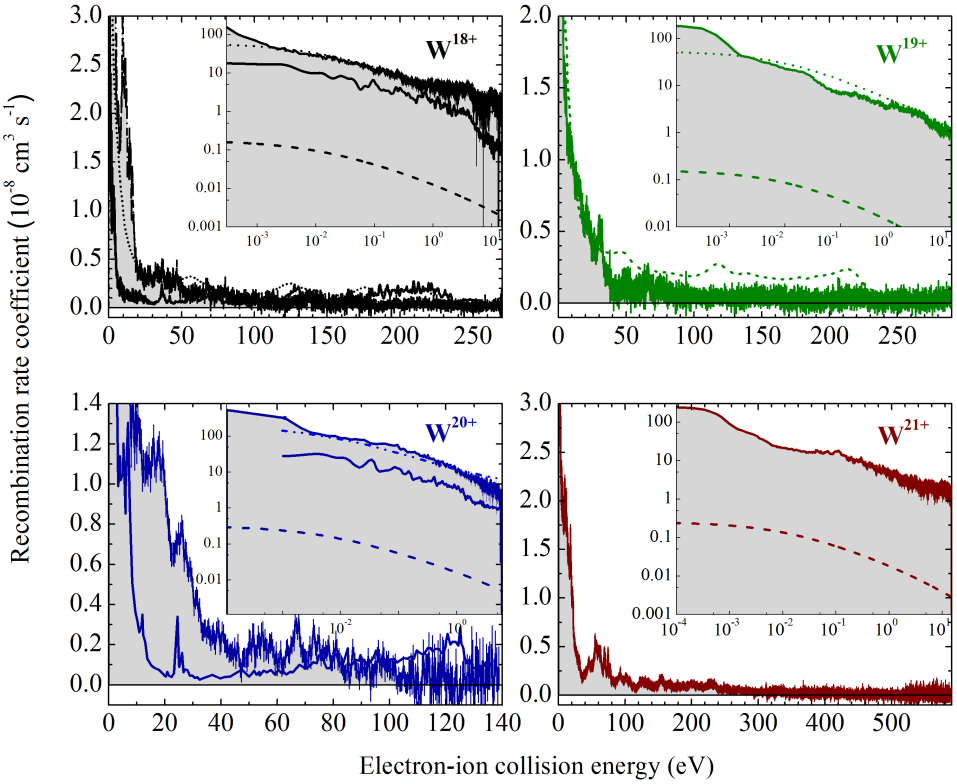

Figure 4.18.: Experimental and theoretical recombination rate coefficients of all measured tungsten charge states, including the previously published W^{20+} [72]. Solid circles including error bars are the experimental plasma rate coefficients, together with the theoretical results by Badnell et al. (solid lines for IC and dotted lines for PD results, dot-dot-dashed for the fully partitioned result without damping used for W^{20+}) and the RR plasma rate coefficient (dashed lines).

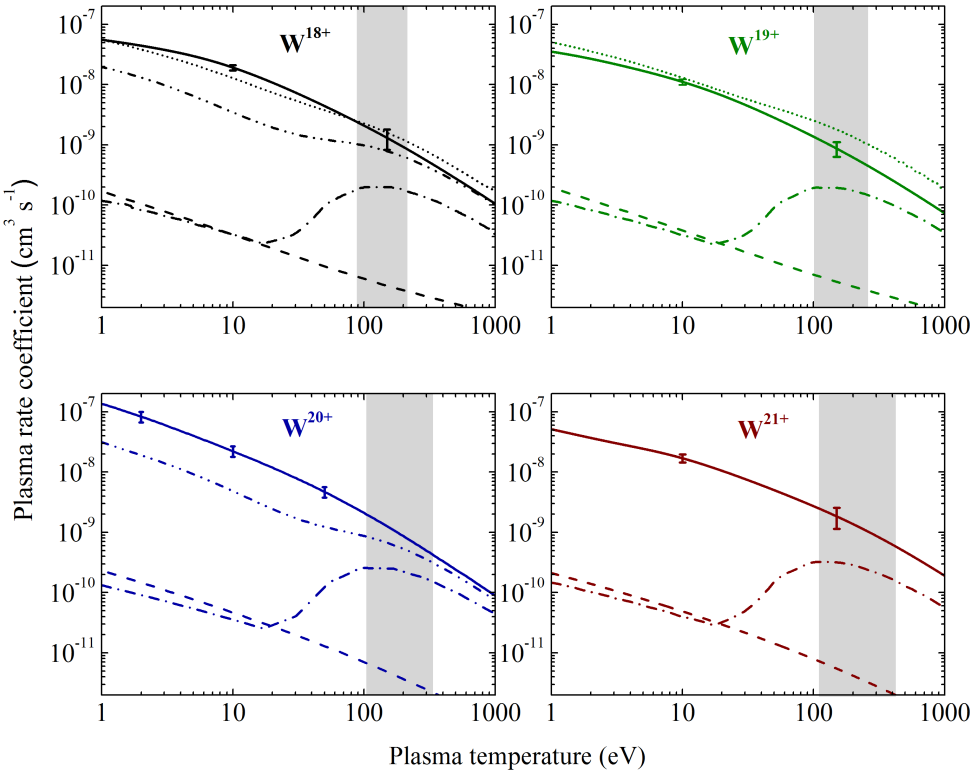

Figure 4.19.: Experimental and theoretical plasma recombination rate coefficients of all measured tungsten charge states, including the previously measured W^{20+} [72]. Solid lines are the experimental results including error bars. They are compared to the theoretical results by Badnell et al. (dot-dot-dashed lines for IC and dotted lines for PD results), the plasma rate coefficients from the ADAS database (dot-dashed lines) and the RR plasma rate coefficient (dashed lines). The shaded areas indicate the energy ranges where, according to [6], the abundance of the charge state exceeds 0.01%.

4.4. Summary and Conclusion

Absolute, merged-beams recombination rate coefficients for highly-charged tungsten with W^{q+} (q = 18, 19, 21) were measured within the scope of this work. The corresponding experimental plasma recombination rate coefficients were derived and compared to the ADAS data presently used by the plasma fusion community. It was found that the ADAS plasma rate coefficients are omitting DR resonances at low collision energies. This results in an underestimation of the plasma rate coefficients for all charge states investigated. Relative differences of a factor 3 to 10 were found when comparing these theoretical plasma rate coefficients to the experimental results in the plasma temperature region where these charge states are expected to be most abundant.

Theoretical calculations are challenging due to the many-electron nature of the problem. The present experiments as well as the earlier result for W^{20+} [72] have provided a solid empirical ground which helped the development of two new theoretical models [60, 135, 137] of these open 4-f-shell systems. Since the standard DR approach cannot account for all relevant many-body interaction, statistical methods have been invoked for the calculation of electron-ion recombination rate coefficients. Though simplifications are necessary for numerical handling of the problems, the resulting model rate coefficients agree remarkably well with the experimental findings for W^{18+}, W^{19+}, and W^{20+}, with theoretical results on W^{21+} being on the way. The comparison with the present experimental results reveals that the newly developed statistical approach is, thus, more able of producing reliable electron-ion recombination rate coefficients for complex ions than any other theoretical approach available.

The experimental recombination rate coefficient exceeds to what has been predicted by earlier simpler theoretical calculations. Thus, inclusion of the new data into the models of the charge balance of tungsten in fusion plasmas will cause the predicted charge-state distribution to change, shifting towards a higher population of tungsten of lower charge states.

The half open 4-f-shell structure of the here presented tungsten ions gives rise to recombination processes via multi-electron excitations. This effect has been shown to be negligible for ions with a nearly-filled 4-f-shell structure [62, 63]. Hence, multi-electron recombination processes are expected to become less important for tungsten ions with an increasing or decreasing number of electrons in the 4-f-shell. There, a better agreement can be expected between the experimental results and the theoretical data of the ADAS database, since these processes are believed to be the main reason for the observed deviations.

5. Development of a Single-Particle Detector for the Cryogenic Storage Ring

The new Cryogenic Storage Ring CSR, which has been described in Chapter 3, will feature a merged electron-ion beams set-up similar to the one of TSR that has been used in the recombination experiments presented in Chapter 4. Also here, single-particle detectors, that can be moved across the CSR beamline, are required for counting of the reaction products from such experiments.

Due to the lower residual-gas density and the low-energetic electrostatic design of CSR (Sect. 3.4.2), electron-ion collision experiments also on singly and weakly-charged ions become possible. Until today, such measurements were hampered by the limitations of room-temperature storage rings. As explained in Sect. 2.2, experimental data on recombination processes of singly-charged heavy ions are relevant for the interstellar chemistry network.

In this chapter, the development and testing of the first single-particle counter for CSR is described in detail. Much of the work has been published independently as a technical paper [127].

5.1. Concept and Design

At the future CSR electron cooler set-up, electron collision experiments leading to ionisation, recombination, or molecular fragmentation of the parent species will produce daughter particles which leave the closed orbit of the stored parent beam in the subsequent deflector because their charge-to-mass ratio is different from the one of the stored primary particles. Rectangular vacuum ports along the beam line are foreseen to house particle detectors off-beam-axis that collect these daughter particles (Fig. 5.1). The vis-à-vis situated ports allow for the installation of two opposed detectors on both sides of the stored parent beam, in order to simultaneously collect ionisation and recombination products as it was done at TSR [135].

The first particle-counting detector for CSR [127] is named COld Moveable PArticle CounTer (COMPACT) and is placed in the deflection corner behind the electron

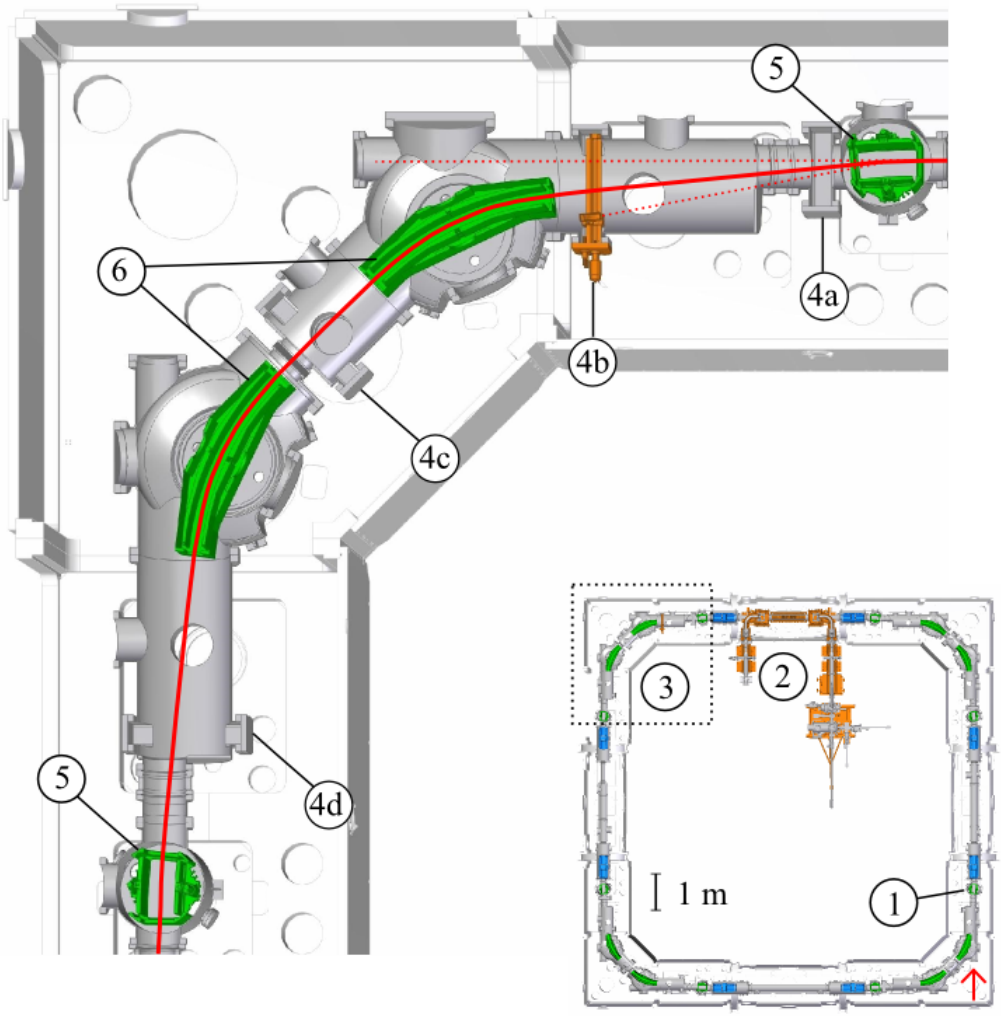

Figure 5.1.: Schematic illustration of CSR (see also Fig. 3.6), magnifying the corner section where reaction products of electron-collision experiments are collected. The detection corner (3) is following the future electron cooler section (2) which is situated in the second straight section after the injection (1). Reaction products with changed charge-to-mass ratio will be separated from the parent beam (red, solid line) by the CSR bending elements (6°deflectors (5) and 39°deflectors (6)). The dotted lines indicate exemplarily the trajectories of neutral product particles and daughter particle with an absolute and relative charge-to-mass ratio of 1. Four rectangular ports ((4a) to (4d)) are foreseen to host counting detectors for collection of these product particles. The first specimen of these detectors is integrated at the detector position (4b).

cooler section at port (4b) (cf. Fig. 5.1) since a wide range of possible product particles from first CSR experiments can be collected at that position. Due to their

charge-to-mass ratio, product particles will have trajectories differing from the stored parent beam after the CSR bending element, hence the detector has to be moveable across the CSR vacuum chamber. The detector has to be movable along a length of only 300 mm in order to cover all positions where daughter particles may possibly impact.In order to obtain absolute cross sections of collision reactions, the efficiency has to be known, especially for the typically low energetic SSR particle beams. The relative difference in charge-to-mass ratio η of daughter (index d) products compared to the parent (index p) beam for the given detector position is

$$\eta = \frac{q_d/m_d}{q_p/m_p} - 1 \tag{5.1}$$

which is limited to a theoretical range for η of

$$-1.4 \leq \eta \leq 1.1 \tag{5.2}$$

for particles of charge qe and mass m. Product particles of higher absolute values of η hit the chamber walls before reaching the detector. For the experimentally important case of a positively charged atomic parent beam, the range $-1 \leq \eta \leq 1$ is most relevant, with the lower and upper boundaries corresponding, respectively, to full neutralisation or ionisation to double charge of the stored parent. At position (4b), the detector itself is partly modular and consists of a translation stage (see Sect. 5.1.3) featuring a thread drive and a movable carriage, and a particle sensor which is mounted on top of the latter. The fully assembled detector is pictured in Fig. 5.2.

All materials of the particle sensor and the translation stage have to meet the demands of the CSR beam-guiding vacuum chamber environment (cf. Sect. 3.4.2), i.e., the design has to work reliably at an ambient temperature of ∼10 K and should be bakeable to a temperature of 250°C. All materials are required to be of very low relative magnetic permeability $\mu_r \leq 1.01$ and to be XHV compatible. In order to meet these demands, only materials from Tab. 5.1 were used for the set-up in the beam-guiding vacuum chamber of CSR.

As described in Sect. 3.4.2, CSR consists of two vacuum vessels. In order to mechanically and electrically operate the detector, further components are needed to interconnect the atmosphere components with those within the beam-guiding vacuum vessel. Since the heat load onto the CSR vacuum cryostat has to be kept at a minimum, a new concept, in particular for the transfer of the rotational motion of the thread drive, induced from the atmosphere side had to be developed, as described in Sect. 5.1.4. Figure 5.3 shows schematically the mechanical parts of the detector.

Besides the highly-charged ion-electron collision experiments COMPACT is primar-

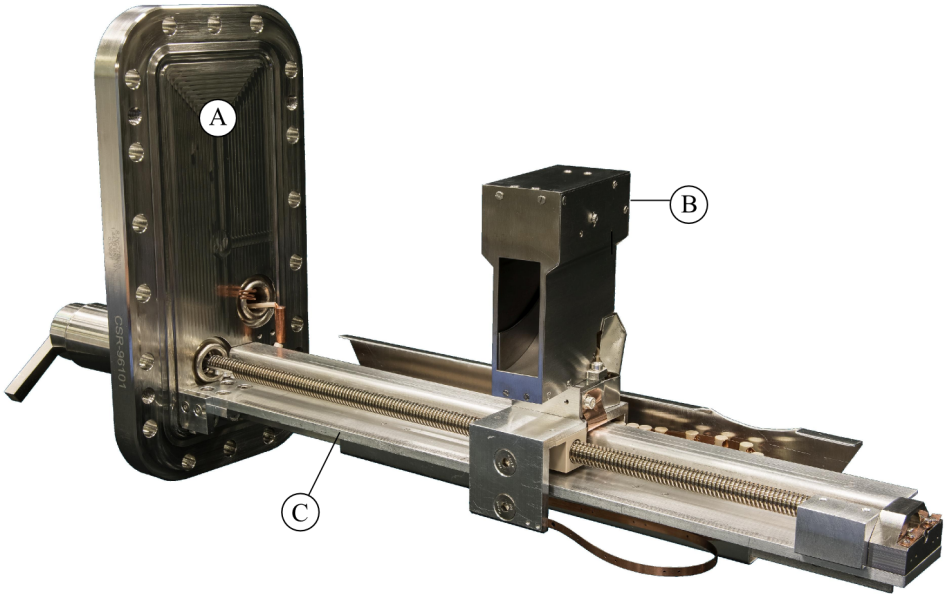

Figure 5.2.: The COMPACT detector is mounted on a rectangular flange of CSR (A) and consists of the detector sensor (B) and a translation stage (C).

Table 5.1.: List of chosen materials for XHV components of the COMPACT detector.

material	designation	application
stainless steel	1.4435 BN2, 1.4404	UHV flanges, detector housing, thread drive, screws
titanium	$TiAl_6V4$ 3.7165	springs
aluminium	Al 99.5	light-weight mechanical components, secondary-electron emitter
copper	Cu-OFE 99.99	electric connections
beryllium copper	BeCu2	springs, electric connections
alumina ceramic	Al_2O_3 99.6	electric isolation
silver	Ag	coating material
Constantan	$Cu_{55}Ni_{44}Mn_1$	resistive wire
sapphire	Al_2O_3 (monochrystals)	electric isolation, thermal coupling
PEEK	$C_{19}H_{14}O_3$	electric isolation, sliding bearings

ily designed for, the detector is capable of counting any product particles that it can reach within its motional range. This includes charged and neutral products from fragmentation processes of molecular ions stored in CSR, as well as ultra violet (UV) photons. UV-photons have been used for first detector tests in CSR, as described in Sect. 5.3.

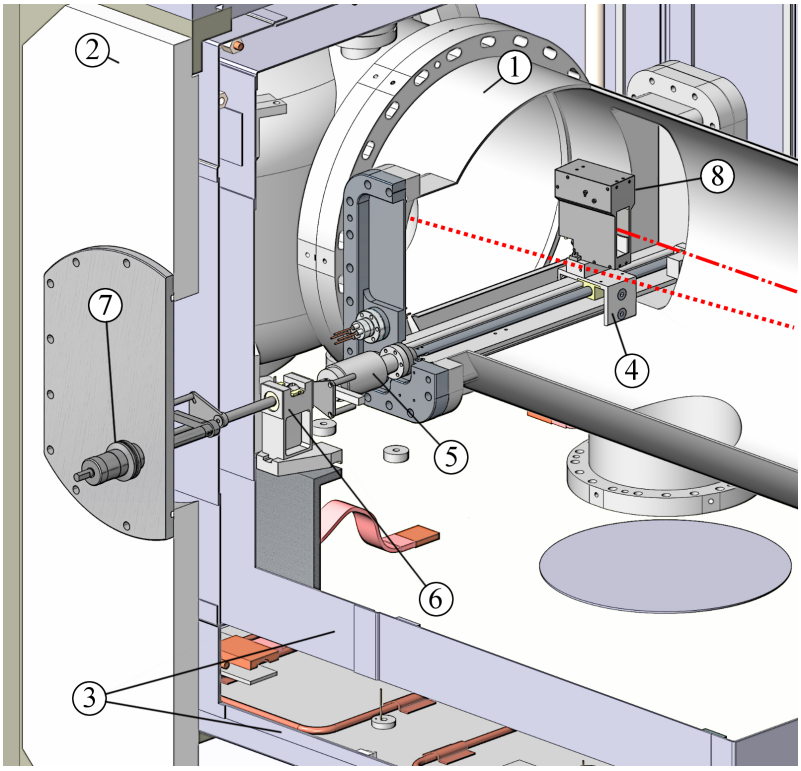

Figure 5.3.: Schematic cut-open illustration of the COMPACT detector within CSR. The CSR cryostat (1) is completely enclosed by the room-temperature isolation vacuum chamber (2). The two thermal radiation shields (3) are surrounding the inner vacuum chamber. The detector mechanics consist of the translation stage in the UHV chamber (4), a bellow-sealed rotary feed-through (5) and an intermediate drive (6) which rests on the base-plate of the 40-K stage and thermally decouples the inner parts from the standard rotary feed-through on the room-temperature chamber wall (7). The detector sensor (8) is modular and was developed independently. The dotted red line represents the closed-orbit trajectory of particles stored in CSR, whereas the dot-dashed red line follows the trajectory of a charge-changed product beam intercepted by the detector.

5.1.1. Detector Sensor

The detector sensor is mounted onto the carriage of the translation stage described in Sect. 5.1.3. The design of the sensor is adapted to the spatial constraints and the experimental conditions of CSR.

5.1.1.1. Choice of Particle Sensor

The choice of the detection principle is restricted by the CSR environment and the experimental parameters. The following considerations were taken into account.

- CSR is designed for a maximum kinetic energy of 300 keV per unit charge. The specific kinetic energies of stored ions and therewith also of daughter particles produced in collision experiments, can be as low as a few keV/u. Penetration depths in solids can thus be as short as 100 nm [163]. Any detection principle requiring the particles to traverse significant layers of passive material before reaching the detection volume (as in e.g. surface-barrier semiconductor detectors) is therefore excluded.
- The TSR single-particle detectors were based on the detection of secondary electrons from a converter cathode by a CEM, a concept which has shown a very good quantum efficiency in the specific energy range of a few keV/u [123]. The secondary-electron principle is expected to work also in a cryogenic environment, while the electron multiplier had to be tested for its performance at such low temperatures.
- Low resistance, extended dynamic range (EDR) micro-channel plates (MCPs) had already been proven to work reliably at temperatures of 20 K and below [164–167]. Up to this date, no data on the cryogenic performance of CEMs were available. It was expected that, due to the steep rise in resistance towards low temperatures, depletion of their single, long channel would prevent electron multiplication.

5.1.1.2. Spatial Constraints

The size of the complete detector sensor is limited by the following consideration.

- The sensor has to fit entirely through the rectangular, 80×200 mm^2 flange of the CSR chamber. Situated after the 6°deflector of CSR, the sensor is also inclined with respect to the axis of the vacuum chamber by 6°. This limits the depth of the housing to less than 80 mm.

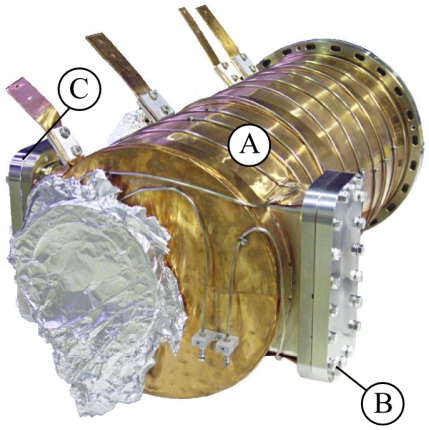

Figure 5.4.: CSR beam-guiding vacuum chamber (A) featuring two opposed, rectangular ports ((B) and (C)) for the installation of up to two variants of the COMPACT detector. This would allow for simultaneous detection of ionisation and recombination products as it was done at TSR.

- As a future upgrade, a second COMPACT-type detector could be mounted to the opposite rectangular flange of CSR (Fig. 5.4). This is possible if the translation stage of the second detector fits above the sensor of the first. The height of the sensor is limited to ∼90 mm.
- Daughter particles of changed charge-to-mass ratios similar to that of the stored beam have trajectories nearby the closed orbit. In order to collect these particles without intersecting the stored beam, the non-sensitive rim of the detector has to be as narrow as possible. Since the realisation of movement in one direction was already challenging, it was decided not to implement a means to vary the vertical position of the detector sensor as it is traditionally done (cf. Sect. 3.4.1.4). In return, the sensitive area of the detector, as described in Sect. 5.1.1, was vertically elongated in order to cover the CSRs vertical acceptance of ±30 mm in applicable extent.

5.1.1.3. Detection Principle and Sensor Design

The actual particle sensor as pictured in Fig. 5.5 is based on the well-established idea of an aluminium converter cathode for secondary-electron emission backed by an electron multiplier. The electrodes are enclosed in a grounded, stainless steel housing preventing disturbances of the CSR ion optics by stray electric fields. The housing has an opening of 20×50 mm^2. For the reasons mentioned above, the rim of the sensor aperture is only 2.5 mm broad. The width of the sensor aperture of 20 mm is chosen such that even at the extreme detector positions, where impinging particles have a maximum horizontal entrance angle of ∼7°, no more than half of the cathode is shaded by the housing. As electron multiplier, a chevron set of EDR MCPs (*Photonis* type 18/12/10/12 D 40:1 EDR, MS) with a sensitive area of 18 mm diameter was chosen. The detector signal is decoupled from a stainless steel

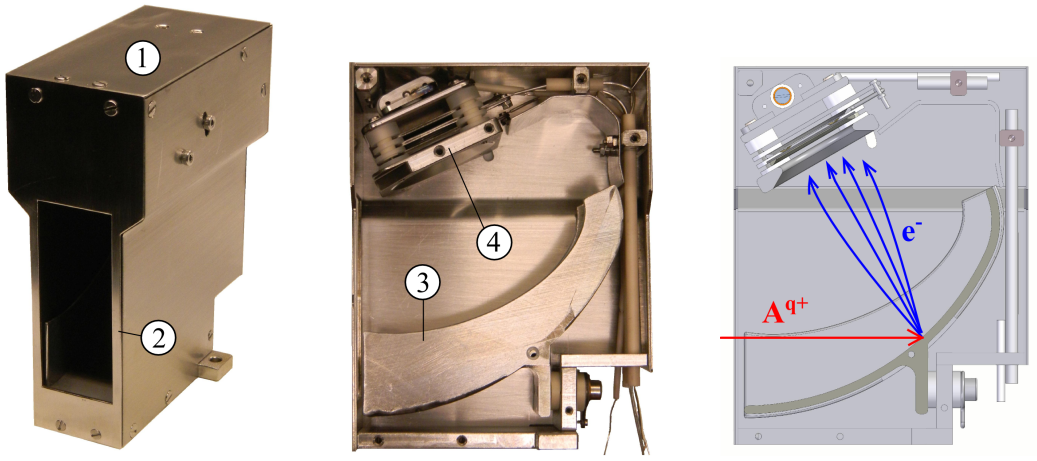

Figure 5.5.: The COMPACT sensor consists of an aluminium converter cathode and an MCP-anode stack completely enclosed in a stainless steel housing (1). The left figure shows the completely assembled COMPACT sensor with the sensor aperture surrounded by the 2.5 mm rim (2). The centre figure is a photography of the sensor before closing the last side plate of the housing, exposing the converter cathode (3) and MCP-anode stack (4). The right panel depicts the detection scheme of the COMPACT sensor. Particles (A^{q+}) impinging onto the converter cathode cause secondary-electron (e^-) emission. These electrons are accelerated towards the MCP-anode stack, causing a current pulse which can be decoupled from the high-voltage line of the anode.

anode. This detection principle features two main advantages: First the MCP is not directly exposed to the impact of heavy particles which could lead to damage of the surface by sputtering. Second, since each impinging particle can release several secondary electrons [168, 169], the detection probability is no longer limited to the open area ratio of the MCP surface and can reach unity (see Sect. 5.2.2.2). Due to the spatial constraints described above it was impossible to closely copy the design of the detectors of Rinn et al. (see Sect. 3.4.1.4, Fig. 3.4). In contrast to those, the sensitive aperture of the COMPACT detector is almost as large as the detector housing. Among others this breaks the convenient cylindrical symmetry of the secondary electron collector optics. A curved shape of the converter cathode (cf. Fig. 5.5) was chosen after simulating the collection efficiency of the detector sensor, as described later.

The values for the standard operating potentials of the COMPACT particle sensor are listed in Tab. 5.2. Incident particles impact onto the converter cathode biased at −400 V. The emitted secondary electrons are accelerated towards the front side of the MCP stack which rests on a potential of +800 V. A potential difference of 1.8 up to 2.0 kV over the two MCPs provides a sufficient secondary-electron multiplication

Table 5.2.: The standard operating potentials of the converter cathode and the MCP-anode stack.

$U_{\text{converter}}$	−400 V
$U_{\text{MCP front}}$	800 V
ΔU_{MCP}	1.8 kV
U_{anode}	3.0 kV

of typically 10^5. The resulting current pulse is collected at the anode, which rests on a potential of +3 kV.

5.1.1.4. Heating Element

A small, bakeable heating element is fixed to the back of the MCP holder in order to locally raise the temperature of the MCPs by few tens of K while operating CSR at its low temperature (see Sect. 5.2.1.1). The heating element is electrically isolated from the MCP electrodes and the anode by sapphire spacers which, simultaneously, provide thermal coupling at low temperatures. The heating element consists of a 0.1 mm thick, 27 cm long Constantan wire wound around ceramic isolators. The wire is spot-welded at one end to a stainless steel fixation at electric ground potential and at the other end to a connector equipped with an M2 screw (cf. Fig. 5.6) through which the electric power is applied. The resistance of the wire is 17 Ω at room temperature and does not significantly change when cooled. The heating element was baked at 260°C without damage. It was successfully tested at a power of 200 mW (cf. Sect. 5.2.1.1).

5.1.1.5. High-Voltage Wiring

The high voltage is fed to the electrodes by 1 mm thick, silver-plated copper wires isolated by ceramic tubes (see Fig. 5.7). All wires are fixed to the electrodes by

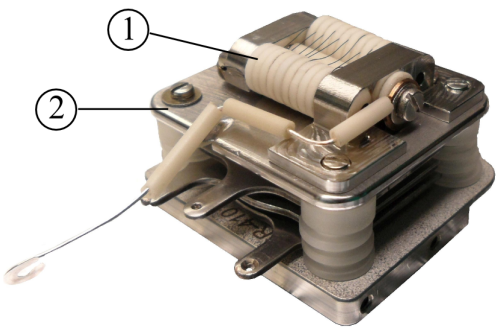

Figure 5.6.: The bakeable, 17 Ω heating element (1) which is mounted at the back side of the MCP-anode stack (2)

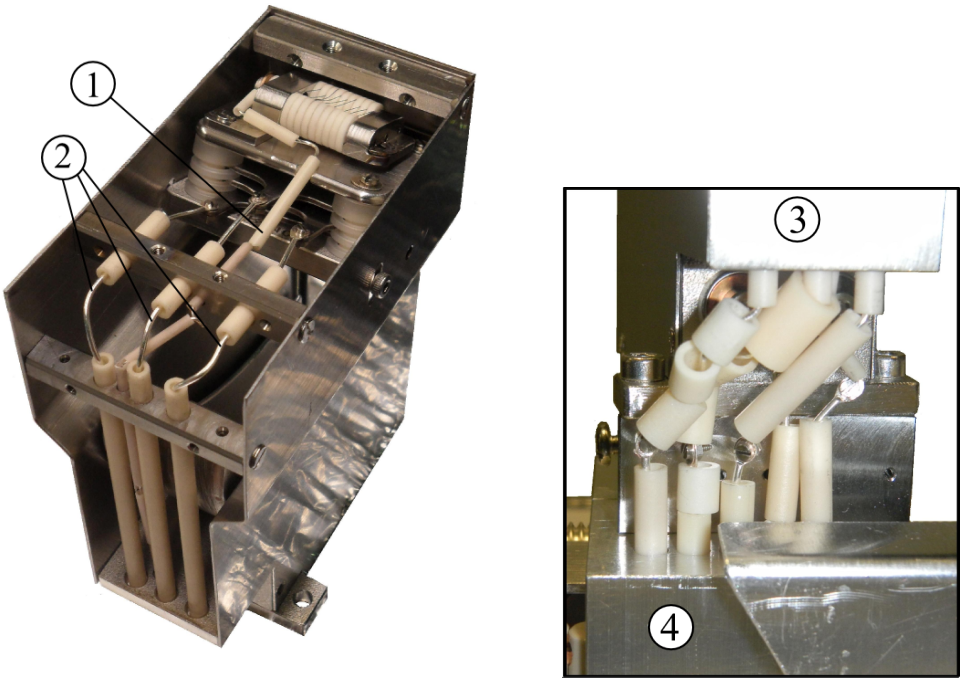

Figure 5.7.: Left panel: Photography showing the power line of the heating element (1) and the high-voltage wires of the MCP electrodes and the anode (2). The high-voltage connection of the converter cathode is not shown since it is connected at the bottom of the housing. The right panel shows all five electrical connections between the detector sensor (3) and the power lines of the carriage (4). These connections are covered by an additional shielding which is not shown.

flattening their ends such that small (1 mm) holes can be drilled through them and then connecting them to the electrode by an M1 screw. Outside the housing all wires are fixed with the same method to the copper wires from the carriage.

5.1.2. Electric Field Simulations

5.1.2.1. Simulated Collection Efficiency

The secondary-electron collection efficiency of the converter cathode and the MCP arrangement was simulated using the charged-particle optics software *SIMION 8.1* [170]. The grounded detector housing, the converter electrode, the MCPs and the anode were defined mathematically in a geometry file. In order to match the conditions of the physical efficiency measurements described later (see Sect. 5.2.2.2), the simulations were done for the extreme case of He^+ with an energy of 6 keV, i.e., an ion of very low rigidity. In CSR, particles of typically much higher energies per unit

charge and higher rigidity can be expected. The simulated ions entered the sensor housing and hit the converter cathode which was on a potential of −400 V. To simulate the collection efficiency of the sensor, each impinging ion was set to create exactly one electron on the converter cathode. The emission velocity vector of the secondary electrons was randomly chosen from a 2π solid angle around the surface normal of the conversion cathode. Their initial kinetic energy of 1 eV corresponds roughly to the peak in energy distribution reported for secondary electrons released from metals by ionic bombardment [168,171,172]. The simulated electrons were accelerated towards the MCP surface which was resting on a potential of +800 V. The collection efficiency was then determined by the ratio of ions entering the aperture of the sensor and the electrons collected by the MCPs.

In each simulation step, one hundred He^+ ions of 6 keV were created as a 2-dimensional Gaussian-shaped beam of 1 mm standard deviation at a few mm distance in front of the sensor aperture. This simulated ion beam was then scanned vertically across the detection aperture in 0.5 mm steps for six characteristic horizontal distances to the sensor aperture centre. All ions which entered the detector housing hit the converter, the collection efficiency is hence only limited by the ability of the converter cathode of focussing the secondary electrons onto the MCP.

The simulated secondary electron collection efficiency is $> 95\%$ over practically the entire area of the sensor aperture. Figure 5.8 shows a model of the converter cathode along with the collection efficiency projected onto the detection aperture of the COMPACT sensor.

Due to the spatial constraints described in Sect. 5.1.1 it was not possible to place the MCPs in the focal point of a simple converter cathode optics as for the TSR-type CEM detectors [123] (Fig. 3.4). During numerical simulations it turned out that the narrow shape of the grounded sensor housing prevented a sufficient focussing of the electrons onto the MCP surface. This problem was addressed by introduction of side panels to the converter cathode. The rectangular shape of the housing could partly be compensated by a curved shape of the cathode. The possibilities to create a lensing effect by either lifting the front side of the MCPs holder to a potential of −400 V or, by covering the sensor aperture with a grid at a potential of −400 V, were briefly investigated, but rejected for the final design.

The simulations were only used to model the collection efficiency of the sensor geometry and not the overall efficiency of the sensor. The influence of the MCPs detection efficiency in conjunction with the number of secondary electrons created on the converter plate was neglected. This issue is addressed theoretically and experimentally in Sect. 5.2.2.2.

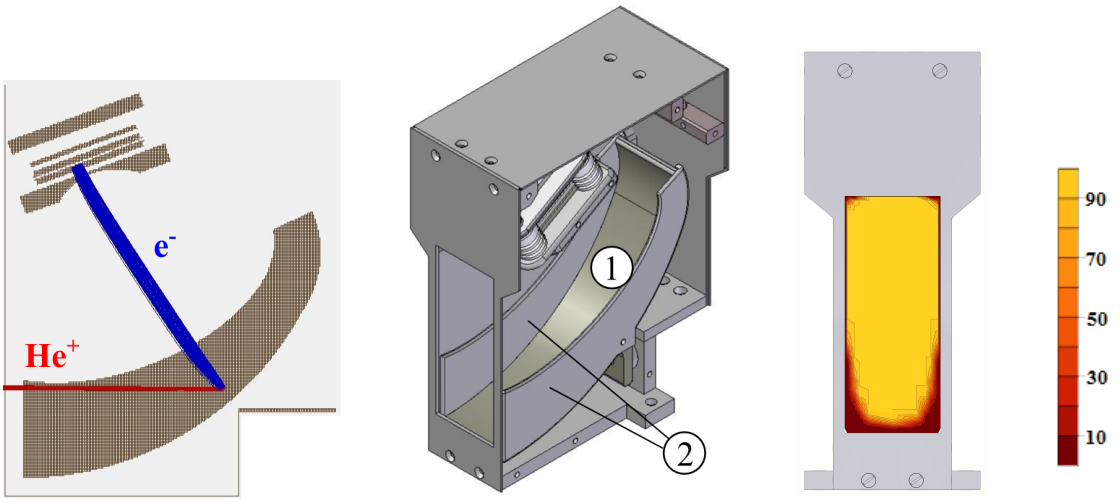

Figure 5.8.: The left panel shows a model of the simulated design of the sensor geometry. He^+ ions of 6 keV A^{q+} (red) are impinging onto the converter cathode, thereby creating secondary electrons e^- (blue). The curved geometry of the converter plate (1) with its asymmetrically shaped side panels (2) is depicted in the model shown in the centre panel. The right panel shows the result of the simulations with numbers given in %. The collection efficiency of the sensor aperture was derived by scanning the area with a simulated ion beam as described in the text.

5.1.2.2. Stray Field

It was decided not to cover the active area of the detector sensor by a grounded mesh. Therefore, the electric field which protrudes through the sensor aperture and its effect on the nearby ion trajectories in CSR had to be calculated. Figure 5.9 shows the potential map in a horizontal plane in the height of the stored beam. The horizontal deflection angle α_x in this plane for a stored particle of charge qe and energy E passing the COMPACT sensor in z direction is approximately given by the formula

$$\alpha_x = \frac{qe}{2E} \int E_x dz \tag{5.3}$$

with E_x being the horizontal component of the electric field perpendicular to the flight direction of the particles. For the extreme case of a proton beam of 20 keV passing the detector sensor in a distance of 5 mm, α_x was found to be less than $2{\times}10^{-7}$ mrad. This is several orders of magnitudes less than the expected beam divergence even for an electron-cooled beam (few 10^{-2} mrad). Therefore, the stray field is not expected to have any influence on the stored particle beam [139].

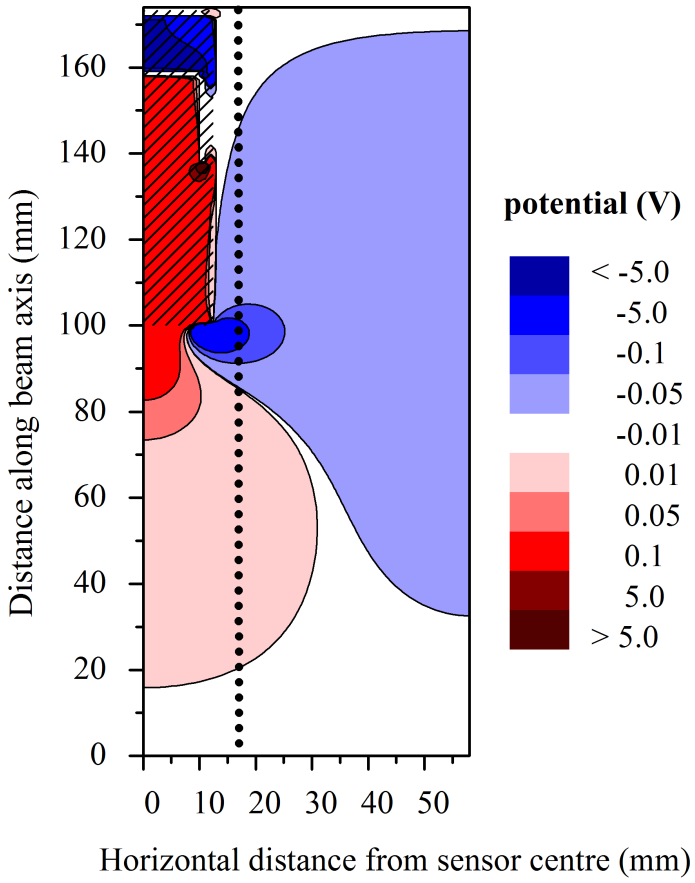

Figure 5.9.: A cut through the electric potential map of the COMPACT sensor at the height of the sensor aperture centre. Since the COMPACT sensor is symmetric with respect to a vertical axis, only one half of the detector is shown (hatched area). The dotted line represent an ion beam passing the detector sensor at a horizontal distance of ∼5 mm.

5.1.3. Translation Stage

As described in Chapter 3, moveable single-particle detectors are standard components of storage rings. Traditionally, these detectors are driven by linear actuators from the atmosphere side which are sealed by long edge-welded bellows. While manufacturers provide no information on their performance in cryogenic environment, excessive compression or expansion of the bellows is believed to cause vacuum leaks due to embrittlement of the stainless steel welding joint. Hence, this technical solution was not considered for CSR. At the DESIREE storage ring stepper motors directly inside the vacuum cryostat drive detectors which are mounted onto moveable carriages [83]. Provided that a suitable distance to the closed orbit of the stored particle beam could have been maintained, the magnetic field induced by these motors might still have been tolerable at CSR. However, also a significant heating effect by the electrical current through the motors was observed, which disturbed the cryogenic environment [83].

It was decided that the COMPACT sensor will be moved by a cryogenic thread drive contained fully within the CSR beam-guiding vacuum chamber and driven by a cryogenic rotary UHV feed-through mounted to the rectangular detector flange. The translation stage design can be adapted to other locations in CSR. Since the detector sensor is a modular component, it can also be combined with other kinds of sensors.

5.1.3.1. Spatial Constraints

A neutral particle detector, NICE [126], is situated next to the 39°deflector in the corner section following the COMPACT detector. Since this detector should not be shaded by the immovable parts of the COMPACT detector, the translation stage must not exceed a height of 50 mm. The width of the translation stage is limited by the 80-mm-wide detector flange. The travel range of the detector is limited by the diameter of the beam line to approximately 300 mm.

5.1.3.2. Thread Drive

The thread drive consists of a 400 mm long, trapezoidal threaded rod (Tr10x2) of V4A stainless steel rotating inside a matching PEEK nut which is fixed at the carriage supporting the detector sensor. The rod is at one end fixed to the rotary feed-through while its other end is guided loosely by a ceramic ball-bearing. The nut has to have a very loose fitting (∼0.2 mm) at room temperature in order to compensate for the different thermal shrinking of PEEK and stainless steel. It was manufactured by first cutting the Tr10x2 thread into the PEEK body at room temperature. Then the nut was cooled down with liquid nitrogen and, while the material was still cold, the thread was recut. In this way, an (unlubricated) cryogenic thread drive was accomplished. The loose guidance at room temperatures of a few tenths of mm is not relevant experimentally as the position of the detector is chosen by observation of the impact of products and needs only to be vaguely determined on an absolute scale.

The threaded rod is fixed to a non-magnetic, rotary UHV feed-through (model L6691301, on CF 16 flange by *Agilent Technologies*). No liquid lubricants are used in any part of the drive to preserve compatibility with cryogenic operation and UHV requirements of CSR.

5.1.3.3. Carriage and Rail

The carriage which is supporting the sensor is low-friction guided by two additional ceramic ball-bearings clinching to an aluminium rail. The carriage is the connection between the static part of the translation stage and the detector sensor and provides the high-voltage and power connections for the sensor (Fig. 5.10). Since the carriage is mainly resting on the ceramic ball-bearings on one side and on the PEEK nut described above, it is in principle isolated against ground. A sliding contact on the beam-facing side of the carriage cannot alone provide a safe connection to the chamber ground. Therefore an additional grounding connection was attached to the carriage using one of the CuBe2 strips described below. The strip is fixed to the carriage at one end and at the other end to the Faraday cage for the high-voltage connections providing the chamber ground. Figure 5.2 shows that the strip has no further guidance. This is acceptable since the grounding strip can only touch parts of the chamber wall and the rail which are on ground potential.

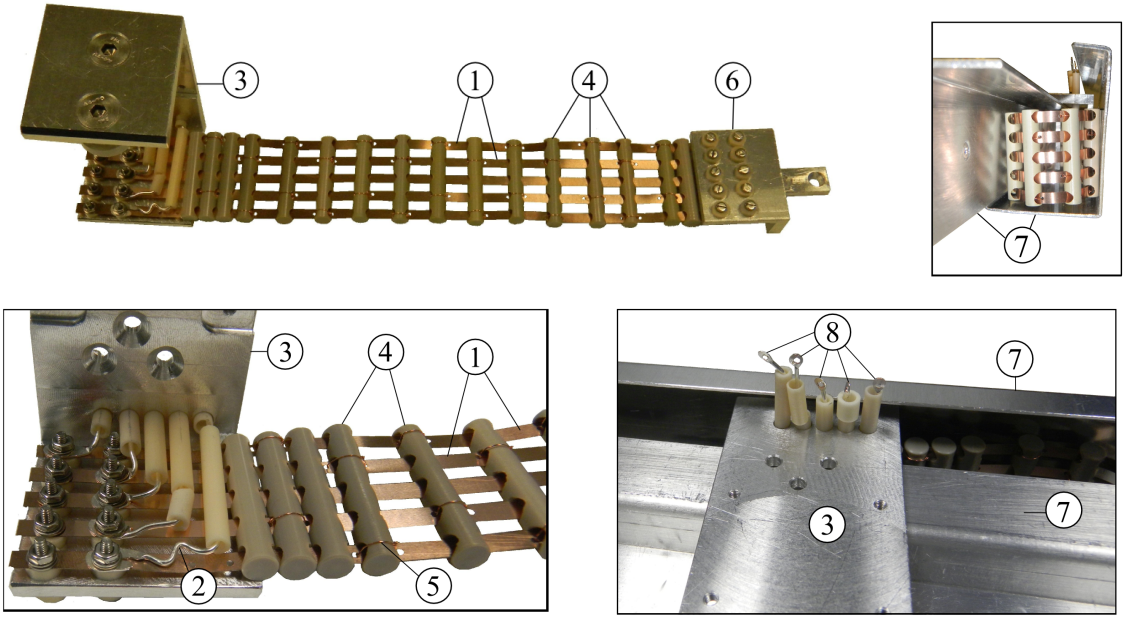

Figure 5.10.: The CuBe2 strips (1) are at one end fixed to the silver coated, copper wires (2) of the carriage (3), which lead to the power connections for the detector sensor (8). On the other side the strips are fixed to a static terminal (6) of the translation stage rail. The strips are isolated against each other by PEEK spacers (4) which are fixed to the strips by thin copper wires (5). They not only isolate the power lines against each other but also provide safe guiding of the CuBe2 strips in the Faraday cage (7).

The rail of the translation stage consists of a guiding platform for the carriage, a

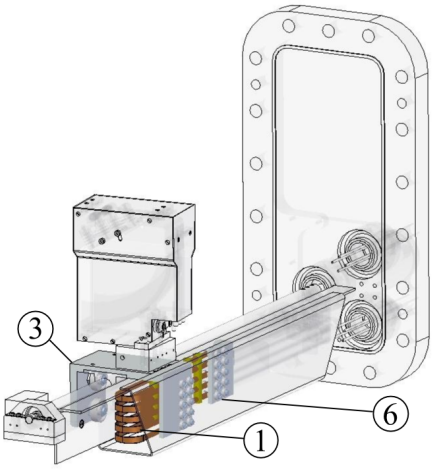

Figure 5.11.: Simplified illustration of the complete COMPACT detector highlighting the CuBe2 strips (1) of the power connections between detector carriage (3) and terminal at the translation stage (6), as also shown in Fig. 5.10.

mounting for the threaded rod and the Faraday cage of the high-voltage connections which are described below.

5.1.3.4. High Voltage Connections

A permanent, high-voltage and power connection between the static part of the translation stage and the moving carriage (Fig. 5.11) is achieved via 0.1 mm thick, 4 mm broad and 250 mm long CuBe2 strips shown in Fig. 5.10. At the moving carriage the CuBe2 strips are connected to silver coated, 1 mm copper wires which are lead to the top of the carriage, providing the power connections for the detector sensor. On the other static end, the strips are connected to the cryogenic, high-voltage feed-throughs of the detector flange.

The strips have been baked at 350°C for two hours in order to harden them, while keeping them elastic enough to bend in the high voltage Faraday cage of the translation stage during motion of the detector sensor. The strips are isolated against the cage by PEEK spacers that keep the CuBe2 strips in line. The PEEK spacers are loosely fixed to the strips by 0.1 mm thin, copper wire preventing them from sliding along the strips in an uncontrolled way.

5.1.4. Isolation-Vacuum Components

In order to thermally decouple the ∼10 K beam-guiding vacuum chamber from the room temperature outside the cryostat, all electrical and mechanical connections had to be designed in order to minimize the heat load on the cryostat.

5.1.4.1. Mechanics

An intermediate drive provides transmission of rotary motion from the atmosphere side actuator to the cryogenic translation mechanics. It is mounted onto the base plate of the 40-K CSR thermal shield (cf. Sect. 3.4.2.4, Fig. 3.8). The thermal decoupling is achieved via nosings of very loose fitting as it can be seen in Fig. 5.3. This still allows for a simple determination of the detector position as the number of full turns introduced from the atmosphere side roughly corresponds to that of the thread drive of the translation stage. However, by applying a certain sequence of partial rotations, it is always possible to position the 40 K-drive in a way that it has neither contact to the room temperature parts, nor to the cold inner chamber. In that way, a nearly perfect thermal isolation among the different temperature stages of the CSR cryostat is guaranteed. The drive is based on a spring loaded sliding bearing with relatively high friction, ensuring that the actuators maintain the desired position. The titanium spring ((3) in Fig. 5.12) and the axis of rotation ((2) in Fig. 5.12) are electrically isolated from the holder by PEEK spacers and bearings. Via an attached sensor wire, the titanium spring can be used to check whether the intermediate drive touches ground potential on any side.

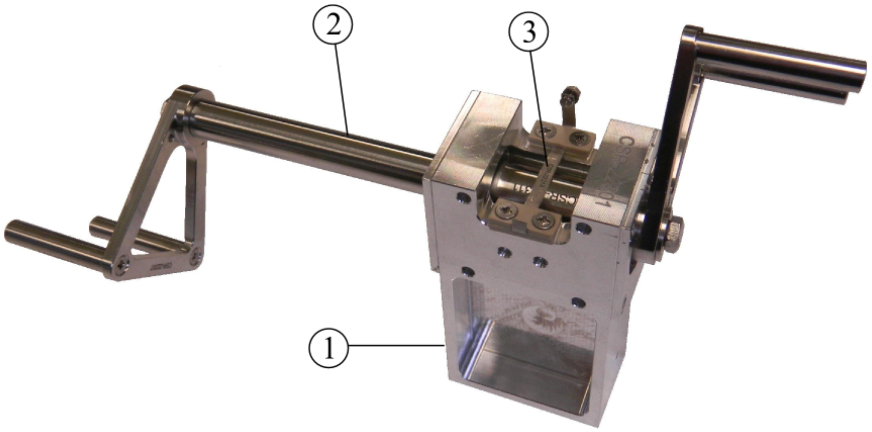

Figure 5.12.: The intermediate drive, which is mounted with the bearing aluminium block (1) onto the base plate of the 40 K-shield of CSR (see Fig. 3.8), thermally decouples the room-temperature actuator from the mechanics of the ∼10 K cold, beam-guiding vacuum chamber. The rotation axis (2) is electrically isolated against the aluminium block. A sensor wire is fixed to the titanium spring (3) that provides a means to check whether the drive is touching ground potential on either side.

5.1.4.2. Electrical Connections

All electronics and power supplies are kept on the atmosphere side of CSR. Within the isolation vacuum chamber, the connections among the electric feed-throughs on the cryogenic beam-guiding vacuum chamber and the feed-throughs on the outer, isolation vacuum chamber are achieved via wires of different thermal and electrical conductivity. In order to provide a sufficiently low electric resistance while simultaneously avoiding excessive head load on the beam-guiding chamber, each wire is a trade-off between thermal and electric conductivity. The high-voltage potentials for the converter and MCP electrodes are provided via Kapton-insulated 0.25-mm thick Manganin wires, each having a low thermal conductivity and a resistance of 10 Ω for the used length of 1.5 m. The connection for the anode not only serves as a carrier for the potential but also transports the fast detector current pulse, consisting of an estimated 10^6 electrons (∼0.1 pC) collected at the anode within a few ns. To preserve the quality of that weak (∼10 μA) current signal on the way to the atmosphere-side circuitry, a screened coaxial cable (*Allectra* 311-KAP-50-RAD, 50 Ω) is used for interconnecting the 10-K and 300-K electric vacuum feed-throughs. The screen is interrupted at both ends of the wire avoiding an unnecessary thermal connection between the atmosphere side of CSR and the cryogenic vacuum chamber. Instead, the screen is thermally and electrically coupled to the 40-K shield and in addition reduced to a single litz wire between the 40-K and 80-K shields of CSR, reducing the thermal load while still ensuring electric connection. For the resistive heating module a 0.25 mm thick PEEK-isolated silver wire was chosen in order to keep the resistance of the wire low compared to the internal resistance of the heating module. All wires are thermally anchored to the 40-K shield. The heat load for the detector is dominated by the anode connection and estimated to amount to 25 (5) mW, a value which is derived from tabulated values for thermal conductivity of an average sample of oxygen free copper [173]. The spring-contact of the 40 K-drive is connected via a similar wire which is used for the heating module.

5.1.5. Electronics on the Atmosphere Side

On the atmosphere side of CSR, the high-voltage potentials for the converter, anode, and MCP input electrodes are generated by standard low-ripple power supplies (*ISEG* NHQ 204M). The potential of the MCP output, provided by a floating high-voltage supply (*Spellman*), is biased by the $U_{\text{MCP front}}$ potential (Tab. 5.2). The bias current across the two MCPs is monitored by a floating nano-amperemeter. The electron current pulses on the anode are separated from the high potential by a 2.2 nF decoupling capacitor. The signal is driven into a 50-Ω current-sensitive fast front-end amplifier (*ORTEC* VT120A) with gain factor 200 and afterwards

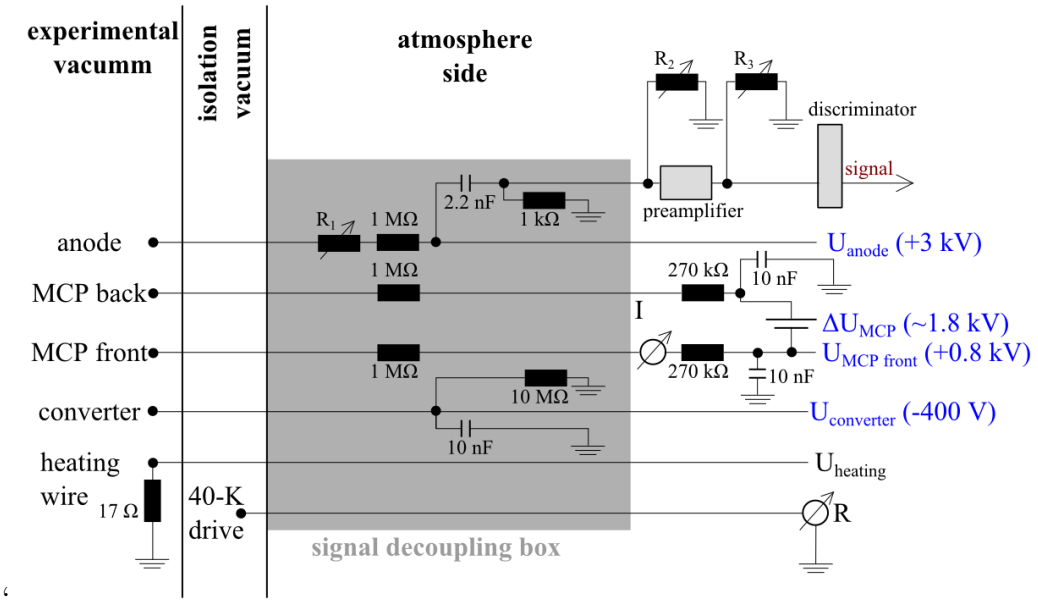

Figure 5.13.: Signal decoupling scheme comprising all electrical connections to the vacuum components. The COMPACT operating potentials (in blue) U_{anode}, ΔU_{MCP}, $U_{\text{MCP front}}$, and $U_{\text{converter}}$ are given within Tab. 5.2. Values for the adjustable resistors are given in the text.

discriminated with a reasonable threshold setting in order to obtain a digital (NIM) signal suitable for pulse counting electronics.

Figure 5.13 shows schematically the electrical connections inside the vacuum as well as the electronics on the atmosphere side. In order to improve the signal quality, several low-pass filters and resistors for noise and reflected-wave suppression were included. The empirically optimised values of the three adjustable resistors found for room-temperature CSR operation of COMPACT are $R_1 = 25\ \Omega$, $R_2 = 150\ \Omega$ and $R_3 = 80\ \Omega$ (Sect. 5.3.1).

5.2. Offline Tests and Characterisations

The wide range of temperatures of CSR, with a bake-out at 250°C and cryogenic operation at 10 K, puts high strain on all materials which are in use. Thermal stress tests of all components, in particular those installed in or at the beam-guiding vacuum chamber, were mandatory. In addition, cryogenic operating tests of the translation stage and the detector sensor were conducted.

The electrical and mechanical feed-throughs of the beam-guiding vacuum chamber

of CSR had to pass three cycles of bake-out and cryogenic test without developing a vacuum leak. The bake-out was usually up to a temperature of 260°C and the cryogenic test was done in a bath of liquid nitrogen (77 K). After these cycles, a concluding helium leak test was carried out to confirm CSR compatibility.

The detector sensor and the translation stage were tested separately due to spatial constraints in the used test set-ups. For the bake-out tests, both assemblies were, one after the other, placed into a vacuum chamber which was then heated up to 260°C with a maximum temperature gradient of 15°C per hour. The maximum temperature was kept for few hours, then the set-up was cooled to room temperature. Before and after the test the tightness of all screws was checked.

Cryogenic operating tests of the particle sensor are presented in Sect. 5.2.1. The cryogenic operating test of the translation stage and the intermediate 40 K-drive of the detector are described in Sect. 5.2.3. Further tests were performed addressing the detection efficiency of the COMPACT sensor. The influence of the secondary electron yield of the converter cathode and the MCPs electron detection efficiency on the absolute detection efficiency of the sensor was investigated theoretically and experimentally. A theoretical description of the detection efficiency is provided in Sect. 5.2.2.1. Details of the experiment are discussed in Sect. 5.2.2.2.

5.2.1. Cryogenic Operating Test of the Detector Sensor

As described in detail in Sect. 5.1.1.1, an MCP-anode set was chosen as a secondary-electron multiplier for COMPACT. In order to ensure reliable operation in CSR, the COMPACT sensor including the MCPs was tested for its operation ability at cryogenic temperatures (Sect. 5.2.1.1). These tests were of particular importance since, even though performance of MCPs at ambient temperatures of down to 12 K have been documented [165], it is well known that the resistance of the semiconducting MCP glasses rise strongly with decreasing temperatures [164, 166, 167] which could lead to problems in CSR operation at 10 K and below.

CEMs are considered as alternative secondary-electron multipliers in future versions of COMPACT. They can produce pulses which might be easier to discriminate, since CEMs collect all secondary electrons produced by the converter cathode into one channel which provides higher gain and stronger pulse height saturation. Therefore, two CEM-detectors of the design of Rinn el al. [123] were tested for their operating ability at 25 K within the test series described in Sect. 5.2.1.2.

5.2.1.1. Cryogenic Test of the COMPACT Sensor

The cryogenic operation tests of the COMPACT sensor were conducted at the cryogenic test bench schematically depicted in Fig. 5.14. The set-up is placed completely in a vacuum chamber and consists of a test cryostat built around a *Leybold* RPK-800 dual-stage pressurised helium refrigerator. The design reflects, at least partly, the thermal structure of CSR: A 400×80 mm^2 copper platform, which is attached to the second stage of the cold head, cools down to 17 K without load and serves as an experimental platform for components foreseen for the CSR beam-guiding vacuum chamber. The platform is completely enclosed by a thermal radiation shield consisting of an aluminium case with a 12 mm-base plate installed on the first stage of the cold head. Several layers of multi-layer insulation (MLI) material further limit radiative heat input into the set-up. The thermal shield cools down to a temperature of 40 K. It can thus also serve as an experimental platform for isolation vacuum components which should be attached to the 40-K shield of CSR. The set-up can be evacuated to a base pressure of 1×10^{-6} mbar by a turbo-molecular pump. Several Pt1000 thermo-sensors are available to monitor the temperature at various positions of the cold head, the shield and the copper platform. Spare sensors can be attached directly to the equipment to be tested. Even though CSR, in cryogenic operation, features ambient temperatures of below 10 K, the cooling power of the cold head and the finite accuracy of the Pt1000 sensors limit the minimum useful temperature of the test bench to 20 K.

Outside the 40 K-shield, an ^{241}Am α source with an activity of 3.4 MBq is attached to the room-temperature vacuum chamber of the test bench. It is kept at a temperature above 273 K. 5.4-MeV α particles can enter the experimental volume by small holes in the insulation layers and in the thermal shield. The particle flux is collimated such, that α particles enter the inner volume of the test set-up at a rate of few 10^3 s^{-1}.

A series of measurements was carried out to examine the performance of the COMPACT detector sensor at cryogenic temperatures. To this end, the detector sensor was placed onto the copper platform directly facing the α emitter. A 100-Ω heating resistance as available off-the-shelf was attached to the platform allowing to raise the temperature of the entire experimental platform by a few tens of K while the cryostat is operating. The converter, MCP front, MCP back, and anode electrodes were separately thermally anchored to the cold-head temperature via their respective high-voltage leads, and a Pt1000 temperature sensor was attached to the outside of the grounded detector housing. The detector was operated with its standard potentials (Tab. 5.2).

The count rate of α particles on the detector was monitored by setting the threshold of the discriminator safely above the electric noise level. The cold head was then

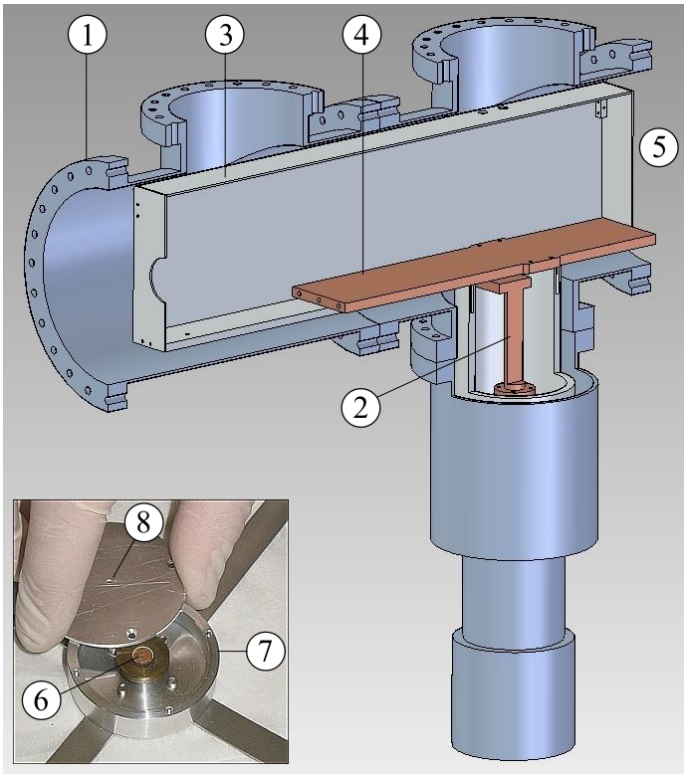

Figure 5.14.: The cryogenic test bench consists of a vacuum chamber (1) housing a dual-stage cold head (2). A thermal shield (3) wrapped in several layers of MLI is attached to the first stage of the refrigerator. The experimental platform (4), which served for cryogenic tests of the detector sensor and the translation stage, is fixed to the second stage and cools down to 20 K. The inset shows the α-emitter (6) in its housing (7) which is fixed to the warm vacuum chamber at position (5). The cover of the housing has a 1 mm aperture (8) collimating the α-particle flux.

switched on and the count rate as well as the temperature of the detector sensor were monitored while cooling. After 20 h the temperature of the detector housing was ∼22 K. Figure 5.15 shows the evolution of the sensor temperature and the count rate of α particles as a function of time. As indicated by the shaded areas, three different regimes can be observed. After pumping for one day to a base pressure of 2.4×10^{-6} mbar, potentials are applied to the electrodes and the detector is operated at room temperature for some days. The count rate, starting from an initial value of 2.7×10^{3} s^{-1} decreases in the following 90 h by 7% to 2.5×10^{3} s^{-1}. This effect in believed to stem from the well-known initial burn-in period [174] where degassing of residual-gas molecules from the channel surfaces changes the gain of the MCPs, and thus the likelihood of the pulses to be positively discriminated.

A second phase started when the cold head was switched on (after 90 h) and the setup cooled to cryogenic temperatures. The dominating effect is here a steep decrease of the count rate by 8% over 20 h to 2.3×10^{3} s^{-1}. Simultaneously the resistance of the MCP stack, derived from the measured bias current, rose from initially 56 MΩ at 300 K to 85 GΩ at 22 K. These findings are similar to what has been observed previously for MCPs at cryogenic temperatures [167]. Again the decrease of the count rate is caused by a reduction of the average pulse height, now as a result of

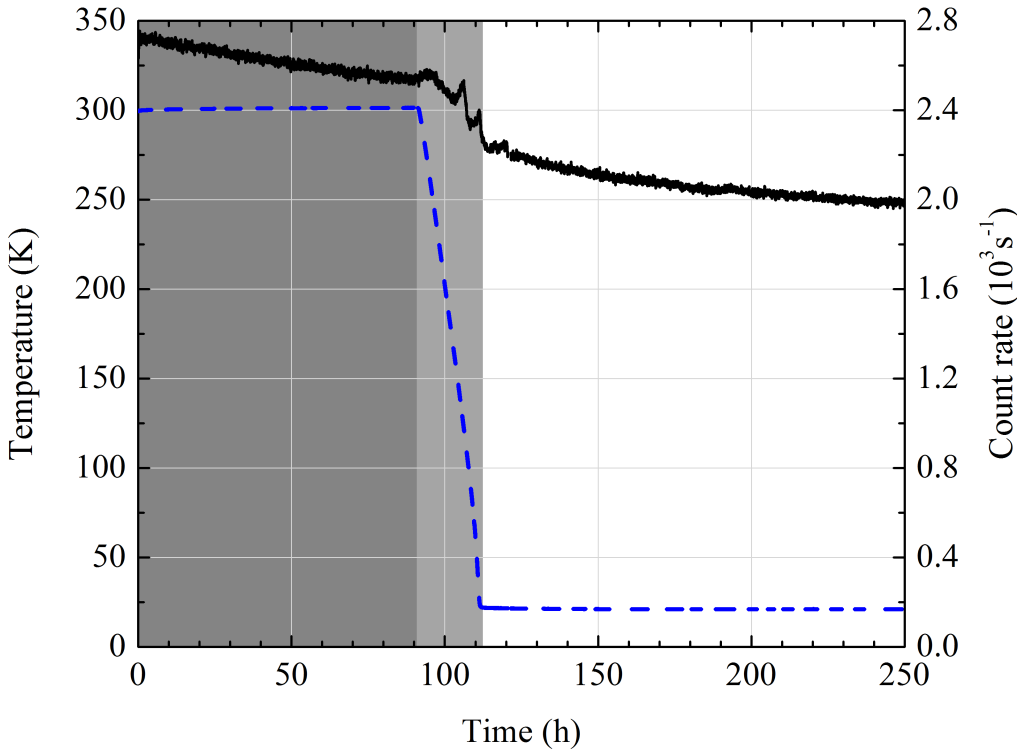

Figure 5.15.: The COMPACT sensor temperature (dashed line) and count rate (solid line) of α particles as a function of time. The shaded areas mark the three discussed phases: burn-in (dark shaded), change in resistance (light shaded) and a process with a longer time constant (not shaded) which is believed to origin from cryo-adsorption of residual-gas particles on the MCP surface.

the temperature dependent recharging resistance of the MCP channels. Due to the rising resistance, once a channel has produced an avalanche of electrons, it needs more time to recharge. Measurements under cryogenic conditions may therefore require adapted, low count rates.

The peak like excursions of the count rate that occurred after about 105 h (Fig.5.15) might be the result of pressure changes by cryo-absorption, an assumption which is supported by the measurements of the residual-gas pressure, but since the vacuum gauge is outside the thermal shield of the cryogenic test bench, the actual pressure at the MCP is uncertain.

In the third phase, starting after ∼110 h in Fig. 5.15, the detector sensor is in a thermal equilibrium and the bias current of the MCPs is constant. Still, a decrease of 20% in the count rate was observed in the following week. This effect cannot be assigned to the change in resistance. As later described in detail, it is believed to stem partly from cryo-adsorption of residual-gas particles onto the cold surface of

the MCPs. The residual gas pressure at CSR will be much lower and therefore this effect is expected to be much lesser in COMPACT operation in the storage ring. Also, part of this pulse amplitude degradation can be restored by local heating of the MCPs, as shown below.

A high-voltage ohmmeter was attached to the electrodes of the MCPs to probe their resistance while cooling. The result plotted against the temperature of the COMPACT housing can be found in Fig. 5.19. However, accurate measurements are only possible in thermal equilibrium of the experimental platform, as the true temperature of the MCPs can only then be assumed to be equal to that measured by the Pt1000 sensors. The commercial 100-Ω heating-resistance was used to obtain a precise calibration of MCP resistance versus temperature. The temperature of the experimental platform including the COMPACT sensor was step-by-step increased using that heating while the bias current on the MCPs was monitored simultaneously. As soon as the current was stable, the detector sensor was assumed to be in thermal equilibrium with the surroundings. Under these conditions, the temperature os the housing is taken to correspond to the MCP temperature. In this way the temperature of the sensor was calibrated against the MCP resistance in the temperature range of 22 to 45 K. The result is shown in Fig. 5.16. The curve provides a means to deduce the MCP resistance from the measured bias current also in future experiments at CSR.

The available cooling power did not allow to cool the test bench to the CSR's ambient temperature of below 10 K. In spite of the fact, that the MCPs still delivered an adequate signal at a temperature of 22 K, the steep rise in resistance towards lower temperatures (Fig. 5.16) might cause problems in CSR operation since it could easily exceed few TΩ for temperatures of 10 K. In order to provide a means to keep the resistance in a region which ensures a reliable operation of the MCP, the COMPACT sensor features a heating element (Sect. 5.1.1.4) which can locally raise the MCP temperature.

By feeding electric current through the Constantan wire, the heating element was operated in order to investigate the response of the count rate to a rise in the MCP temperature. Figure 5.17 shows the count rate of α particles, the temperature of the sensor housing, and the temperature of the MCPs obtained from the measured bias current via the calibration described above. The different shaded areas of the plot define different work points of the heating. A heating power of 85 mW was applied first, resulting in an MCP temperature of 29 K. It took about 2 h until the temperature of the MCPs had stabilized. By applying a heating power of 200 mW, the temperature of the MCPs could be raised by more than 20 K with respect to the starting temperature of 23 K. The MCP resistance was lowered to less than 5 GΩ after 80 min of heating. In contrast to the significant temperature rise of the MCPs, the temperature of the sensor housing did not increase by more than 1 K when the

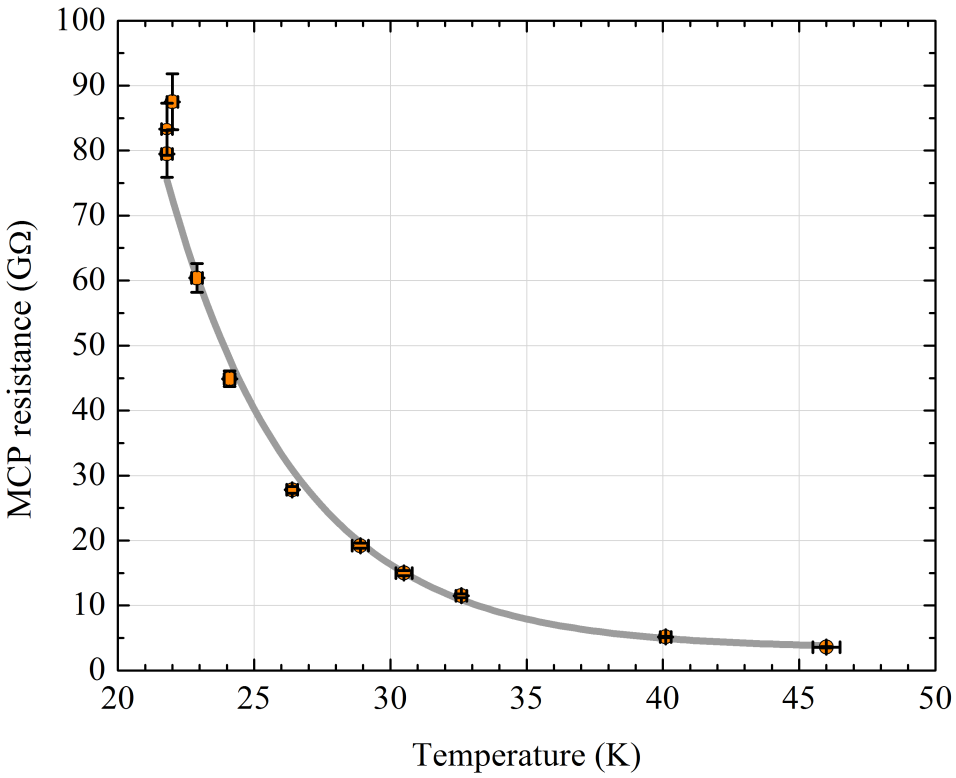

Figure 5.16.: The filled circles show the MCP resistance derived from the measured MCP bias current. The resistance could be reduced by heating with the 100 Ω-heater to below 4 GΩ. The grey line is an exponential fit $R_{\mathrm{MCP}}(T) = 3.36 + 6876 * e^{-T/4.78}$ to the data which was used as calibration function.

maximum heating power of 200 mW was applied. The thermal coupling of the MCP holder to the housing is apparently weak enough to allow for a rise in temperature which is strongly localised to the MCP and anode structure.

The current of the heating element had no impact on the signal quality received from the COMPACT anode but the resulting rise in MCP temperature led to a significant increase of the pulse amplitudes. This is clearly visible in the count rate of α particle pulses above the discrimination threshold. Figure 5.17 shows that the count rate quickly increased by 5% when switching on the heating element. The second rise, due to the increase of heating power from 0.085 mW to 0.2 mW, is delayed by 0.5 h and provided a gain of 10% in count rate. After turning down the heating power to 0 W, the count rate follows with a delay of 1 h, but stays on a 15% higher level than before the heating processes. This effect cannot be assigned to a change in MCP resistance as this is the same before and after the thermal cycle. Instead, it is believed to originate from desorption of previously cryo-adsorbed residual-gas molecules from the MCP surfaces when locally heating the MCP to a higher temperature than

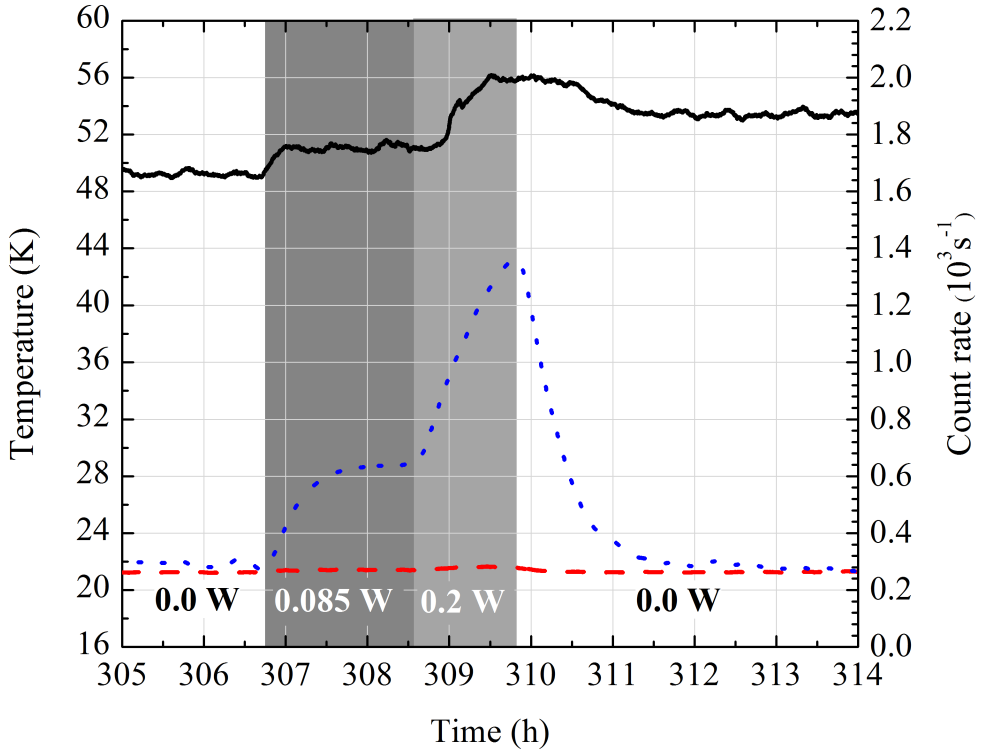

Figure 5.17.: The COMPACT heating element was used to locally raise the temperature of the detector (dotted line) to more than 43 K. While the count rate on the MCPs (solid line) reacted quickly, the temperature of the sensor housing (dashed line) was almost unaffected. The shaded areas indicate the different heating powers applied to the heating element.

the surroundings. During the experiment, the effect could be observed repeatedly, supporting the explanation by cryo-adsorption on the MCP surfaces. CSR will start its cold operation from a much better base pressure, hence the effect is expected to be smaller when the detector is operated in the CSR vacuum.

Following the positive test results, a similar heating element was introduced to the detectors of the beam-imaging system of CSR in order to provide a possibility to locally heat their MCP phosphor-anode stacks [86] as well.

5.2.1.2. Cryogenic Tests with CEM Detectors

Keeping in mind that, in principle, the COMPACT sensor can be replaced by various kinds of sensors which are suitable for CSR conditions, a CEM-based particle sensor, of a design which was adapted from Rinn et al. [123] (Sect. 3.4.1.4), was tested for

its ability to operate at cryogenic temperatures. In two consecutive measurements, different CEMs were tested by incorporating them into the sensor housing (Fig. 3.4). In a first attempt, a standard, high resistance CEM (*Philipps* type X 719 BL) was used as secondary electron multiplier. In a second test, the standard CEM was replaced by a low-resistance EDR CEM (*Photonis* type 7010M C EDR).

The cryostat described in Sect. 5.2.1.1 was employed as an experimental platform. It was not possible to fix a sensor directly on the CEM to monitor its temperature. Therefore, in a preliminary test only, no potentials were applied to the CEM and one Pt1000 sensor was placed at the converter cathode while the other was attached to the detector housing. The detector housing was fixed onto the copper mounting stage which is connected to the second stage of the cryopump (Fig. 5.14). Subsequently, the set-up was cooled down to a temperature of 30 K.

It was found that the temperature of the converter cathode directly follows the temperature of the detector housing. Since converter cathode and CEM are fixed to the same ceramic rods (cf. Fig. 3.4, Sect. 3.4.1.4) connecting them thermally to the detector housing, it is assumed that the temperature of the converter and, hence, of the housing also reflects the temperature of the CEM.

For the subsequent operating test of the *Philipps* CEM, the temperature sensor at the converter cathode was removed. The detector was placed into the chamber facing the ^{241}Am source allowing α particles to irradiate the converter electrode. The operating potentials as summarised Tab. 3.1 were applied. The CEM signal was driven into the COMPACT fast preamplifier and amplified further using an ORTEC 474 timing filter amplifier before being fed into a linear discriminator of a certain trigger threshold. While monitoring the count rate after the discriminator, the set-up was cooled down to 20 K. The resistance at various temperatures was measured via a high-voltage ohmmeter.

Figure 5.18 shows the mean count rate as measured by the *Philipps* CEM as a function of the detector housing temperature. Two main slopes in the rate can be observed (shaded areas in Fig. 5.18). The first one starting at around 225 K was not investigated further, but could stem from a change in alignment between the α-source, collimator and detector aperture due to thermal contraction. The second strong drop in signal rate starts at 100 K. It is caused by the steep raise in resistance of the CEM which would reduce the pulse heights of the α pulses to below the discriminator threshold. This assumption is supported by the resistance curve shown in Fig. 5.19 as well as by the fact, that practically all thermal shrinking occurs between 300 K and 100 K, so that further misalignment of the apertures below 100 K can be excluded. Starting from originally about 400 MΩ at room temperature, the CEM resistance rose steeply towards lower temperatures, exceeding 1 TΩ at 25 K. Even by increasing the gain voltage of the CEM no signals could be observed. It can be concluded that the high resistance causes electron depletion in the long channel of

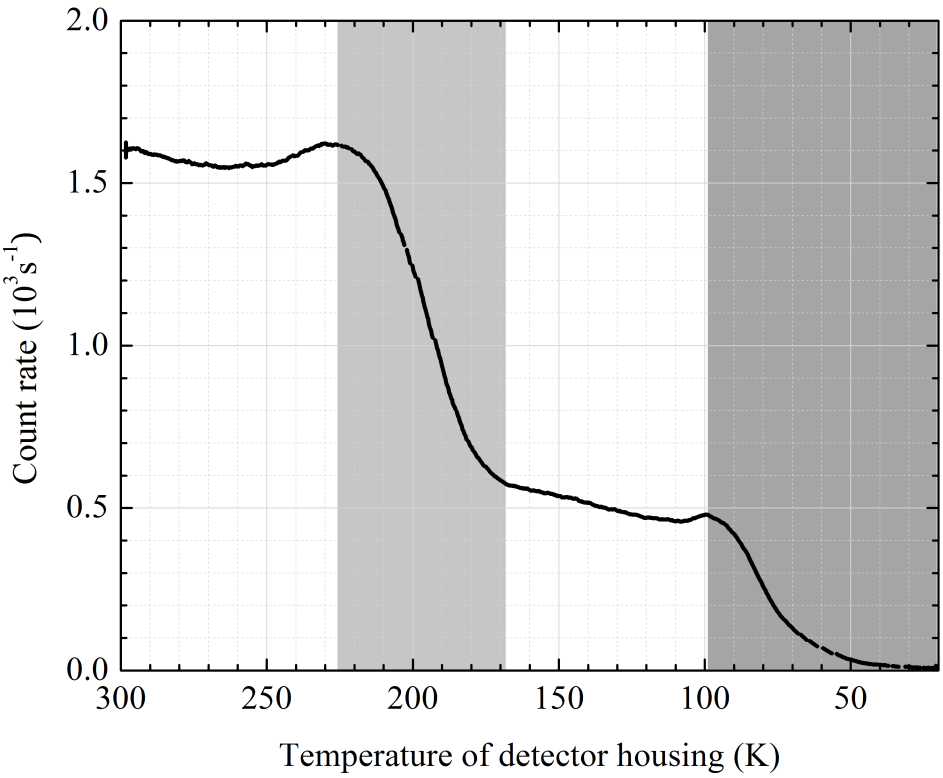

Figure 5.18.: The count rate of the standard *Philipps* CEM versus the temperature of the detector housing. The two shaded areas indicate the tree observed regimes explained in the text. Below temperatures of about 50 K the CEM is virtually blind.

the CEM which prevents secondary electrons from the converter cathode to trigger an avalanche at very low temperatures. After warming the test cryostat the CEM worked at room temperature as before.

The *Philipps* CEM was replaced by a EDR MCP by *Photonis* for a second operational test. With about 70 MΩ at 300 K, the EDR CEM has a resistance which is about one order of magnitude lower than the resistance of the standard CEM. The sensor was mounted onto the copper plate of the cryostat in the same way as it was done in the previous tests. The detector, initially, was also operated with the potentials given in Tab. 3.1 and the system was cooled down to a minimum temperature of 23 K while simultaneously monitoring the signals caused by the α particles on the detector.

As already observed in the cryogenic test of the standard CEM, the amplitudes of the α particle induced current pulses decreased with decreasing temperatures. However, for the EDR CEM, it was always possible to increase the pulse heights by application of a higher gain voltage. At the final temperature of 23 K, the gain

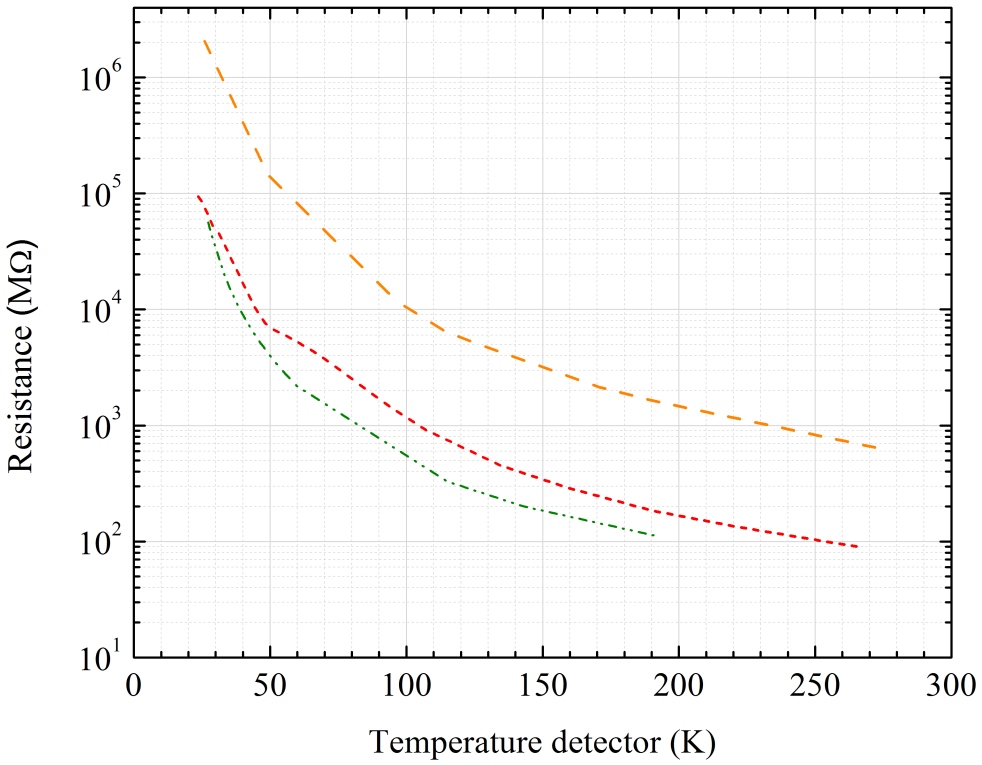

Figure 5.19.: Resistance curves of the two tested CEMs and the COMPACT MCPs. The yellow, long-dashed line is the resistance curve of the standard *Philipps* CEM while the red, short-dashed line belongs to the *Photonis* EDR CEM. The lowest resistance curve (green, dot-dot-dashed) is recorded for the EDR MCPs which are in use in the COMPACT detector.

potential difference of the detector was set to $\Delta U_{\mathrm{CEM}} = 3$ kV. Even though the pulses were then smaller than in room-temperature operation, the EDR CEM appeared to work as reliably as the EDR MCPs (Sect. 5.2.1.1) at a temperature close to 20 K.

The resistance of the EDR CEM amounted to about 90 GΩ at a temperature of 23 K. Fig. 5.19 shows the resistance curves of both tested CEMs and of the EDR MCPs of the COMPACT sensor. While the standard CEM has a resistance which is by more than an order of magnitude higher, the EDR CEM and the EDR MCPs show similar behaviours across the entire temperature range. Hence, EDR CEMs seems to be suitable replacements for EDR MCPs in future COMPACT-type single-particle sensors. For cryogenic operation at CSR it is however recommended to include a similar heating element as incorporated in the COMPACT sensor (Sect. 5.1.1.4), since smooth performance at 10 K or below cannot be guaranteed.

5.2.2. Detection Efficiency

The detection efficiency of a plain MCP detector directly exposed to the particles to be detected is given by the efficiency $\varepsilon_{\mathrm{MCP}}$ of the MCP itself. However, by introducing a converter cathode of secondary electron yield γ collecting those secondaries onto the MCP efficiently, the overall detection efficiency can be increased significantly. In the following the overall COMPACT sensor efficiency is characterised theoretically (Sect. 5.2.2.1) and experimentally (Sect. 5.2.2.2).

5.2.2.1. Theoretical Description of the Detection Efficiency

Primary particles entering the COMPACT sensor impact onto the aluminium converter cathode leading to the emission of a number of secondary electrons which are then accelerated towards the MCP surface. Depending on the surface condition of the cathode, the secondary-electron yield γ may vary spatially across the cathode. Theoretically, the number of electrons can then be described by a Pólya distribution, as well established in the context of statistical models of secondary emission from discrete-dynode electron multipliers [175–177]. The basic idea is that for each specific point of impact on the cathode the number of emitted secondary electrons follows a Poisson distribution of mean γ, whereas the local value for γ varies from point to point following a Laplace distribution. Since the probability for secondary electrons reaching the MCPs surface might fluctuate spatially as well, γ is in addition weighted with the collection efficiency ε_c. A defining quantity of the secondary emission and collection process is hence the product $\gamma\varepsilon_c$. The Pólya distributed probability $W_n(\tilde{\gamma}, b)$ for n secondary electrons being collected at the MCP input surface upon impact of a given primary particle onto the converter surface is described by

$$W_n(\tilde{\gamma}, b) = \frac{\tilde{\gamma}^n}{n!}(1 + b\tilde{\gamma})^{-n-1/b} \prod_{i=0}^{n-1}(1 + ib) \quad \text{with} \quad 0 \leq b \leq 1 \tag{5.4}$$

where $\tilde{\gamma}$ is the average secondary electron yield weighted with the probability ε_c for an electron reaching the MCP surface, i.e., $\tilde{\gamma} = \langle\gamma\varepsilon_c\rangle$. The dimensionless parameter b is the relative variance [176] of the product $\gamma\varepsilon_c$, hence $0 \leq b \leq 1$. The distribution features two extreme cases: If $b = 0$, meaning that there is no variation in $\gamma\varepsilon_c$ over the area of impact, the Pólya distribution reduces to a Poisson distribution. In the limit of $b = 1$, the Pólya distribution converges to the negatively exponential Furry distribution [176] describing a large variance of $\gamma\varepsilon_c$ over the irradiated cathode area.

The probability for an electron impinging onto the MCP to trigger an avalanche in a channel is denoted in the following as $\varepsilon_{\mathrm{MCP}}$. For n electrons being emitted by one primary particle on the converter, the total number k of electrons triggering a

channel avalanche in the MCPs is binomially distributed with $B_k(\varepsilon_{\mathrm{MCP}}, n)$. Since the number n of secondary electrons is itself Pólya-distributed according to Eq. 5.4, the number k of MCP avalanches per primary ion is distributed according to

$$P_k = \sum_{n=k}^{\infty} B_k(\varepsilon_{\mathrm{MCP}}, n)\, W_n(\tilde{\gamma}, b) = \sum_{n=k}^{\infty} \binom{n}{k} \varepsilon_{\mathrm{MCP}}^k (1-\varepsilon_{\mathrm{MCP}})^{n-k}\, W_n(\tilde{\gamma}, b) \tag{5.5}$$

The COMPACT detector in CSR will mainly be irradiated by a product beam generated by electron collisions with a cooled, low-emittance ion beam [178]. The irradiated area of the converter cathode can therefore be smaller than 0.01 mm^2. Assuming that the spatial variation of $\gamma\varepsilon_c$ is negligibly small within this area, b may be taken to be 0, hence Eq. 5.4 becomes equal to a Poisson distribution of a mean $\tilde{\gamma}$, causing the overall distribution of Eq. 5.5 to become

$$P'_k = \lim_{b\to 0} P_k = \sum_{n=k}^{\infty} \binom{n}{k} \varepsilon_{\mathrm{MCP}}^k (1-\varepsilon_{\mathrm{MCP}})^{n-k} \frac{\tilde{\gamma}^n}{n!} e^{-\tilde{\gamma}} = \frac{(\varepsilon_{\mathrm{MCP}}\varepsilon_c\gamma)^k}{k!} e^{-\varepsilon_{\mathrm{MCP}}\varepsilon_c\gamma} \tag{5.6}$$

An incident particle is recorded if at least one electron is detected by the MCPs. The overall detection efficiency of the COMPACT sensor comprising the secondary-electron yield of the converter, the collection efficiency of the sensor geometry, as well as the detection efficiency of the MCPs, can eventually be given as

$$\varepsilon = 1 - P'_0 = 1 - e^{-\varepsilon_{\mathrm{MCP}}\varepsilon_c\gamma} \tag{5.7}$$

According to the SIMION simulations which have been presented in Sect. 5.1.1, the collection efficiency ε_c of the converter is $\geq 95\%$ over practically the entire detector aperture (Fig. 5.8). Consequently, ε is depends on the detection efficiency of the MCPs for 1.2-keV electrons ($\varepsilon_{\mathrm{MCP}}$) and on the local secondary electron yield γ. Theoretically, these numbers are hard to predict. Since an electron is only detected if it triggers an electron avalanche in an MCP channel, it is common practice to use the open area ratio of the MCPs of 0.6 as estimate for $\varepsilon_{\mathrm{MCP}}$, although somewhat higher values for electron energies around 1 keV have been reported [179–182]. The secondary-electron yield γ is even harder to assess. Electron ejections from metal surfaces are known to be surface-sensitive processes. Hence γ depends not only on the energy of the impinging particle and the cathode material, but also on the chemical composition and thickness of any oxide or other adsorption layers that may have formed even on an originally clean surface [168,169,175,183]. Even though these surface phenomena are hard to predict theoretically, it is safe to assume that, given a proper velocity of the impinging ions, on average several secondary electron are emitted. Figure 5.20 shows the overall detection efficiency of COMPACT calculated theoretically by employing Eq. 5.7. It shows, that $\varepsilon \geq 95\%$ for $\gamma > 5$. A systematic error of 33% as an estimated combined, relative uncertainty on $\varepsilon_{\mathrm{MCP}}\varepsilon_c$ is given

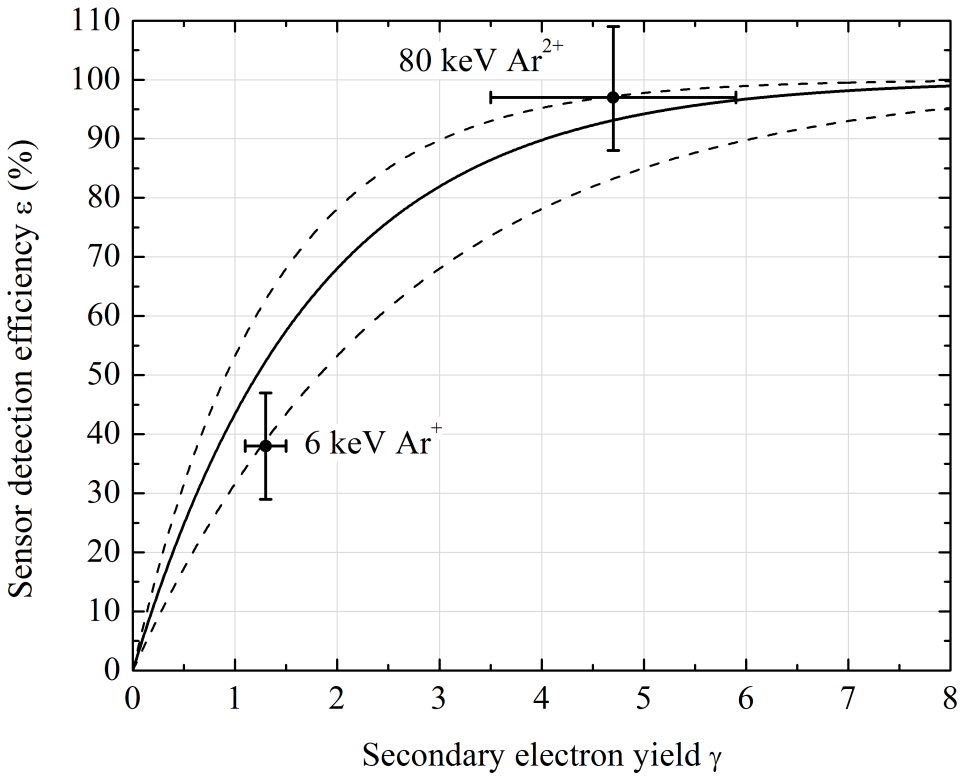

Figure 5.20.: The theoretical sensor detection efficiency ε (solid line) as a function of the secondary-electron yield γ from Eq. 5.7 with $\varepsilon_{\mathrm{MCP}} = 0.6$ and $\varepsilon_c = 0.95$. The dashed lines represent an estimated combined uncertainty of 33% on ε. The filled circles are the two experimentally derived efficiencies including their total uncertainties.

within the graph.

The secondary electrons which are detected by the MCPs are assumed to impinge into different MCP channels. While, for high numbers of impinging electrons, the output signal of a CEM is damped due to the space-charge limit of the electron avalanche, the output signal amplitude of the MCPs is therefore expected to be proportional to the number of electrons succeeding to penetrate into an MCP channel. If the pulse height distribution for one electron is already known, this characteristics provides a means to determine the average number of produced secondary electrons from a second measured pulse height distribution (Sect. 5.3.1.2).

5.2.2.2. Experimental Detection Efficiency

In order to support the theoretical approach developed in Sect. 5.2.2.1, the experimental detection efficiency was analysed in two measurements on ions of different energies.

Efficiency Measurement with 6-keV Ar^+

In a first experiment, the mean secondary-electron yield of the converter γ for 6-keV Ar^+ ions entering the detector roughly in the centre of its sensitive area, was determined. To this end, the detector was placed in a vacuum chamber featuring a small Penning ion source. A 20 mm-diameter Faraday cup, featuring a repeller electrode for secondary-electron suppression and a 4 mm-hole in the bottom was placed approximately centred in front of the COMPACT sensor. The measurement principle was such, that an ion beam of up to 1 nA of 6-keV Ar^+ (150 eV/u) was alternatingly steered onto the bottom of the cup and then through the hole onto the converter cathode of the COMPACT sensor. A preliminary measurement showed that the beam envelope was small enough to fit entirely through the 4 mm circular aperture. The secondary-electron yield γ was determined by alternatively measuring the ion current I_{ion} on the Faraday Cup and the current on the converter electrode I_{con} with a floating nanoamperemeter. The MCP was on operation potential (see Tab. 5.2) in order to provide the correct electric field lines. However, its active area was covered by a sheet metal, in order to protect it from the high-currents released from the converter plate. The ion current from the ion source was stable enough that I_{ion} could be assumed not to have changed in-between two steerer settings. Hence, the mean number of secondary electrons per ion γ emitted by the converter cathode can be derived from

$$\gamma = \frac{I_e}{I_{\text{ion}}} = \frac{I_{\text{con}} - I_{\text{ion}}}{I_{\text{ion}}} \tag{5.8}$$

since I_{con} is the sum of both the current from the impinging ions I_{ion} onto the converter and the current originating from the emitted secondary electrons I_e. The number of secondary electrons emitted from the converter electrode for an impinging 6-keV Ar^+ ion was determined to be $\gamma_{\text{exp,6-keVAr}^+} = 1.3\,(2)$.

Subsequently, the hole in the Faraday cup was reduced to a pinhole aperture of a diameter of 10.5 (5) μm. This is much smaller than the beam envelope at the Faraday cup, and hence decreased the rate of particles that could reach the COMPACT sensor to a value suitable for single-pulse counting at the MCP-anode stack, whose protective cover could hence be removed. By employing the method developed by Rinn et al. [123], the total experimental detection efficiency for 6-keV Ar^+ was determined by steering the ion beam across the pinhole aperture in two dimensions (x, y) while simultaneously measuring the count rate and the ion current. Since the

fraction of the ion beam entering the aperture was very small (∼0.001%) its effect on the ion current measured in the Faraday cup was negligible.

In each measurement step the count rate r_{ij} and the corresponding ion current $I_{i,j}$ was recorded. The experimental efficiency is then given by

$$\varepsilon_{\text{exp}} = \frac{qeA}{a} \sum_{i,j} \frac{r_{ij}}{Iij} \tag{5.9}$$

with q being the charge state of the impinging ion, e the elementary charge, a the area of the pinhole and A the rectangular area enclosed by four neighbouring steerer settings

$$A = (x_{i+1} - x_1) \times (y_{j+1} - y_j) \quad . \tag{5.10}$$

A was obtained from a calibration of the electrostatic steerer, which was done by steering the beam all across the known aperture of the Faraday cup in two dimensions.

In this way, a detection efficiency for 6-keV Ar^+ ions of $\varepsilon_{\text{exp}} = 38\,(9)\%$ was obtained. The large statistical error is due to the poor focussing and collimation properties of the small Penning source which produced a large background rate and an asymmetric, steeply peaked beam shape (Fig. 5.21). The high background signal had to be subtracted from the beam-induced count rate, and hence led to a quite large uncertainty on r_{ij}. Moreover, the irregular shape of the ion current density, as visible in Fig. 5.21, limited the maximum allowed total current I_{ion}, in an effort to keep the MCP count rate below 10^5 s^{-1} at all measurement steps. In return, this resulted in a relatively large error on I_{ij}. In addition to these statistical uncertainties, there are systematic uncertainties, dominated by the size of the pinhole aperture a. Direct microscopic measurement of the pinhole diameter yielded a value of 10.5±5 μm corresponding to a relative systematic uncertainty of ∼9% on ε_{exp}. Since the 12.7-μm thickness of the aperture is comparable to the pinhole diameter of of 10.5 μm, the angle of incidence of the ion beam onto the cup causes an additional, asymmetric uncertainty of the aperture size. The angular uncertainty is estimated to be ±3°at most, corresponding to an uncertainty of $^{+0}_{-8}$% on the projected pinhole size and, hence, an error of $^{+8}_{-0}$% on the experimental detector efficiency ε_{exp}. The obtained value for $\varepsilon_{6-\text{keVAr}^+}$ of $\gamma_{6-\text{keVAr}^+}$ is shown in Fig. 5.20 together with the theoretical calculations for the detection efficiency.

Efficiency Measurement with 80-keV Ar^{2+}

Following the experiment with 6-keV Ar^+ ions, a second efficiency measurement was conducted using 80-keV Ar^{2+} ions. While the measurement principle remained

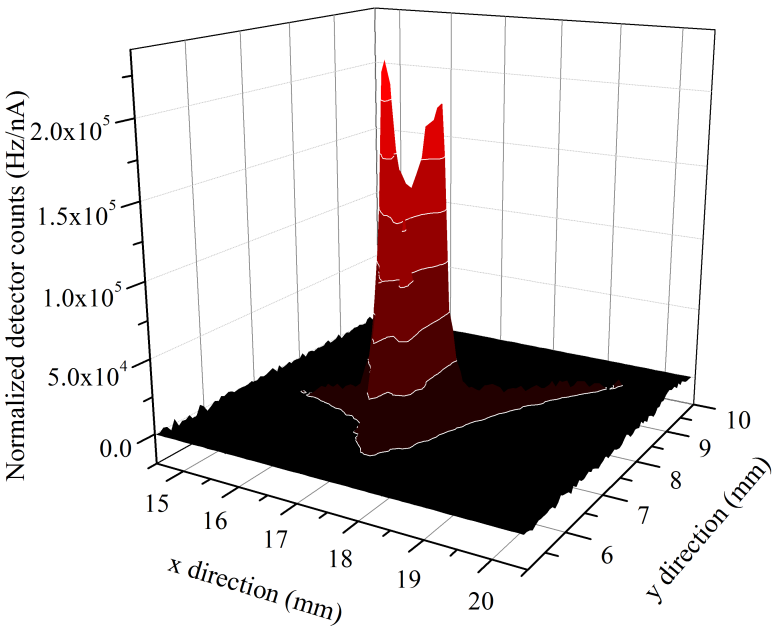

Figure 5.21.: Beam profile of the 6-keV Ar^+ beam used for the first efficiency measurements. Even though the method is in principle not sensitive to the beam profile, its irregular shape made background subtraction difficult, leading to a large uncertainty in the results.

the same, the Faraday cup and the sensor were moved to the CSR injection accelerator where 80-keV Ar^{2+} (2 000 eV/u) was generated in a Penning-type ion source. The beam from the source was momentum-selected in a 90°dipole magnet and collimated to a size of 2.6×2.7 mm^2 at the position of the experiment (Fig. 5.22). The opening of the Faraday cup was reduced to a diameter of 10.25 (5) mm and an additional shield was placed into the beamline in front of the cup in order to prevent stray ions from entering the detector sensor. The thereby achieved signal-to-background ratio was approximately 10 and much improved as compared to the low-energy Ar^+ ion source set-up described above.

The measurements with Ar^{2+} of 80 keV energy resulted in an experimental detection efficiency for $\varepsilon_{80-\mathrm{keV}Ar^{2+}} = 97\,(3)\%$. No direct measurement on the secondary-electron yield of 80-keV Ar^{2+} was performed, due to the limited availability of the high-energy accelerator platform. However, for both experiments, 6-keV Ar^+ and 80-keV Ar^{2+}, the pulse height distribution was recorded. As discussed before, the pulse height is proportional to the number of secondary electrons triggering an avalanche at the MCPs which, for a narrow impinging particle beam as delivered by the pinhole cup, are Poisson-distributed according Eq. 5.6 around a mean value of $\varepsilon_{\mathrm{MCP}}\varepsilon_c\gamma$. By comparing the mean pulse height of 6-keV Ar^+ to the one for 80-keV Ar^{2+}, it was found that the latter was higher by a factor of 3.6 (7). Hence, a secondary-electron yield of $\gamma_{80-\mathrm{keV}Ar^{2+}} = 4.7\ (1.2)$ could be derived. This value, as well as the observed secondary-electron yield of 1.3 (2) for 6 keV Ar^+, is lower than previously published observations for Argon impacting onto contaminated Al surfaces [184, 185], but still significantly higher than what has been reported for atomically clean Al

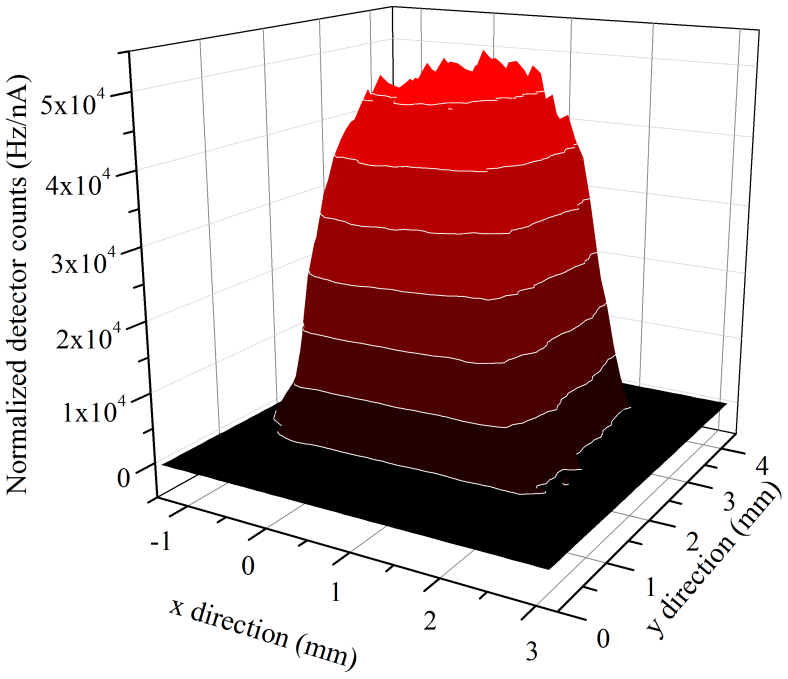

Figure 5.22.: Beam-profile of 80-keV Ar^{2+}. The second efficiency measurements were conducted with the CSR ion source which produced a nicely defined ion beam of 80-keV Ar^{2+}. The beam was cut down to a size of 2.6×2.7 mm^2 in advance of the Faraday cup.

targets [169, 186].

The experimental detection efficiency together with its total uncertainty, including also the systematic errors already discussed for the measurements on Ar^+, is summarised in Fig. 5.20. Both experimental results agree with the theoretical model for the detectors detection efficiency developed in Sect. 5.2.2.1.

5.2.3. Cryogenic Tests of the Translation Mechanics

In order to assure a smooth operation in CSR, the translation stage without the detector sensor was tested for its performance at low temperatures in the cryogenic test set-up described in detail in Sect. 5.2.1.1. In a first test, the rotary UHV feed-through by *Agilent Technologies* was fixed to the experimental platform of the cryogenic test bench (Fig. 5.14) and cooled down to 22 K. A thermally decoupling drive—similar, but not identical to the one to be implemented at CSR—allowed to rotate the feed-through at low temperatures. Even though the UHV feed-through is only specified down to a temperature of 77 K, it performed more than 20 000 turns at 22 K without developing a leak, as was tested, after rewarming, with a helium leak detector.

A second test was conducted of the full UHV translation stage of COMPACT (see Fig. 5.2) including the rotary feed-through, the rail, the thread drive, the carriage and several of the CuBe2 electric power lines. Due to the spatial constraints of the

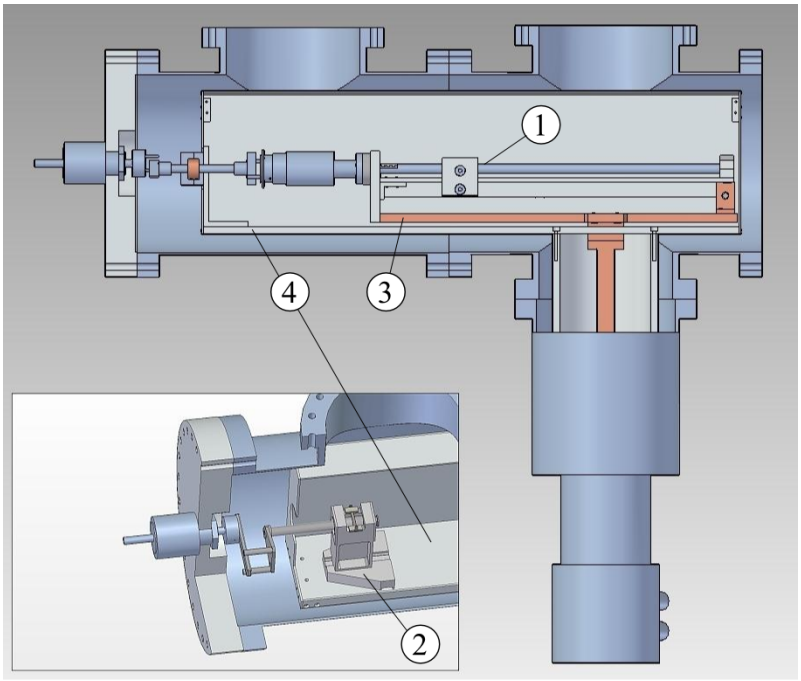

Figure 5.23.: Schematic illustration of the cryogenic test set-up used for the translation stage (1) and the 40 K-drive ((2), inset). The translation stage was attached to the experimental copper platform (3) which was kept at a temperature below 30 K during the test, while the drive, which has only to be tested at a temperature of 40 K, is fixed to the thermal shield (4) of the test cryostat.

test vacuum cryostat, it was not possible to include the particle detector sensor into the test. Instead, a similarly massive aluminium block of ∼200 g was mounted onto the carriage to simulate the stess onto the mechanical components by the weight of the sensor. Figure 5.23 shows a schematic illustration of the set-up. The set-up was cooled and the carriage was moved along the full stroke of the rail 200 times, corresponding to a total of 30 000 turns of the cryogenic tread drive. The movement of the carriage as well as the thermal contact to room temperature caused by the intermediate drive caused a slow rise in the temperature during operation of the translation stage. Therefore short breaks had to be included, during which the set-up could cool. In this way it was possible to keep the temperature below 30 K at all times. No deterioration of either the PEEK/stainless steel drive or the electric connections was observed after the test.

A separate test was carried out on the 40 K-drive, which is designed to thermally decouple the room temperature, outer feed-through from the cryogenic, inner feed-through. As shown in the inset of Fig. 5.23, the drive was fixed to the thermal shield of the cryogenic test bench. Since the thermal shield of the test bench is not spacious enough to allow rotation of the complete 40 K-drive, the actuator at one

end of the drive was removed. In that way, the mechanics were successfully tested at a temperature of 40 K.

5.3. CSR Operation

5.3.1. Room-Temperature Operation

The commissioning of CSR [86] at room temperature took place in March 2014. The storage ring was first baked out at an intermediate temperature of 120°C. Since most of the CSR pumping facilities had still to be installed, the vacuum in the beam-guiding chamber was only in the lower 10^{-7} mbar range. The isolation vacuum chamber was pumped as well, mainly for the sake of safe high-voltage operations. The laser interaction section had not yet been installed. Therefore, only reactions of the stored beam with the residual-gas particles could be used for detector tests.

The storage ring was operated with a beam of 50-keV N_2^+ ions produced from the injection accelerator, in order to allow operational tests of the installed detectors. Upon colliding with a residual-gas particle (X), kinetic energy can be transferred to the electronic shell of the N_2^+ molecule, resulting, mostly, in the excitation to a dissociating state that causes breakup into a neutral/charged fragment pair, each fragment carrying approximately 25 keV of kinetic energy. The reaction is given by

$$N_2^+ + X \rightarrow X + N + N^+ \quad . \tag{5.11}$$

The two reaction fragments are separated from the parent N_2^+ in the deflecting elements of CSR. The corresponding parameters η from Eq. 5.1 are -1.0 for N and $+1.0$ for N^+, respectively. These values are within the detection range given in Sect. 5.1, hence the products of collision reactions occurring in the straight section of the future electron cooler could be counted selectively by moving the COMPACT sensor to the corresponding positions. The detector was operated with the potentials given in Tab. 5.2. Figure 5.24 shows an averaged pulse shape produced by impact of 25-keV N^+ particles onto the COMPACT detector at room temperature. Despite the long signal line connecting the anode in the UHV chamber to the decoupler/preamplifier circuitry on the atmosphere side of CSR, the signal is followed by only little ringing, allowing for a low discrimination threshold of a few 10 mV. As described in Sect. 5.1.5, the signal is measured after a 50-Ω current-sensitive amplifier with a gain factor of 200. By integration, the number of electrons which created the pulse on the anode can roughly be estimated from the pulse shape of Fig. 5.24 to be $2{\times}10^6$. Assuming a gain of $5\,(3){\times}10^5$ for the MCP-stack, the average number of secondary electrons impinging onto the MCP surface is derived to be $\gamma\varepsilon_c = 10\,(6)$ (cf. Sect 5.2.2.1).

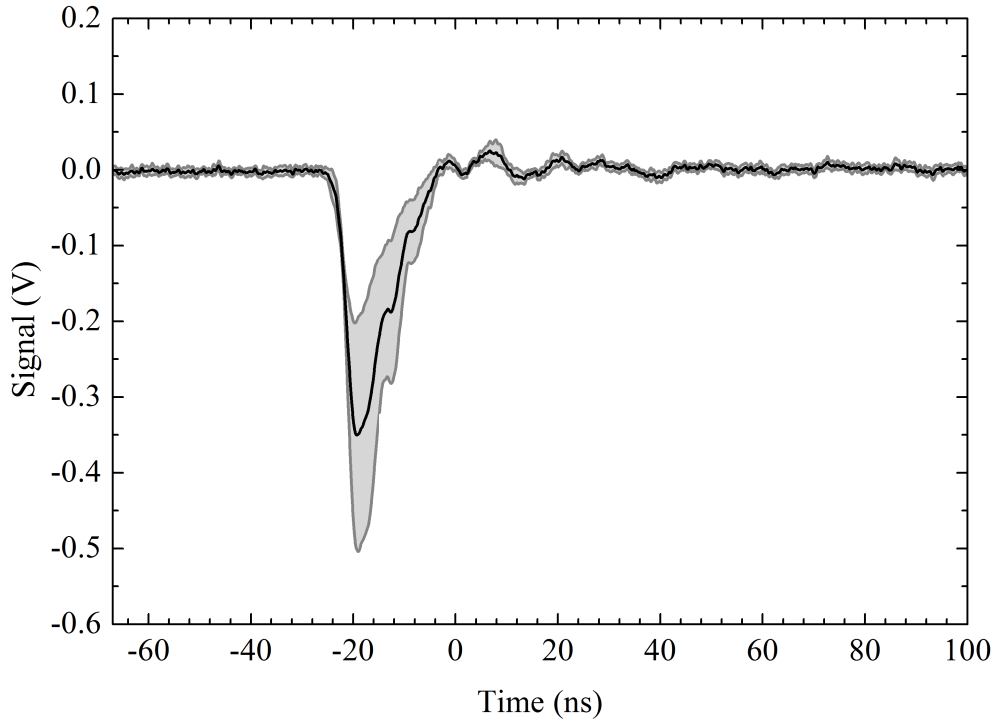

Figure 5.24.: An averaged anode pulse shape obtained from 25-keV N^+ ions impinging onto the detector. After decoupling from the high voltage of the anode, the current pulses were driven into a 50-Ω resistor and amplified by a factor of 200 to yield the voltage pulses shown here (cf. Sect. 5.1.5). The signal quality allows for a low discrimination threshold of few 10 mV.

5.3.1.1. Ion-Beam Lifetime Measurements at 300 K

The lifetime of the stored N_2^+-beam was measured by monitoring the count rate of N^+ product particles versus storage time. Count rates of up to 10^5 s^{-1} were recorded directly after injection, followed by an exponential decay due to the decreasing stored ion current. A lifetime of $\tau = 1.12\,(2)$ ms was derived from the measured curve in Fig. 5.25. This lifetime which matches the anticipated lifetime of the ions due to residual-gas collisions (Eq. 3.8). The data are averaged over several thousand individual ion injections into the storage ring. After 15 ms, corresponding to ∼250 revolutions of the stored ion bunch, the measured count rate vanished, revealing that the EDR MCP stack is effectively free of any dark count rate, even during room-temperature operation.

The injected N_2^+ beam had a bunch length of only 29 m, corresponding to 80% of the 35.4-m closed-orbit circumference of CSR. This caused a sharp modulation in the count rate of the detector, as seen in Fig. 5.26. In addition betatron oscillation cause a weaker modulation of the measured count rate since the amplitude of the oscillation

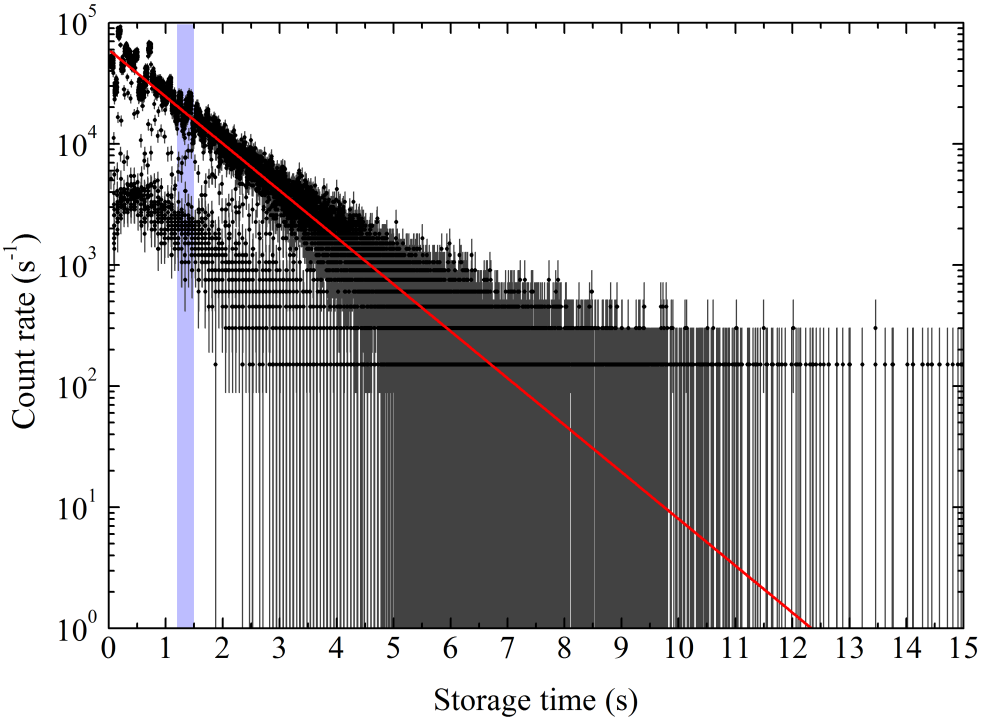

Figure 5.25.: Lifetime measurement for a 25-keV N_2^+ beam stored in CSR. The count rate of N^+ product particles (black dots) from residual-gas collisions onto the detector was measured as a function of storage time. The dark-grey error bars indicate the counting statistical uncertainty. The red line is an exponential decay fit of the stored ion beam with lifetime $\tau = 1.12\,(2)$ ms.

is larger than the detector acceptance. This is due to a slight misalignment of the injected beam during these first CSR experiments.

5.3.1.2. Pulse Height Spectrum

Based on the model for the secondary-electron multiplication and detection developed in Sect. 5.2.2.1, some level of understanding of the pulse height distribution measured in the experiment on collisional dissociation of N_2^+ can be obtained. Considering our results of Sect. 5.2.2.2, it can be assumed that an impinging 25-keV N^+ ion released on the average several secondary electrons γ from the converter cathode, of which, in average, $\tilde{\gamma}$ impinge onto the MCP input electrode. Since the parent beam of N_2^+ was uncooled, the daughter particles N and N^+ were expected to irradiate the full sensitive area of the sensor, hence the number k of secondary electrons triggering an avalanche in the MCPs is then governed by the Pólya statistics given in Eq. 5.4. The pulse height spectrum is characterised by the electric response of the MCP stack to these k electron avalanches. In order to deduce $\tilde{\gamma}$ from the

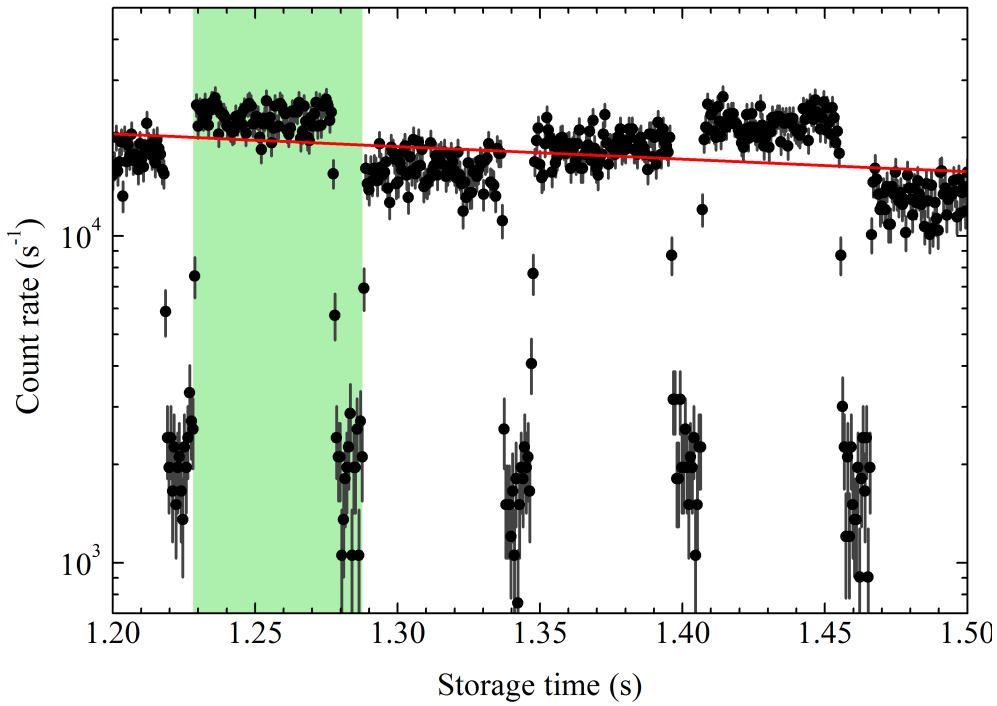

Figure 5.26.: The periodic, sharp modulation of the measured N^+ count rate (black dots) is a characteristic of the bunched beam passing the detector only during 80% of one revolution. One period of revolution is exemplarily indicated by the green, shaded area. The modulation in the amplitude between the revolutions is believed to stem from betatron oscillations, as explained in the text. The figure is a close-up of the shaded area in Fig. 5.25.

experimental data of N^+, knowledge of the pulse height spectrum for exactly $k = 1$ electrons triggering an electron avalanche in the MCPs is needed.

An ultraviolet (UV) AlGaN light emitting diode (LED, *SETi* UVTOP 240) is permanently installed in CSR in the corner section preceding the future electron cooler. For testing purposes, the diode can irradiate the COMPACT and NICE [126] detectors by an uncollimated beam of 245-nm photons. Since the photon energy of 5.1 (1) eV allows only to eject a maximum of one single electron from the converter cathode, no more than $k = 1$ avalanches can be triggered in the MCPs. The UV diode can hence be used to measure the required single-electron pulse height spectrum.

With f_1 being the pulse height spectrum corresponding to the $k = 1$ electron avalanche triggered in the MCPs, the response for precisely $k = 2$ electron cascades is given by the convolution $f_2 = f_1 * f_1$, and for precisely k cascades by $f_k = f_1 * f_{k-1}$. The theoretical pulse height spectrum F for N^+ ions can thus be

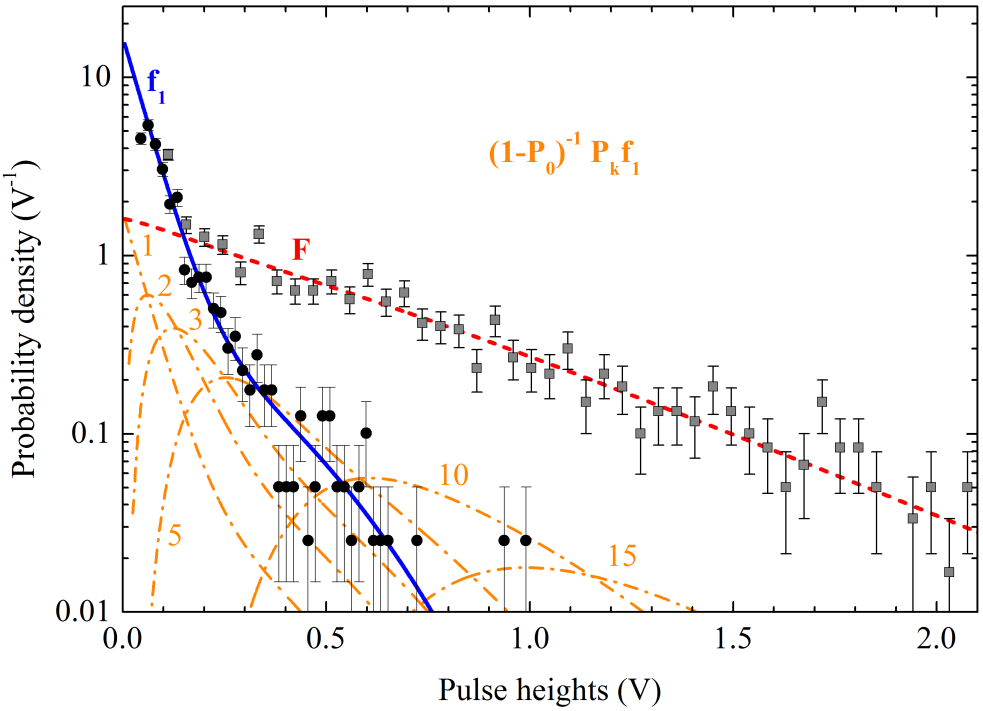

Figure 5.27.: Measured pulse height spectra for UV irradiation (filled circles) and for 25-keV N^+ ions (filled squares). The solid, blue curve (f_1) is a fit to the UV-induced single secondary-electron spectrum. The dashed red line (F) is modelled from the latter assuming Pólya-distributed secondary-electron numbers k. Some individual contributions $P_k f_k$ (dot-dashed, orange lines) are labelled 1 to 15 (see text).

modelled from the measured single-electron detector response f_1 as

$$F = (1 - P_0)^{-1} \times \sum_{k=1}^{\infty} P_k f_k \tag{5.12}$$

where the values of P_k are given by Eq. 5.5 as a function of the parameters $\tilde{\gamma}$ and b. The normalisation factor $(1 - P_0)^{-1}$ accounts for the non-vanishing probability (P_0) for an ion to produce no signal.

Figure 5.27 shows the normalised pulse height spectra derived from the measured MCPs response for UV photons and N^+ particles. Empirically, the UV response is found to be well reproduced by the sum of an exponential decay and a Gaussian centred at zero. The modelled pulse height spectrum F for N^+ particles is derived from f_1 by numerically computating the convolutions f_k up to $k = 150$. By fitting Eq. 5.12 to the data, the best agreement between experiment and model is obtained for $\tilde{\gamma} = 10\,(1)$ and $b = 0.8\,(2)$ (see Eq. 5.5). The uncooled, broad particle beam was

expected to have irradiated a large area of the converter cathode. A large value of b was therefore to be expected. Since the Pólya parameter b is the relative variance [176] of the distribution of $\gamma\varepsilon_c$, this corresponds roughly to values $\gamma\varepsilon_c \approx 10\,(9)$ across the entire converter cathode area for 25-keV N^+ particles. This value is in agreement with the value of $\gamma\varepsilon_c \approx 10\,(6)$ estimated from the pulse shape shown in Fig. 5.24.

It should be noted that the model fit function F depends quite strongly on the low-energy part (≤ 50 mV) of f_1 which, as visible in Fig. 5.27, has not been measured but extrapolated. Hence, the model for F is bound to a large systematic uncertainty. Still, it seems that basic understanding of the pulse height spectra can be obtained from Eq. 5.5. Moreover, this modelling provides another evidence that keV/u-ions are detected with practically 100% detection efficiency. The measured pulse height spectrum for 25-keV N^+ shows that the loss in detection efficiency by a discrimination threshold of a few 10 mV is only small (a few 10^{-2}).

5.3.2. Cryogenic Operation

In early 2015, CSR was prepared for the commissioning at cryogenic temperatures. Prior to cooling, the storage ring was baked at a temperature of 180°C and the NEG pumps were activated. The CSRs pumping facilities had been installed completely, and consequently the residual-gas pressure was much lower (1×10^{-10} mbar at room temperature after bakeout) than in the initial test phase (Sect. 5.3.1). While CSR was cooled to its cryogenic operating temperature, the diagnostic systems and the detector array, consisting of the COMPACT and NICE detectors, were characterised using a stored 60-keV Ar^+ beam. First, preliminary results are presented in the following sections.

At an ambient temperature of 5 K, COMPACT was moved along the full length of the translation stage several times, showing that the cryogenic thread drive (see Sect. 5.1.3.2) can safely be operated at such low temperatures. While moving the detector, the temperature of the vacuum chamber locally rose by less than 1 K. Once the detector was at rest and the intermediate rotary drive was decoupled, the chamber cooled down to its initial temperature.

5.3.2.1. Storage Times of a 60-keV Ar^+ Beam at Different Temperatures of CSR

COMPACT was used to determine the lifetime of the stored 60-keV Ar^+ beam at several temperatures of the beam-guiding vacuum chamber. Products from collisions between the ion beam and the residual-gas particles were monitored as a function of

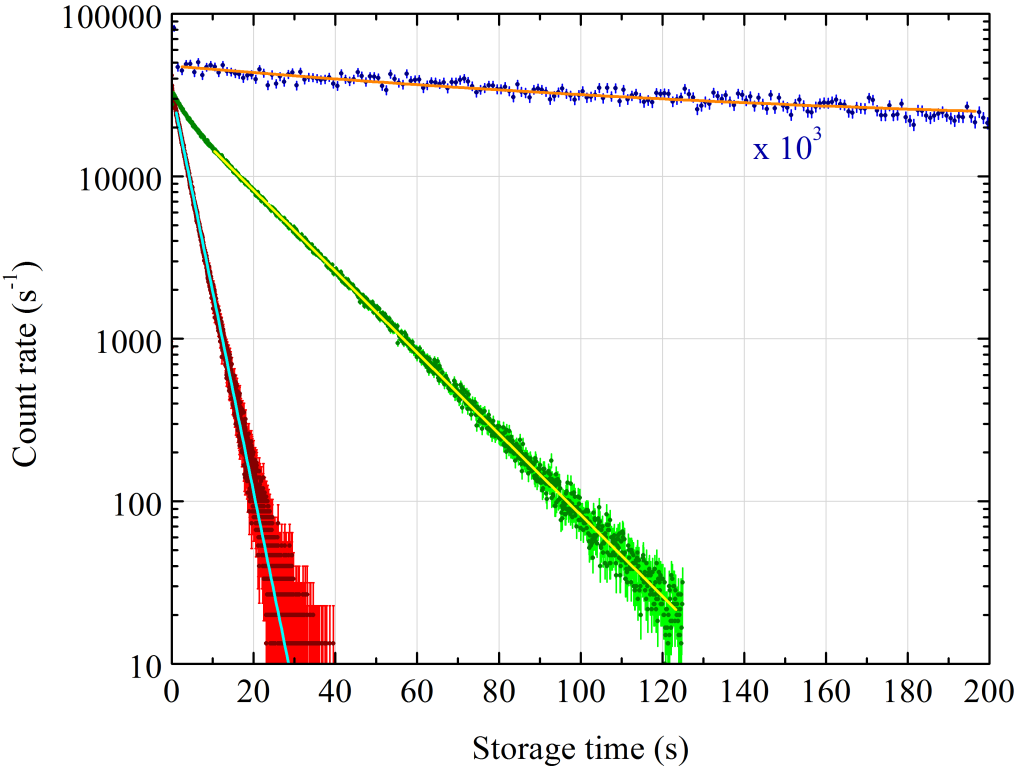

Figure 5.28.: Beam lifetime measurements of 60-keV Ar^+ stored at different temperatures of CSR. The red dots are the lifetime measurements performed at a storage ring temperature of 260 K, the green dots are the measurements at 110 K, and the blue dots represent the lifetime measurement at an ambient temperature of about 5 K. For better illustration, the data of the 5-K measurement are multiplied by a factor of 10^3. The error bars represent the counting statistical error bars. During cooling of the storage ring, the lifetime increased from about 3.52 (1) s at 260 K to about 276 (7) s at 5 K. The (cyan, yellow, and orange) lines are the exponential decays fitted to the data obtained at a temperature of 260 K, 110 K, and 5 K, respectively.

storage time. Figure 5.28 shows the obtained beam-decay curves at chamber temperatures of 260 K, 110 K, and 5 K. Each data set was generated by averaging over a few injection cycles. The beam lifetimes were determined by fitting an exponential decay function to the data points. The background count rate was measured independently by dumping the remaining ion beam at the end of each measurement. The beam lifetimes obtained from the measurements, shown in Fig. 5.28, were 3.52 (1) s, 17.4 (2) s, and 276 (7) s at chamber temperatures of 260 K, 110 K, and 5 K, respectively. Since the analysis of systematic uncertainties is still ongoing, the given error bars represent only the standard error of the numerical fit.

At chamber temperatures above 100 K, the lifetimes were determined by monitoring neutral Ar particles, formed by electron capture of Ar^+, on the COMPACT detector (red and green data sets in Fig. 5.28). Towards lower temperatures, the production rate of neutral Ar particles decreased due to the decreasing residual-gas particle density caused by cryo-absorption at the cold surfaces. Consequently, the lifetime of the stored Ar^+ beam increased. At a temperature of 5 K, the rate of neutral Ar particles generated within the straight, future electron cooler section was too low to be detected. This indicates that in this section the residual gas density was very low. However, right in front of the detector, a vacuum tube connecting the cold, beam-guiding vacuum chamber to a room-temperature ion-getter pump, generated a gas target in close vicinity of the detector. Residual-gas particles which were ionised by the stored Ar^+ beam had a small probability of reaching COMPACT and could thus be used as a proxy signal for the beam lifetime. The beam decay curve which was obtained from this beam-induced signal is shown in Fig. 5.28 (blue data points).

5.3.2.2. Pulse Height Spectra

The pulse heights generated in the MCPs were analysed for different CSR temperatures. Pulse height distributions, both for 60-keV Ar particles and for UV photons, were recorded at ambient temperatures of 200 K and 10 K, respectively. As visible in Fig. 5.29, neither the distribution for high-energetic Ar particles nor the distributions of the UV photons changed significantly with temperature. Thus, it can be concluded that at the given count rates, electron depletion of the MCPs due to their high resistance at 10 K cryogenic temperatures does not compromise the operation of the detector.

5.3.2.3. Cryogenic Heating Element

Despite of the fact that the detector operated successfully also at very low temperatures, the function of the MCP heating element was tested. By application of a heating power of 80 mW, the MCP resistance dropped in one hour from the initially $\sim$100 GΩ to $\sim$10 GΩ. Using the calibration curve of Fig. 5.16, a temperature of the MCP of approximately 35 K can be derived. Heating of the MCP might be helpful once the detector operates at higher count rates.

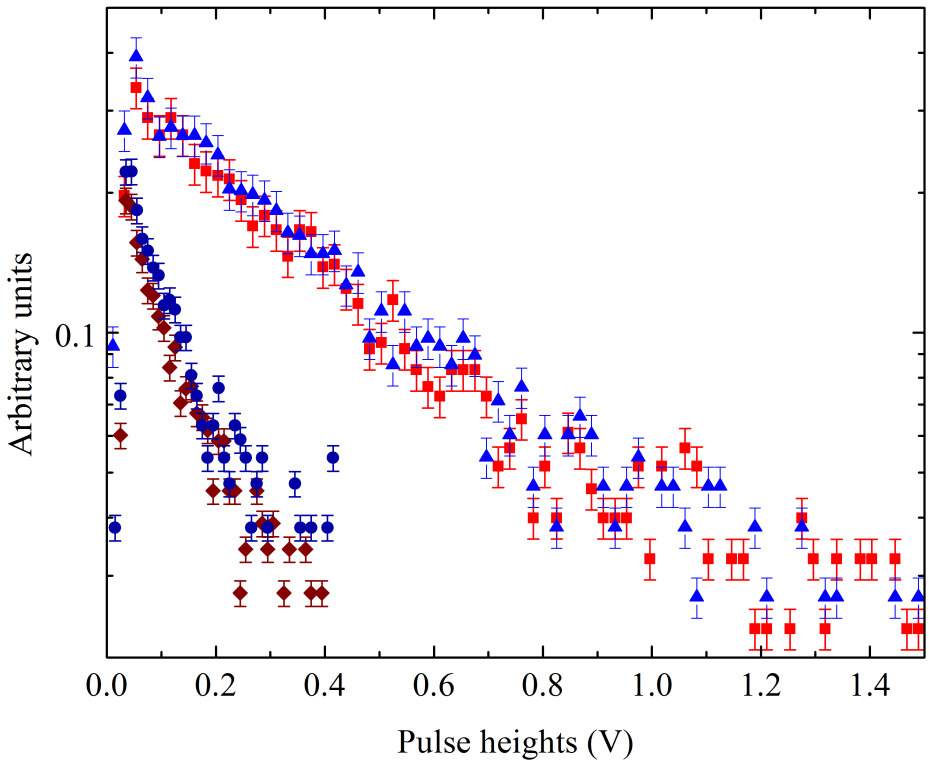

Figure 5.29.: Pulse height distributions of 60-keV Ar particles and UV photons at COMPACT. The red squares and the light-blue triangles represent the pulse height distributions for the high-energetic Ar particles, measured at CSR temperatures of 200 K and 10 K, respectively. The blue filled circles and the brown diamonds correspond to the pulse height distribution induced by UV photons irradiation at the same temperatures.

5.4. Summary and Outlook

A movable, single-particle counting detector for the CSR has been developed, characterised, and successfully commissioned. This 'COMPACT' detector consists of a translation stage and a particle sensor which is based on secondary-electron detection by an MCP-anode stack. The design is suitable for operation in a cryogenic ultra-high vacuum environment and bakeable to high (250°C) temperature.

The collection efficiency of the sensor has been simulated and experimentally investigated. At the typical beam energies of CSR a detection efficiency close to 100% can be expected.

In order to provide reliable operation at cryogenic temperatures, a small heating element for locally raising the MCP temperature, has been integrated. After a series of

offline tests had shown that the detector is suitable for cryogenic operation, COMPACT was successfully integrated into CSR and operated at ambient temperatures of less than 10 K.

Cryogenic operation tests on the TSR-type CEM detectors revealed that variants of these secondary-electron multipliers may be equally suitable for CSR operation. CEMs are therefore considered as candidates for detector sensors at other positions in CSR. The COMPACT translation stage is in principle capable of carrying various kinds of sensors. In the present design, the stage provides five power connections to the sensor. This number could easily be enlarged to six or seven with only small modifications.

Along with the CSR electron cooler, a second COMPACT-type detector will be integrated at position (4a) of Fig. 5.1. This detector will be able to count daughter particles with high relative changes in charge-to-mass ratio η. Since the impact angles of the product particles are then larger than at position (4b), the new detector sensor at position (4a) will feature a broader detection window. Also at the future ion-neutral interaction experiment variants of the COMPACT detector will be used to detect product particles at positions (4a) and (4b), Fig. 5.1.

6. Conclusion and Outlook

On two different examples, this work has laid out how heavy-ion storage rings can be used to address problems of plasma physics. The studies were performed during a transient, but technically and experimentally very interesting, phase in scientific research on stored ion beams at the Max Planck Institute for Nuclear Physics. This work involved both, the now decommissioned storage ring TSR as an example of a traditional high-energy experimental platform, and the new cryogenic and electrostatic storage ring CSR which, in Heidelberg, marks the onset of a new era of research on mainly low-energetic ionic processes.

As it has been shown in Chapter 2, experimental studies of electron-ion recombination processes are needed to predict ion charge balances as a function of statistical properties of a high-temperature plasma. Using the well-established, merged electron-ion beams set-up at the storage ring TSR, absolute recombination rate coefficients of highly-charged tungsten ions W^{q+} (q = 18,19,21) for collision energies of up to few 100 eV could be obtained (Chapter 4). The corresponding, experimentally derived plasma rate coefficients show the deficits of the wide-spread but over-simplified model that is currently used to calculate theoretical plasma recombination rate coefficients for predicting tungsten charge balances in tokamak plasmas. In a fruitful interplay between experimental and theoretical physics, the data has also been used to probe new, more reliable numerical predictions of the recombination rate coefficients for such open-f shell ions.

With the Heidelberg Tandem Van-De-Graff injector and the storage ring TSR decommissioned at the end of 2012, further measurements on highly-charged tungsten ions must be conducted at different accelerator laboratories. One opportunity could be the planned re-commissioning of TSR at the ISOLDE facility of CERN [81]. Though the main focus of that project lies in the use of TSR as an accumulation and storage ring for radioactive nuclei, a charge breeder may enable experiments on highly-charged stable ions as part of a secondary scientific program.

The adaption of the proven experimental techniques used at TSR to the newly commissioned CSR facility is challenging, mainly due to the cryogenic operating temperature and the much lower ion energies of the new storage ring. The movable, cryogenic single-particle detector, which has been developed and tested within this work, will be part of the new merged electron-ion beams facility at CSR. The COMPACT detector, presented in Chapter 5, has shown to be a reliable and powerful

instrument for single, low-energetic particle detection in a cryogenic environment. The storage ring's electrostatic bending elements along with the movable detector sensor serve as a product mass spectrometer for collision and photon interaction studies with charged molecular and atomic ions.

While in the early commissioning experiments reported here, only naturally occurring residual-gas molecules could act as collision partners, implementation of the CSR electron cooler will enhance the set-up into a platform for precision experiments on electron-ion collisions. Further experimental facilities at CSR, like the ion-neutral-atom merged-beams interaction section and a supersonic jet target experiment, that are currently being developed, require fast product particle sensors similar to the one developed in this work. Hence, based on the results presented in this work, variants of the COMPACT detector set-up are currently being developed.

In the foreseeable future CSR will be the only cryogenic storage ring featuring a fully functional electron cooler. It provides unique possibilities for ambitious studies of electron-ion collisions, which are very difficult in standard laboratory environments due to thermal radiation or short beam storage times. Examples are the dissociative recombination of rovibrational ground-state molecular ions or the dielectronic recombination of singly-charged atomic ions. Also these futures studies are expected to deliver data that is important for reliable modelling of steady states and evolution of plasmas–with emphasis now on low-temperature environments like the cold cores of interstellar molecular clouds.

The CSR storage ring and accelerator are, however, flexible enough to enable research outside that primary experimental program. Installation of an electron cyclotron resonance (ECR) ion source at the CSR injector will allow to produce highly-charged ions, which can be stored for long times due to the extremely good vacuum conditions of the cryogenic environment. Together with the merged electron-ion beams set-up and COMPACT-type highly efficient single-particle detectors, this will enable a continuation of the experimental work also on electron-ion collision processes relevant for high-temperature plasma environments.

Appendices

A. A Program for Computation of Level Populations

The initial level populations for the measured tungsten charge states were computed using *WOLFRAM MATHEMATICA* (Sect. 4.1.1). The program code is provided in the following.

```
(* Reads a file *.oic containing radiative transition rates
and plots state populations as function of time *)

(* The content of the *.oic-file is assumed to be organized
as follows *)

(* 1st line: <nstates> [number of states] *)
(* 2nd line: arbitrary content (ignored)*)
(* next <nstates> lines: K LV T 2S+1 L 2J CF (EK-E1)/RY *)
(* next 2 lines: arbitrary content (ignored) *)
(* all subsequent lines: *)
(* CF LV W CF LV W AR*SEC DEL(RYD) E-G(RYD) *)


(* some energy coversion factors *)
Ryd2eV = 13.6057; (* Rydberg -> eV *)
Icm2eV = 1.24E-4; (* inverse cm -> eV *)


filename = SystemDialogInput[``FileOpen'', ``*.oic''];
fin = OpenRead[filename];
nstates = Read[fin, Number]; (* number of states *)
Read[fin, String];
states = ReadList[fin, {Number, Number, Number, Number,
Number, Number, Number, Number}, nstates];
(* state information *)
Read[fin, String];
rates = ReadList[fin, {Number, Number, Number, Number,
```

```
Number, Number, Number, Number}]; (* transition rates *)
Close[fin];

nstates = Input[``number of states:'', nstates];
nrates = Length[rates];

(* sort rates into a matrix *)
Clear[A, sumA];
A = Array[0 &, {nstates, nstates}];
sumA = Array[0 &, nstates];
For[i = 0, i < nrates, i++;
 If[Mod[i, 10000] == 0, Print[i]];
 nini = Position[states[[All, 2]], rates[[i, 2]], 1]
[[1]][[1]];
  If[nini > nstates, Continue[]];
 nfin = Position[states[[All, 2]],rates[[i, 5]], 1]
[[1]][[1]];
  If[nfin > nstates, Continue[]];
 Arad = Abs[rates[[i, 7]]];
 A[[nfin, nini]] += Arad;
 sumA[[nini]] += Arad;
]
A += DiagonalMatrix[-sumA];

(* display 10 x 10 submatrix for visual inspection *)
MatrixForm[A[[1 ;; 10, 1 ;; 10]]]

(* export lifetimes to file *)
lsymb = {S, P , D, F, G, H, I, K, L, M, N, O, Q, R, T, U,
V, W, X, Y, Z};
levfilename = StringJoin[DirectoryName[filename],
FileBaseName[FileNameTake[filename]], ``_lev.dat''];
Export[levfilename, Table[{states[[i, 1]], states[[i, 2]],
states[[i, 3]], StringJoin[ToString[Abs[states[[i, 4]]]],
ToString[lsymb[[1 + states[[i, 5]]]]], ToString[states[[i,
6]]* 0.5]], states[[i, 7]],Ryd2eV * states[[i, 8]],
FortranForm[1.0/sumA[[i]]]}, {i, 1, nstates}]];


EnergyConversion = Ryd2eV;

(* specify initial populations: Boltzmann or statistical *)
```

```
kbT = Input[``Electron temperture at stripping (eV, 0
results in statistical populations):'', 0];
IF[kbT > 0,
 X0 = Table[(states[[i, 6]] + 1) * Exp[-states[[i, 8]] *
 EnergyConversion/kbT], {i, 1, nstates}],
 (* Boltzmann distribution *)
 X0 = Table[(states[[i, 6]] + 1), {i, 1, nstates}]];
(* statistical populations *)
X0 /= Total[X0]; (* nomalise initial values *)

(* set up system system of rate equations *)
(* vector with elements y_i[t] *)
X[t_] = Map[Subscript[y, #][t]&, Table[i, {i, 1, nstates}]];
(* rate equations *)
system = MapThread[#1 == #2 &, {X'[t], A.X[t]}];
(* initial population values *)
initial = MapThread[#1 == #2 &, {X[0], X0}];
TableForm[Table[{initial[[i]], system[[i]]}, {i, 1,
nstates}], TableAlignments -> {Left, Center},
TableSpacing -> {2, 5}];


(* solutions of the rate equations *)
analytic_flag := TRUE;
If[TrueQ[analytic_flag],{sol = Simplify[DSolve[{system,
initial}, X[t], t]];
Column[sol[[1, All]], Alignment -> Left, Spacings -> 2]},
sol = NDSolve[{system, initial}, X[t], {t, 0, 100},
Method -> {``EquationSimplification'' -> ``Solve''}]];


levels = {1, 4, 5, 6, 7, 8, 9, 10, 28, 29, 34, 46, 71 ,74};

Off[General::ovfl, General::unfl, InterpolatingFunction::
dmval, InterpolatingFunction::dprec];

levsymb = Table[StringJoin[``\!\ ( \ (\ )\ ^'',
ToString[Abs[states[[i,4]]]], ``\ )\! \ ('',
ToString[lsymb[[1 + states[[i,5]]]]], ``\_ \('',
ToString[states[[i,6]]], ``/2 \) \)''], {i, levels}];

strlabel = If[kbT > 0,strlabel = StringJoin[k_BT = ,
```

```
ToString[kbT], ``eV''], ``statistical population'']];
strlabel = StringJoin[FileNameTake[filename],`` \ n'',
ToString[nstates], ``states \ n'', strlabel, `` \ n'']];

popplot = LogLogPlot[{Evaluate[X[t][[levels]]/.sol]},
{t, 10^-3, 10^2}, PlotRange -> {{10^-3, 10^2}, {10^-3, 2.0}},
PlotLegends -> LineLegend[levsymb, LegendLabel -> strlabel,
LabelStyle -> Small], ImageSize -> Scaled[0.8], Frame ->
True, FrameLabel -> {``Time (s)'', ``Level population''},
LabelStyle -> {FontFamily -> Helvetica}, Background -> None]

(* compose file name *)
plotfilename = StringJoin[DirectoryName[filename],
 FileBaseName[FileNameTake[filename]], ``_'',
ToString[nstates], ``_'', ToString[kbT]];

(* save plot in pdf format *)
Export[StringJoin[plotfilename, ``.pdf''], popplot];

(* save data in ascii format *)
Export[StringJoin[plotfilename, ``.dat''], Table[{
FortranForm[t], FortranForm[Evaluate[X[t][[levels]]]/.sol],
FortranForm[Evaluate[Sum[X[t][[i]], {i, 1, nstates}]/.sol]]},
{t, Table[10^(0.2x), {x, -50, 10}]}], ``CSV''];
```

Bibliography

[1] S. Schippers. private communication, (2015). 22

[2] L. De Broglie, "Recherches sur la théorie des Quanta.", *Ann. Phys. (Paris)*, **3**, 22-128, (1925). 21

[3] P. Debye, "Introductory paper – part I: Mobilities of ions. Report on conductivity of strong electrolytes in dilute solutions", *Trans. Faraday Soc.*, **23**, 334-340, (1927). 22

[4] A. D. Whiteford, *On the spectral emission of impurity species for diagnostic application to magnetically confined fusion plasmas*. PhD thesis, University of Strathclyde, (2004). 23

[5] D. W. Savin, "Ionization and recombination with electrons: Laboratory measurements and observational consequences", *AIP Conf. Proc.*, **774**, 297, (2005). 23

[6] T. Pütterich, *Investigations on Spectroscopic Diagnostic of High-Z Elements in Fusion Plasmas*. PhD thesis, University of Augsburg, Germany, (2005). 24, 26, 80, 84, 86, 95, 96, 99

[7] S. D. Loch, J. A. Ludlow, M. S. Pindzola, A. D. Whiteford, and D. C. Griffin, "Electron-impact ionization of atomic ions in the W isonuclear sequence", *Phys. Rev. A*, **72**, 052716, (2004). 24

[8] H. P. Summers and M. G. O'Mullane, *Nuclear Fusion Research: The atomic data and analysis structure*. Springer Verlag, (2005). 24

[9] H. P. Summers and R. W. P. McWhirter, "Radiative power loss from laboratory and astrophyical plasmas. I. Power loss from plasmas in steady-state ionisation balance", *J. Phys. B*, **12**, 2387, (1979). 25

[10] H. Zohm, C. Angioni, R. Arslanbekov, C. Atanasiu, G. Becker, W. Becker, K. Behler, K. Behringer, A. Bergmann, R. Bilato, V. Bobkov, D. Bolshukhin, T. Bolzonella, K. Borrass, M. Brambilla, F. Braun, A. Buhler, A. Carlson, G. Conway, D. Coster, R. Drube, R. Dux, S. Egorov, T. Eich, K. Engelhardt, H.-U. Fahrbach, U. Fantz, H. Faugel, K. Finken, M. Foley, P. Franzen,

J. Fuchs, J. Gafert, K. Fournier, G. Gantenbein, O. Gehre, A. Geier, J. Gernhardt, T. Goodman, O. Gruber, A. Gude, S. Günter, G. Haas, D. Hartmann, B. Heger, B. Heinemann, A. Herrmann, J. Hobirk, F. Hofmeister, H. Hohenöcker, L. Horton, V. Igochine, A. Jacchia, M. Jakobi, F. Jenko, A. Kallenbach, O. Kardaun, M. Kaufmann, A. Keller, A. Kendl, J.-W. Kim, K. Kirov, R. Kochergov, H. Kollotzek, W. Kraus, K. Krieger, T. Kurki-Suonio, B. Kurzan, P. Lang, C. Lasnier, P. Lauber, M. Laux, A. Leonard, F. Leuterer, A. Lohs, A. Lorenz, R. Lorenzini, C. Maggi, H. Maier, K. Mank, M.-E. Manso, P. Mantica, M. Maraschek, E. Martines, K.-F. Mast, P. McCarthy, D. Meisel, H. Meister, F. Meo, P. Merkel, R. Merkel, D. Merkl, V. Mertens, F. Monaco, A. Mück, H. Müller, M. Münich, H. Murmann, Y.-S. Na, G. Neu, R. Neu, J. Neuhauser, F. Nguyen, D. Nishijima, Y. Nishimura, J.-M. Noterdaeme, I. Nunes, G. Pautasso, A. Peeters, G. Pereverzev, S. Pinches, E. Poli, M. Proschek, R. Pugno, E. Quigley, G. Raupp, M. Reich, T. Ribeiro, R. Riedl, V. Rohde, J. Roth, F. Ryter, S. Saarelma, W. Sandmann, A. Savtchkov, O. Sauter, S. Schade, H.-B. Schilling, W. Schneider, G. Schramm, E. Schwarz, J. Schweinzer, S. Schweizer, B. Scott, U. Seidel, F. Serra, S. Sesnic, C. Sihler, A. Silva, A. Sips, E. Speth, A. Stäbler, K.-H. Steuer, J. Stober, B. Streibl, E. Strumberger, W. Suttrop, A. Tabasso, A. Tanga, G. Tardini, C. Tichmann, W. Treutterer, M. Troppmann, H. Urano, P. Varela, O. Vollmer, D. Wagner, U. Wenzel, F. Wesner, E. Westerhof, R. Wolf, E. Wolfrum, E. Würsching, S.-W. Yoon, Q. Yu, D. Zasche, T. Zehetbauer, and H.-P. Zehrfeld, "Overview of ASDEX Upgrade results", *Nucl. Fusion*, **43**, 1570, (2003). 25

[11] J. G. Matthews and the ASDEX-Upgrade Team, "Plasma operation with an all metal first-wall: Comparison of an ITER-like wall with a carbon wall in JET", *J. Nucl. Mater.*, **438**, S2-S10, (2010). 25

[12] R. A. Pittsa, S. Carpentier, F. Escourbiac, T. Hirai, V. Komarov, S. Lisgo, A. S. Kukushkin, A. Loarte, M. Merola, A. Sashala Naik, R. Mitteau, M. Sugihara, B. Bazylev, and P. Stangeby, "A full tungsten divertor for ITER: Physics issues and design status", *J. Nucl. Mater.*, **438**, S48-S56, (2013). 25

[13] ITER Group, "Overview and summary", *Nucl. Fusion*, **39**, 2137, (1999). 25

[14] R. Aymar, P. Barabaschi, and Y. Shimomura, "The ITER design", *Plasma Phys. Control. Fusion*, **44**, 519, (2002). 25

[15] T. Pütterich, R. Neu, R. Dux, A. Whiteford, M. O'Mullane, and the ASDEX Upgrade Team, "Modelling of measured tungsten spectra from ASDEXUpgrade and predictions for ITER", *Plasma Phys. Control. Fusion*, **50**, 085016, (2008). 25

[16] R. Neu, V. Bobkov, R. Dux, J. C. Fuchs, O. Gruber, A. Herrmann, A. Kallenbach, H. Maier, M. Mayer, T. Pütterich, V. Rohde, A. C. C. Sips, J. Stober,

K. Sugiyama, and the ASDEX Upgrade Team, "Ten years of W programme in ASDEX Upgrade - challenges and conclusions", *Phys. Scr.*, **T138**, 014038, (2009). 25

[17] R. Neu, the ASDEX Upgrade Team, the EU PWI Taskforce, and the JET EFDA Contributors, "Preparing the scientific basis for an all metal ITER", *Plasma Phys. Control. Fusion*, **53**, 124040, (2011). 25

[18] V. Philipps, "Tungsten as material for plasma-facing components in fusion devices", *J. Nucl. Mater.*, **415**, S2-S9, (2011). 25

[19] www.iter.org. 26

[20] R. A. Pitts, A. Kukushkin, A. Loarte, A. Martin, M. Merola, C. E. Kessel, V. Komarov, and M. Shimada, "Status and physics basis of the ITER divertor", *Phys. Scr.*, **T138**, 014001, (2009). 26

[21] T. Pütterich, R. Neu, R. Dux, A. Whiteford, M. O'Mullane, H. Summers, and the ASDEX Upgrade Team, "Calculation and experimental test of the cooling factor of tungsten", *Nucl. Fusion*, **50**, 025012, (2010). 25

[22] C. Breton, C. de Michelis, M. Finkenthal, and M. Mattioli, "Ionization equilibrium of selected elements from neon to tungsten of interest in tokamak plasma research", *EUR-CEA-FC–948*, **10**, 18, (1978). 25

[23] J. Abdallah Jr., J. Colgan, R. E. H. Clark, C. J. Fontes, and H. L. Zhang, "A collisional-radiative study of low temperature tungsten plasma", *J. Phys. B*, **44**, 075701, (2011). 25

[24] R. P. Doerner, M. J. Baldwin, and P. C. Stangeby, "An equilibrium model for tungsten fuzz in an eroding plasma environment", *Nucl. Fusion*, **51**, 043001, (2011). 25

[25] H. P. Summers, "ADAS users manual", *JET-IR*, **06**, (1994). 25, 77, 78, 80, 81, 84, 85, 86, 95, 96

[26] N. R. Badnell, M. G. O'Mullane, H. P. Summers, Z. Altun, M. A. Bautista, J. Colgan, T. W. Gorczyca, D. M. Mitnik, M. S. Pindzola, and O. Zatsarinny, "Dielectronic recombination data for dynamic finite-density plasmas I. Goals and methodology", *Astron. Astrophys.*, **406**, 1151–1161, (2003). 25, 33

[27] A. Burgess, "A general formula for the estimation of dielectronic recombination co-efficients in low-density plasmas.", *Astrophys. J.*, **141**, 1588, (1965). 26, 32

[28] D. Smith, "The ion chemistry of interstellar clouds", *Chem. Rev.*, **92**, 1473-1485, (1992). 27

[29] I. W. M. Smith, ed., *Low Temperatures and Cold Molecules*. Imperial College Press, (2008). 27

[30] W. W. Dudley and D. A. Williams, *Interstellar Chemistry*. Academic Press, (1984). 27

[31] A. G. G. M. Tielens, *The Physics and Chemistry of the Interstellar Medium*. Cambridge Univ. Press, (2005). 27

[32] E. Herbst, "The chemistry of interstellar space", *Chem. Soc. Rev.*, **30**, 168-176, (2001). 27

[33] J. Lyman Spitzer, *Physical Processes in the Interstellar Medium*. WILEY-VCH Verlag GmbH & Co. KGaA, (2004). 27

[34] P. Bryans, H. Kreckel, E. Roueff, V. Wakelam, and D. W. Savin, "Molecular cloud chemistry and the importance of dielectronic recombination", *Astrophys. J.*, **694**, 286-293, (2009). 27

[35] N. R. Badnell, "Radiative recombination data for modeling dynamic finite-density plasmas", *Astrophys. J.*, **167**, 334, (2006). 27

[36] T. Quinteros, H. Gao, D. R. DeWitt, R. Schuch, M. Pajek, S. Asp, , and D. Belkić, "Recombination of D^+ and He^+ ions with low-energy free electrons", *Phys. Rev. A*, **51**, 1340, (1995). 27

[37] A. A. Saghiri, J. Linkemann, M. Schmitt, D. Schwalm, A. Wolf, T. Bartsch, A. Hoffknecht, A. Müller, W. G. Graham, A. D. Price, N. R. Badnell, T. W. Gorczyca, and J. A. Tanis, "Dielectronic recombination of ground-state and metastable Li^+ ions", *Phys. Rev. A*, **60**, R3350(R), (1999). 27

[38] T. Mohamed, D. Nikolić, E. Lindroth, S. Madzunkov, M. Fogle, M. Tokman, and R. Schuch, "Dielectronic recombination of lithiumlike beryllium: A theoretical and experimental investigation", *Phys. Rev. A*, **66**, 022719, (2002). 27

[39] T. P. Snow and V. M. Bierbaum, "Ion chemistry in the interstellar medium", *Annu. Rev. Anal. Chem.*, **1**, 229-259, (2008). 27

[40] A. Müller, "Electron-ion collisions: Fundamental processes in the focus of applied reseach", *Adv. At. Mol. Opt. Phys.*, **55**, 293-417, (2008). 28

[41] A. Burgess, "Delectronic recombination and the temperature of the solar corona.", *Astrophys. J.*, **139**, 776, (1964). 28, 32

[42] T. Stoehlker, "Strong alignment observed for the time-reversed photoionization process studied in relativistic collisions with bare uranium ions", *Phys. Rev. L*, **79**, 3270, (1997). 28

[43] D. W. Savin, S. M. Kahn, J. Linkemann, A. A. Saghiri, M. Schmitt, M. Grieser, R. Repnow, D. Schwalm, A. Wolf, T. Bartsch, C. Brandau, A. Hoffknecht, A. Müller, S. Schippers, M. H. Chen, and N. R. Badnell, "Dielectronic recombination in photoionized gas. II. Laboratory measurements for Fe XVIII and Fe XIX", *Astrophys. J. Suppl. Ser.*, **123**, 687, (1999). 29, 65

[44] M. Schnell, G. Gwinner, N. R. Badnell, M. E. Bannister, S. Böhm, J. Colgan, S. Kieslich, S. D. Loch, D. Mitnik, A. Müller, M. S. Pindzola, S. Schippers, D. Schwalm, W. Shi, A. Wolf, and S.-G. Zhou, "Observation of trielectronic recombination in Be-like Cl ions", *Phys. Rev. Lett.*, **91**, 043001, (2003). 29

[45] C. Beilmann, Z. Harman, P. H. Mokler, S. Bernitt, C. H. Keitel, J. Ullrich, and J. R. Crespo López-Urrutia, "Major role of multielectronic K-L intershell resonant recombination processes in Li- to O-like ions of Ar, Fe, and Kr", *Phys. Rev. A*, **88**, 062706, (2013). 29

[46] A. Hoffknecht, O. Uwira, S. Schennach, A. Frank, J. Haselbauer, W. Spies, N. Angert, P. H. Mokler, R. Becker, M. Kleinod, S. Schippers, and A. Müller, "Recombination of $Au^{25+}$with free electrons at very low energies", *J. Phys. B*, **31**, 2415, (1991). 30, 33, 57, 90

[47] M. S. Pindzola, N. R. Badnell, and D. C. Griffin, "Validity of the independent-process and isolated-resonance approximations for electron-ion recombination", *Phys. Rev. A*, **46**, 5725-5729, (1992). 30

[48] H. A. Kramers, "On the theory of X-ray absorption and of the continuous X-ray spectrum", *Philos. Mag.*, **46**, 836-871, (1923). 30

[49] M. Stobbe, "Zur Quantenmechanik photoelektrischer Prozesse", *Ann. Phys.*, **399**, 661-715, (1930). 31

[50] H. Bethe and E. Salpeter, *Quantum Mechanics of One- and Two-Electron Systems*. Springer Verlag, (1957). 31

[51] M. Pajek and R. Schuch, "Radiative recombination of bare ions with low-energy free electrons", *Phys. Rev. A*, **45**, 7894, (1992). 31

[52] A. Ichihara and J. Eichler, "Cross sections for radiative recombination and the photoelectric effect in the K, L and M shells of one-electron systems with $1 \leq Z \leq 112$ calculated within an exact relativistic description", *At. Data Nuc. Data Tab*, **74**, 1-121, (2000). 31

[53] V. M. Shabaev, V. A. Yerokhin, T. Beier, and J. Eichler, "QED corrections to the radiative recombination of an electron with a bare nucleus", *Phys. Rev. A*, **61**, 052112, (2000). 31

[54] B. W. Shore, "Dielectronic recombination", *Astrophys. J.*, **158**, 1205-1218, (1969). 31

[55] P. J. Storey, "Recombination processes", *Planetary Nebulae*, 199-208, (1983). 33

[56] A. Burgess and H. P. Summers, "The effects of electron and radiation density on dielectronic recombination", *Astrophys. J.*, **157**, 1007, (1969). 33

[57] J. W. Mather, "Formation of a high-density deuterium plasma focus", *Phys. Fluids*, **8**, 366, (1965). 33

[58] R. L. Watterson, R. E. Slusher, and C. M. Surko, "Low-frequency density fluctuations in a tokamak plasma", *Phys. Fluids*, **28**, 2857, (1985). 33

[59] T. Umebayashi, "The density of charged particles in very dense interstellar clouds", *Prog. Theor. Phys.*, **69**, 480-502, (1983). 33

[60] N. Badnell, C. Ballance, D. Griffin, and M. O'Mullane, "Dielectronic recombination of W^{20+} ($4d^{10}4f^{8}$): Adressing the half-open f shell", *Phys. Rev. A*, **85**, 052716, (2012). 33, 57, 58, 71, 87, 89, 91, 100

[61] D. W. Savin, T. Bartsch, M. H. Chen, S. M. Kahn, D. A. Liedahl, J. Linkemann, A. Müller, M. Schmitt, D. Schwalm, and A. Wolf, "Dielectronic recombination in photoionized gas: The importance of fine-structure core excitations", *Astrophys. J.*, **489**, 115, (1997). 33

[62] S. Schippers, D. Bernhardt, M. Grieser, M. Hahn, C. Krantz, M. Lestinsky, O. Novotný, R. Repnow, D. W. Savin, A. Wolf, and A. Müller, "Recombination of Au^{20+} at low electron-ion collision energies", *Phys. Scr.*, **T144**, 014039, (2011). 33, 100

[63] C. P. Ballance, D. C. Griffin, S. D. Loch, and N. R. Badnell, "Dielectronic recombination of Au^{20+}: a theoretical description of the resonances at low electron energies", *J. Phys. B: At. Mol. Opt. Phys*, **45**, 045001, (2012). 33, 100

[64] M. A. Levine, R. E. Marrs, J. R. Henderson, D. A. Knapp, and M. B. Schneider, "The electron beam ion trap: A new instrument for atomic physics measurements", *Phys. Scr.*, **T22**, 157, (1988). 35

[65] J. Rausch, A. Becker, K. Spruck, J. Hellhund, J. A. Borovik, K. Huber, S. Schippers, and A. Müller, "Electron impact single and double ionization of W^{17+}", *J. Phys. B*, **44**, 165202, (2011). 35

[66] E. M. McMillan, "The synchrotron – a proposed high energy particle accelerator", *Phys. Rev.*, **68**, 143, (1945). 35

[67] M. L. Oliphant, J. S. Gooden, and G. S. Hide, "The acceleration of charged particles to very high energies", *Proc. Phys. Soc.*, **59**, 666, (1947). 35

[68] M. Grieser, D. Habs, R. Hahn, C. M. Kleffner, R. Repnow, M. Stampfer, E. Jaeschke, and M. Steck, "Advanced stacking methods using electron cooling at the TSR Heidelberg", *IEEE Particle Accelerator Conference, San Francisco*, **5**, 2817 - 2819, (1991). 36, 44, 82

[69] K. Abrahamsson, G. Andlera, L. Bagge, E. Beebe, P. Carlé, H. Danared, S. Egnell, K. Ehrnstén, M. Engström, C. J. Herrlander, J. Hilke, J. Jeansson, A. Källberg, S. Leontein, L. Liljeby, A. Nilsson, A. Paal, K.-G. Rensfelt, U. Rosengård, A. Simonsson, A. Soltan, J. Starker, M. af Ugglas, and A. Filevich, "CRYRING - a synchrotron, cooler and storage ring", *Nucl. Instrum. Methods Phys. Res. A*, **79**, 269-272, (1993). 36

[70] B. Franzke, "The heavy ion storage and cooler ring project ESR at GSI", *Nucl. Instrum. Methods Phys. Res. B*, **24-25**, 18-25, (1987). 36

[71] A. Wolf, J. Berger, M. Bock, D. Habs., B. Hochadel, G. Kilgus, G. Neireither, U. Schramm, D. Schwalm, E. Szmola, A. Müller, M. Wagner, and R. Schuch, "Experiments with highly-charged ions in the storage ring TSR", *Z. Phys. D*, **21**, 69-75, (1991). 36, 47

[72] S. Schippers, D. Bernhardt, A. Müller, C. Krantz, M. Grieser, R. Repnow, A. Wolf, M. Lestinsky, M. Hahn, D. W. Savin, and O. Novotný, "Dielectronic recombination of xenonlike tungsten ions", *Phys. Rev. A*, **83**, 012711, (2011). 36, 47, 57, 58, 74, 77, 91, 98, 99, 100

[73] M. Hahn, A. Becker, M. Grieser, C. Krantz, M. Lestinsky, A. Müller, O. Novotný, R. Repnow, S. Schippers, K. Spruck, A. Wolf, and D. W. Savin, "Storage ring cross-section measurements for electron impact single and double ionization of Fe^{9+} and single ionization of Fe^{10+}", *Astrophys. J.*, **760**, 80, (2012). 36

[74] O. Novotný, A. Becker, H. Buhr, C. Domesle, W. Geppert, M. Grieser, C. Krantz, H. Kreckel, R. Repnow, D. Schwalm, K. Spruck, J. Stützel, B. Yang, A. Wolf, and D. W. Savin, "Dissociative recombination measurements of HCl^+ using an ion storage ring", *Astrophys. J.*, **777**, 54, (2013). 36, 68

[75] P. Seelig, S. Borneis, A. Dax, T. Engel, S. Faber, M. Gerlach, C. Holbrow, G. Huber, T. Kühl, D. Marx, K. Meier, P. Merz, W. Quint, F. Schmitt, M. Tomaselli, L. Völker, H. Winter, M. Würtz, K. Beckert, B. Franzke, F. Nolden, H. Reich, M. Steck, and T. Winkler, "Ground state hyperfine splitting of hydrogenlike $^{207}Pb^{81+}$ by laser excitation of a bunched ion beam in the GSI experimental storage ring", *Phys. Rev. Lett.*, **81**, 4824, (1998). 36

[76] M. B. Någård, J. B. C. Pettersson, A. M. Derkatch, A. Al Khalili, A. Neau, S. Rosén, M. Larsson, J. Semaniak, H. Danared, A. Källberg, F. Österdahl, and M. af. Ugglas, "Dissociative recombination of $D^+(D_2O)_2$ water cluster ions with free electrons", *J. Chem. Phys.*, **117**, 5264, (2002). 36

[77] U. V. Pedersen, M. Hyde, S. P. Møller, and T. Andersen, "Lifetime measurement of He^- utilizing an electrostatic ion storage ring", *Phys. Rev. A*, **64**, 012503, (2001). 36

[78] J. U. Andersen, P. Hvelplund, S. B. Nielsen, S. Tomita, H. Wahlgreen, S. P. Møller, U. V. Pedersen, J. S. Forster, and T. J. D. Jørgensen, "The combination of an electrospray ion source and an electrostatic storage ring for lifetime and spectroscopy experiments on biomolecules", *Rev. Sci. Instrum.*, **73**, 1284, (2002). 36

[79] T. Tanabe and K. Noda, "Storage of bio-molecular ions in the electrostatic storage ring", *Nucl. Instrum. Methods Phys. Res. A*, **496**, 233-237, (2003). 36

[80] P. Spiller and G. Franchetti, "The FAIR accelerator project at GSI", *Nucl. Instrum. Methods Phys. Res. A*, **561**, 305-309, (2006). 36

[81] M. Grieser, Y. A. Litvinov, R. Raabe, K. Blaum, Y. Blumenfeld, P. A. Butler, F. Wenander, P. J. Woods, M. Aliotta, A. Andreyev, A. Artemyev, D. Atanasov, T. Aumann, D. Balabanski, A. Barzakh, L. Batist, A. Bernardes, D. Bernhardt, J. Billowes, S. Bishop, M. Borge, I. Borzov, F. Bosch, A. J. Boston, C. Brandau, W. Catford, R. Catherall, J. Cederkäll, D. Cullen, T. Davinson, I. Dillmann, C. Dimopoulou, G. Dracoulis, C. E. Düllmann, P. Egelhof, A. Estrade, D. Fischer, K. Flanagan, L. Fraile, M. A. Fraser, S. J. Freeman, H. Geissel, J. Gerl, P. Greenlees, R. E. Grisenti, D. Habs, R. von Hahn, S. Hagmann, M. Hausmann, J. J. He, M. Heil, M. Huyse, D. Jenkins, A. Jokinen, B. Jonson, D. T. Joss, Y. Kadi, N. Kalantar-Nayestanaki, B. P. Kay, O. Kiselev, H.-J. Kluge, M. Kowalska, C. Kozhuharov, S. Kreim, T. Kröll, J. Kurcewicz, M. Labiche, R. C. Lemmon, M. Lestinsky, G. Lotay, X. W. Ma, M. Marta, J. Meng, D. Mücher, I. Mukha, A. Müller, A. S. J. Murphy, G. Neyens, T. Nilsson, C. Nociforo, W. Nörtershäuser, R. D. Page, M. Pasini, N. Petridis, N. Pietralla, M. Pfützner, Z. Podolyák, P. Regan, M. W. Reed, R. Reifarth, P. Reiter, R. Repnow, K. Riisager, B. Rubio, M. S. Sanjari, D. W. Savin, C. Scheidenberger, S. Schippers, D. Schneider, R. Schuch, D. Schwalm, L. Schweikhard, D. Shubina, E. Siesling, H. Simon, J. Simpson, J. Smith, K. Sonnabend, M. Steck, T. Stora, T. Stöhlker, B. Sun, A. Surzhykov, F. Suzaki, O. Tarasov, S. Trotsenko, X. L. Tu, P. V. Duppen, C. Volpe, D. Voulot, P. M. Walker, E. Wildner, N. Winckler, D. F. A. Winters, A. Wolf, H. S. Xu, A. Yakushev, T. Yamaguchi, Y. J. Yuan, Y. H. Zhang, ,

and K. Zuber, "Storage ring at HIE-ISOLDE - technical design report", *Eur. Phys. J. Spec. Topics*, **207**, 1-117, (2012). 36, 44, 45, 58, 149

[82] S. P. Møller and U. V. Pedersen, "ELISA - an electrostatic storage ring for atomic physics", *Proc. 6th European Particle Accelerator Conference*, 73, (1997). 36, 38

[83] R. D. Thomas, H. T. Schmidt, G. Andler, M. Björkhage, M. Blom, L. Brännholm, E. Bäckström, H. Danared, S. Das, N. Haag, P. Halldén, F. Hellberg, A. I. S. Holm, H. A. B. Johansson, A. Källberg, G. Källersjö, M. Larsson, S. Leontein, L. Liljeby, P. Löfgren, B. Malm, S. Mannervik, M. Masuda, D. Misra, A. Orbán, A. Paál, P. Reinhed, K.-G. Rensfelt, S. Rosén, K. Schmidt, F. Seitz, A. Simonsson, J. Weimer, H. Zettergren, and H. Cederquist, "The double electrostatic ion ring experiment: A unique cryogenic electrostatic storage ring for merged ion-beams studies", *Rev. Sci. Instrum.*, **82**, 065112, (2011). 36, 113

[84] S. Jinno, T. Takao, Y. Omata, A. Satou, H. Tanuma, T. Azuma, H. Shiromaru, K. Okuno, N. Kobayashi, and I. Watanabe, "TMU electrostatic ion storage ring designed for operation at liquid nitrogen temperature", *Nucl. Instrum. Methods Phys. Res., Sect. A*, **532**, 477-482, (2004). 36

[85] C. P. Welsch, J. Ullrich, C. G. ner, K.-U. Kühnel, A. Schempp, H. Schmidt-Böcking, and R. Dörner, "Electrostatic ring as the central machine of the Frankfurt Ion Storage Experiments", *Phys. Rev. Spec. Top. Accel. Beams*, **7**, 080101, (2004). 36

[86] M. Grieser, A. Becker, K. Blaum, S. George, C. Krantz, S. Vogel, A. Wolf, and R. von Hahn, "The status of the diagnostic system at the cryogenic storage ring CSR", *Proceedings - IPAC*, THPME121, (2014). 36, 50, 54, 126, 138

[87] Y. Nakano, W. Morimoto, T. Majima, J. Matsumoto, H. Tanuma, H. Shiromaru, and T. Azumaa, "A cryogenic electrostatic storage ring project at RIKEN", *J. Phys.: Conf. Ser.*, **388**, 142027, (2012). 36

[88] M. Lange, M. Froese, S. Menk, J. Varju, R. Bastert, K. Blaum, J. R. C. López-Urrutia, F. Fellenberger, M. Grieser, R. von Hahn, O. Heber, K.-U. Kühnel, F. Laux, D. A. Orlov, M. L. Rappaport, R. Repnow, C. D. Schröter, D. Schwalm, A. Shornikov, T. Sieber, Y. Toker, J. Ullrich, A. Wolf, and D. Zajfman, "A cryogenic electrostatic trap for long-time storage of keV ion beams.", *Rev. Sci. Instrum.*, **81**, 055105, (2010). 37

[89] J. Levin, U. Hechtfischer, L. Knoll, M. L. Saathoff, R. Wester, A. Wolf., D. Schwalm, and D. Zajfman, "Photodissociation spectroscopy of OH^+ molecular ions at the TSR storage ring", *Hyperfine Interact.*, **127**, 267-270, (2000). 39

[90] S. M. Trujillo, R. H. Neynaber, and E. W. Rothe, "Merging beams, a different approach to collisional cross section measurements", *Rev. Sci. Instrum.*, **37**, 1655-1661, (1966). 39

[91] R. A. Phaneuf, C. C. Havener, G. H. Dunn, and A. Müller, "Merged-beams experiments in atomic and molecular physics", *Rep. Prog. Phys.*, **62**, 1143, (1999). 39, 40

[92] G. I. Budker and A. N. Skrinskii, "Electron cooling and new possibilities in elementary particle physics", *Usp. Fiz. Nauk*, **124**, 561-595, (1978). 41

[93] D. S. Hall and G. Gabrielse, "Electron cooling of protons in a nested penning trap", *Phys. Rev. Lett.*, **77**, 1962-1965, (1996). 41

[94] D. Liesen, "Electron cooling of heavy ion beams", *Phys. Scr.*, **36**, 723-729, (1987). 41

[95] S. Kieslich, S. Schippers, W. Shi, A. Müller, G. Gwinner, M. Schnell, A. Wolf, E. Lindroth, and M. Tokman, "Determination of the 2s-2p excitation energy of lithiumlike scandium using dielectronic recombination", *Phys. Rev. A*, **70**, 042714, (2004). 42

[96] M. Larsson, "Dissociative recombination with ion storage rings", *Annu. Rev. Phys. Chem.*, **48**, 151-79, (1997). 42

[97] A. Lampert, A. Wolf, D. Habs, J. Kenntner, G. Kilgus, D. Schwalm, M. S. Pindzola, and N. R. Badnell, "High-resolution measurement of the dielectronic recombination of fluorinelike selenium ions", *Phys. Rev. A*, **53**, 1413Ũ1423, (1996). 42, 72

[98] D. Bernhardt, C. Brandau, Z. Harman, C. Kozhuharov, A. Müller, W. Scheid, S. Schippers, E. W. Schmidt, D. Yu, A. N. Artemyev, I. I. Tupitsyn, S. Böhm, F. Bosch, F. J. Currell, B. Franzke, A. Gumberidze, J. Jacobi, P. H. Mokler, F. Nolden, U. Spillman, Z. Stachura, M. Steck, , and T. Stöhlker, "Breit interaction in dielectronic recombination of hydrogenlike uranium", *Phys. Rev. A*, **83**, 020701, (2011). 42, 47, 67

[99] A. Müller, "Plasma rate coefficients for highly charged ion-electron collisions: New experimental access via ion storage rings", *Int. J. Mass Spectrom.*, **192**, 9-22, (1999). 43

[100] E. Jaeschke, D. Krämer, W. Arnold, G. Bisoffi, M. Blum, A. Friedrich, C. Geyer, M. Grieser, D. Habs, H.-W. Heyng, B. Holzer, R. Ihde, M. Jung, R. N. K. Matl, A. Noda, W. Ott, B. Povh, R. Repnow, F. Schmitt, M. Steck, and E. Steffens, "The Heidelberg test storage ring for heavy ions TSR", *Proceedings - EPAC Rome*, **1**, 365, (1988). 44

[101] P. Baumann, M. Blum, A. Friedrich, C. Geyer, M. Grieser, B. Holzer, E. Jaeschke, D. Krämer, C. Martin, K. Matl, R. Mayer, W. Ott, B. Povh, R. Repnow, M. Steck, E. Steffens, and W. Arnold, "The Heidelberg heavy ion test storage ring TSR", *Nucl. Instrum. Methods Phys. Res.*, **268**, 531-537, (1988). 44

[102] D. Habs, W. Baumann, J. Berger, P. Blatt, A. Faulstich, P. Krause, G. Kilgus, R. Neumann, W. Petrich, R. Stokstad, D. Schwalm, E. Szmola, K. Welti, A. Wolf, S. Zwickler, E. Jaeschke, D. Krämer, G. Bisoffi, M. Blum, A. Friedrich, C. Geyer, M. Grieser, H. Heyng, B. Holzer, R. Ihde, M. Jung, K. Matl, W. Ott, B. Povh, R. Repnow, M. Steck, E. Steffens, D. Dutta, T. Kühl, and D. Marx, "First experiments with the Heidelberg test storage ring TSR", *Nucl. Instrum. Methods Phys. Res., Sect. B*, **43**, 390-410, (1989). 44

[103] D. Bernhardt, A. Becker, M. Grieser, M. Hahn, C. Krantz, M. Lestinsky, O. Novotný, R. Repnow, D. W. Savin, K. Spruck, A. Wolf, A. Müller, and S. Schippers, "Absolute rate coefficients for photorecombination and electron-impact ionization of magnesiumlike iron ions from measurements at a heavy-ion storage ring", *Phys. Rev. A*, **90**, 012702, (2014). 44, 65

[104] M. Grieser, D. Habs, R. von Hahn, C. Ellert, C. M. Kleffner, J. Liebmann, R. Repnow, D. Schwalm, M. Stampfer, A. Wolf, E. Jaeschke, and S. Papureanu, "Recent development at the Heidelberg heavy ion cooler storage ring TSR", *Proceedings - EPAC*, **1**, 152-157, (1992). 44

[105] S. Schröder, R. Klein, N. Boos, M. Gerhard, R. Grieser, G. Huber, A. Karafillidis, M. Krieg, N. Schmidt, T. Kühl, R. Neumann, V. Balykin, M. Grieser, D. Habs, E. Jaeschke, D. Krämer, M. Kristensen, M. Music, W. Petrich, D. Schwalm, P. Sigray, M. Steck, B. Wanner, , and A. Wolf, "First laser cooling of relativistic ions in a storage ring", *Phys. Rev. Lett.*, **64**, 2901, (1990). 44

[106] E. Träbert, A. G. Calamai, J. D. Gillaspy, G. Gwinner, X. Tordoir, and A. Wolf, "Intercombination and forbidden transition rates in C- and N-like ions (O^{2+}, F^{3+}, and S^{9+}) measured at a heavy-ion storage ring", *Phys. Rev. A*, **62**, 022507, (2000). 44

[107] S. Schippers, E. W. Schmidt, D. Bernhardt, A. M. D. Yu, M. Lestinsky, D. A. Orlov, M. Grieser, R. Repnow, and A. Wolf, "Storage-ring measurement of the hyperfine induced $^{47}Ti^{18+}(2s2p\,^3P_0 \rightarrow 2s^2\,^1S_0)$ transition rate", *Phys. Rev. Lett.*, **98**, 033001, (2007). 44

[108] H. Buhr, M. B. Mendes, O. Novotný, D. Schwalm, M. H. Berg, D. Bing, O. Heber, C. Krantz, D. A. Orlov, M. L. Rappaport, T. Sorg, J. Stützel, J. Varju, A. Wolf, and D. Zajfman, "Energy-sensitive imaging detector applied

to the dissociative recombination of D_2H^+", *Phys. Rev. A*, **81**, 062702, (2010). 44

[109] C. Nordhorn, D. Bing, H. Buhr, M. Grieser, O. Heber, C. Krantz, M. B. Mendes, R. R. amd Dirk Schwalm, A. Shornikov, J. Stützel, A. Wolf, O. Novotný, M. Lestinsky, Å. Larson, M. Stenrup, and A. E. Orel, "Branching ratios in dissociative recombination of formyl and isoformyl cations", *J. Phys.: Conf. Ser.*, **300**, 012004, (2011). 44

[110] D. Fischer, D. Globig, J. Goullon, M. Grieser, R. Hubele, V. L. B. de Jesus, A. Kelkar, A. LaForge, H. Lindenblatt, D. Misra, B. Najjari, K. Schneider, M. Schulz, M. Sell, and X. Wang, "Ion-lithium collision dynamics studied with a laser-cooled in-ring target", *Phys. Rev. Lett.*, **109**, 113202, (2012). 44

[111] R. Schuch, "Atomic physics at the Heidelberg test storage ring (TSR)", *Nucl. Instrum. Methods Phys. Res.*, **B24/25**, 11-17, (1987). 45

[112] D. A. Orlov, M. Lestinsky, F. Sprenger, D. Schwalm, A. S. Terekhov, and A. Wolf, "Ultra-cold electron beams for the Heidelberg TSR and CSR", *AIP Conf. Proc,*, **821**, 478, (2006). 45

[113] M. Steck, G. Bisoffi, M. Blum, A. Friedrich, C. Geyer, M. Grieser, B. H. H. Jaeschke, M. J. J. Krämer, K. M. M. Ott, and R. Repnow, "Electron cooling of heavy ions", *Nucl. Instrum. Methods Phys. Res., Sect. A*, **287**, 324-327, (1990). 45

[114] H. Danared, G. Andler, L. Bagge, C. J. Herrlander, J. Hilke, J. Jeansson, A. Källberg, A. Nilsson, A. Paál, K.-G. Rensfelt, U. R. rd, J. Starker, and M. af Ugglas, "Electron cooling with an ultracold electron beam", *Phys. Rev. Lett.*, **72**, 3775-3778, (1994). 45

[115] S. Pastuszka, U. Schramm, M. Grieser, C. Broude, R. Grimm, D. Habs, J. Kenntner, H.-J. Miesner, T. S. ler, D. Schwalm, and A. Wolf, "Electron cooling and recombination experiments with an adiabatically expanded electron beam", *Nucl. Instrum. Methods Phys. Res., Sect. A*, **369**, 11-22, (1996). 45

[116] A. Hoffknecht, T. Bartsch, S. Schippers, A. Müller, N. Eklöw, P. Glans, M. Beutelspacher, M. Grieser, G. Gwinner, A. A. Saghiri, and A. Wolf, "Recombination of F^{6+} with free electrons at very low energies", *Phys. Scr.*, **T80**, 298-300, (1999). 45

[117] A. Wolf, G. Gwinner, J. Linkemann, A. A. Saghiri, M. Schmitt, D. Schwalm, M. Grieser, M. Beutelspacher, T. Bartsch, C. Brandau, A.Hoffknecht, A. Müller, S. Schippers, O. Uwira, and D. W. Savin, "Recombination in electron coolers", *Nucl. Instrum. Methods Phys. Res. A*, **441**, 183-190, (2000). 47

[118] F. Sprenger, M. Lestinsky, D. Orlov, D. Schwalm, and A. Wolf, "The high-resolution electron-ion collision facility at TSR", *Nucl. Instrum. Methods Phys. Res. A*, **532**, 298-302, (2004). 45

[119] C. Krantz, *Intense Electron Beams from GaAs Photocathodes as a Tool for Molecular and Atomic Physics*. PhD thesis, Ruperto-Carola University of Heidelberg, Germany, (2009). 45, 46, 50

[120] R. Repnow, "Progress and upgrading of the Heidelberg high current injector", *PRAMANA*, **59**, 835-848, (2002). 47

[121] S. Schippers, A. Müller, G. Gwinner, J. Linkemann, A. A. Saghiri, and A. Wolf, "Storage ring measurement of the C IV recombination rate coefficient", *Astrophys. J.*, **555**, 1027-1037, (2001). 47, 74

[122] E. W. Schmidt, D. Bernhard, A. Müller, S. Schippers, S. Fritzsche, J. Hoffmann, A. Jaroshevich, C. Krantz, M. Lestinsky, D. A. Orlov, A. Wolf, D. Lukiċ, and D. W. Savin, "Electron-ion recombination of Si IV forming Si III: Storage-ring measurement and multiconfiguration Dirac-Fock calculations", *Phys. Rev. A*, **76**, 032717, (2007). 47

[123] K. Rinn, A. Müller, H. Eichenauer, and E. Salzborn, "Development of single-particle detectors for keV ions", *Rev. Sci. Instrum.*, **53**, 829, (1982). 48, 59, 68, 106, 111, 120, 126, 133

[124] A. Shornikov, D. A. Orlov, C. Krantz, A. S. Jaroshevich, and A. Wolf, "Maximum intensity, transmission limited cold electron beams from GaAs photocathode in the eV and sub-eV kinetic energy range", *Phys. Rev. Spec. Top. Accel. Beams*, **17**, 042802, (2014). 50

[125] C. Krantz, F. Berg, K. Blaum, F. Fellenberger, M. Froese, M. Grieser, R. von Hahn, M. Lange, F. Laux, S. Menk, R. Repnow, A. Shornikov, and A. Wolf, "The cryogenic storage ring and its application to molecular ion recombination physics", *J. Phys.: Conf. Ser.*, **300**, 012010, (2011). 50

[126] A. Becker, R. v. Hahn, O. Novotný, K. Spruck, S. Vogel, A. Wolf, and C. Krantz, "Neutral imaging detector". to be published, (2015). 52, 114, 141

[127] K. Spruck, A. Becker, F. Fellenberger, M. Grieser, R. v. Hahn, V. Klinkhamer, O. Novotný, S. Schippers, S. Vogel, A. Wolf, and C. Krantz, "An efficient, movable single-particle detector for use in cryogenic ultra high vacuum environments", *Rev. Sci. Instrum.*, **86**, 023303, (2015). 52, 54, 101

[128] R. von Hahn, F. Berg, K. Blaum, J. C. Lopez-Urrutia, F. Fellenberger, M. Froese, M. Grieser, C. Krantz, K.-U. Kühnel, M. Lange, S. Menk, F. Laux, D. Orlov, R. Repnow, C. Schröter, A. Shornikov, T. Sieber, J. Ullrich, A. Wolf, M. Rappaport, and D. Zajfman, "The electrostatic cryogenic storage ring CSR

– mechanical concept and realization", *Nucl. Instrum. Methods Phys. Res., Sect. B*, **269**, 2871-2874, (2011). 53

[129] Q. S. Shu, R. W. Fast, and H. L. Hart, "Heat flux from 277 to 77 K through a few layers of multilayer insulation", *Cryogenics*, **26**, 671-677, (1986). 53

[130] Ruag Space GmbH (Austria), "Datasheet brochure for vacuum thermal insulation", (2012). 53

[131] A. Petrignani, S. Altevogt, M. H. Berg, D. Bing, M. Grieser, J. Hoffmann, B. Jordon-Thaden, C. Krantz, M. B. Mendes, O. Novotný, S. Novotny, D. A. Orlov, R. Repnow, T. Sorg, J. Stützel, A. Wolf, H. Buhr, H. Kreckel, V. Kokoouline, and C. H. Greene, "Resonant structure of low-energy H^{3+} dissociative recombination", *Phys. Rev. A*, **83**, 032711, (2011). 54

[132] F. Grussie, *in preperation*. PhD thesis, Ruprecht-Karls-Universität Heidelberg, (2015). 54

[133] R. Otto, A. von Zastrow, T. Best, and R. Wester, "Internal state thermometry of cold trapped molecular anions", *Chem. Phys.*, **15**, 612, (2013). 55

[134] G. F. Gribakin and S. Sahoo, "Mixing of dielectronic and multiply excited states in electron-ion recombination: a study of Au^{24+}", *J. Phys. B: At. Mol. Opt. Phys.*, **36**, 3349, (2003). 57, 87

[135] K. Spruck, N. R. Badnell, C. Krantz, O. Novotný, A. Becker, D. Bernhardt, M. Grieser, M. Hahn, R. Repnow, D. W. Savin, A. Wolf, A. Müller, and S. Schippers, "Recombination of W^{18+} ions with electrons: Absolute rate coefficients from a storage-ring experiment and from theoretical calculations", *Phys. Rev. A*, **90**, 032715, (2014). 57, 58, 71, 74, 87, 91, 92, 94, 95, 100, 101

[136] V. Dzuba, V. Flambaum, G. Gribakin, and C. Harabati, "Chaos-induced enhancement of resonant multielectron recombination in highly charged ions: Statistical theory", *Phys. Rev. A.*, **86**, 022714, (2012). 57, 58, 71, 87, 89, 90, 91, 92, 93, 94

[137] V. A. Dzuba, V. V. Flambaum, G. F. Gribakin, C. Harabati, and M. G. Kozlov, "Electron recombination, photoionization, and scattering via many-electron compound resonances", *Phys. Rev. A*, **88**, 062713, (2013). 57, 90, 91, 93, 100

[138] N. R. Badnell, K. Spruck, C. Krantz, O. Novotný, A. Becker, D. Bernhardt, M. Grieser, M. Hahn, R. Repnow, D. W. Savin, A. Wolf, A. Müller, and S. Schippers, "Recombination of W^{19+} ions with electrons: Absolute rate coefficients from a storage-ring experiment and from theoretical calculations", *in preperation*, (2015). 58, 78, 91, 96

[139] M. Grieser. private communication, (2014). 59, 112

[140] M. Lestinsky, *High-Resolution Electron Collision Spectroscopy with Multicharged Ions in Merged Beams*. PhD thesis, Ruperto-Carola University of Heidelberg, Germany, (2007). 59, 68

[141] N. R. Badnell, "A Breit-Pauli distorted wave implementation for autostructure", *Comput. Phys. Commun.*, **182**, 1528-35, (2011). 60, 88

[142] N. R. Badnell. private communication, (2014). 60, 61

[143] M. Lestinsky, N. R. Badnell, D. Bernhardt, D. Bing, M. Grieser, M. Hahn, J. Hoffman, B. Jordan-Thaden, C. Krantz, O. Novotný, D. A. Orlov, R. Rempow, A. Shornikov, A. Müller, S. Schippers, A. Wolf, and D. W. Savin, "Electron-ion recombination of Mg^{6+} forming Mg^{5+} and of Mg^{7+} forming Mg^{6+}: Laboratory measurements and theoretical calculations", *Astrophys. J.*, **758**, 40, (2012). 60

[144] S. Wolfram, "The mathematica book", *Cambridge University Press and Wolfram Research, Inc.*, **100**, 61820-7237, (2000). 61

[145] A. Kramida and T. Shirai, "Energy levels and spectral lines of tungsten, W III through W LXXIV", *At. Data Nucl. Data Tables*, **95**, 305-474, (2009). 61, 62, 63, 67

[146] G. Kilgus, D. Habs, D. Schwalm, A. Wolf, N. Badnell, and A. Müller, "High-resolution measurement of dielectronic recombination of lithiumlike Cu^{26+}", *Phys. Rev. A*, **46**, 5730, (1992). 65, 71, 72

[147] M. Lestinsky, N. R. Badnell, D. Bernhardt, M. Grieser, J. Hoffmann, D. Lukić, A. Müller, D. A. Orlov, R. Repnow, D. W. Savin, E. W. Schmidt, M. Schnell, S. Schippers, A. Wolf, and D. Yu, "Electron-ion recombination of Fe X forming Fe IX and of Fe XI forming Fe X: Laboratory measurements and theoretical calculations", *Astrophys. J.*, **698**, 648Ũ659, (2009). 68

[148] M. Hahn, D. Bernhardt, M. Lestinsky, A. Múller, O. Novotný, S. Schippers, A. Wolf, and D. W. Savin, "Storage ring measurement of electron impact ionization for Mg^{7+} forming Mg^{8+}", *Astrophys. J.*, **712**, 1166, (2010). 68

[149] H. B. Pedersen, H. Buhr, S. Altevogt, V. Andrianarijaona, H. Kreckel, L. Lammich, N. de Ruette, E. M. Staicu-Casagrande, D. Schwalm, D. Strasser, X. Urbain, D. Zajfman, and A. Wolf, "Dissociative recombination and low-energy inelastic electron collisions of the helium dimer ion", *Phys. Rev. A*, **72**, 012712, (2005). 69

[150] O. Novotný, N. R. Badnell, D. Bernhardt, M. Grieser, M. Hahn, C. Krantz, M. Lestinsky, A. Müller, R. Repnow, S. Schippers, A. Wolf, and D. W. Savin, "Electron-ion recombination of Fe XII forming Fe XI: Laboratory measurements and theoretical calculations", *Astrophys. J.*, **753**, 57, (2012). 69

[151] T. F. Gallagher, *Rydberg Atoms (Cambridge Monographs on Atomic, Molecular, and Chemical Physics 3)*. Cambridge Univ. Press, (1994). 73

[152] G. Gwinner, A. Hoffknecht, T. Bartsch, M. Beutelspacher, N. Eklöw, P. Glans, M. Grieser, S. Krohn, E. Lindroth, A. Müller, A. Saghiri, S. Schippers, U. Schramm, D. Schwalm, M. Tokman, G. Wissler, and A. Wolf, "Influence of magnetic fields on electron-ion recombination at very low energies", *Phys. Rev. Lett.*, **84**, 4822-4825, (2000). 76

[153] M. Hörndl, S. Yoshida, A. Wolf, G. Gwinner, and J. Burgdörfer, "Enhancement of low-energy electron ion recombination in a magnetic field : Influence of transient field effects", *Phys. Rev. Lett.*, **95**, 243201, (2005). 76

[154] M. F. Gu, "The flexible atomic code", *Can. J. Phys.*, **86(5)**, 675-689, (2008). 87

[155] M. J. Li, Y. B. Fu, G. D. Zhang, Y. Z. Zhang, C. Z. Dong, and F. Koike, "Dielectronic recombination of the 4p and 4d open sub-shell tungsten ions", *J. Phys.: Conf. Ser.*, **488**, 062022, (2014). 87

[156] M. Li, Y. Fu, M. Su, C. Dong, and F. Koike, "Dielectronic recombination of Br-like tungsten ions", *Plasma Sci. Technol.*, **16**, 182-187, (2014). 87

[157] C. Krantz, K. Spruck, N. R. Badnell, A. Becker, D. Bernhardt, M. Grieser, M. H. O. Novotný, R. Repnow, D. W. Savin, A. Wolf, A. Müller, and S. Schippers, "Absolute rate coefficients for the recombination of open-f-shell tungsten ions", *J. Phys.: Conf. Ser.*, **488**, 012051, (2014). 87

[158] Y. Hahn, "Theory of dielectronic recombination", *Adv. At. Mol. Phys.*, **21**, 123-196, (1985). 88

[159] D. M. Mitnik, M. S. Pindzola, and N. R. Badnell, "Total and partitioned recombination cross sections for F^{6+}", *Phys. Rev. A*, **59**, 3592-3600, (1999). 88

[160] G. F. Gribakin, A. A. Gribakina, and V. V. Flambaum, "Quantum chaos in multicharged ions and statistical approach to the calculation of electron-ion resonant radiative recombination.", *Aust. J. Phys.*, **52**, 443-457, (1999). 88, 89

[161] V. V. Flambaum, A. A. Gribakina, G. F. Gribakin, and C. Harabati, "Electron recombination with multicharged ions via chaotic many-electron states", *Phys. Rev. A*, **66**, 012713, (2002). 90

[162] http://aphysics2.lanl.gov. 94

[163] J. F. Ziegler, "SRIM-2003", *Nucl. Instrum. Methods Phys. Res., Sect. B*, **219-220**, 1027-1036, (2004). 106

[164] P. Roth and G. W. Fraser, "Microchannel plate resistance at cryogenic temperatures", *Nucl. Instrum. Methods Phys. Res., Sect. A*, **439**, 134-137, (2000). 106, 120

[165] S. Rosén, H. T. Schmidt, P. Reinhed, D. Fischer, R. D. Thomas, , and H. Cederquist, "Operating a triple stack microchannel plate-phosphor assembly for single particle counting in the 12-300 K temperature range.", *Rev. Sci. Instrum.*, **78**, 113301, (2007). 106, 120

[166] K.-U. Kuehnel, C. D. Schröter, and J. Ullrich, "Operating MCP detectors at cryogenic temperatures", *Proceedings - EPAC Genoa*, TUPC055, (2008). 106, 120

[167] J. A. Schecker, M. M. Schauer, K. Holzscheiter, and M. H. Holzscheiter, "The performance of a microchannel plate at cryogenic temperatures and in high magnetic fields, and the detection efficiency for low energy positive hydrogen ions", *Nucl. Instrum. Methods Phys. Res., Sect. A*, **320**, 556-561, (1992). 106, 120, 122

[168] E. M. Baroody, "A theory of secondary electron emission from metals", *Phys. Rev.*, **78**, 780-787, (1950). 108, 111, 131

[169] R. A. Baragiola, E. V. Alonso, J. Ferron, and A. Oliva-Florio, "Ion-induced electron emission from clean metals", *Surf. Sci.*, **90**, 240-255, (1979). 108, 131, 136

[170] D. A. Dahl, "SIMION for the personal computer in reflection", *Int. J. Mass Spectrom.*, **200**, 3-25, (2000). 110

[171] G. Wehner, "Energieverteilung der von 2, 5, 10 und 15 keV He- und Ar-Ionen an Molybdän ausgelösten Elektronen", *Z. Phys.*, **193**, 439-442, (1966). 111

[172] N. Colombie, C. Benazeth, J. Mischler, and L. Viel, "Angular and energetic distribution of secondary electrons emitted by solid targets under ionic bombardment", *Radiat. Eff.*, **18**, 251-255, (1973). 111

[173] E. Marquardt, J. Le, and R. Radebaugh, "Cryogenic material properties database", *11th International Cryocooler Conference*, (2000). 118

[174] O. Siegmund, "Preconditioning of microchannel plate stacks", *Proc. SPIE*, **1072**, 111, (1989). 122

[175] L. A. Dietz and J. Sheffield, "Spectrometer for measuring secondary electron yields induced by ion impacts on thin film oxide surfaces", *Rev. Sci. Instrum.*, **44**, 183, (1973). 130, 131

[176] J. R. Prescott, "A statistical model for photomultiplier single-electron statistics", *Nucl. Instrum. Methods*, **39**, 173-179, (1966). 130, 143

[177] G. Lakits, F. Aumayr, and H. Winter, "Statistics of ion-induced electron emission from a clean metal surface", *Rev. Sci. Instrum.*, **60**, 3151, (1989). 130

[178] D. A. Orlov, H. Fadil, M. Grieser, C. Krantz, J. Hoffmann, O. Novotný, S. Novotny, and A. Wolf, "Electron cooling with photocathode electron beams applied to slow ions at TSR and CSR", *Proceedings - COOL*, FRM1C03, (2007). 131

[179] M. Galanti, R. Gott, and J. F. Renaud, "A high resolution, high sensitivity channel plate image intensifier for use in particle spectrographs", *Rev. Sci. Instrum.*, **42**, 1818, (1971). 131

[180] J. L. Wiza, "Microchannel plate detectors", *Nucl. Instrum. Methods*, **162**, 587-601, (1979). 131

[181] G. W. Fraser, "The electron detection efficiency of microchannel plates", *Nucl. Instrum. Methods*, **206**, 445-449, (1983). 131

[182] A. Müller, N. Djurić, G. H. Dunn, and D. S. Belić, "Ansolute detection efficiency of microchannel plates for 0.1-2.3 keV electrons and 2.1-4.4 keV Mg^+ ions", *Rev. Sci. Instrum.*, **57**, 349-353, (1986). 131

[183] R. Moshammer and R. Matthäus, "Secondary electron emission by low energy ion impact", *J. Phys. Colloques*, **50**, 111, (1989). 131

[184] P. Schackert, "Zur Sekundärelektronenemission durch Argonionen und Argonatome im Energiebereich von 1 bis 20 keV", *Z. Phys.*, **197**, 32-40, (1966). 135

[185] L. E. Collins and P. T. Stroud, "The multiple emission of electrons in a secondary-electron particle counter", *Br. J. Appl. Phys.*, **18**, 1121, (1967). 135

[186] G. D. Magnuson and C. E. Carlston, "Electron ejection from metals due to 1- to 10-keV noble gas ion bombardment. I. Polycrystalline materials", *Phys. Rev.*, **129**, 2403, (1962). 136

Aknowledgements

This work would not have been possible without the support of many colleagues and my family.

First, I would like to thank those who initially enabled that work: Stefan Schippers, for accepting me as a doctoral student and being a really patient doctoral father (always waiting for me to finish the analysis of the tungsten data), and Andreas Wolf for taking me in and promoting the COMPACT project. I'm grateful that in this way I had the opportunity of being part of two storage ring projects and I hope that I could contribute my part.

In addition I would like to thank Claude Krantz whom I could always count on even though laboratory work, measurements, and analysis took sometimes until midnight. He was always keeping me on track for the project, prevented me from destroying (even more) expensive laboratory equipment, and he played a major role in the development of COMPACT. Also, he did a really good job in reading and polishing this thesis.

I'm grateful for all the support I received from the CSR crews, the mechanical workshops (König's men, Koschorreck and Co, Hahn/Falkenthal workshop, Kaiser's workshop, and the main workshop) as well as the scientific staff (the Wolf-group and the guys living in the accelerator building). I was really relieved that no one was angry at me when I forced us to vent CSR during commissioning in 2014 :o)

Last I would like to thank my family and especially my puma for being helpful and supportive without ever doubting me or my decisions. Who would I be without them.

Versicherung

Ich erkläre:

Ich habe die vorgelegte Dissertation selbstständig und ohne unerlaubte fremde Hilfe und nur mit der Hilfe angefertigt, die ich in der Dissertation angegeben habe.

Alle Textstellen, die wörtlich oder sinnesgemäß aus veröffentlichten Schriften entnommern sind, und alle Angaben, die auf mündlichen Auskünften beruhen, sind als solche kenntlich gemacht.

Bei den von mir durchgeführten und in der Dissertation erwähnten Untersuchungen habe ich die Grundsätze guter wissenschaftlicher Praxis, wie sie in der „Satzung der Justus-Liebig-Universität Gießen zur Sicherung guter wissenschaftlicher Praxis“ niedergelegt sind, eingehalten.

Heidelberg, 30. Mai 2015 _____